THE UNIVERSITY *of* EDINBURGH

Thermal Hall and Heat Capacity Studies of Topological Magnetic Insulators and Superconductors

Luke Pritchard Cairns

Doctor of Philosophy
The University of Edinburgh
December 2020

Abstract

This thesis describes the development, and implementation, of effective low temperature thermal measurements, and their application in investigating the thermal transport and heat capacity of topological systems.

The first investigation concerns the quantum magnet $SrCu_2(BO_3)_2$. This material is a physical realisation of the Shastry-Sutherland model - a two-dimensional square lattice, solved to have a ground state of singlets on diagonal bonds. A number of theoretical studies have suggested that the material should host a topological phase of magnetic excitations (or triplons), which may manifest a thermal Hall effect - arguably the best experimental probe of neutral, topologically non-trivial quasiparticles. However, within the measured experimental resolution, the material exhibits no thermal Hall signal. The theory relies on triplon-triplon interactions being negligible, such that the triplon number is conserved. The results suggest that - in the temperature range under investigation - this is not a fair assumption. Additionally, an identical procedure has been used to investigate $Lu_2V_2O_7$ - a material that has been shown to exhibit a thermal Hall effect, of a similar magnitude to that which was predicted for $SrCu_2(BO_3)_2$. This measurement was successful in replicating those previous results, and thus demonstrated the feasibility of detecting a similar signal in $SrCu_2(BO_3)_2$.

The same experimental procedure has also been adapted in order to investigate the thermal transport properties of the heavy fermion superconductor UPt_3 at mK temperatures. This experiment was intended to test a recent theoretical prediction that the low temperature B-phase should exhibit a zero-field anomalous thermal Hall effect. Observation of such an effect would be the first definitive proof of bulk chiral superconductivity. Although no zero-field signal was found, the material does exhibit a thermal Hall effect approaching the in-field B-C transition (between two superconducting phases). Further measurements have

sought to clarify the origin of this effect, and in particular, whether it might be linked to the chirality of the superconducting state.

Finally, the specific heat of the heavy fermion compounds UAu_2 and UTe_2 has been measured at mK temperatures, with a bespoke heat capacity stage. In the former, the specific heat shows non-Fermi liquid behaviour, deep within an antiferromagnetically ordered phase. This contrasts with the majority of heavy fermion compounds, wherein non-Fermi liquid behaviour is attributed to a close proximity to a magnetic quantum critical point. Additionally, the specific heat indicates there is a magnetic phase transition at high fields, at which point the material reverts to a Fermi liquid behaviour. This implies the quantum critical behaviour in UAu_2 is tied to the antiferromagnetic order. UTe_2 is a heavy fermion superconductor, anticipated to host a topological form of superconductivity. For this material, specific heat measurements have been employed to demonstrate that the superconducting properties vary with composition. Most notably, the residual specific heat as $T \rightarrow 0$ appears to be negatively correlated with the superconducting transition temperature. This contradicts a recent hypothesis that the residual contribution is due to only one spin direction being paired in the superconducting state.

Lay Summary

The 2016 Nobel Prize was awarded for "theoretical discoveries of topological phase transitions and topological phases of matter". This was the culmination of decades of research, transforming topology from a mathematical abstraction into a core concept in condensed matter physics. The next step is to exploit this newfound understanding in order to manufacture new technologies. For example, topological insights have already given birth to the fields of spintronics - which has the potential to drastically improve the efficiency of computer memory and logic - and topological superconductivity - the key to a new kind of *quantum* computing.

The revolutionary materials central to these new technologies will likely be realised in electronic systems. However, whilst a number of compounds have already been demonstrated to host topologically non-trivial phases of electrons, these are far from being commercially useful. In order to make this jump, we first require a fuller understanding of the physical consequences of topology in real materials, something which is severely complicated in electronic systems by the strong interactions between electrons.

Fortunately, topological phenomena are not confined to just electronic systems - magnetic excitations, lattice vibrations and photons have all been demonstrated - under appropriate conditions - to be topologically non-trivial. In these bosonic systems, the interactions between particles are weak, and as a result, such systems have recently been pushed into the research spotlight, in the hope that their comparative 'simplicity' might pave the way to a mastery of their electronic counterparts. This is at the heart of our own research interest.

The hallmark of a topological system - regardless of constituent particles - is an edge current, which circulates in a single direction. If a thermal gradient is applied to a material which hosts an edge current, this current will become unbalanced,

and the result will be a thermal gradient perpendicular to that which is applied. This phenomenon is known as the thermal Hall effect, and has emerged as one of the best probes of topological non-triviality in systems with charge-neutral excitations. In this work, we have used measurements of the thermal Hall effect in order to investigate two topological materials. The first - $SrCu_2(BO_3)_2$ - is an example of a bosonic topological insulator, wherein collective magnetic excitations are anticipated to be topologically non-trivial, and therefore give rise to a thermal Hall effect. The second - UPt_3 - is instead expected to host a topological form of superconductivity. In this material, it is the excitations of the superconducting state that are topologically non-trivial, and manifest as a thermal Hall effect.

Declaration

I declare that this thesis was composed by myself, that the work contained herein is my own except where explicitly stated otherwise in the text, and that this work has not been submitted for any other degree or professional qualification except as specified.

(*Luke Pritchard Cairns, December 2020*)

Acknowledgements

First and foremost I would like to thank my supervisor, Andrew Huxley, for giving me the opportunity to do this research, and then for the many, many hours spent in the lab and in discussion. I would also like to thank Chris O'Neill for his help and guidance throughout, as well as the other members of my group - Oliver Entwisle, Chris Clark, Callum Stevens and Hector Leong - for their advice and assistance. In addition, I would like to thank Harry Keen, Gavin Woolman and Iain Muntz, for the hours spent avoiding work.

I would like to thank the mechanical and electronic workshops in Edinburgh, and in particular Derek Low, Mike Fisher, Richard Taylor and Bojan Masic, for their help in the construction of my experiments, and for fixing my mistakes. Also, thanks go to Xiao Wang for his assistance in operating the PPMS. In St.Andrews, I would like to thank Callum Smith and Chris Watson, for countless helium transfers, and extreme patience. Also in St.Andrews, thanks go to Jean-Phillipe Reid and Andreas Rost, for their expertise in all things green cryostat.

Additionally, I would like to thank my friends - Alex, Paddy, Ollie, Dave, Josh and James - for keeping me entertained throughout, as well as my siblings - Christian, Ben, Josh, Matthew, Kelly and Danielle - for always keeping me on my toes. I would like to thank my parents for giving me every opportunity in the world, and for their support no matter which path I chose. Finally, I would like to thank Janna, for being alongside me every step of the way.

Contents

Chapter 1

Introduction

Science is driven by a cooperation between experiment and theory. As such, it is essential to appreciate and understand the theory which underlies any experimental investigation. That is the aim of this chapter - to introduce those subjects which form the basis of our investigations.

We begin with a discussion of topological non-triviality; a concept which has become widespread in modern condensed matter physics, and indeed relevant to potentially all of the materials contained within this thesis. Unconventional superconductivity will then briefly be introduced; being one of the defining characteristics of all of the heavy fermion compounds which feature. Finally, we conclude with a discussion of the versatility of thermal measurements, and specifically, how one might disentangle the various temperature and field dependent contributions.

1.1 Topology in Condensed Matter

Until recently, quantum states of matter were thought to be entirely described - at least phenomenologically - by Landau theory, and thus classified by the principle of spontaneous symmetry breaking. However, it has become clear that there are topological phases which cannot be described by a local order parameter, and therefore do not fit into this framework. The topological revolution began with the discovery of the quantum Hall effect, and continues to this day with the drive to realise topological states of ever more exotic collective excitations. Lately, the

focus has swung towards bosonic systems, in the hope that their comparative 'simplicity' might lead to a better understanding of their strongly interacting, fermionic counterparts. The hunt is also on for materials which might host a topological form of superconductivity, and by extension, the Majorana particles which form the basis of quantum computing.

Unfortunately, it is notoriously difficult to access the signatures of topological non-triviality by experiment. In bosonic systems, such as $SrCu_2(BO_3)_2$ (Chapter 3), the topologically non-trivial component is often electrically neutral. Alternatively, in materials such as UPt_3 or UTe_2 (Chapter 4 and Section 5.3 respectively), the topological features are contained within, and obscured by, the superconducting state. In both of these systems however, the topological phenomena reveal themselves via an anomalous thermal current, and may therefore be probed by a measurement of transverse thermal conductivity. This section aims to make clear what constitutes a topologically non-trivial material, and why such a material should play host to an anomalous Hall effect.

Quantifying Topology

Topology is the study of geometric properties which are preserved through smooth deformations. For example, as shown in Figure 1.1, a rich tea biscuit is topologically distinct from a party ring - the two may be smoothly deformed into a sphere and a torus respectively, but not one another. For two-dimensional surfaces such as these, topological distinction may be made more formal via the Gauss-Bonnet theorem,

$$\chi = \frac{1}{2\pi} \int_S K dA, \tag{1.1}$$

where K is the Gaussian curvature, and χ is the Euler characteristic. This states that, for a boundaryless, two-dimensional surface, the integral of the Gaussian curvature over the entire surface only depends on χ, which is a measure of the number of holes in the surface. χ is therefore perhaps the simplest example of a topological invariant.

For a one-dimensional curve, the curvature is a measure of how fast the unit tangent vector to the curve rotates. This can be straightforwardly extended to the situation above - K being the product of the two principal curvatures - but it will be useful to define curvature more generally, using parallel transport. This is the method of transporting a vector about a surface, without rotating it about the

axis normal to that surface. Importantly, when the vector is parallel transported around a closed loop, the degree to which the vector is rotated with respect to its original orientation provides some measure of the curvature. This is illustrated for a sphere in Figure 1.1.

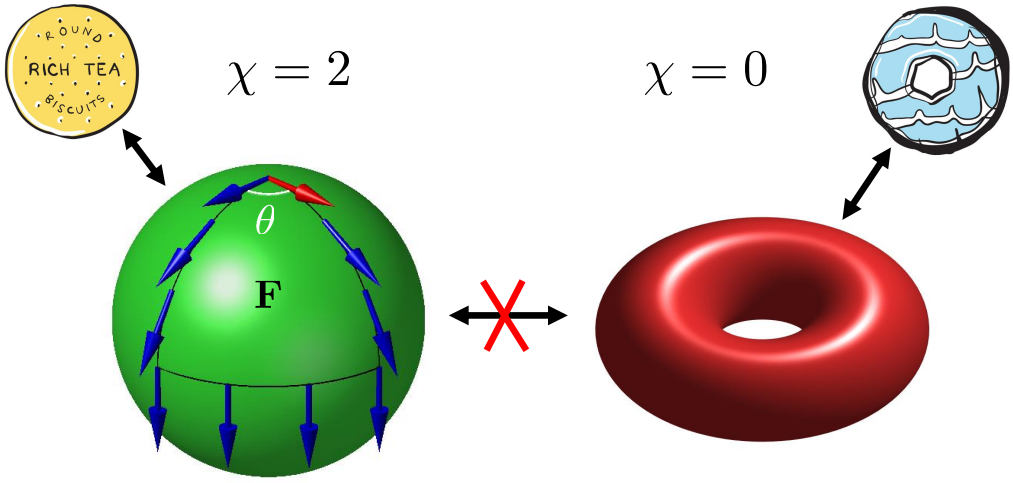

Figure 1.1 *The sphere (rich tea biscuit) and torus (party ring) have different Euler characteristics (χ), and are therefore topologically distinct. Also shown is the parallel transport of a vector around a closed loop on the surface of the sphere. θ, the geometric phase, is the angle by which the vector must be rotated in order to return to its original orientation, and provides some measure of $\mathbf{F}$, the curvature of the area enclosed by the path taken.*

Let us now formalise the relation between the curvature of a surface and parallel transport across that surface [1]. We begin with a orthonormal reference frame, $(\mathbf{n}, \mathbf{e}^1, \mathbf{e}^2)$, where $\mathbf{n}(\mathbf{r})$ is the vector normal to the surface at $\mathbf{r}$, and $\mathbf{e}^i$ are therefore tangential. In order to parallel transport this frame across the surface, the condition to be fulfilled is that

$$\boldsymbol{\phi}^* \cdot \dot{\boldsymbol{\phi}} = 0, \tag{1.2}$$

where

$$\boldsymbol{\phi} = \frac{\mathbf{e}^1 + i\mathbf{e}^2}{\sqrt{2}}, \tag{1.3}$$

a complex unit vector, and the overdot indicates the time derivative.

In order to quantify the degree of rotation as this reference frame is parallel transported across the surface, we require a second, fixed, frame $(\mathbf{n}(\mathbf{r}), \mathbf{t}^1(\mathbf{r}), \mathbf{t}^2(\mathbf{r}))$, defined at every point on the surface, where again, $\mathbf{n}$ is the vector normal to the

surface, and $\mathbf{t}^i$ are tangential. As with the transported frame, this fixed frame may be expressed as

$$\mathbf{u}(\mathbf{r}) = \frac{\mathbf{t}^1(\mathbf{r}) + i\mathbf{t}^2(\mathbf{r})}{\sqrt{2}}. \tag{1.4}$$

At any point $\mathbf{r}$, and after a time t, the transported frame $\boldsymbol{\phi}$ and the local frame $\mathbf{u}$ will be related by

$$\boldsymbol{\phi}(t) = e^{-i\theta(t)}\mathbf{u}(\mathbf{r}(t)), \tag{1.5}$$

or in words, the transported frame must be rotated by an angle $\theta(t)$ in order to coincide with the fixed frame. Inserting this expression into the condition for parallel transport (Equation 1.2) then gives

$$\boldsymbol{\phi}^* \cdot \dot{\boldsymbol{\phi}} = -i\dot{\theta}\mathbf{u}^* \cdot \mathbf{u} + \mathbf{u}^* \cdot \dot{\mathbf{u}} = 0, \tag{1.6}$$

and therefore, for parallel transport around a closed loop $\mathcal{C}$,

$$\theta = \mathrm{Im} \oint_{\mathcal{C}} \mathbf{u}^* \cdot d\mathbf{u}. \tag{1.7}$$

This process is illustrated in Figure 1.2.

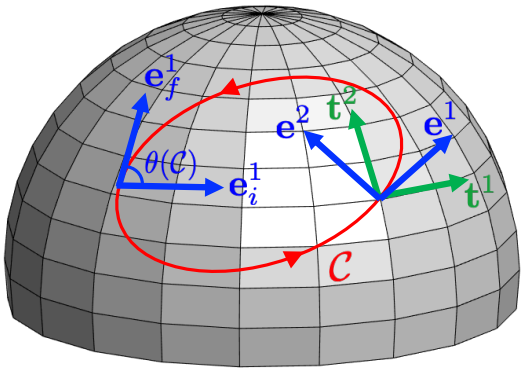

Figure 1.2 *Schematic to show parallel transport of the reference frame $\boldsymbol{\phi} \sim \mathbf{e}^1 + i\mathbf{e}^2$ across the surface of a sphere, as described in the text. $\mathbf{e}_i^1$ and $\mathbf{e}_f^1$ are the initial and final reference frame vectors respectively, with $\theta(\mathcal{C})$ the geometric phase acquired when moving around the closed loop $\mathcal{C}$. Also included is an example of the local frame, $\mathbf{u} \sim \mathbf{t}^1 + i\mathbf{t}^2$, defined at every point on the surface.*

Finally - and in anticipation of what follows - we can relate the so-called anholonomy angle $\theta(\mathcal{C})$ to the curvature of the surface. In doing this, we first

define the vector field,

$$A_i(\mathbf{R}) = \mathrm{Im}\left[u_j^*(\mathbf{R})\frac{\partial u_j(\mathbf{R})}{\partial R_i}\right], \tag{1.8}$$

where $\mathbf{R}$ represents a coordinate system on the surface, and we have employed Einstein summation notation. This is otherwise known as the connection, as it provides the relation between - or 'connects' - nearby points on the surface. Note this is a gauge dependent property, defined by the choice of local vectors $\mathbf{u}$. From this follows the curvature,

$$\mathbf{F} = \nabla \times \mathbf{A}, \tag{1.9}$$

which is instead gauge invariant. Using these expressions, we can re-express the anholonomy angle as

$$\theta = \oint_{\mathcal{C}} \mathbf{A} \cdot d\mathbf{r} = \iint_S \mathbf{F} \cdot d\mathbf{S}, \tag{1.10}$$

where, in deriving the second expression, we have used Stokes' theorem. Hence, the geometric phase acquired when moving around a closed loop depends solely on the area and curvature of the surface enclosed [2].

Topology in Physical Systems

This idea appears rather abstract, but is in fact ubiquitous in quantum mechanics. Consider a system of n non-degenerate levels, described by

$$H(\mathbf{X})|n(\mathbf{X})\rangle = E_n(\mathbf{X})|n(\mathbf{X})\rangle, \tag{1.11}$$

where $\mathbf{X}$ are a set of external parameters. If we change these parameters slowly - such that the system evolves adiabatically - but then ultimately return the system to its original condition, an arbitrary state will have evolved as

$$|n\rangle' = e^{i\gamma} e^{-\frac{i}{\hbar}\int_0^t E_n dt'}|n\rangle. \tag{1.12}$$

The situation described is analogous to the parallel transport of a vector around a surface, with the vector being replaced by an eigenstate, and the surface being parameter space. As such, γ in this expression is also a geometric phase. The second factor is the dynamical phase, present for any energy eigenstate which evolves as a function of time, and is irrelevant to this discussion.

This geometric phase is obviously inherent to quantum mechanics, but it was

long assumed that it could be removed by an appropriate gauge transformation [3]. Further, the phase of a wavefunction will not change the expectation value of a Hermitian operator, and thus has no bearing on any observable quantity. As a result, the geometric phase was initially deemed inconsequential. However, in a seminal paper [4], Berry showed that the geometric phase acquired over a *closed* cycle is a gauge invariant quantity and must therefore have a physical significance.

This so-called Berry phase is particularly relevant to condensed matter physics. In a crystalline material, the one-electron wavefunctions may be written in Bloch form, as

$$|\psi_{n\mathbf{k}}(\mathbf{r})\rangle = e^{i\mathbf{k}\cdot\mathbf{r}}|u_{n\mathbf{k}}(\mathbf{r})\rangle, \tag{1.13}$$

where n is the band index, $\mathbf{k}$ is the crystal momentum, and $|u_{n\mathbf{k}}(\mathbf{r})\rangle$ is an eigenstate periodic on the unit cell. Two features in particular make this framework particularly amenable to the analysis above:

(i) The single particle states can be labeled by their crystal momentum $\mathbf{k}$ - this may therefore play the role of the surface, or parameter space.

(ii) This surface (the Brillouin zone) is periodic - making it straightforward, in the majority of cases, to integrate over a closed loop.

As such, and following an identical procedure as in the derivation of the geometric phase (Equation 1.10), we may define the *Berry* phase as

$$\gamma_n = \oint_C \mathcal{A}_n \cdot d\mathbf{k} = \int_S \mathcal{F}_n d^2\mathbf{k}, \tag{1.14}$$

where $\mathcal{A}$ is the Berry connection, given by

$$\mathcal{A}_n = i\langle u_{n\mathbf{k}}(\mathbf{r})|\nabla_{\mathbf{k}}|u_{n\mathbf{k}}(\mathbf{r})\rangle, \tag{1.15}$$

and $\mathcal{F}$ the Berry curvature, with

$$\mathcal{F}_n = \nabla \times \mathcal{A}_n. \tag{1.16}$$

As with the geometric phase that comes from the parallel transport of a vector, the Berry phase acquired over a closed loop is a gauge invariant property that depends only on the area and curvature of the loop traversed across the Brillouin zone [5].

Before discussing some Berry phase phenomena - and ultimately how this is related to our experimental investigations - it is worth re-introducing the concept of topological invariance. Recall the Gauss-Bonnet theorem (Equation 1.1), which states that the integral of the Gaussian curvature over a closed, two-dimensional surface will be equal to an integer topological invariant - the Euler characteristic. We are now in a position to generalise this statement; instead, the *Berry* curvature integrated over any closed surface, regardless of dimension, will be equal to an integer topological invariant. This topological invariant is known as the Chern number. More formally, this may be expressed as

$$\int \mathcal{F}_{ij} dS^{ij} = 2\pi C, \tag{1.17}$$

where C is the Chern number. In this expression, we have dropped the explicit band dependence n, and also employed Einstein summation notation in order to emphasise that this remains true regardless of dimension [6].

In a crystalline material, the above expression implies that we can ascribe a topological invariant to any *filled* band, as only a filled band may be regarded as a closed surface. This condition is naturally satisfied in the bands of an insulator. Therefore, two insulators may be topologically distinct from one another based on the topology of their respective band structures. Put more formally, two insulators are only topologically equivalent if there is an adiabatic path connecting them along which the energy gap remains finite. As such, at an interface between two topologically distinct materials, there must be a point where the energy gap vanishes, corresponding to a topological phase transition. This is the basis for the conducting states found on the surfaces of those materials termed topological insulators.

An Example - The Two-Band Model

We now consider the most tractable example of a Berry phase effect, contained within a two-band model [7]. Although simple, this model is relevant to a wide range of systems, and will be especially useful in describing the material $SrCu_2(BO_3)_2$ (Chapter 3), as well as helping to understand topological superconductivity in the next section. The Hamiltonian for such a system is given by

$$H(\mathbf{k}) = \varepsilon(\mathbf{k})\mathbf{I} + \mathbf{d}(\mathbf{k}) \cdot \boldsymbol{\sigma}, \tag{1.18}$$

where $\boldsymbol{\sigma}$ are the Pauli matrices. If we employ spherical coordinates and parametrise the $\mathbf{d}$-vector as $\mathbf{d} = |d|(\sin\theta\cos\phi, \sin\theta\sin\phi, \cos\theta)$, the normalised eigenstates will be given by

$$|+\rangle = \begin{pmatrix} e^{-i\phi}\cos\frac{\theta}{2} \\ \sin\frac{\theta}{2} \end{pmatrix} \qquad |-\rangle = \begin{pmatrix} e^{-i\phi}\sin\frac{\theta}{2} \\ -\cos\frac{\theta}{2} \end{pmatrix}, \tag{1.19}$$

with energy eigenvalues $\varepsilon \pm |d|/2$ (although we may set $\varepsilon = 0$ without loss of generality). Hence, if $\mathbf{d}(\mathbf{k})$ is non-zero for all $\mathbf{k}$, this model could represent an insulator.

The Berry curvature may be calculated from Equations 1.15 and 1.16. Reverting to Cartesian coordinates, this is given by

$$\mathcal{F}_{\mp} = \pm\frac{1}{2}\frac{\mathbf{d}}{|\mathbf{d}|^3}, \tag{1.20}$$

where $\mp$ labels the lower/upper band. This is equivalent to the field generated by a monopole of strength $\pm\frac{1}{2}$, located at $\mathbf{d} = 0$, which is the point at which the two energy levels coincide. Degeneracies in the spectrum of the Hamiltonian therefore act as singularities of Berry curvature, or as sources/sinks of Berry curvature flux.

In order to see this more clearly, it is helpful to draw an analogy to electrodynamics, and specifically between the magnetic field - a field in real space - and the Berry curvature - a field in parameter space. Extending this analogy, the Berry connection is equivalent to the magnetic vector potential, and the Berry phase to the magnetic flux. Therefore, the Berry phase acquired over a closed loop $\mathcal{C}$, taken in parameter space, will be equal to the amount of flux passing through the surface enclosed by that loop. This is illustrated in Figure 1.3. By extension, the Berry curvature of a closed surface will be equal to the number of Berry monopoles contained within that surface, multiplied by 2π. This follows from the fact that for a closed loop on the surface, the inside/outside of that loop (red/yellow regions in Figure 1.3) is arbitrary, and therefore the two surface integrals must agree with one another up to a multiple of 2π. This was Dirac's original argument for the quantisation of the magnetic monopole.

All of this is simply a restatement of the fact that the integral of the Berry curvature over a close surface will be equal to a topological invariant - the Chern number. In condensed matter physics, a filled band constitutes a closed surface, and may therefore be assigned a topological invariant. Any such surface

which surrounds a Berry monopole - which we now define as a degeneracy in the spectrum of the Hamiltonian - will then have a non-zero Chern number, and is thus topologically non-trivial.

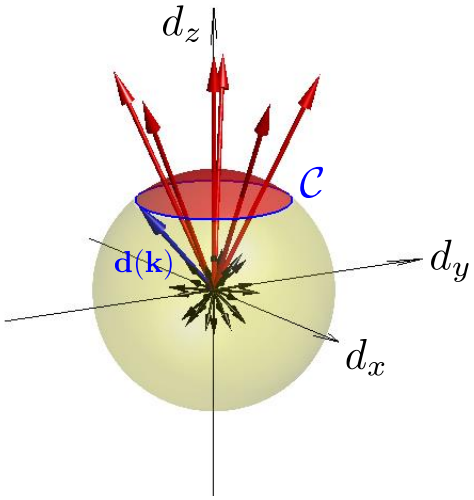

Figure 1.3 *Schematic to show a closed surface surrounding a Berry monopole of strength $\frac{1}{2}$, located at the origin of parameter space, as in the two-level model discussed in the text. For a closed surface, the Berry curvature will be equal to the number of Berry monopoles contained within the surface, quantised in units of 2π. The blue line, labelled $\mathcal{C}$, shows a closed path taken in parameter space. The Berry phase acquired around $\mathcal{C}$ is related to the amount of flux passing through the enclosed surface. Note however, the enclosed surface (red or yellow) is an arbitrary choice.*

The Integer Quantum Hall Effect

Looking towards our own investigations, the next step will be to establish why a topologically non-trivial band should give rise to anomalous transport terms. The integer quantum Hall effect (IQHE) was first observed experimentally in 1980 [8], and marked the beginning of a topological revolution in condensed matter physics. In the original IQHE experiment, it was found that in a strong magnetic field, the Hall conductivity of a two-dimensional electron gas is exactly quantised in units of e^2/h, or that

$$\sigma_{xy} = n\frac{e^2}{h}. \tag{1.21}$$

This result can be derived in a number of ways. Perhaps most famously, the TKNN paper demonstrated that the Hall conductivity could be expressed as the

integral of the Berry curvature over all filled bands [9]. As such, n in the above expression will be the sum of the Chern numbers for each of those bands, and will therefore be quantised. Whilst this is elegant, in anticipation of what follows, we will instead derive the above expression using the semiclassical equations of motion of an electron wave packet.

The electron wave packet is a linear combination of Bloch waves (Equation 1.13), chosen such that the wave packet is localised to some extent in both $\mathbf{r}$ and $\mathbf{k}$ space. The central positions of the wave packet may be described by the semiclassical equations of motion

$$\hbar\dot{\mathbf{x}} = \frac{\partial\varepsilon_n(\mathbf{k})}{\partial\mathbf{k}} + \hbar\dot{\mathbf{k}} \times \mathcal{F}_n(\mathbf{k}), \tag{1.22}$$

$$\hbar\dot{\mathbf{k}} = -e\nabla U(\mathbf{r}) + e\dot{\mathbf{x}} \times \mathbf{B}, \tag{1.23}$$

where $\varepsilon_n(\mathbf{k})$ is the band energy and U is the electrostatic potential. The velocity thus comprises both the familiar band dispersive term, as well as an anomalous Berry curvature dependent term. This additional term was originally derived in order to explain the anomalous Hall effect in a ferromagnetic materials [10], and has only recently been re-interpretted as a Berry phase effect [11].

From the above expressions, it is clear that the anomalous velocity will always be perpendicular to an applied electric field, and therefore, Bloch bands with non-zero Berry curvature will result in a Hall effect. Specifically for a two-dimensional system, the transverse conductivity will be

$$\sigma_{xy} = -\frac{e^2}{\hbar}\sum_n \int_{BZ} \frac{d^2\mathbf{k}}{2\pi}\mathcal{F}_{n,z}(\mathbf{k})\rho^F(\varepsilon_n(\mathbf{k})), \tag{1.24}$$

where the sum is over all bands, the integral is over the Brillouin zone and $\rho^F(\varepsilon_n(\mathbf{k}))$ is the Fermi-Dirac distribution function. It follows that for a two-dimensional band insulator at zero temperature

$$\sigma_{xy} = -\frac{e^2}{\hbar}\sum_{n\in occ.} C_n, \tag{1.25}$$

or that the transverse conductivity is the sum of the Chern numbers of all occupied bands. Note that, in the original experiment, the applied magnetic field was acting to divide the conduction bands into Landau levels - thus rendering the material a band insulator - rather than to drive the IQHE. Occupied, topologically non-trivial bands are the only requirement for an IQHE.

Equation 1.24 is relevant to a range of systems. For example, it is a starting point in deriving the intrinsic anomalous Hall effect in ferromagnets, wherein the local Berry curvature can drive a Hall effect in partially occupied bands [3]. This can be viewed as the unquantised version of the IQHE. The same equation may also be used to understand the spin Hall effect [12], in which the spin up and spin down electrons move in opposite directions. In a nonmagnetic material, as a result of the spin-orbit interaction, opposite spin electrons will have a Berry curvature of opposite sign. Equation 1.24 then tells us that the two spin directions will acquire an anomalous velocity of the opposite sign, and that there will be two separate spin currents with opposite chirality.

From the above, a Berry curvature induced anomalous current appears fairly universal. However, in many situations this contribution may be neglected entirely [3]. To see this, consider the expression for the electron wave packet velocity (Equation 1.22) and in particular, the effect of symmetry operations. We find that, for a time reversal symmetric system,

$$\mathcal{F}_n(-\mathbf{k}) = -\mathcal{F}_n(\mathbf{k}), \tag{1.26}$$

whereas for a system with inversion symmetry,

$$\mathcal{F}_n(-\mathbf{k}) = \mathcal{F}_n(\mathbf{k}). \tag{1.27}$$

As such, a system with both time reversal and inversion symmetry will have zero Berry curvature, and therefore no topological contribution to the transverse conductivity.

The Magnon Hall Effect

We now finally turn to look at Berry phase effects in a system of magnons, and specifically, the conditions necessary for such a system to exhibit a thermal Hall effect [13]. The derivation will proceed in a similar fashion to that outlined above - utilising a semiclassical theory of Berry curvature dynamics - albeit with a few essential differences. Unlike with the electrical Hall effect, the measured transverse current will differ from the carrier number current. Additionally, the magnon is a boson, and will therefore obey Bose-Einstein statistics. And finally, an applied thermal gradient will necessarily have an influence on the distribution function; this 'external force' must therefore be introduced slightly more subtly, as

compared to the electric field in the previous example. As such, we first consider a system in thermal equilibrium.

The semiclassical equations of motion (Equations 1.22 and 1.23) describe the time evolution of a electron wave packet. A magnon can also be treated using the same framework. Specifically, the semiclassical equations of motion for a magnon wave packet become

$$\hbar\dot{\mathbf{x}} = \frac{\partial\varepsilon_n(\mathbf{k})}{\partial\mathbf{k}} + \hbar\dot{\mathbf{k}} \times \mathcal{F}_n(\mathbf{k}), \tag{1.28}$$

$$\hbar\dot{\mathbf{k}} = -\nabla U(\mathbf{r}), \tag{1.29}$$

where $U(\mathbf{r})$ is a generic potential. If we consider a finite two-dimensional sample, $U(\mathbf{r})$ might be the confining potential at the sample boundary. For example, taking an edge parallel to y, such that $U(x = a) = 0$ inside the sample and $U(x = b) = \infty$ outside, we have for the edge current

$$\begin{aligned} I_y &= \int_a^b dx \frac{1}{\hbar V} \sum_{n,\mathbf{k}} \rho^B(\varepsilon_{n,\mathbf{k}} + U(\mathbf{r}))[\nabla U(\mathbf{r}) \times \boldsymbol{\mathcal{F}}_n(\mathbf{k})]_y \\ &= -\frac{1}{\hbar V} \sum_{n,\mathbf{k}} \int_{\varepsilon_{n,\mathbf{k}}}^{\infty} d\varepsilon \rho^B(\varepsilon) \mathcal{F}_{n,z}(\mathbf{k}), \end{aligned} \tag{1.30}$$

where ρ^B is the Bose-Einstein distribution function and V is the sample area. Note that the band dispersive term, or group velocity, from Equation 1.28 has been ignored, as this will cancel for a sum over a system in thermal equilibrium.

Obviously the above expression is independent of the edge direction; the magnon edge current only requires a spatially varying potential (and that the magnon bands have a Berry curvature) to be non-zero. As such, even in thermal equilibrium there will be a edge current. Consider now that a thermal gradient is applied to the sample. As illustrated in Figure 1.4 (a), this will act to unbalance the edge currents, and give rise to a transverse temperature gradient. Therefore, even in this gross simplification, we have a thermal Hall effect.

This picture is somewhat misleading - in a real material, the magnon coherence length rarely exceeds the sample dimensions. Instead therefore, we might imagine that the magnon is confined within a coherence length [14]. As such, we slightly extend our schematic, and divide the two-dimensional sample into smaller regions, with the magnon subject to a confining potential at the edge of each smaller region. The magnon current will therefore circulate the edge of each of these

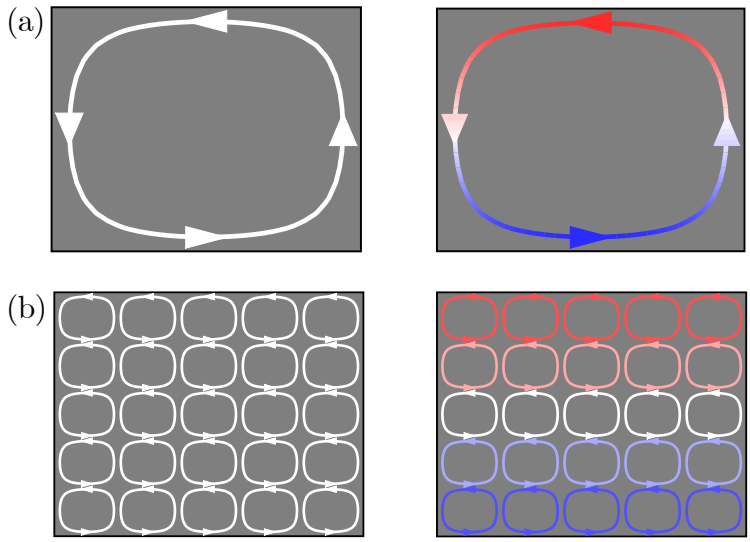

Figure 1.4 *(a) Schematic of the magnon edge current moving perpendicular to the sample edge; the application of a thermal gradient results in a transverse temperature gradient. (b) Schematic of magnon edge currents circulating smaller regions, which similarly gives a transverse current when a thermal gradient is applied to the sample.*

regions, and in thermal equilibrium, the currents around neighbouring regions will exactly cancel, leaving only a current circulating the sample edge. However, once a thermal gradient is applied, there is no longer complete cancellation in the bulk. As a result, there is now a thermal current perpendicular to the applied thermal gradient, and throughout the sample. Although still phenomenological, this schematic perhaps makes the origins of a thermal Hall effect more transparent, and is illustrated in Figure 1.4 (b).

To make this more formal, we begin by extending Equation 1.30 to include both sides of a region of confining potential, and also account for any temperature difference between the two sides. With reference to the schematic in Figure 1.5, and specifically for the current density along y, we have

$$\begin{aligned} j_y = \frac{1}{w}\Bigg[&\int_a^{b_2} dx \frac{1}{\hbar V} \sum_{n,\mathbf{k}} \rho^B \left(\varepsilon_{n,\mathbf{k}} + U(\mathbf{r}); T\left(\frac{w}{2}\right)\right) \frac{\partial U(\mathbf{r})}{\partial x} \mathcal{F}_{n,z}(\mathbf{k}) \\ &+ \int_{b_1}^{a} dx \frac{1}{\hbar V} \sum_{n,\mathbf{k}} \rho^B \left(\varepsilon_{n,\mathbf{k}} + U(\mathbf{r}); T\left(-\frac{w}{2}\right)\right) \frac{\partial U(\mathbf{r})}{\partial x} \mathcal{F}_{n,z}(\mathbf{k}) \Bigg], \end{aligned} \tag{1.31}$$

or more generally,

$$\mathbf{j} = \nabla \times \frac{1}{\hbar V} \sum_{n,\mathbf{k}} \int_{\varepsilon_{n,\mathbf{k}}}^{\infty} \rho^B(\varepsilon) \boldsymbol{\mathcal{F}}_n(\mathbf{k}) d\varepsilon. \tag{1.32}$$

However, as previously mentioned, the magnon number current is not the same as the thermal current $\mathbf{j}_Q$. Rather, the two are related by $\mathbf{j}_Q = \mathbf{j}_E - \mu\mathbf{j}$, where

$$\mathbf{j}_E = \nabla \times \frac{1}{\hbar V} \sum_{n,\mathbf{k}} \int_{\varepsilon_{n,\mathbf{k}}}^{\infty} \varepsilon \rho^B(\varepsilon) \boldsymbol{\mathcal{F}}_n(\mathbf{k}) d\varepsilon \tag{1.33}$$

is the energy current density, and μ the chemical potential.

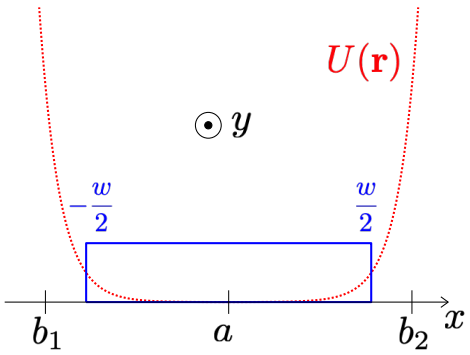

Figure 1.5 *Schematic to help visualise the situation described by Equation 1.31. The sample, of width w along x, is in blue, and the corresponding confining potential $U(\mathbf{r})$ is in red.*

Finally, we look to calculate an experimentally measurable property - the transverse thermal conductivity. In order to do this, and following a framework developed to treat a system of electrons [15], we consider the linear response to thermal (or chemical potential) gradients

$$\mathbf{j} = L_{11}[-\nabla U - \nabla\mu] + L_{12}\left[T\nabla\left(\frac{1}{T}\right)\right] \tag{1.34}$$

$$\mathbf{j}_Q = L_{21}[-\nabla U - \nabla\mu] + L_{22}\left[T\nabla\left(\frac{1}{T}\right)\right], \tag{1.35}$$

where in this case, μ is the magnon chemical potential. The transverse thermal conductivity is then defined as $\kappa^{xy} = L_{22}^{xy}/T$. Therefore, for a thermal gradient

in the y-direction, the current densities will be given by

$$\begin{Bmatrix} j \\ j_E \end{Bmatrix}_x^{\Delta T} = T\left[\frac{\partial}{\partial y}\left(\frac{1}{T}\right)\right]\sum_{n,\mathbf{k}}\int_{\varepsilon_{n,\mathbf{k}}}^{\infty}\begin{Bmatrix} 1 \\ \varepsilon \end{Bmatrix}\frac{\varepsilon-\mu}{\hbar V}\left(\frac{\partial \rho^B}{\partial \varepsilon}\right)\mathcal{F}_{n,z}(\mathbf{k})d\varepsilon, \tag{1.36}$$

where, for clarity,

$$\frac{\partial \rho^B(\varepsilon)}{\partial T} = (\varepsilon-\mu)\frac{\partial \rho^B(\varepsilon)}{\partial \varepsilon}T\frac{\partial}{\partial T}\left(\frac{1}{T}\right). \tag{1.37}$$

The thermal Hall conductivity is therefore

$$\kappa^{xy} = -\frac{k_B^2 T}{\hbar V}\sum_{n,\mathbf{k}} c_2(\rho^B(\varepsilon_{n\mathbf{k}}))\mathcal{F}_{n,z}(\mathbf{k}), \tag{1.38}$$

where

$$c_2(\rho^B) = (1+\rho^B)\left[\log\left(\frac{1+\rho^B}{\rho^B}\right)\right]^2 - (\log\rho^B)^2 - 2\mathrm{Li}_2(-\rho^B), \tag{1.39}$$

and $\mathrm{Li}_2(z)$ is the polylogarithm function. Importantly, Equation 1.38 reveals that the thermal Hall effect will depend on magnitude of the Berry curvature in thermally occupied parts of the magnon band structure, and therefore will not be quantised.

A thermal Hall effect carried by magnons has only been observed in a handful of materials [16–18], in part due to the stringent requirements any material must fulfil in order to exhibit an experimentally detectable signal. Aside from the material playing host to magnetic excitations, ideally these excitations should also be non-interacting. Magnon-magnon interactions will violate the conservation of the magnon number, and hence complicate the above analysis. Further, the magnon bands must possess a non-zero Berry curvature. The most straightforward way to achieve this is via the Dzyaloshinskii-Moriya interaction, which is analogous to the spin-orbit interaction for electrons (and will be discussed further in Chapter 3). Essentially, this gives the periodic part of the Bloch wavefunction some $\mathbf{k}$-dependence; a necessity for a finite Berry curvature (Equation 1.16). Note, the aforementioned symmetry restrictions are still relevant. Finally, as with the IQHE, the above derivation includes no mention of an applied magnetic field. However, in almost all systems to exhibit a thermal Hall effect of magnons, an applied field is utilised to induce topological transitions. All these considerations will be relevant to the discussion of $SrCu_2(BO_3)_2$ in

1.2 Unconventional Superconductivity

Superconductivity is broadly divided into two categories - conventional and unconventional. At the most fundamental level, the conventional superconducting state only breaks gauge symmetry - the condensate has a phase coherence - whereas the unconventional state breaks symmetries in addition to this. As such, unconventional superconductivity can refer to a number of different pairing states, building in complexity. At present, conventional superconductivity is the only form which has an established microscopic description - the celebrated BCS theory. All other forms of superconductivity must instead be described using phenomenological models. However, as will be discussed, this is a powerful tool in linking the symmetries of the superconducting condensate to its thermodynamic properties.

In a conventional superconductor, the superconducting gap function is isotropic, reflecting the isotropic pairing interaction between electrons. This interaction comes in the form of a retarded attraction, deriving from electron-phonon interactions, and thus relies on the electrons moving much faster than the ions. However, in the materials which form the basis of our investigation, this is not a fair assumption. UPt_3, UTe_2 and UAu_2 are all heavy fermion materials, wherein strong correlations lead to the electrons having large effective masses. In these materials, retardation effects are not sufficient to overcome the Coulomb repulsion between electrons. Despite this, all three materials exhibit superconductivity, implying that the electrons must bind in higher angular momentum channels, so as to overcome the short range Coulomb repulsion. The attractive interaction, and by extension, the superconducting condensate, will be anisotropic. By definition, these materials are therefore unconventional superconductors.

Cooper Pairing

A precursor to - and essential ingredient of - the full BCS theory was the realisation that two electrons sitting on the Fermi surface can be bound by an arbitrarily weak attractive interaction. This bound state has been subsequently labelled, eponymously, a Cooper pair. The formation of a Cooper pair does

not require a precisely specified interaction, only that there exists a filled Fermi surface. Therefore, in anticipation of a discussion of unconventional superconductivity, we consider two electrons - sitting on top of a zero temperature, filled Fermi surface - interacting via an unspecified, spin-independent potential $V(\mathbf{r}_1 - \mathbf{r}_2)$ [19].

This is a quantum mechanical problem, and so in order to establish whether a bound state exists it is natural to begin with the Schrödinger equation. For this system, we have

$$-\frac{\hbar^2}{2m}(\nabla_1^2 + \nabla_2^2)\psi(\mathbf{r}_1, \mathbf{r}_2) + V(\mathbf{r}_1 - \mathbf{r}_2)\psi(\mathbf{r}_1, \mathbf{r}_2) = \left(\Delta + \frac{\hbar^2 k_F^2}{m}\right)\psi(\mathbf{r}_1, \mathbf{r}_2), \quad (1.40)$$

where the energy has been split into the Fermi surface contribution and Δ. We expect the lowest energy state to be that of zero momentum, and therefore the two electrons should have opposite momenta. Following the standard procedure for eigenenergy solutions, we transfer the above expression to momentum space, which gives

$$\frac{\hbar^2 k^2}{m} g(\mathbf{k}) + \int \frac{d^3k'}{(2\pi)^3} V(\mathbf{k} - \mathbf{k}') g(\mathbf{k}') = \left(\Delta + \frac{\hbar^2 k_F^2}{m}\right) g(\mathbf{k}), \quad (1.41)$$

where $g(\mathbf{k})$ is the two-electron wavefunction. The interaction is now a function of the difference between the initial and final pair momenta, and may be expanded in spherical harmonics, as

$$V(\mathbf{k} - \mathbf{k}') = \sum_{l=0}^{\infty} V_l(k, k') \sum_{m=-l}^{l} Y_{lm}(\hat{\mathbf{k}}) Y_{lm}^*(\hat{\mathbf{k}}'), \quad (1.42)$$

where $\hat{\mathbf{k}} = \frac{\mathbf{k}}{k_F}$.

At this point, BCS theory takes only the isotropic, s-wave ($l = 0$) interaction, which clearly gives the most straightforward results. We will remain general, but instead note that each value of the angular momentum l corresponds to a different solution $\{g_l(\mathbf{k}), \Delta_l\}$. As such, by similarly expanding $g(\mathbf{k})$ in terms of spherical harmonics, and using the orthonormality of Y_{lm}, we arrive at

$$g_l(\mathbf{k}) = \frac{N_0 V_l \int_0^{\varepsilon_l} d\xi g_l(\mathbf{k})}{2\xi - \Delta_l}, \quad (1.43)$$

where N_0 is density of states at the Fermi energy for electrons of one spin

orientation, and the integration over wave vectors has been replaced by an integration over the energy $\xi = \frac{\hbar^2 k^2}{2m} - \varepsilon_F$. In this integration, we have made the useful approximation - also employed in the original BCS theory - that the interaction is only non-zero (and negative) within ε_l of the Fermi energy. Finally, assuming the interaction is sufficiently weak, the above expression can be solved to give

$$\Delta_l = -2\varepsilon_l \exp\left(-\frac{2}{N_0 V_l}\right). \tag{1.44}$$

Hence, any arbitrary attractive interaction will act to lower the energy of two electrons sat on the Fermi surface, and they will bind to form a Cooper pair.

The Cooper pair dimension (ξ_0) can be estimated from the uncertainty relation as $\frac{\hbar v_F}{\Delta}$, where v_F is the Fermi velocity. Importantly, in all the superconducting systems discovered to date, this is significantly larger than the electron mean separation. This implies that superconductivity must be treated as a many body problem. The analysis is therefore significantly more complex than the above, however, the assertion that an arbitrarily weak attractive force between electrons will lead to the formation of Cooper pairs still holds. In the many body problem, Δ_l instead corresponds to a gap opening at the Fermi energy [20]. The symmetries of this gap are crucial in determining the properties of the superconductor.

Symmetry of the Pair Wavefunction

We now slightly extend the above treatment to include the spin structure of the paired state [19, 21]. Electrons are fermions, and must therefore obey Fermi statistics; specifically, the total wavefunction must be antisymmetric under particle exchange. This wavefunction may be expressed

$$\Psi^l_{\mathbf{s}_1,\mathbf{s}_2}(\mathbf{k}) \sim g(\mathbf{k})\chi_s(\mathbf{s}_1,\mathbf{s}_2), \tag{1.45}$$

as a product of the orbital and spin components. As such, if the orbital component is an antisymmetric function, the spin part must be symmetric, and vice versa.

As above, the orbital component can be expressed as an expansion of the spherical harmonic functions,

$$g(\mathbf{k}) = \sum_{m=-l}^{l} a_{lm} Y_{lm}(\hat{\mathbf{k}}). \tag{1.46}$$

This will be (anti)symmetric for (odd) even l. The spin component, χ_s, is instead

a product of the two single electron spin wavefunctions,

$$\chi_s(\mathbf{s}_1, \mathbf{s}_2) = \begin{pmatrix} |\uparrow\uparrow\rangle & |\uparrow\downarrow\rangle \\ |\downarrow\uparrow\rangle & |\downarrow\downarrow\rangle \end{pmatrix}. \tag{1.47}$$

There is only one antisymmetric spin combination - aptly named the spin-singlet - which takes the form $|\uparrow\downarrow\rangle - |\downarrow\uparrow\rangle$. For this $S = 0$ configuration, the total pair wavefunction will therefore be

$$\Psi^l \sim \begin{pmatrix} 0 & g(\mathbf{k}) \\ -g(\mathbf{k}) & 0 \end{pmatrix} = g(\mathbf{k}) i\sigma_y, \tag{1.48}$$

where l is even and σ_y is a Pauli matrix. Alternatively, there are three symmetric spin combinations - $|\uparrow\uparrow\rangle$, $|\uparrow\downarrow\rangle + |\downarrow\uparrow\rangle$ and $|\downarrow\downarrow\rangle$. This $S = 1$ (spin-triplet) configuration therefore corresponds to a pair wavefunction

$$\Psi^l \sim \begin{pmatrix} g_1(\mathbf{k}) & g_2(\mathbf{k}) \\ g_2(\mathbf{k}) & g_3(\mathbf{k}) \end{pmatrix}, \tag{1.49}$$

where l is odd and each $g_i(\mathbf{k})$ will have different coefficients a^i_{lm} in the expansion of spherical harmonics. The triplet pair wavefunction is traditionally recast in a similar form to the singlet pair wavefunction, as

$$\Psi^l \sim \begin{pmatrix} -d_x(\mathbf{k}) + id_y(\mathbf{k}) & d_z(\mathbf{k}) \\ d_z(\mathbf{k}) & d_x(\mathbf{k}) + id_y(\mathbf{k}) \end{pmatrix} = (\mathbf{d}(\mathbf{k})\boldsymbol{\sigma}) i\sigma_y, \tag{1.50}$$

such that the pairing state may be expressed as a vector $\mathbf{d}(\mathbf{k})$. Each component of this $\mathbf{d}$-vector is therefore given by

$$d_\alpha(\mathbf{k}) = \sum_{m=-l}^{l} b^\alpha_{lm} Y_{lm}(\hat{\mathbf{k}}), \tag{1.51}$$

and the coefficients b^α_{lm} fully describe the superconducting state.

This formalism may seem somewhat abstract, however the Cooper pair wavefunction is intimately tied to the superconducting gap function. Specifically, the many body approach reveals that the quasiparticle excitation energies in the superconducting state are given by

$$E_{\mathbf{k}} = \sqrt{\xi^2_{\mathbf{k}} + \Delta^2_{\mathbf{k}}}, \tag{1.52}$$

where ξ_k is the energy of excitations measured with respect to the Fermi energy, and $\Delta_{\mathbf{k}}$ is the superconducting gap function, defined by

$$\Delta_{\mathbf{k}}^2 = \begin{cases} \Delta^2 |g(\mathbf{k})|^2 & \text{Singlet pairing} \\ \Delta^2 |\mathbf{d}(\mathbf{k})|^2 \pm |\mathbf{d}^*(\mathbf{k}) \times \mathbf{d}(\mathbf{k})| & \text{Triplet pairing} \end{cases} \tag{1.53}$$

Hence, the gap function will share the symmetries of the Cooper pair wavefunction. Note, the factor $|\mathbf{d}^*(\mathbf{k}) \times \mathbf{d}(\mathbf{k})|$ will only be non-zero in the case of non-unitary pairing.

An Example - ^{3}He

Before considering how the Cooper pair wavefunction can form in a crystalline environment, we first look at an example in ^{3}He [19, 22]. A ^{3}He atom is a neutral fermion, implying that a system of ^{3}He atoms will form a Fermi surface. As such, ^{3}He is exactly analogous to the hypothetical electron gas, often employed to replicate more complex systems. Further, ^{3}He remains a fluid to the lowest measurable temperatures, at which any potential impurities will have literally frozen out. Therefore, at extremely low temperatures, ^{3}He represents arguably the most accurate experimental probe of a theoretical model in all of science.

Below $\sim$ 2 mK, ^{3}He will condense to form a superfluid. Superfluidity is analogous to superconductivity, but characterised by zero viscosity rather than zero resistivity. Importantly, the superfluid state in ^{3}He shares a number of similarities with the superconducting state in UPt_3, discussed in Chapter 4. In both materials, the Cooper pairs condense with a non-zero angular momentum, driven by strong correlations, and mediated by magnetic fluctuations. Further, both ^{3}He and UPt_3 have been predicted to exhibit a thermal Hall effect as a result of the same mechanism [23, 24]. As such, ^{3}He is a useful tool in understanding those materials which form the basis of our experimental investigations.

The superfluid phase of ^{3}He comprises Cooper pairs bound in an $l = 1$, or p-wave, state. From the previous discussion, the pair wavefunction will therefore require 9 complex functions to be fully defined - those being the three coefficients in each expansion describing the components of the $\mathbf{d}$-vector. However, to simplify the analysis, the spherical harmonics Y_{1m} may be expressed as linear combinations of

the vector $\hat{\mathbf{k}}$. The $\mathbf{d}$-vector can therefore be rewritten as a 3×3 matrix,

$$d_\alpha(\mathbf{k}) = A_{\alpha i}\hat{k}_i. \tag{1.54}$$

The Cooper pair wavefunction can have a number of different symmetries, and indeed, multiple superfluid phases are realised as a function of temperature, pressure and field in ^{3}He.

	$\mathbf{d}(\mathbf{k})$	$A_{\alpha i}$	Ψ
A	$(\hat{k}_x + i\hat{k}_y, 0, 0)$	$\begin{pmatrix} 1 & i & 0 \\ 0 & 0 & 0 \\ 0 & 0 & 0 \end{pmatrix}$	$\begin{pmatrix} -\hat{k}_x - i\hat{k}_y & 0 \\ 0 & \hat{k}_x + i\hat{k}_y \end{pmatrix}$
A_1	$(\hat{k}_x + i\hat{k}_y, i\hat{k}_x - \hat{k}_y, 0)$	$\begin{pmatrix} 1 & i & 0 \\ i & -1 & 0 \\ 0 & 0 & 1 \end{pmatrix}$	$\begin{pmatrix} \hat{k}_x + i\hat{k}_y & 0 \\ 0 & 0 \end{pmatrix}$
B	$\hat{\mathbf{k}}$	$\begin{pmatrix} 1 & 0 & 0 \\ 0 & 1 & 0 \\ 0 & 0 & 1 \end{pmatrix}$	$\begin{pmatrix} -\hat{k}_x - i\hat{k}_y & \hat{k}_z \\ \hat{k}_z & \hat{k}_x + i\hat{k}_y \end{pmatrix}$

Table 1.1 *The three phases of superfluid ^{3}He, described using the $\mathbf{d}$-vector, corresponding matrix and pair wavefunction.*

Rather than discussing each phase in turn, we list all three for comparison in Table 1.1, with schematics of the corresponding pair wavefunction and superconducting gap function in Figure 1.6, alongside the full phase diagram. From all this, we note some important points relevant for future discussions:

- Pairing states with non-zero angular momentum are possible (such as the A-phase). These states break time reversal symmetry, and are often described as chiral. As will be discussed, the predicted thermal Hall effect in ^{3}He and UPt_3 relies on the condensate having a non-zero angular momentum.

- As mentioned, the gap function mimics the symmetries of the $\mathbf{d}$-vector. In the A-phase, both vanish along the z-axis, which can give rise to zero-energy quasiparticle excitations. These excitations, and by extension the points at which the gap vanishes, will influence the thermodynamic properties of unconventional superconductors, as discussed in the next section.

- The A- and B-phases are topologically distinct due to the point nodes in the A-phase gap function. This idea will be returned to in the discussion of topological superconductivity.

- Non-unitary pairing states are possible. In the A_1-phase, an applied field leads to the condensation energy being different for $|\uparrow\uparrow\rangle$ and $|\downarrow\downarrow\rangle$ pairs. As such, Cooper pairs only form from spins parallel to the applied field.

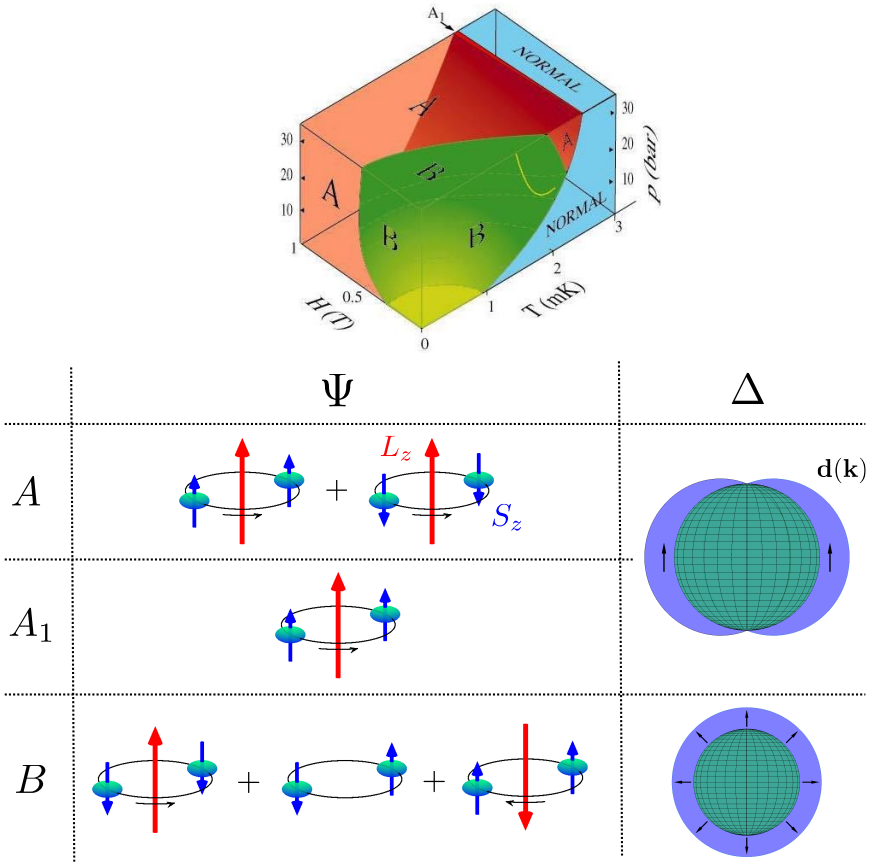

Figure 1.6 *Phase diagram of superfluid ^{3}He, alongside schematics of the Cooper pair wavefunction in each phase and the corresponding superconducting gap function. Also included in the gap function schematic is the direction of the* **d***-vector, given by the black arrows. Note that although the A and A_1 phases have the same gap function, in the latter, only one spin direction is paired. Phase diagram taken from [25].*

Superconductivity in a Crystal

Before finally considering superconductivity inside a crystal, let us first revisit the isotropic case, wherein the Cooper pair wavefunction is not constrained by the symmetries of the lattice. This is primarily to make familiar the nomenclature traditionally used to treat superconductivity inside crystalline materials.

We use isotropic to imply that the Cooper pairs form in a rotationally symmetric space. As discussed, the pair wavefunction is naturally defined as an expansion of spherical harmonic functions, with the set of functions in the expansion given by the angular momentum of the Cooper pair. For each value of angular momentum, l, there are $2l+1$ functions, Y_{lm}, which form a *complete basis*. In other words, if a function which is a linear combination of Y_{lm} is rotated, the resulting function will also be a linear combination of Y_{lm}. This implies that each value of l labels an *irreducible representation* (IR) of the rotationally symmetric space group - $SO(3)$.

Recall the Cooper pair problem, wherein each value of angular momentum corresponds to a different solution $\{g_l(\mathbf{k}), \Delta_l\}$. In a real material, each IR instead corresponds to a different superconducting state, each of which will condense on a different energy scale. Take ^{3}He as an example - the Cooper pairs are unconstrained by symmetry, and states with all angular momenta exist, however it is the p-wave ($l=1$) IR which corresponds to the superconducting state with the highest transition temperature, and that which is realised at the superfluid transition.

Let us now use this same framework to characterise the superconducting states within a crystal [26]. The crystalline lattice can be described as having a particular point group symmetry; this point group may be divided into its irreducible representations - which we label Γ. Each Γ has an associated set of basis functions $f_{\Gamma m}$, defined on the Brillouin zone, all of which must transform in a similar manner under the symmetry operations of the point group. Finally, for each IR, the corresponding Cooper pair wavefunctions can be written as an expansion of the associated basis functions, as

$$g(\mathbf{k}) = \sum_{m=1}^{d_\Gamma} \eta_{\Gamma m} f_{\Gamma m}(\hat{\mathbf{k}}) \tag{1.55}$$

in the singlet case, or

$$d_\alpha(\mathbf{k}) = \sum_{m=1}^{d_\Gamma} \eta_{\Gamma m} f^\alpha_{\Gamma m}(\hat{\mathbf{k}}) \tag{1.56}$$

for triplet pairing, where d_Γ is the dimension of the IR Γ. As before, the different IRs of the crystal point group correspond to different solutions, or superconducting states with different critical temperatures.

The above expressions are almost identical to Equations 1.46 and 1.51, which

describe the Cooper pair wavefunction in an isotropic medium. However, in Equation 1.56, for the case of triplet pairing, the basis functions $f^{\alpha}_{\Gamma m}$ have been expressed as vectors, rather than the coefficients $\eta_{\Gamma m}$. This to account for strong spin-orbit coupling, wherein the basis functions are more conveniently defined with respect to the crystal axes. For the materials under investigation, it is safe to assume strong spin-orbit coupling, and hence we only treat that case.

At present, there is no fully accepted microscopic theory to describe the unconventional superconductivity in any material. However, Ginzburg-Landau theory provides a phenomenological framework with which to interpret any form of superconductivity. This derives from Landau's theory of second order phase transitions, and expands the superconducting free energy in terms of a complex order parameter, which falls to zero at the transition temperature. Importantly, from the above expressions, the thermodynamic state of any superconducting system is completely defined by the coefficients $\eta_{\Gamma m}$. These coefficients may therefore be taken as the superconducting order parameter. In the absence of a microscopic theory, this provides the link between experimentally observable thermodynamic properties and the symmetries of the superconducting gap function.

An Example - UTe_2

To make the above more tangible, let us consider the superconducting state of UTe_2, which is also the focus of Section 5.3. The material crystallises in an orthorhombic structure with a D_{2h} point group symmetry, corresponding to three 2-fold axes of rotational symmetry (C_2^{α}), three mirror planes perpendicular to each axis (σ^{α}) and a centre of inversion (i). In the language of symmetry groups, the normal state is described by

$$G = D_{2h} \times U(1) \times T, \tag{1.57}$$

where $U(1)$ is the gauge group and T represents time reversal symmetry. Note that, without strong spin-orbit coupling, this would also include the $SO(3)$ group acting on the spin degree of freedom.

Shown in Table 1.2 are all of the irreducible representations of the D_{2h} point group, alongside the residual symmetry group, simplest representative function and nodal features for each. Note, there are an infinite number of basis functions

for each irreducible representation. For example, the B_{1g} wavefunction might be written

$$g(\mathbf{k}) = \eta_{B_{1g}} \sum_{i=1}^{\infty} c_i f_{B_{1g}i}(\hat{\mathbf{k}}). \tag{1.58}$$

Particular nodal features (gapless regions) will be present regardless of the basis function chosen, however, additional 'accidental' nodes are possible.

Γ	Residual Group	$f_\Gamma(\hat{\mathbf{k}})$	$\mathbf{f}_\Gamma(\hat{\mathbf{k}})$	Nodes
A_{1g}	$D_{2h} \times T$	1	-	None
B_{1g}	$D_2(C_2^z) \times i \times T$	$k_x k_y$	-	Line
B_{2g}	$D_2(C_2^y) \times i \times T$	$k_x k_z$	-	Line
B_{3g}	$D_2(C_2^x) \times i \times T$	$k_y k_z$	-	Line
A_{1u}	$D_2 \times i(E) \times T$	-	(ak_x, bk_y, ck_z)	None
B_{1u}	$D_2(C_2^z) \times i(E) \times T$	-	$(ak_y, bk_x, ck_x k_y k_z)$	Point
B_{2u}	$D_2(C_2^y) \times i(E) \times T$	-	$(ak_z, bk_x k_y k_z, ck_x)$	Point
B_{3u}	$D_2(C_2^x) \times i(E) \times T$	-	$(ak_x k_y k_z, bk_z, ck_y)$	Point

Table 1.2 *The irreducible representations* (Γ) *of the* D_{2h} *point group, alongside the corresponding residual group symmetry (where* $D_2(C_2^\alpha)$ *implies that only the* C_2^α *transformation leaves the representation unchanged), representative gap function (the simplest basis function of the IR) and resultant nodal features in the superconducting gap.*

From Table 1.2, the D_{2h} point group has 8 IRs, with 4 for each of singlet (g) and triplet (u) pairing. The A_{1g} representation is the s-wave conventional case, treated in the original BCS theory. The residual symmetry groups serve to re-iterate the statement that conventional superconductivity only breaks $U(1)$ gauge symmetry, whereas unconventional superconductivity will break additional symmetries.

Importantly, in this example, each of the representations is one-dimensional ($d_\Gamma = 1$), and can therefore be described by a one-dimensional order parameter, η_Γ. In this case, the Ginzburg-Landau free energy functional is given by

$$f[\eta] = \alpha(T - T_c)|\eta|^2 + \beta|\eta|^4 + \frac{\hbar^2}{2m_{ij}} \partial_i \eta^* \partial_j \eta. \tag{1.59}$$

This treatment may be extended to account for multi-dimensional IRs, or external fields. Both will be relevant to the discussion of multi-phase superconductivity in UPt_3, in Section 4.

Surprisingly, the physical reality in UTe_2 is not so simple - the material has been observed to possess multiple superconducting phases [27]. Recall the example of ^{3}He, where the multiple phases result from pressure (or field) lifting

the degeneracy of a multi-component order parameter. UTe_2 only has one-dimensional representations, and so instead it must be that two different IRs are accidentally degenerate. The Ginzburg-Landau free energy will therefore be a combination of the free energy expansions for each order parameter, and also include coupling terms between them. The problem is somewhat simplified by the material being centrosymmetric, which implies there cannot be a superposition of spin singlet and triplet pairing. However, it is still a difficult one, and as will be discussed in Section 5.3, the nature of superconductivity in UTe_2 is at present unsolved.

Finally, Table 1.2 also includes the nodal features in the superconducting gap, or the nature of the gapless regions, for each IR. Note however, these features obviously require that there be a Fermi surface in the direction of the node. As will be discussed in the following sections, the position and nature of the gap nodes are essential in determining the thermodynamic properties of unconventional superconductors.

Topological Superconductivity

Finally, we briefly introduce the subject of topological superconductivity - relevant to the prediction of a thermal Hall effect in UPt_3 [28], and potentially to the superconductivity in UTe_2 [29]. A topological superconductor (TSC) may be classified as either strong or weak [30]. A strong TSC is analogous to a topological insulator - both possess topologically non-trivial bands separated by a fully-opened gap. Alternatively, a weak TSC refers to a nodal superconductor, where the points at which the gap closes (rather than the bands) may be assigned a topological invariant. As discussed in Section 1.1, at boundaries between topologically distinct materials, there will exist topologically-protected edge states. In both classes of TSC, these edge states are associated with Majorana fermions, defined as a particle which is its own antiparticle. It is hoped that these emergent quasiparticles - and their associated exchange statistics - might form the basis of quantum computing, hence the fervent current interest [31].

In order to aid this discussion, we briefly introduce the Bogoliubov-de Gennes (BdG) Hamiltonian [32]. Most generally, for a spinless (or equivalently, spin-

polarised) superconductor, this reads

$$\mathcal{H} = \frac{1}{2}\sum_{\mathbf{k}} \phi^{\dagger}_{\mathbf{k}} \mathcal{H}(\mathbf{k}) \phi_{\mathbf{k}} \tag{1.60}$$

$$= \frac{1}{2}\sum_{\mathbf{k}} \begin{pmatrix} c^{\dagger}_{\mathbf{k}} & c_{-\mathbf{k}} \end{pmatrix} \begin{pmatrix} h(\mathbf{k}) & \Delta(\mathbf{k}) \\ \Delta^{*}(\mathbf{k}) & -h(-\mathbf{k}) \end{pmatrix} \begin{pmatrix} c_{\mathbf{k}} \\ c^{\dagger}_{-\mathbf{k}} \end{pmatrix}, \tag{1.61}$$

where $c^{(\dagger)}_{\mathbf{k}}$ are the fermionic annihilation (creation) operators, $\Delta(\mathbf{k})$ is the superconducting gap function and $h(\mathbf{k})$ is the normal state dispersion. This expression derives from the superconducting mean-field Hamiltonian, and introduces redundant, negative energy solutions in order to more straightforwardly diagonalise $\mathcal{H}(\mathbf{k})$. This redundancy reflects the particle-hole symmetry of the superconducting state, wherein the quasiparticle excitations are a superposition of particle and hole excitations.

For our own purposes, the above expression is useful in re-interpreting the superconducting band structure as comprising just two bands - an empty/filled band above/below zero energy (formerly the Fermi energy), separated by a gap $\Delta(\mathbf{k})$. In Section 1.1, a two-band model was used to demonstrate that bands (or singular points of degeneracy) may be designated topological invariants, and thus classified as topologically non-trivial. Similarly, and following an identical procedure, the above Hamiltonian is sufficient in exemplifying both classes of topological superconductivity. However, in line with our own experimental interests, we only consider weak topological superconductivity here.

Again, we use ^{3}He as a material example, and specifically the A-phase of ^{3}He, which can be considered the prototype for a nodal superconductor [33]. Recall from the previous section, this phase contains spin-polarised Cooper pairs, defined by $\mathbf{d}(\mathbf{k}) = (\hat{k}_x + i\hat{k}_y, 0, 0)$. The BdG Hamiltonian is therefore given by

$$\mathcal{H}(\mathbf{k}) = \begin{pmatrix} \xi_{\mathbf{k}} & \frac{\Delta}{k_F}(k_x + ik_y) \\ \frac{\Delta}{k_F}(k_x - ik_y) & -\xi_{\mathbf{k}} \end{pmatrix} \tag{1.62}$$

$$= \mathbf{N}(\mathbf{k}) \cdot \boldsymbol{\tau}, \tag{1.63}$$

where $\mathbf{N}(\mathbf{k}) = (\frac{\Delta}{k_F}k_x, -\frac{\Delta}{k_F}k_y, \xi_{\mathbf{k}})$ and τ_i are the Pauli matrices acting in particle-hole space, as emphasised by the change of notation ($\sigma_i \to \tau_i$). This second expression makes blatant the analogy between this and the two band model

(Equation 1.18). The energy solutions are therefore given by

$$E_{\mathbf{k}} = \pm\sqrt{\xi_{\mathbf{k}}^2 + \Delta^2/k_F^2(k_x^2 + k_y^2)}, \tag{1.64}$$

and the two bands are degenerate at $(0, 0, \pm k_F)$, as anticipated.

Similar to the two-band model in Section 1.1, the unit vector $\hat{\mathbf{n}}(\mathbf{k}) = \frac{\mathbf{N}(\mathbf{k})}{|\mathbf{N}(\mathbf{k})|}$ can provide some measure of topological character. Specifically, we have that

$$C = \frac{1}{4\pi}\int_S d^2\tilde{\mathbf{k}}\ \hat{\mathbf{n}}(\mathbf{k}) \cdot \left[\frac{\partial\hat{\mathbf{n}}(\mathbf{k})}{\partial k_1} \times \frac{\partial\hat{\mathbf{n}}(\mathbf{k})}{\partial k_2}\right], \tag{1.65}$$

or that the integral of the Berry curvature over a closed surface S (where $\tilde{\mathbf{k}} = (k_1, k_2)$ parameterises the surface) will be equal to the Chern number (C) of that surface, multiplied by 2π. From the above - and as illustrated in Figure 1.3 - we find that if a surface encloses a single point of degeneracy, it will have a non-zero Chern number, whereas if the surface encloses neither (or both) points of degeneracy, the Chern number will be zero. As such, the nodes in the superconducting gap have a topological charge ± 1, and are protected. More generally, in three dimensions, a singular touching point between two non-degenerate bands, with a linear dispersion in all directions, is referred to as a Weyl point. The majority of nodal superconductors are therefore equivalently Weyl superconductors.

We now demonstrate that, despite the bands in a nodal superconductor being (globally) topologically trivial, there will still be edge states [34]. The above implies that point nodes, or Weyl points, act as sources and sinks of Berry curvature flux. Consider then a flat surface S perpendicular to k_z, extending to the edge of the Brillouin zone, and with $|k_z| < k_F$ (lying between the two Weyl points). This surface may be viewed as a two-dimensional Brillouin zone, with two well separated bands throughout. However, due to the Weyl points - or equivalently, points of degeneracy in parameter space - these bands must be topologically non-trivial. This two-dimensional surface therefore represents a two-dimensional strong TSC, and by extension, will host topologically-protected edge states. If we then define a sample surface perpendicular to either $\hat{k}_x$ or $\hat{k}_y$, this two-dimensional strong TSC will have a single zero-energy state on the surface Brillouin zone. Further, if we make a stack of these two-dimensional strong TSCs, each with $|k_z| < k_F$, then each will contribute a single zero-energy state, and the result will be a *line* of zero-energy states (or a Fermi arc) on the surface Brillouin zone, connecting the projection of the two Weyl points. This

is illustrated in Figure 1.7. This is the basis for the prediction of a topological thermal Hall effect in UPt_3, and will therefore be returned to in Chapter 4.

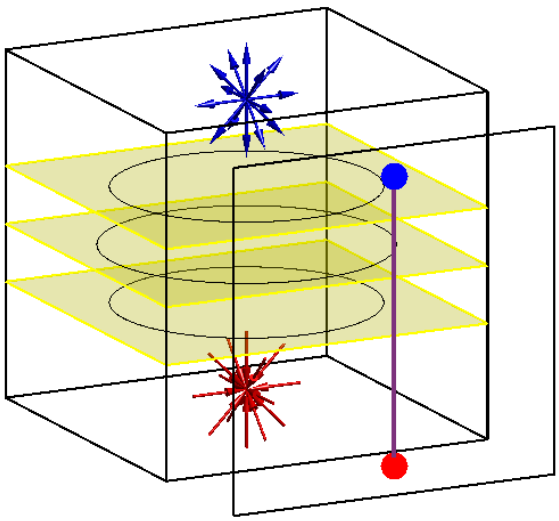

Figure 1.7 *Schematic to show the two Weyl points in the gap function of the ^3He A-phase, acting as a source and sink of Berry curvature. The empty cube is the bulk Brillouin zone, and each yellow surface individually represents a two-dimensional strong topological superconductor. The black circle on each yellow surface is the intersection of the Fermi surface. The empty square represents the surface Brillouin zone, with the projection of the two Weyl points shown by the red and blue dots, and the Fermi arc given by the purple line between them.*

1.3 The Versatility of Thermal Measurements

The unspecified nature of thermal measurements is both a strength and a weakness. Being sensitive to any form of thermal excitation, a measurement of the specific heat or thermal conductivity will unavoidably capture a wide range of phenomena. The challenge is then to disentangle the various contributions, to prise useful information from the data. This is often not straightforward. What follows is a summary of those contributions most relevant to our own investigations, to aid this disentanglement in future discussions. This is by no means an exhaustive list, but demonstrates to some extent the versatility of thermal measurements.

1.3.1 Specific Heat

The molar heat capacity, or the specific heat, is defined by the quantity of heat which must be provided to one mole of substance in order to raise its temperature by 1 K. Measured at a constant volume, the specific heat is therefore given by

$$C_V = \left(\frac{dQ}{dT}\right)_V = T\left(\frac{\partial S}{\partial T}\right)_V = \left(\frac{\partial U}{\partial T}\right)_V, \tag{1.66}$$

where Q is the applied heat, S is the entropy and U is the internal energy of the system [35]. The specific heat therefore measures how rapidly the internal energy varies as a function of temperature, and as such, is particularly sensitive to phase transitions. In an experiment, it is actually the specific heat at a constant pressure which is measured; however, for solids at low temperatures, the difference between the two quantities is negligible. Hence we will continue to refer to the heat capacity at a constant volume, which is more useful in this context.

Insulators - In an insulator - and in fact any solid material at high temperatures - the predominant contribution to the internal energy will be from lattice vibrations. The Debye model sets a material-dependent maximum frequency for these vibrations, and thus calculates a finite internal energy by summing the energies of each acoustic mode up to this cut-off frequency. Lattice vibrations are bosonic excitations, and the expected occupation of each mode is given by the Bose-Einstein distribution function. The calculated internal energy can then be differentiated as a function of temperature in order to give the specific heat,

$$C_{ph} = 9R\left(\frac{T}{\Theta_D}\right)^3 \int_0^{x_D} \frac{x^4 e^x dx}{(e^x-1)^2} \overset{T\ll\Theta_D}{\longrightarrow} \frac{12\pi^4 R}{5\Theta_D^3} T^3, \tag{1.67}$$

where $x_D = \Theta_D/T$, and $\Theta_D = \hbar\omega_D/k_B$ is the Debye temperature, defined by the cut-off frequency ω_D. The Debye temperature may be estimated from sound velocity measurements, and is typically a few hundred degrees Kelvin. For low temperature measurements, the above approximation is therefore usually valid, and the lattice vibrations will contribute a T^3 dependence to the specific heat.

Metals - For a metal, we must also consider the electronic contribution to the specific heat. For our purposes, it is sufficient to consider a free electron gas, with internal energy given by

$$U = 2\int_0^\infty \varepsilon \rho^F(\varepsilon, \mu, T) D(\varepsilon) d\varepsilon, \tag{1.68}$$

where $\rho^F(\varepsilon, \mu, T)$ is the Fermi-Dirac distribution for a chemical potential μ, $D(\varepsilon)$ is the density of states at ε, and the factor of 2 accounts for both spin directions. The low temperature specific heat can then be calculated via the use of a Sommerfeld expansion, with the lowest order term given by

$$C_e = \frac{\pi^2}{3} k_B^2 D(\varepsilon_F) T = \gamma T, \tag{1.69}$$

where $\mu(T \to 0) \simeq \varepsilon_F$, the Fermi energy. At low temperatures, the heat capacity of a metal is therefore

$$C = C_e + C_{ph} = \gamma T + \beta T^3. \tag{1.70}$$

Commonly, C/T is plotted against T^2, in order to give a line with gradient β and intercept γ.

γ is the Sommerfeld coefficient and, from the above expression, this is dependent on the density of states at the Fermi energy. It may also be expressed as

$$\gamma = \frac{k_B^2}{4} \frac{2m^*}{\hbar^2} k_F, \tag{1.71}$$

or as a function of the size of the Fermi surface k_F, as well as the quasiparticle mass m^*, which can effectively exceed the free electron mass through interactions with the periodic potential of a crystalline material. The Sommerfeld coefficient therefore provides some measure of the strength of these interactions. This is particularly relevant to the discussion of heavy fermion materials in Chapter 5.

Superconductors ($T \sim T_c$) - The lattice contribution will not necessarily remain constant through the superconducting transition. However, for the low-T_c systems involved in our investigations, this will be negligible and therefore we only consider the electronic contribution here [36, 37]. Again for a free-electron gas, the entropy may be expressed

$$S = -2k_B \sum_{\mathbf{k}} \left[\rho_{\mathbf{k}}^F \ln \rho_{\mathbf{k}}^F + (1 - \rho_{\mathbf{k}}^F) \ln(1 - \rho_{\mathbf{k}}^F) \right] \tag{1.72}$$

where $\rho_{\mathbf{k}}^F$ is the Fermi-Dirac distribution at an energy $E_{\mathbf{k}} = \sqrt{\xi_{\mathbf{k}}^2 + \Delta(T)^2}$, modified by the superconducting gap $\Delta(T)$, which we take to be isotropic. The

specific heat may then be calculated using Equation 1.66, and is given by

$$C_{es} = \frac{D(E_F)}{T} \int_{-\infty}^{\infty} \left(-\frac{\partial \rho_{\mathbf{k}}^F}{\partial E_{\mathbf{k}}} \right) \left(E_{\mathbf{k}}^2 - \frac{T}{2} \frac{d\Delta^2}{dT} \right) dE, \tag{1.73}$$

where $D(E_F)$ is the density of states at the Fermi energy. Above the transition temperature (T_c) - setting $\Delta = 0$ - the normal state behaviour is recovered. However, directly below T_c, the superconducting state has an additional contribution - the applied heat can go towards breaking Cooper pairs. This gives rise to a discontinuity in the specific heat, where

$$\left. \frac{C_{es} - C_{en}}{C_{en}} \right|_{T_c} = \frac{\Delta C}{\gamma T_c}. \tag{1.74}$$

The magnitude of the superconducting jump provides some measure of the strength of the attractive interaction binding Cooper pairs. For example, BCS theory - which only considers weak-coupling - gives $\frac{\Delta C}{\gamma T_c} = 1.43$. In unconventional superconductors, gap anisotropy can also act to decrease the magnitude of the jump [21].

Superconductors ($T \to 0$) - In the low temperature limit, where the energy gap is saturated, the specific heat may be expressed

$$C_{es} = \frac{2}{T} \int_0^{\infty} \left(-\frac{\partial \rho^F}{\partial E} \right) D(E) E^2 dE. \tag{1.75}$$

This will be dominated by the quasiparticle density of states $D(E)$, and the specific heat is therefore sensitive to the topology of the superconducting gap [21]. Shown in Figure 1.8 is the density of states, and corresponding low-temperature specific heat, for an isotropic gap, a gap with point nodes, and a gap with line nodes. Note the markedly different behaviour for a gapless/fully-gapped superconductor. Impurities will act to smear out any gapless regions, and give a finite density of states at zero energy [38]. As a result, the power law dependencies given in Figure 1.8 (b) may no longer be valid. A measurement of the low-temperature specific heat is therefore less decisive in distinguishing between nodal superconductors with different topologies.

Other Contributions - We briefly mention some other phenomena which are relevant to our investigations:

- Magnetic excitations - the contribution from magnons may be calculated in

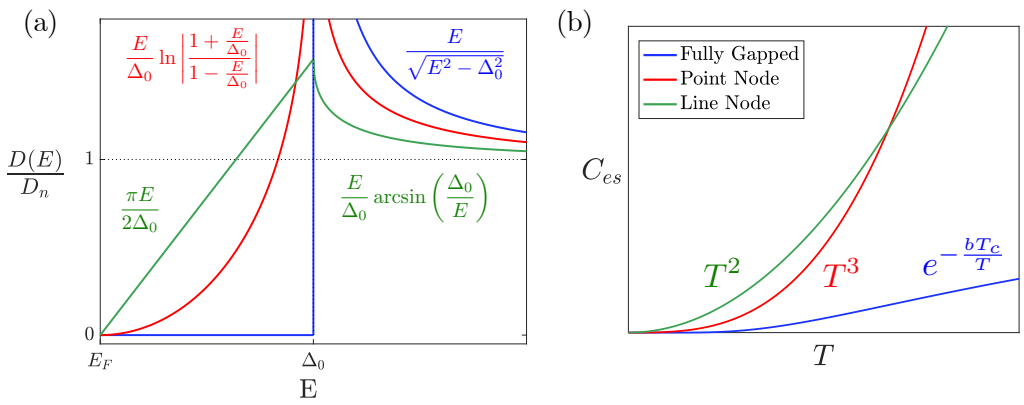

Figure 1.8 *(a) Ratio of the superconducting density of states $D(E)$ to the normal state density of states D_n, plotted for an isotropic gap (blue), a gap with point nodes (red), and a gap with line nodes (green). E_F is the normal state Fermi energy and Δ_0 is the maximum gap magnitude. (b) Low temperature electronic specific heat for the three different kinds of gap.*

a similar way to that for phonons above [35]. This gives a $T^{3/2}$ dependence for magnetic excitations on top of a ferromagnetic ground state, and a T^3 dependence for an antiferromagnet.

- Schottky anomaly - this corresponds to a peak in the low temperature specific heat, occurring for a system with a limited number of discrete energy levels. This occurs for all the materials under investigation, and is therefore discussed more thoroughly in Appendix C.

- Phase transitions - these may broadly be divided into two classes, labelled by the order of the lowest derivative of the free energy that shows a discontinuity at the transition temperature. A first order phase transition will therefore result in a discontinuity in the specific heat, whereas a second order transition will not.

1.3.2 Thermal Conductivity

The thermal conductivity is a measure of a material's ability to conduct heat, and is defined by

$$\kappa = -\frac{\mathbf{Q}}{\boldsymbol{\nabla} T}, \tag{1.76}$$

where $\mathbf{Q}$ is the heat flow per unit area and $\boldsymbol{\nabla} T$ is the resultant temperature gradient [39]. The thermal conductivity κ is therefore a second-rank tensor,

although this section will only refer to the longitudinal thermal conductivity. Unlike the specific heat this is a directional probe, and only sensitive to diffusive excitations. As such, the thermal conductivity is particularly useful in revealing real (or momentum) space anisotropies.

In order to derive a more useful expression for the thermal conductivity, we consider thermal conduction in a gas of unspecified particles, each of which has a heat capacity c [39]. In the presence of a temperature gradient $\boldsymbol{\nabla} T$, the energy of a particle, travelling with velocity $\mathbf{v}$, will change according to

$$\frac{\partial E}{\partial t} = c\mathbf{v} \cdot \boldsymbol{\nabla} T. \tag{1.77}$$

If we then assume a particle will travel a distance $v\tau$ before being scattered, where τ is the relaxation time, the average heat flow per unit area will be

$$\mathbf{Q} = -\frac{1}{3} C\tau v^2 \boldsymbol{\nabla} T, \tag{1.78}$$

where all particles have been summed over, and C is the total heat capacity. Finally, from Equation 1.76, we have that

$$\kappa = \frac{1}{3} C v^2 \tau. \tag{1.79}$$

The thermal conductivity is therefore proportional to the specific heat. Importantly, this remains valid regardless of excitation. Further, the contributions due to different excitations may be summed to give the total thermal conductivity. Although clearly over-simplistic in its derivation, this expression will be sufficient in explaining the behaviour of all the relevant phenomena.

Insulators - A thermal current inside an insulator will be primarily carried by lattice vibrations. These will be affected by various scattering processes, each with an associated scattering rate τ_i^{-1}. Matthiessen's rule tells us that the various scattering rates may be determined independently and then summed over, which implies that

$$\frac{1}{\tau} = \sum_i \frac{1}{\tau_i} \implies \frac{1}{\kappa} = \sum_i \frac{1}{\kappa_i}. \tag{1.80}$$

At low temperatures, the phonon mean free path will be limited by impurities and the sample boundaries, both of which have a temperature independent scattering rate. Note however, in a polished sample, the phonons will have an increased likelihood of scattering specularly from the boundary, and will therefore have a

significantly enhanced mean free path. Regardless, due to the constant scattering rate associated with both processes, the low-temperature thermal conductivity is determined by the specific heat, and will exhibit a T^3 dependence. At higher temperatures, the lattice specific heat will be constant, and the thermal conductivity will instead be dominated by the phonon-phonon scattering rate. Specifically, Umklapp scattering - wherein the scattered phonon momentum falls outside the Brillouin zone, and therefore opposes the thermal current - has a scattering rate which is linear in T, implying the thermal conductivity should show a reciprocal temperature dependence at high temperatures. This behaviour is illustrated in Figure 1.9 (a).

Metals - Matthiessen's rule is equally applicable to a system of electrons. In this case, the dominant scattering rates will come from interactions with impurities ($\tau^{-1} \propto T^0$), electrons ($\propto T^2$) and phonons ($\propto T^3$). The low temperature thermal conductivity will therefore be dominated by the T-linear specific heat, whilst at higher temperatures, the electron mean free path will be limited by electron and phonon scattering, and the thermal conductivity will exhibit a reciprocal temperature dependence. Unlike with the specific heat, in a metal, the phonon contribution to the thermal conductivity will be negligible at all temperatures. The resultant behaviour is shown in Figure 1.9 (b).

We briefly mention the Wiedemann-Franz law, which states that the ratio of the electrical (σ) and thermal conductivities should be proportional to temperature, or that

$$\frac{\kappa_e}{\sigma} = \frac{\pi^2 k_B^2 T}{3e^2} = L_0 T, \tag{1.81}$$

with $L_0 = 2.44 \times 10^{-8}$ WΩK^{-2}. This is derived from a semiclassical theory of electron dynamics, and is valid when the scattering rate is equal for the two conductivities, which occurs at high temperatures, or at very low temperatures (except in very pure samples). In our own investigations, this often acts as a useful sanity check.

Superconductors ($T \sim T_c$) - In order to treat the thermal conductivity of a superconductor, we consider the two-fluid model. This divides the system into a superfluid part - which comprises Cooper pairs which cannot transport heat - and the normal fluid, with a thermal conductivity

$$\kappa^{es} = \frac{1}{3}\left[\frac{\pi^2}{3} k_B^2 D(\varepsilon_F) T\right] v_F^2 \tau, \tag{1.82}$$

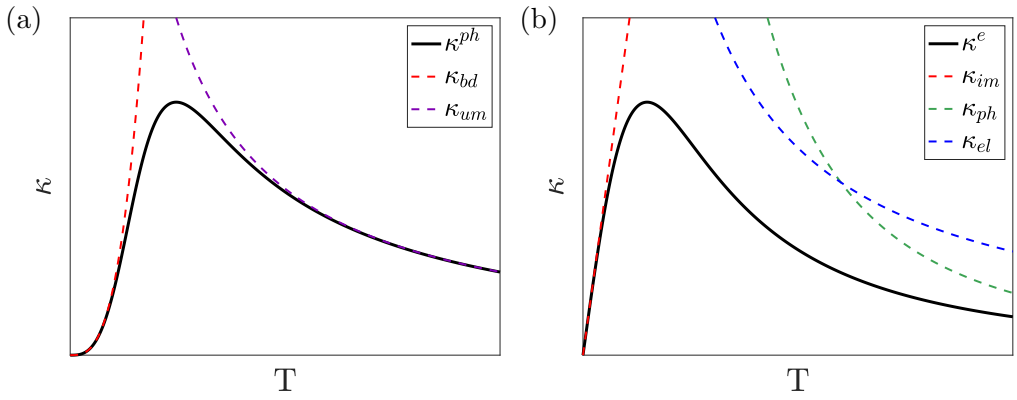

Figure 1.9 *Thermal conductivity plotted as a function of temperature for (a) an insulator (κ^{ph}), also included is the thermal conductivity with only boundary effects (κ_{bd}), and with only Umklapp scattering (κ_{bd}); or (b) a metal (κ^{e}), where, similarly, the thermal conductivity only due to impurity (κ_{im}), phonon (κ_{ph}) and electron scattering (κ_{el}) has been included.*

where the low-temperature electronic specific heat has been included explicitly, and v_F is the Fermi velocity. In the superconducting state, $D(\varepsilon_F)$ and τ both have a significant temperature dependence. Hence, rather than being linear in temperature, the thermal conductivity will depend on how these two quantities compete. For example, in a high purity superconductor directly below the transition temperature, $D(\varepsilon_F)$ will decrease more rapidly than τ can increase, and hence the thermal conductivity will decrease. Conversely, in some of the high-T_c cuprates, an increase of the thermal conductivity is observed upon cooling through T_c [40].

Superconductors ($T \to 0$) - At very low temperatures, the scattering rate will saturate - limited by the impurity density - whereas the normal fluid density of states will continue to decrease [41]. In a fully-gapped superconductor, the thermal conductivity will therefore fall to zero, as there are no thermally excited quasiparticles available to carry heat. In a gapless superconductor however, the zero-energy nodal quasiparticles will instead give a finite thermal conductivity at $T = 0$. Further, for a line node, we find that $D(\varepsilon_F)$ and τ are, respectively, proportional and inversely proportional to the impurity bandwidth, implying that the residual thermal conductivity will be independent of the impurity concentration. This is a powerful tool in identifying nodes in the superconducting gap. Finally, similar to the specific heat, the $T \to 0$ thermal conductivity varies as a function of the density of states, and will therefore exhibit power law

dependencies in nodal superconductors. Specifically, in a pure material, line nodes will give a T^2 dependence and point nodes a T^3 dependence [21].

Superconductors in Field - With the application of a magnetic field H, a type-II superconductor will be penetrated by normal state vortices, separated by a distance $d \sim 1/\sqrt{H}$ [41]. Normal state particles have an exponentially small probability to tunnel between vortices and hence, in a fully-gapped superconductor at $T \to 0$, the finite field thermal conductivity will be non-zero, or

$$\kappa^{es} \sim e^{-\alpha\sqrt{\frac{H_{c_2}}{H}}}, \tag{1.83}$$

where α is a constant and H_{c_2} is the upper critical field. In a gapless superconductor, the nodal quasiparticles remain the dominant thermal carriers, and instead, the supercurrents encircling the normal state vortices act to Doppler shift the quasiparticle velocities. As illustrated in Figure 1.10, this similarly shifts the density of states, with $D(\varepsilon_F) \sim \sqrt{H}$. From Equation 1.82 - and in the regime where the scattering rate is limited by the impurity density rather than the vortex separation - the thermal conductivity will vary as

$$\kappa^{es} \sim \sqrt{H}. \tag{1.84}$$

Therefore, the field dependence of the low temperature thermal conductivity is an effective means of determining whether the superconducting gap function possesses gapless regions.

1.3.3 Thermal Hall Effect

The thermal Hall (or Righi-Leduc) effect is analogous to the electrical Hall effect, and refers to a thermal gradient that is generated in the presence of an applied thermal current and a magnetic field, all of which are mutually perpendicular. In a two-dimensional geometry, the thermal Hall conductivity is given by the off-diagonal components of κ in Equation 1.76.

As discussed in Section 1.1, a topologically non-trivial material will host dispersionless edge states. In the presence of a thermal gradient, the chirality of these states should give rise to a transverse thermal current, and as such, a measurement of the transverse thermal conductivity is an effective probe of topological phenomena. Note that this topologically driven transverse

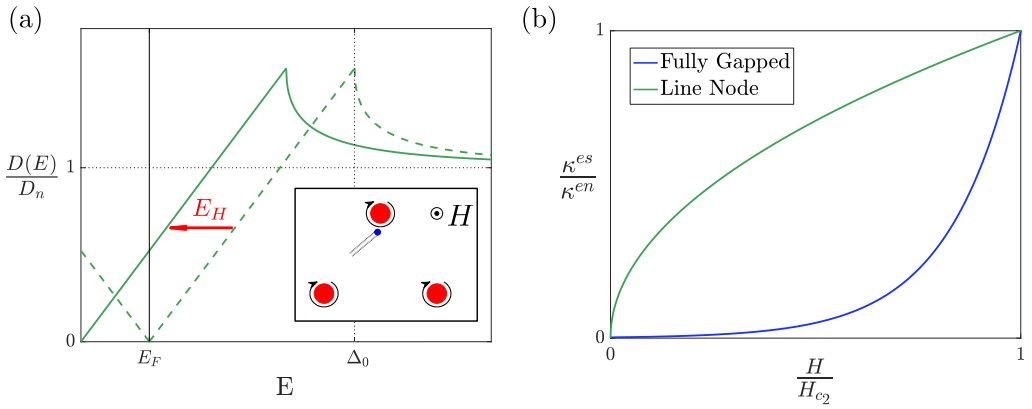

Figure 1.10 *(a) The superconducting density of states $D(E)$ for a type-II superconductor with line nodes, shifted by E_H due to the velocity of the quasiparticles being Doppler shifted by the suppercurrents which encircle the normal state vortices. The inset illustrates this schematically, with a quasiparticle (blue) passing close to the normal state vortex (red). (b) The ratio of the superconducting thermal conductivity (κ^{es}) to the normal state thermal conductivity (κ^{en}), plotted as a function of field in order to demonstrate the marked differences between a fully gapped superconductor and a superconductor with a line node.*

conductivity does not require an applied field, however in the majority of cases, an applied field is necessary in order to tune topological transitions. We therefore briefly discuss some features of the normal thermal Hall effect, such that they may be distinguished from the underlying topological phenomena.

Insulators - Phonons are electrically neutral, and therefore cannot be directly influenced by an applied magnetic field. Despite this, a thermal Hall effect carried by phonons has been observed in some systems. For example, as a result of anisotropic scattering by magnetic impurities in the paramagnetic insulator $Tb_3Gd_5O_{12}$ [42], or instead via a coupling to the spin-lattice in some multiferroics [43].

Metals - In the ordinary electrical Hall effect, the transverse electrical resistivity of a single band is given by

$$\rho_{xy} = \frac{\mu_0 H}{ne}, \tag{1.85}$$

where μ_0 is the Bohr magneton, H is an applied field and n is the charge current density. The charge carriers will also carry heat, and the transverse thermal resistivity w_{xy} should similarly vary linearly with applied field. Borrowing from

Section 2 (Equation 2.6), the transverse thermal conductivity is given by

$$\kappa_{xy} = \frac{w_{xy}}{w_{xx}^2 + w_{xy}^2}. \tag{1.86}$$

where w_{xx} is the longitudinal thermal resistivity. Since $w_{xx} \gg w_{xy}$, if the longitudinal thermal resistivity has a negligible field dependence, we have that $\kappa_{xy} \propto B$. Similar to ρ_{xy}, the transverse thermal conductivity also has the power to distinguish between particle and hole currents, although only for a single band. Finally, the Wiedemann-Franz law (Equation 1.81) is equally applicable to transverse electronic currents.

Superconductors - Near the transition temperature, the transverse thermal conductivity will be dominated by the normal state electrons. However, as $T \to 0$, the Bogoliubov quasiparticles become the principal thermal carriers. As discussed in Section 1.2, these excitations are particle/hole superpositions, and - due to the particle-hole symmetry of the superconducting state - the transverse contributions should therefore sum to zero.

Chapter 2

Experimental Methods

This section details the experimental setup and measurement procedure employed in our investigations in order to determine the thermal conductivity and heat capacity of various materials. The two properties will be discussed separately, in each case starting with the theoretical basis, before detailing the steps we have taken to translate this into an effective, low temperature measurement. First however - to avoid repetition - those aspects common to both measurements will briefly be discussed.

2.1 General Considerations

The Sample

The most integral part of any measurement is the sample. The basis for condensed matter theory is the crystalline lattice - a perfectly uniform arrangement of atoms, the physics of which (for the most part) may be described by considering just a single unit cell. As experimentalists, we strive to recreate this theorist's playground, and thus perform measurements on high purity single crystals. The growth of such crystals is a science in itself, and we therefore only briefly mention some methods by which the crystals used in our investigations have been grown:

- Optical floating zone technique - ellipsoidal mirrors focus light onto a small area of a polycrystal, which then melts onto a seed crystal

below. The molten zone is slowly moved upwards along the polycrystal, which leaves a crystalline rod in its wake. Using this technique, single crystals of $SrCu_2(BO_3)_2$ and $Lu_2V_2O_7$ have been grown - respectively - by Dharmalingam Prabhakaran at the University of Oxford, and Robin Perry at University College London.

- The Czochralski method - the appropriate masses of constituent materials are loaded into a crucible, pumped down to ultra high vacuum and heated above melting point. A seed crystal is then lowered into the molten mixture and slowly extracted, such that the crystal solidifies around the seed. For metallic samples, heating via RF induction will simultaneously levitate the molten mixture above the crucible, further preventing contamination. Single crystals of UPt_3 and UAu_2 were grown by this method, by Andrew Huxley and Chris O'Neill respectively.

- Chemical vapour transport - the appropriate masses are loaded into a vacuum sealed quartz tube alongside a transport agent, such as iodine. A temperature gradient is then applied along the tube in order to exploit the diffusive nature of the exo/endothermic reaction with the transport agent, and crystals are deposited at one end of the tube. Single crystals of UTe_2 were grown by this method, by Callum Stevens.

Thanks go to all of the crystal growers mentioned above, without whom this work would not have been possible.

A crystal plucked from the growth will rarely be suitable for experiment. More likely, the sample must first be oriented and cut to the appropriate dimensions. We orient our samples using Laue X-ray diffraction (Appendix A.1), and then cut using either a spark cutter (metals) or wire saw (insulators). Finally, the material properties can be used as a gauge of sample quality. In a metallic sample, the residual-resistance ratio - the ratio of the room temperature resistance to that at zero temperature - should scale with impurity concentration [44]. For insulating materials, the sample quality is less straightforward to determine, and other techniques - such as the thermal conductivity or specific heat - must be employed. However, regardless of material property, the sample quality requires a wealth of prior experimental work to be accurately calibrated.

Measurement Techniques

In any thermal measurement, the basic principle is the same: apply heat to a sample and then measure the response. We thus require a heater, which can provide a variable and measurable heating power to the sample, and a thermometer, with a monotonic temperature dependence of some parameter, which may therefore be calibrated. Further, the analysis is greatly simplified if the measured response is solely due to the applied heat. This requires that the sample environment should remain at a constant temperature throughout the measurement. We will now describe the essential features of such a measurement, with the specific instruments and measured components listed in Table 2.1.

The experimental setup is arranged on a sample stage, alongside a calibrated thermometer and a heater, such that the stage temperature may be accurately measured and controlled. The sample stage is electrically wired and thermally anchored to a probe, which is evacuated and inserted into the cryostat. The probe is cooled via contact with either a bath of liquid ^{4}He, or in the case of the dilution refrigerator, the mixing chamber.

The sample stage thermometer is a resistor, with a resistance that varies monotonically with temperature. The resistance is measured using a Lakeshore temperature bridge, and converted to temperature using a thermometer-specific calibration file. The heater is also a resistor, but with an approximately constant resistance, such that a known power may be provided by varying the current, via Joule heating ($P = I^2R$). This current is set by the same instrument, and the temperature is stabilised through a PID feedback loop. The PID values must be set manually, with the optimal values dependent on the specific measurement (varying with temperature, magnetic field, sample stage, etc.). Using this method, we are able to stabilise the sample stage temperature to $< 0.001T$, across all temperatures.

As with the sample stage thermometer and heater, all the measured components in these investigations are simply specialised resistors (Table 2.1). This is largely due to the capability we have to manipulate electrical currents - and measure voltages - with extreme accuracy. In these investigations, resistance measurements have almost exclusively been made using a standard, low noise, 4-probe technique [44], with an alternating current source coupled to a phase sensitive detector. A schematic of a typical resistance measurement is shown in Figure 2.1. Note also the high frequency noise filters - to remove RF noise picked

Measured Component	Model	Measuring Instrument(s)
Sample Stage Thermometer	**RX-102B-CB** *CX-1050-SD*	**LS370** *LS340*
Sample Thermometer	**RX-102B-BR** *CX-1050-BR*	Keithley 6221/ SR7265
Sample Heater	5 kΩ Strain Gauge	Agilent B2962A/ Keithley 2182A

Table 2.1 *List of the specific components used in our investigations. A component in bold/italics has been used exclusively at mK/^{4}He temperatures.*

up by those wires outside the cryostat - and twisted pairs wherever possible - to reduce induced pick-up voltage from stray fields. The one exception is the measurement of the heater resistance. In these investigations, the heater is supplied by a direct current, and is therefore instead measured using a DC voltmeter. In this case, the applied current is sufficiently large that the resistance measurement remains reasonably accurate.

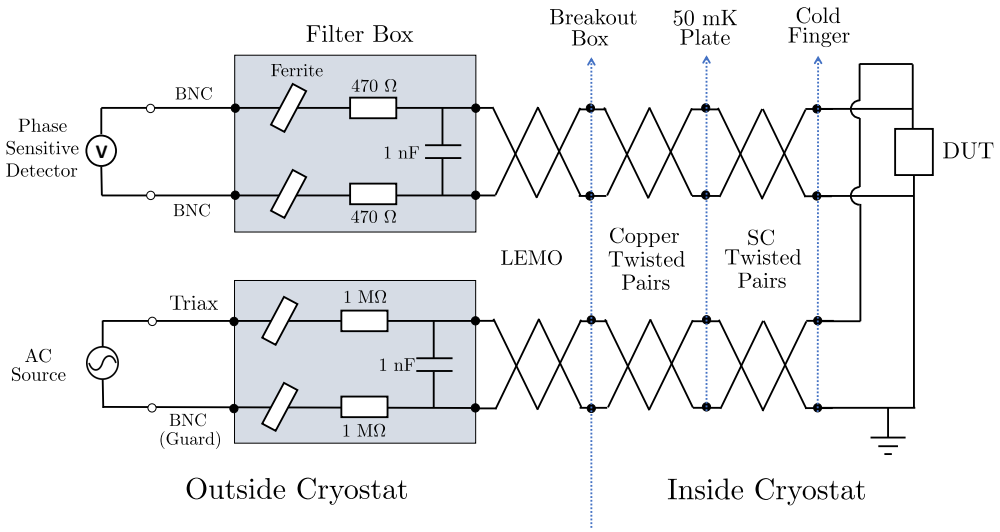

Figure 2.1 *Typical resistance measurement for a high resistance (>1 kΩ) component in the dilution refrigerator. In a ^{4}He cryostat, the superconducting twisted pairs would not be present. For measurements of a low resistance component - for example a metallic sample - the resistors in the current source filter box would have a lower resistance, and we might use a low temperature transformer in order to boost the measured voltage.*

Thermometer Calibration

As previously mentioned, the sample stage thermometers have been purchased alongside a calibration file, whereas the sample thermometers have not. Instead, we must perform our own calibration - this is by far the most integral part of the analysis. The sample thermometers used in these investigations are either Lakeshore Cernox or ruthenium oxide bare chip resistors (Table 2.1), chosen for their large temperature range of sensitivity and low magnetoresistance. These are both semiconductors, with a resistance that varies logarithmically with temperature. The specific choice of thermometer is dictated by the temperature range under investigation.

There are studies to suggest that, in both types of thermometer, thermal cycling can lead to small offsets in the temperature dependence of the measured resistance [45, 46]. Therefore, rather than prepare just a single thermometer-specific calibration file, we have chosen to re-calibrate the sample thermometers during each individual data run. The process of a measurement is thus as follows:

(i) Stabilise the sample stage temperature.

(ii) Measure the sample thermometer resistance - we assume that the entire sample stage is in thermal equilibrium, and this resistance therefore corresponds to the temperature given by the calibrated sample stage thermometer.

(iii) Turn the sample heater on and measure the response of the sample - the exact procedure at this step is specific to the material property under investigation and will therefore be detailed in the following sections.

(iv) Turn the sample heater off, set a new temperature and begin the process again.

In general, the temperature is stabilised faster if the temperature is increased between subsequent measurements.

The above procedure will give discrete points, at a definite resistance and temperature. The calibration accuracy thus relies on an appropriate interpolation between these points. For this, we use the purely phenomenological function

$$\frac{1}{T} = \sum_{n=0}^{n} a_n \left[\log\left(\frac{R}{R_{RT}}\right) \right]^n, \tag{2.1}$$

where R_{RT} is the room temperature resistance and a_n are the fitting parameters. It is tempting to arbitrarily increase n - the order of the polynomial - in order to give the smallest residuals at each calibration point. However, realistically, the resistance should increase monotonically with decreasing temperature. This sets a useful upper bound on the order of the polynomial, and typically, n has ranged between 3 and 7 in our analyses. As shown in Figure 2.2, this is sufficient to give an adequate fit.

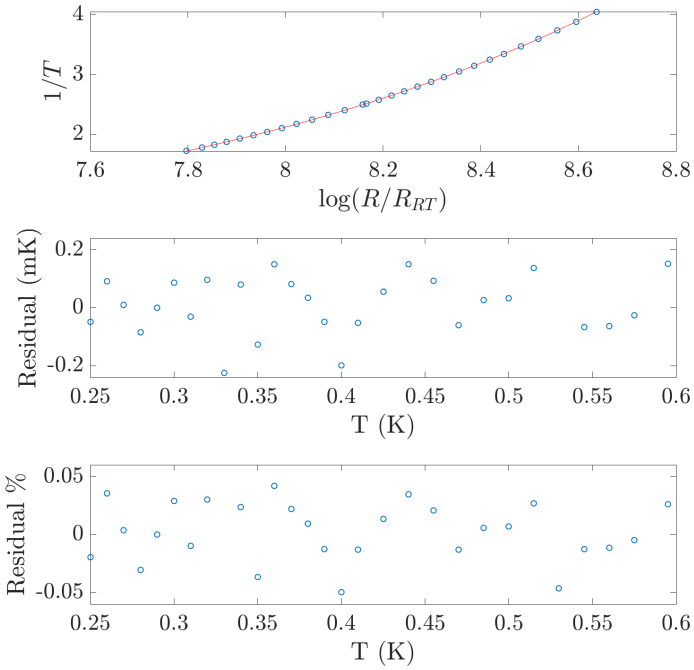

Figure 2.2 *Typical thermometer calibration using Equation 2.1. This particular calibration was for a RuO_2 thermometer in zero field, with $n = 3$.*

For a single measurement across a large range of temperatures, it is sometimes advantageous to divide the full temperature range into overlapping regions, each of which has a separate calibration curve. The points at which the calibrations overlap should then give identical results. Finally, note that when increasing the temperature between subsequent measurements, stage (iii) in the above procedure will heat the sample outside the calibrated temperature range. It is therefore necessary to measure a few more calibration points at higher temperatures, so as to avoid wasting data points which cannot be converted to temperature.

Measurements in Field

When measuring in an applied magnetic field, we must also consider that the electrical components will have a magnetoresistance; this is particularly important for the thermometry. Specifically, due to magnetoresistance, the calibration file for the sample stage thermometer will no longer be valid. As a result, we must use a different procedure in order to calibrate the sample thermometer. Two alternative methods for calibrating in field are:

(A) Attach a second calibrated thermometer to the probe, in such a place that it is outside the magnetic field, but still thermally linked to the sample stage. The calibration can then be performed by a similar method, but using this thermometer. This is only possible due to the extremely localised nature of the applied field (in our dilution refrigerator, at a distance of 40 cm above the field centre, the field strength has dropped to ~ 0.05 % of its maximum value).

(B) Measure the sample stage heater power required to reach each temperature in zero field, then apply an identical power in field. The thermometer may then be calibrated if we assume this gives an identical temperature as in zero field.

Method (B) relies on the sample stage heater having a negligible magnetoresistance, and we have therefore employed method (A). This method suffers as a result of the thermal gradient between the out-of-field thermometer and the sample stage. However, this can be measured in zero field, and corrected for during the calibration procedure.

In an applied field, the thermometer resistance will vary as a function of both temperature and field, implying there should be a calibration *surface*. However, in our investigations, the accuracy of the thermometer calibration is paramount. Therefore, in order to avoid the additional inaccuracy which results from a two-dimensional calibration, we have exclusively taken data sets at a constant field, such that we may construct in situ, constant field, temperature calibration curves. The in-field calibration procedure is thus identical to that which has been described previously.

Thermal Isolation

One final aspect that all thermal measurements share is the need to thermally isolate specific components. For example, in order to provide an adequate thermal link between the sample and the cryostat, the sample stage must be constructed using a material with high thermal conductivity (typically OFHC copper). In comparison to the sample, the sample stage will thus act as a thermal reservoir. The sample thermometer must therefore be thermally isolated from - but electrically connected to - the sample stage. If not, any heat applied to the sample will immediately dissipate into the thermal reservoir, and the thermometer will be incapable of measuring changes in the sample temperature. As such, the material components in a thermal measurement must be carefully chosen so as to manipulate the flow of heat, in order to give a measurable signal. The methods of thermally isolating particular components are largely measurement specific, and will therefore be discussed in the following sections.

2.2 Thermal Transport Measurements

In order to design an experiment to measure the thermal transport coefficients of a material, we begin by considering the definition of thermal conductivity - given in Section 1.3 -

$$\mathbf{Q} = -\kappa \boldsymbol{\nabla} T, \tag{2.2}$$

where $\mathbf{Q}$ is the heat flow per unit area and $\boldsymbol{\nabla} T$ is the resultant temperature gradient [39]. For our experimental purposes, this expression may be written more explicitly as

$$\begin{pmatrix} Q_x \\ Q_y \end{pmatrix} = - \begin{pmatrix} \kappa_{xx} & \kappa_{xy} \\ \kappa_{yx} & \kappa_{yy} \end{pmatrix} \begin{pmatrix} \nabla_x T \\ \nabla_y T \end{pmatrix}. \tag{2.3}$$

where κ_{ij} are the coefficients we wish to measure. To this end, we note some simplifications:

(i) $Q_y = 0$ - we assume that, in an experiment, we can apply heat solely along a single direction.

(ii) $\kappa_{xx} = \kappa_{yy}$ - we assume that the perpendicular and longitudinal conductivities are identical. This is true for the materials in these investigations.

(iii) $\kappa_{xy} = -\kappa_{yx}$ - a manifestation of Onsager's reciprocal relations [15].

Under these simplifications, the above expression reduces to the pair of simultaneous equations

$$Q_x = -\kappa_{xx}\nabla_x T - \kappa_{xy}\nabla_y T \tag{2.4}$$

$$0 = -\kappa_{xy}\nabla_x T - \kappa_{xx}\nabla_y T. \tag{2.5}$$

which may be solved to give

$$\begin{Bmatrix}\kappa_{xx}\\ \kappa_{xy}\end{Bmatrix} = \frac{1}{w_{xx}^2 + w_{xy}^2}\begin{Bmatrix}w_{xx}\\ w_{xy}\end{Bmatrix}, \tag{2.6}$$

where

$$w_{xi} = -\frac{\nabla_i T}{Q_x} \tag{2.7}$$

are the thermal resistivities. Therefore, in order to calculate the thermal transport coefficients, we must simultaneously measure both perpendicular temperature gradients, as well as the heating power supplied to the sample.

Experimental Procedure

In our thermal conductivity investigations, we have employed the potentiometric, steady-state method [39] - alternative methods will be discussed at the end of this section. For this, a constant heater power is applied to the sample, the system is allowed to reach a new thermal equilibrium, and then the thermal gradients across the sample are measured. This constitutes step (iii) of the overall method outlined in the previous section. Let us now make clear how this procedure can be used to measure the thermal conductivity of a material.

Shown in Figure 2.3 (a) is a schematic of our experimental setup, alongside an example of a sample which has been prepared for measurement. For this configuration, the terms Equation 2.7 are given by

$$Q_x = \frac{P}{wt}, \tag{2.8}$$

where P is the power supplied by the sample heater, w is the width of the sample and t is the thickness, and

$$\nabla_i T = -\frac{\Delta_{ix} T}{l_{ix}}, \tag{2.9}$$

which implies that

$$\nabla_x T = \frac{\Delta T_x}{l} = \frac{T_3 - T_1}{l}, \tag{2.10}$$

and

$$\nabla_y T = \frac{\Delta T_y}{w} = \frac{T_1 - T_2}{w}, \tag{2.11}$$

where, with reference to the schematic in Figure 2.3 (a), l is the distance between contacts 1 and 3 and T_i is the temperature measured at the thermometer i. From Equation 2.6 - and assuming that $w_{xx} \gg w_{xy}$ - we therefore have that

$$\kappa_{xx} = \frac{P}{\Delta T_x}\frac{l}{wt}, \tag{2.12}$$

the longitudinal thermal conductivity, and

$$\kappa_{xy} = \frac{P\Delta T_y}{(\Delta T_x)^2}\frac{l^2}{w^2 t} = \kappa_{xx}\frac{\Delta T_y}{\Delta T_x}\frac{l}{w}, \tag{2.13}$$

the transverse thermal conductivity, or thermal Hall effect.

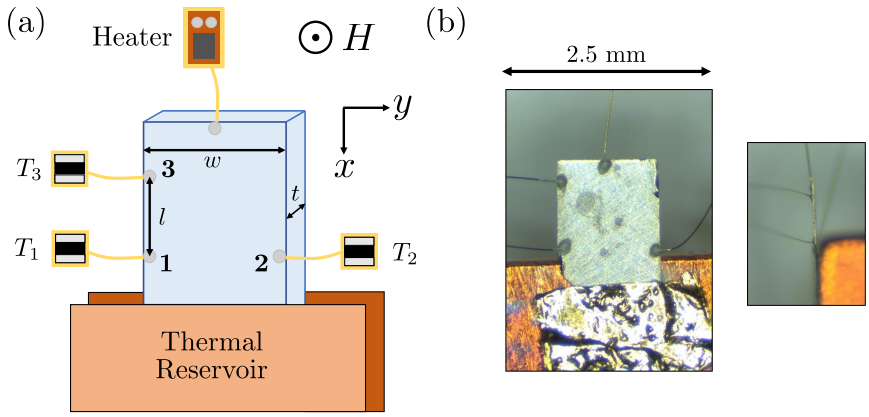

Figure 2.3 *(a) Schematic of our setup for a thermal Hall measurement, with the components described in the text. (b) Microscope image of a sample which has been prepared for measurement, before it has been clamped between the two copper plates. The second image shows a side-on microscope image of the same sample, which we have polished to* ~ 50 *μm (for comparison, the attached wires are* 25 *μm).*

In order to calculate the thermal coefficients, we therefore require a simultaneous measurement of the temperature at positions 1, 2 and 3 on the sample. This measurement must be taken with the sample in thermal equilibrium, whilst a known heat is provided by the sample heater. The accuracy of this measurement is thus critically dependent on both the thermometer calibrations and the thermal

stability of the sample stage, both of which have been discussed in the previous section. Shown in Figure 2.4 is a portion of a typical data set, with the various stages of this steady-state method labelled for clarity.

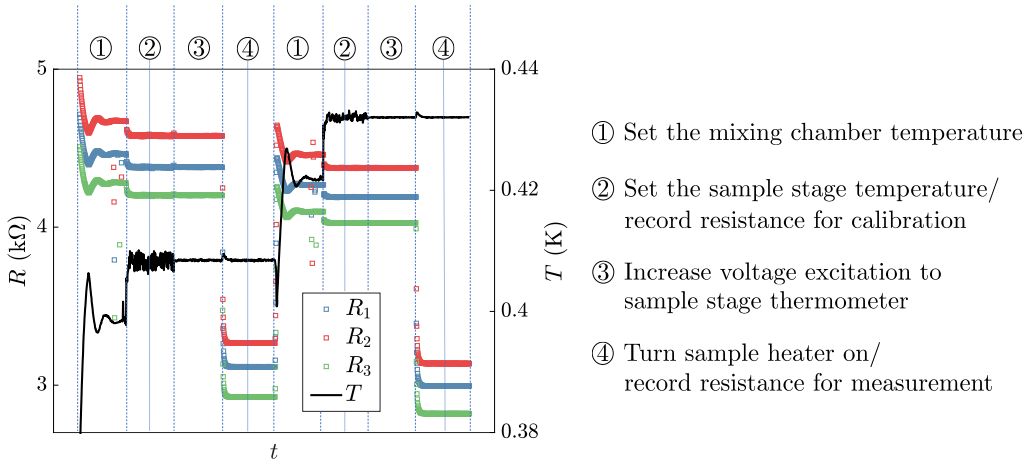

Figure 2.4 *Portion of a thermal transport measurement data set, taken in the dilution refrigerator. Plotted as a function of time are the three thermometer resistances (blue, red and green) and the sample stage thermometer temperature (black). Also labelled are the different stages of the measurement procedure. Step ③ is included to improve the sample stage temperature stability, however the voltage excitation is large enough that Joule heating can affect the measurement, hence the absolute temperature at the sample stage thermometer is not necessarily accurate during stages ③ and ④.*

Experimental Setup and 'Feasibility' Calculation

The method outlined above implicitly assumes that the temperature measured by the thermometer T_i exactly corresponds to the temperature at position i on the sample, and similarly, that the measured heater power flows entirely through the sample. For this to be the case, the measured components must be perfectly thermally isolated from everything except the sample. Unfortunately however, due to the requirement that the components be electrically wired to the sample stage and rigidly fixed in place to avoid vibrations, this is not feasible. Instead, via an assiduous choice of material components, it is possible to manipulate the flow of thermal current and severely limit the heat leakage away from the sample, thus reducing this as a source of inaccuracy.

This is especially important in our investigations, where the anticipated thermal Hall signals are often at the limits of experimental detection. As such, before

assembling an experiment, it is good practice to estimate whether - at a reasonable heat supplied to the sample - the setup is capable of producing a measurable signal. We will now walk through the details of such a feasibility calculation, primarily to discuss some of the methods employed to reduce heat leakage in our experimental setup.

Heat flow in a system can be treated in an analogous way to the flow of current in an electrical circuit, in that

$$I = \frac{V}{R} \quad \rightarrow \quad P = \frac{\Delta T}{R_{th}} \left(= \frac{\Delta T \kappa A}{l} \right), \tag{2.14}$$

where R_{th} is the thermal resistance, and the final expression is taken from Equation 2.12, with A the cross-sectional area perpendicular to the flow of heat. To see why this is useful, consider the extended schematic of our experimental setup shown in Figure 2.5 (a) (the various components will be described in detail in what follows). This entire setup may be reduced to a simple circuit diagram, shown in Figure 2.5 (b), and therefore - if all the thermal resistances are known - it is possible to calculate the ratios of thermal current through each. Importantly, this allows us to calculate the thermal current, and thus thermal gradients, across the sample, in order to determine whether a particular setup can produce a measurable signal. We will now discuss how the various thermal links in our setup have been designed in order to maximise this signal.

Sample - thermometer - The thermal link between the sample and thermometer is made by a 25 µm gold or 50 µm silver wire, so as to minimise the thermal resistance. For a metallic sample, the contacts are spot welded, whereas for an insulator they are instead fixed with DuPont 6838 silver epoxy. This is a heat cured - and therefore permanent - conductive paste, chosen over its air-dry counterpart largely due to the higher thermal conductivity. The other end of the wire is then spot welded to a 10 µm thick gold sheet. The bare chip thermometer is sanded to approximately half its thickness, and then the underside is fixed to this gold sheet, also with silver epoxy. To ensure good thermal contact, the thermometer is held in place with crossover tweezers whilst the silver epoxy is cured. Finally, one of the electrical contacts is thermally linked to the gold sheet via silver epoxy.

The thermal resistance of the silver epoxy has been estimated from prior thermal conductivity data [47]. The thermal resistances of the gold/silver wires/sheet are instead estimated from electrical resistivity data [48], alongside the Wiedemann-

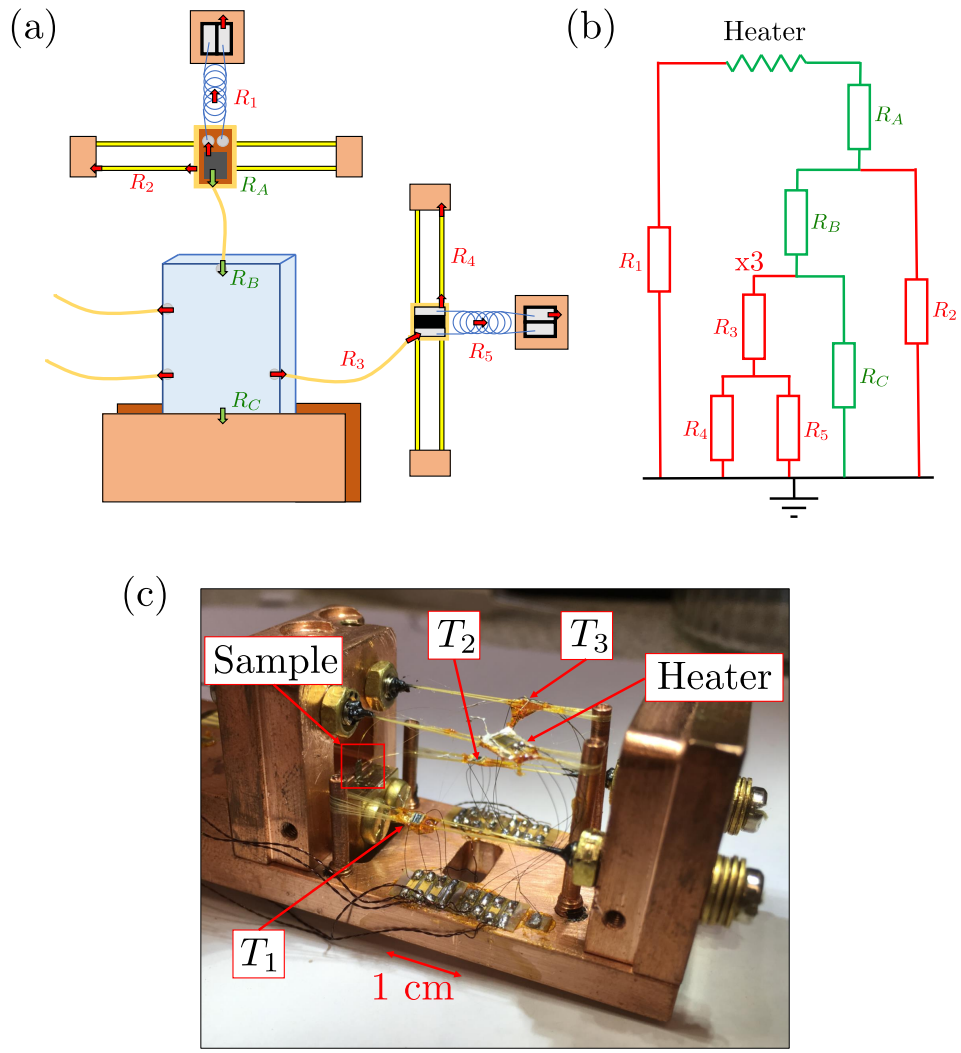

Figure 2.5 *(a) Extended schematic of our experimental setup, including the sample, heater and one thermometer, with the thermal resistances also labelled. The green arrows show the desired direction of heat flow, whereas the red arrows correspond to heat leakage. The various components are detailed in the text. (b) The associated thermal circuit diagram, used for the feasibility calculation. (c) Camera image of our setup. A microscope image of the sample (red square) is shown in Figure 2.3 (b). Note, this does not include coiled wires between the measured components and the sample stage; these were deemed unnecessary as this setup was exclusively used for measurements below 800 mK, and in low fields.*

Franz law (Section 1.3), which we assume to be valid at the low temperatures of our investigations.

Sample - heater - This thermal link is made in an identical fashion to the sample-

thermometer link. In all our measurements, a strain gauge acts as the sample heater. This has been chosen for its approximately constant resistance, regardless of temperature or applied field. The strain gauge base is made from a polyimide compound, with a sufficiently large thermal conductivity that there is no need to additionally make contact between the gold base and the electrical contacts [49].

Thermometer/heater - sample stage - As previously mentioned, this thermal link must be minimised, despite there being an electrical connection. At mK temperatures, this contradiction is straightforwardly overcome by the use of superconducting, 50 µm $Nb_{0.52}Ti_{0.48}$ wires. This material has a $T_c \sim 9$ K and an $H_{c_2} \sim 14$ T [50], so we may assume there will be a negligible thermal conductivity at low temperatures and field. However, at higher fields, care must be taken not to exceed the critical current. For higher temperature measurements, we instead use 50 µm manganin wire - a compound with a reasonable electrical conductivity, but poor thermal conductivity [44]. Finally, in both cases, the wire is tightly coiled so as to increase the length and therefore the thermal resistance.

Additionally, the components must be held firmly in place, in order to avoid noise from vibrations. This creates another thermal link which must be minimised. In our setup, the components are fixed to taut DuPont Kevlar 29 wires using GE 7031 varnish. This amorphous solid actually has a reasonably high thermal conductivity [51], and is primarily used for its low temperature adhesive properties. The high thermal resistance instead comes from the kevlar wires [52]. Problems arise however due to the kevlar expanding as the temperature is reduced, such that the wires lose tension [53]. To combat this, the kevlar wires are tensioned (at room temperature) using the setup shown in Figure 2.6. The crinkle washers are necessary to counteract the expansion of the kevlar, and keep the wires taut at low temperatures.

Sample - sample stage - From the circuit diagram in Figure 2.5 (b), it is clear that the unwanted heat leakage will scale approximately as the ratio of this thermal resistance to the total thermal resistance of all other thermal pathways. It is therefore essential that the thermal link between the sample and the stage is excellent. At higher temperatures, we have found it sufficient to attach the sample to a 1 mm silver wire using silver epoxy, which is then soldered to the body of the cold finger. At lower temperatures however, this gives too large a thermal resistance. The sample must instead be sandwiched between two 10 µm gold sheets, and then forcibly clamped between two OFHC copper blocks, as shown in Figure 2.5 (c).

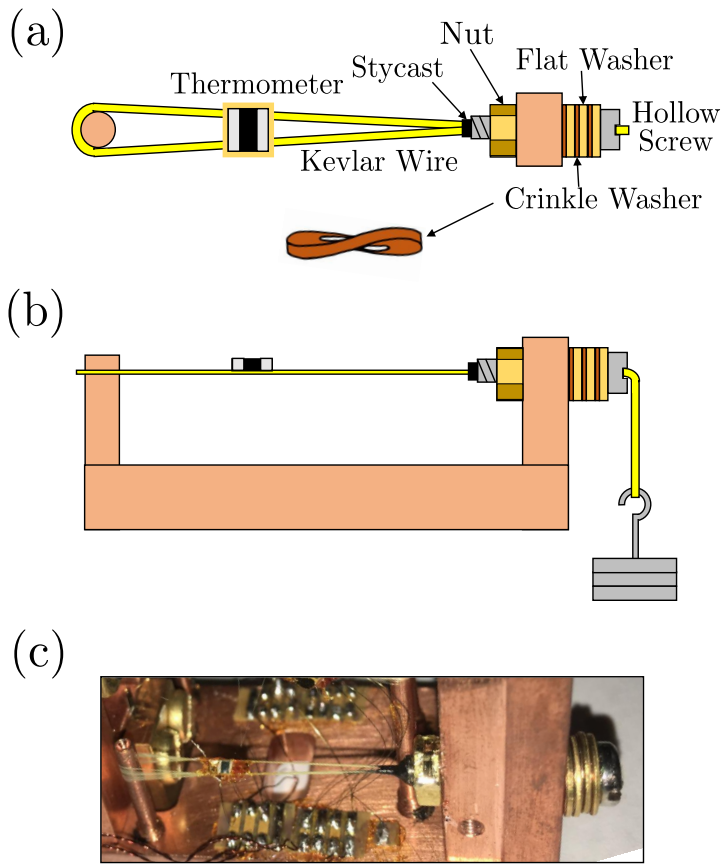

Figure 2.6 *(a) Schematic of the support for a single thermometer. The kevlar wire is threaded through a hollow screw, around the copper post and then back through the screw. The screw is then threaded through alternating crinkle and regular washers, and tightened using the nut. Also shown is a crinkle washer before being flattened, and therefore put under tension. (b) The kevlar wire is tensioned by hanging an adjustable weight and then gluing with stycast, which is left to set over 24 hours. (c) Camera image corresponding to the schematics.*

Sample dimensions - As is clear from Equations 2.12 and 2.13, the sample dimensions may be manipulated in order to increase the measurement sensitivity. Specifically, for a longitudinal thermal conductivity measurement, it is desirable to maximise l, and therefore have a rod-like sample. Alternatively, in our thermal Hall investigations, the signal may be improved by reducing the sample thickness t. To this end, we have designed a micrometre polishing jig, as shown in Figure 2.7. Using this instrument, we are able to achieve sample thicknesses of $< 50\,\mu\text{m}$ (an example is shown in Figure 2.3 (b)). However, sample fragility often becomes a limiting factor in reaching smaller thicknesses.

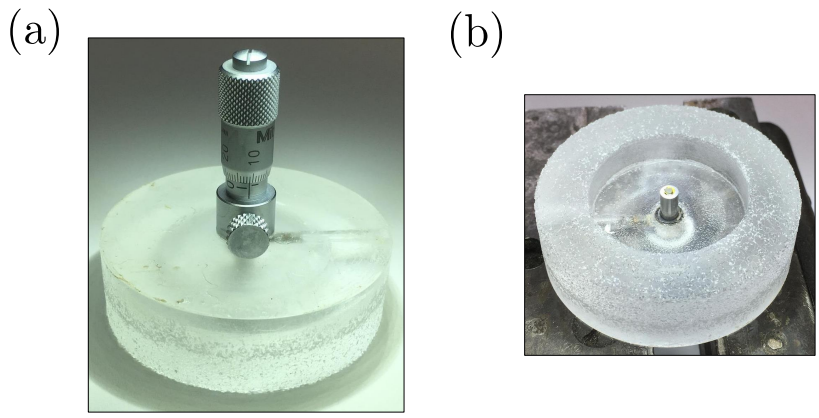

Figure 2.7 *Camera images of our polishing jig. (a) From above, showing how the micrometre screw gauge head has been fixed to a quartz base, such that (on a flat surface) the micrometre is zeroed when the measuring face is aligned with the quartz base. (b) From underneath, showing a sample fixed to the measuring face of the micrometre with GE varnish. The sample thickness may therefore be measured by placing the polishing jig on a flat surface and turning the micrometre until a small resistance is felt. The appropriate thickness of sample to be removed can then be set by extending the micrometre face beyond the quartz base, securing it in place with the locking pin, and lightly moving the base in a circular fashion across sandpaper.*

The values which enter into this feasibility calculation must obviously vary with temperature, as do the materials being considered. It is therefore not particularly useful to reproduce a temperature-specific full calculation here. Instead, we simply note that in all our investigations, we were confident of the necessary sensitivity before assembling the experiment. This is borne out by our results, in Sections 3.3 and 4.3. Finally, an image of the mK experimental setup has been included in Figure 2.5 (c), and the higher temperature setup is shown in Section 3.3 (Figure 3.14).

Thermal Hall Effect Measurements

We now discuss some considerations specific to a measurement of the transverse thermal - or thermal Hall - conductivity.

Heater power - The power supplied to the sample should be large enough to give a measurable signal, but not so large that the sample temperature deviates significantly from that of the sample stage. At higher temperatures, too large a

heater power can also lead to heat leakage through thermal radiation [44] - an example of this occurring is discussed in Section 3.3.2, including a estimation of the radiated heat. In our investigations, we set $\Delta T_x \sim 0.05T$; this is controlled by the direct current supplied to the heater. Specifically, from Equation 2.12 - and in the knowledge that the power comes from Joule heating (with $P = I^2R$) - the required heater current is given by

$$I = \sqrt{\frac{0.05T\kappa_{xx}wt}{Rl}}, \tag{2.15}$$

where R is the electrical resistance of the heater, assumed constant in this calculation. Therefore, in the majority of our investigations, the first data run is solely to determine the longitudinal thermal conductivity of the sample, such that ΔT_x can be accurately set in subsequent runs.

Antisymmetrising ΔT_y - The measured ΔT_y will often be dominated by the longitudinal temperature gradient, as a result of contact misalignment. This is demonstrated in the exaggerated schematic in Figure 2.8. In order to cancel out this contribution, the data can be antisymmetrised. This involves measuring ΔT_y at both positive and negative field, and then taking the difference between the two values in order to extract the Hall signal (δT_H). More explicitly,

$$\Delta T_y^{AS} = \frac{\Delta T_y^+ - \Delta T_y^-}{2} \tag{2.16}$$

$$= \frac{(\delta T_{xx} + \delta T_H) - (\delta T_{xx} - \delta T_H)}{2} = \delta T_H, \tag{2.17}$$

where $\Delta T_y^{+/-}$ is the thermal gradient at positive/negative field, and δT_{xx} is the longitudinal gradient due to contact misalignment. Note, this method relies on the positive and negative fields being identical in magnitude. To ensure this is the case, we measure the applied field using a Hall sensor, positioned as close to the sample as possible.

Contributions from the measuring apparatus - Previous studies have shown that the thermal reservoir - being metallic - can contribute to the measured thermal Hall effect [54]. To avoid this, at higher temperatures, the sample can instead be attached to an insulating material with good thermal conductivity (such as a LiF crystal), which is in turn thermally anchored to the sample stage. At lower temperatures however, this method produces too large a thermal resistance between the sample and sample stage. Instead, as detailed in Section 4.3, we have performed a number of checks to ensure that the thermal Hall signal is intrinsic

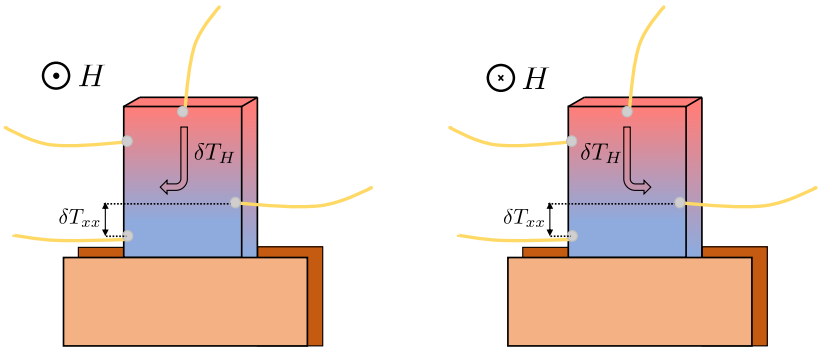

Figure 2.8 *Schematic to illustrate how the longitudinal signal δT_{xx} - arising from contact misalignment - may be removed by antisymmetrising the data, in order to isolate the Hall signal δT_H.*

to the sample.

Additionally, the current through the resistive thermometers may induce a self-heating, which can contribute to the measured signal. This power is easily calculable, and the current has been set - in a similar manner to the heater current - such that there is a negligible heating at all temperatures. Further, any contribution from this effect should be significantly reduced upon antisymmetrising the data. In order to avoid this potential complication, previous studies have used capacitive thermometry [55, 56], or a thermocouple [57], in order to measure the transverse temperature gradient. Unfortunately however, at lower temperatures, neither of these techniques are sufficiently accurate for our purposes.

Ensuring no heat leakage - In these investigations, we require the optimum sensitivity in order to detect small transverse thermal gradients. The accuracy of a measurement may be improved by increasing the heater power to the sample. However, if this is set too high, problems arise due to heat leakage via - for example - thermal radiation. In order to check for this, we note that the thermal conductivity - being a material property - should remain constant regardless of the heater power. Therefore, after increasing the heater power we first measure the thermal conductivity of the sample, to ensure that it has remained constant.

Maximum sensitivity - Theoretical papers which predict a thermal Hall effect will often calculate a peak signal, in order to demonstrate the feasibility of experimental detection. However, the majority fail to consider that the

experimentally measured signal will also vary as a function of the thermal conductivity (Equation 2.13). As such, a better gauge of feasibility is instead given by the thermal Hall angle,

$$\theta_{TH} = \tan^{-1}\left(\frac{\kappa_{xy}}{\kappa_{xx}}\right) \sim \frac{\kappa_{xy}}{\kappa_{xx}}, \tag{2.18}$$

where the approximation is almost always valid, as $\kappa_{xx} \gg \kappa_{xy}$. In our investigations, we have been able to achieve a sensitivity of $\theta_{TH} \sim 10^{-3}$.

Validating the experimental apparatus - As previously mentioned, tiny extrinsic contributions can easily be misinterpreted as thermal gradients in the sample. We would therefore benefit from some method of verifying that the experimental apparatus is capable of detecting the anticipated signal. For our higher temperature measurements this is straightforward - a number of materials have previously been demonstrated to exhibit a thermal Hall effect of a similar magnitude to that which has been predicted to occur in $SrCu_2(BO_3)_2$. As described in Section 3.4, we have successfully measured a thermal Hall effect in one of these materials - $Lu_2V_2O_7$ - and so have some confidence that our setup should be capable of measuring a similar signal in $SrCu_2(BO_3)_2$. Unfortunately, due to the novelty of these measurements, there is not such a simple check for our mK setup. Instead, as detailed in Section 4.3, we have a number of measures in place to ensure the detected signal is intrinsic to the sample. Additionally, the thermal conductivity - which comes as a necessary by-product of any thermal Hall measurement - can act as a useful sanity check.

Alternative Methods

There are various alternative steady state methods employed to measure the thermal conductivity [58]. The majority of these have been designed to overcome deficiencies in the potentiometric method - such as the radial heat flow method to avoid radiative heat losses [59], or the comparative method to avoid dependence on the heater power [39]. However, these methods are designed specifically to measure the longitudinal thermal conductivity, whereas we additionally require the transverse component.

One alternative steady state method that might be adapted to a measurement of the thermal Hall effect is the parallel thermal conductance technique [60]. This has been designed as a variation of the potentiometric technique for samples which

are too brittle to support heater or thermometer contacts. This would certainly apply to our samples if we wished to thin them any further. In this method, the heater, thermal reservoir and thermometry are all contained within the sample support. The thermal conductance of this support is then measured with and without the sample, and the difference taken between the two values in order to give the thermal conductance of the sample. This method might straightforwardly be extended to measure the transverse thermal conductivity. However, for our purposes, it seems unlikely that thinning the sample might compensate for the accuracy lost from performing an indirect measurement.

There are additionally transient methods capable of measuring the thermal conductivity. These methods do not require the sample to reach thermal equilibrium, and are therefore capable of faster data acquisition than steady state methods. For example, the pulsed power technique uses a similar setup to our own measurements, but instead applies a periodically varying heater power to the sample, whilst the temperature of the thermal reservoir is steadily made to drift [61]. The thermal conductivity can then be extracted from the time evolution of the heater and thermal reservoir temperatures. However, this method makes a number of simplifying assumptions in order to fit the data, and therefore lacks the accuracy required for our measurements of the thermal Hall conductivity.

Transient methods are more often employed to determine the thermal conductivity of thin films. In this case, the potentiometric steady state method is not possible due to the thermal contact between the thin film sample and the underlying substrate. In the 3ω method [62], an alternating current of frequency ω is passed through a metallic strip which has been deposited onto the thin film sample to act as a heater. Heat flow in the sample will then drive a characteristic response in the measured voltage of the heater, at a frequency of 3ω, allowing the thermal conductivity of the sample to be determined. The 3ω signal is typically $\sim 10^{-3}$ smaller than the applied voltage, and therefore it is difficult to determine even the longitudinal thermal conductivity by this method. However, this method may still become relevant to the future of thermal Hall measurements, as thin film deposition is becoming an increasingly prevalent and effective means of sample synthesis. Further, and importantly, the method has recently been demonstrated as being capable of measuring the off-diagonal terms in the thermal conductivity tensor [63].

2.3 Specific Heat Measurements

The heat capacity of a sample is defined as

$$C = \lim_{\Delta T \to 0} \frac{\Delta Q}{\Delta T}, \tag{2.19}$$

or the amount of heat (ΔQ) required to uniformly raise the temperature by ΔT. In a specific heat measurement, we therefore wish to monitor the sample temperature as it responds to a known heating power. This would appear similar to the thermal conductivity measurement discussed in the previous section. Crucially however, a measurement of the specific heat takes place out of thermal equilibrium. The method by which the data is acquired, and subsequently analysed, can thus significantly impact the accuracy of the interpretation.

Experimental Principle

Let us first consider the ideal scenario [64], and then build to a more realistic model. In this perfect setup, the sample, heater and thermometer are linked with zero thermal resistance, such that the heater power will be entirely provided to the sample, and similarly, the measured temperature will be exactly that of the sample. Further, the heater and thermometer should have zero specific heat, such that the measured specific heat will be solely that of the sample. This situation is schematised by the circuit shown in Figure 2.9 (b), where we have additionally included a thermal link between the setup and a thermal reservoir (the sample stage), through which the system can dissipate heat.

For our experimental purposes, Equation 2.19 may be rewritten as

$$C = \frac{dQ}{dt}\frac{dt}{dT} \implies C\frac{dT}{dt} = P, \tag{2.20}$$

where C is the sample specific heat, T is the sample temperature and P is the power supplied to the sample. The heating power experienced by the sample will be equal to the difference between the power supplied by the heater, $P_H(t)$, and

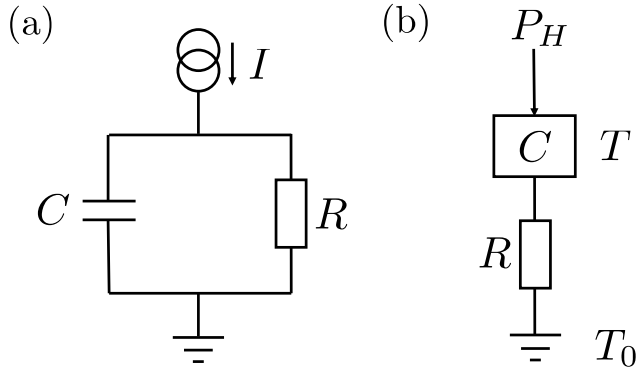

Figure 2.9 *(a) Electrical analog, and (b) heat flow circuit, of the ideal relaxation time setup. C is the sample specific heat, R is the thermal resistance between the sample (at temperature T) and the thermal reservoir (T_0), and P_H is the power supplied by the sample heater.*

that leaving the sample via the thermal link to the thermal reservoir, or

$$C\frac{dT}{dt} = P_H(t) - P_{loss}(t) \tag{2.21}$$

$$= P_H(t) - \frac{T(t) - T_0}{R}, \tag{2.22}$$

where T_0 is the temperature of the thermal reservoir and R is the thermal resistance of the link. We assume that the system is in thermal equilibrium at a time $t = 0$ (with $P_H(0) = 0$ and $T(0) = T_0$), and that we provide a constant power P_C for $t > 0$. The above expression may then be solved to give the time evolution of the sample temperature,

$$T(t) = T_0 + P_C R(1 - e^{-\frac{t}{RC}}). \tag{2.23}$$

This implies that, if the heater power and the temperature of the thermal reservoir are maintained constant, the sample temperature will exponentially decay towards a new thermal equilibrium with a time constant $\tau = RC$, and a maximum temperature rise $P_C R = \Delta T$. The specific heat is thus given by

$$C = \frac{\tau}{R} = \frac{P_C \tau}{\Delta T}. \tag{2.24}$$

The above discussion describes the relaxation time method [64]. By providing a known, constant power to the sample, the specific heat may be determined by

characterising the exponential decay of the sample temperature towards thermal equilibrium. As such, the accuracy of this method relies heavily on an appropriate fitting of the temperature profile, from which the time constant τ may be extracted. An example of a typical measurement is shown in Figure 2.11. For reasons which will become clear, this first approximation is known as the 1-τ model.

We now relax the assumption of a negligible resistance between the thermometer and the sample [65]. We also consider that the the sample platform - which includes the heater and thermometer - will have a finite specific heat. A revised schematic is shown in Figure 2.10. Note that, in this more realistic scenario, it is not possible to directly measure the sample temperature and we must instead infer it from a measurement of the platform - or addenda - temperature.

Similar to Equation 2.22, we consider the total power supplied to the addenda and the sample in order to give

$$C_a \frac{dT_a}{dt} = P_H(t) - \frac{T_a(t) - T_0}{R} - \frac{T_a(t) - T(t)}{r} \tag{2.25}$$

and

$$C \frac{dT}{dt} = -\frac{T(t) - T_a(t)}{r} \tag{2.26}$$

respectively, where C_a and T_a are the specific heat and temperature of the addenda, and r is the thermal resistance between the sample and platform. Without derivation, these simultaneous equations may be solved to give the time evolution of the addenda temperature under the same conditions as before,

$$T_a(t) = T_0 + A_1(1 - e^{-\frac{t}{\tau_1}}) + A_2(1 - e^{-\frac{t}{\tau_2}}), \tag{2.27}$$

where $A_1 + A_2 = \Delta T$. Hence, the finite thermal resistance between the sample and the measuring platform has the effect of introducing a second relaxation time to the temperature evolution. This analysis is therefore often referred to as the 2-τ model [65]. A typical measurement for a system with finite r is illustrated in Figure 2.11, showing the effect of the two different decay times.

Finally, from the above we can derive the sample specific heat,

$$C = \frac{\tau_1}{R}\left(1 - \frac{\tau_2}{RC_a}\right) + \frac{\tau_2}{R} - C_a, \tag{2.28}$$

where, as before, $R = \Delta T / P_C$. Hence, in this more realistic scenario, the specific

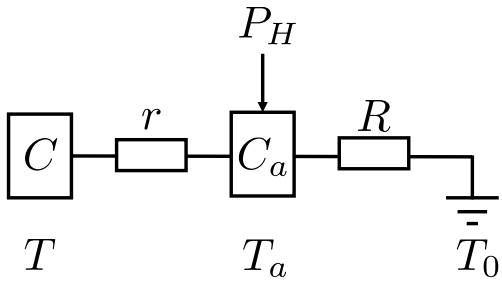

Figure 2.10 *Heat flow circuit considered by the 2-τ model. We now additionally have C_a, the addenda specific heat (with temperature T_a), and r, the finite thermal resistance between the sample and the sample platform.*

heat may similarly be determined by characterising an exponential decay. Note however, the above expression implies that the sample specific heat can only be known once the addenda specific heat has been measured. This measurement is performed separately, with the sample removed. It is therefore beneficial to ensure that the addenda specific heat is small compared to the sample specific heat, and well behaved in the temperature range under consideration, such that the sample specific heat may be straightforwardly extracted from the data.

Finally, note that for the case of a perfect thermal link between the sample and the platform, the above expression reduces to

$$C = \frac{\tau_1}{R} - C_a, \tag{2.29}$$

which is simply the 1-τ expression with the addenda contribution subtracted. In the majority of our investigations, we have that $r \to 0$, such that the above expression is adequate in determining the specific heat. However, our higher temperature data has been analysed using the 2-τ model. For measurements in the dilution refrigerator, we still make use of the relaxation time method, but have instead designed a bespoke analysis in order to better represent some of the features of our experimental procedure. This analysis requires some explanation of our experimental setup however, and we thus save the details of this analysis for Appendix B.

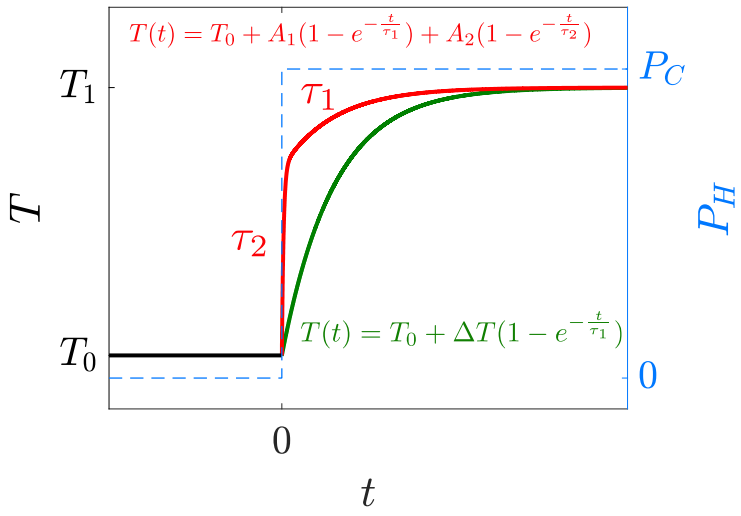

Figure 2.11 *Measurement procedure considered by the 1- and 2-τ models, plotting both the temperature of the sample thermometer and heater power as a function of time. The green temperature curve shows the ideal situation, with just a single exponential adequately describing the data. The red temperature curve is typical of a system with a finite resistance r between the sample and sample stage, such that the data is better described by a 2-τ model.*

Experimental Setup

As with our thermal conductivity investigations, we essentially have two different setups to measure the specific heat, each designed to give accurate results in a different temperature range. At higher temperatures, we have used the heat capacity option on a Quantum Design Physical Property Measurement System (PPMS). The setup and measurement procedure is described extensively in [66], and therefore we will not go into any detail here. Instead, we focus on our own setup, which has been designed to be effective at mK temperatures. This was largely inherited from Oliver Entwisle, a former PhD student in our group, and is described in detail in his thesis [67]. We will instead simply mention the essential features, before discussing some adjustments we have made to the setup and data acquisition in order to improve the accuracy of the measurements.

The experimental setup is shown in Figure 2.12. It shares a number of elements with the thermal conductivity stage detailed in the previous section, and so we will only describe these briefly. The setup comprises a 10 µm gold sheet as the sample platform, with a ruthenium oxide bare chip resistor and a carbon resistor

(to be discussed) acting, interchangeably, as the heater and thermometer. These are both contacted and attached to the sample platform using DuPont 6838 silver epoxy. The thermal link to the sample stage - or thermal reservoir - is made by 25 µm gold wires, which are spot welded to the gold sheet at one end, and clamped between two OFHC copper plates at the other. The electrical connections to the measured components are made by coiled, 50 µm, superconducting $Nb_{0.52}Ti_{0.48}$ wires. The sample platform is then adhered to a crosshair of taut DuPont Kevlar 29 wires using GE 7031 varnish.

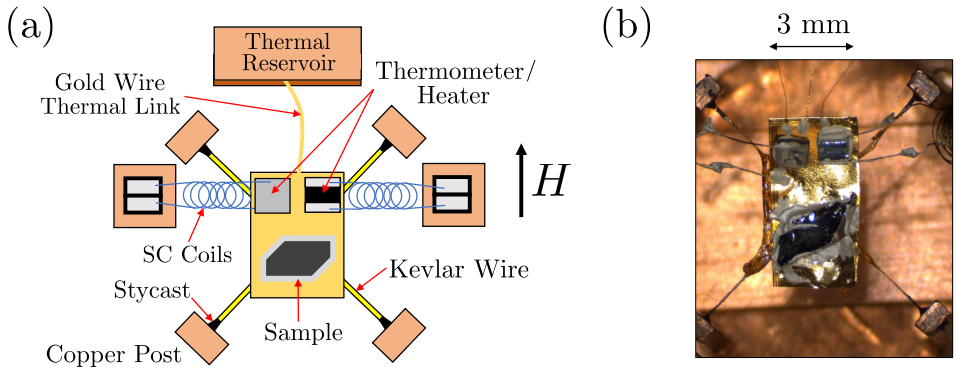

Figure 2.12 *(a) Schematic of our mK temperature specific heat setup, with the various components labelled. (b) Microscope image of the setup, configured in an identical way to the schematic. Note, the reason for the excess silver paint is due to this stage having been used multiple times prior to this measurement. In any case, we prioritise thermal contact between the sample and sample stage over reducing the addenda contribution, especially as the silver epoxy contributes negligibly to the specific heat as compared to the heavy fermion samples under investigation.*

As with the thermal conductivity measurements, it was useful to run a feasibilty calculation prior to assembly. This is far more straightforward in this instance, simply being the ratio of the thermal resistance of the gold wires to that of the kevlar crosshair mount and coiled electrical contact wires. Without explicit calculation, this setup provides sufficient thermal isolation of the sample platform that we can be confident there should be minimal heat leakage. We now discuss some additional considerations specific to this setup.

Sample - The size of the signal may be increased simply by increasing the sample mass. However, our measurements are exclusively performed on single crystals, and therefore this is often a limiting factor rather than a means of enhancement. Fortunately, the smallest mass sample measured in this work was ∼10 mg, which

is more than adequate considering the heavy fermion nature of those materials under investigation. Additionally, for measurements in field, the sample should be oriented appropriately. In our setup, an applied field will run parallel to the gold sheet, as indicated in Figure 2.12 (a).

In an effort to minimise the thermal resistance between the sample and the platform - and thus simplify the data analysis - the thermal link is made using DuPont 4929N silver epoxy, with the sample being held down by crossover tweezers whilst the epoxy is air dried. In order to make the best thermal contact, the adhered face should be approximately flat. The reasons for not using the higher thermal conductivity heat-cured silver epoxy are threefold: (i) the majority of samples under investigation will oxidise readily in air - the air-dry epoxy sets much faster, (ii) we have no effective means of heating the sample platform once it has been loaded onto the sample stage, and (iii) it is desirable to re-use the sample platform, such that the addenda measurement does not have to be repeated for every sample; this is not possible with the permanent heat-cured epoxy.

Heater / Thermometer - Various configurations for the sample heater and thermometer have been attempted previously [67]. As shown in Figure 2.12, the current assembly has a ruthenium oxide (RuO_2) bare chip resistor alongside a carbon resistor (CR), working interchangeably as the thermometer and heater. The RuO_2 is an excellent thermometer above ~ 130 mK, however below this temperature the resistance becomes too large and somewhat unpredictable. Instead, the CR resistance varies logarithmically, and consistently, at temperatures below ~ 300 mK, but is approximately constant at higher temperatures. We therefore swap the thermometer and heater around 200 mK, with some temperature overlap in the two measurements to ensure consistency. The temperature-resistance curves for the two components are shown in Figure 2.13.

The CR is simply the resistive element of a commercially available circuit resistor, previously demonstrated to be an effective thermometer to temperatures as low as 5 mK [68]. In order to fashion the CR shown in Figure 2.12 (b), the circuit resistor was stripped to leave just the resistive element, which was then cut into approximately 1 mm cubes using a wire saw. A thin film of silver was then evaporated onto the surface, in order to reduce the contact resistance. Thanks go to Coinneach Dover, formerly of the University of Edinburgh School of Engineering, for help with this step. Finally, four of the silver plated faces were sanded down, leaving two opposite faces with electrical contact pads. These were then wired up in a similar manner to the RuO_2 thermometer, as described

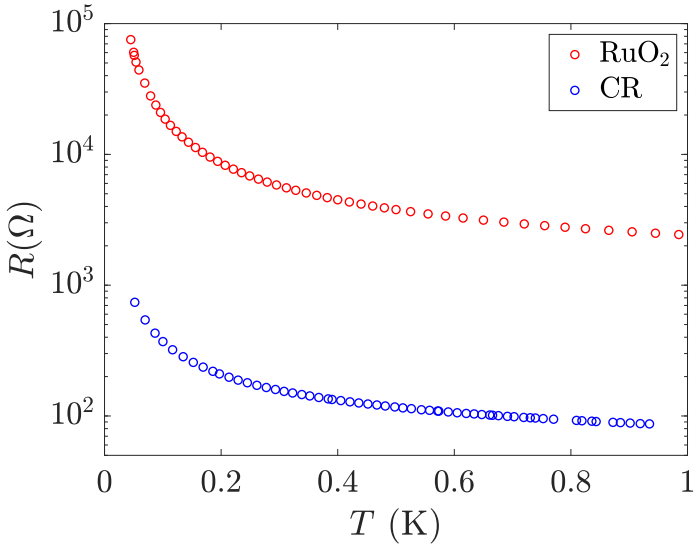

Figure 2.13 *Comparison of the temperature-resistance curves for a RuO_2 thermometer (red) and a carbon resistor (blue).*

in the previous section.

Measurement Procedure

In these measurements, the overall method of acquiring data - and the thermometer calibration - is identical to that which is described in Section 2.1. This discussion is therefore limited to step (iii) of that procedure.

Shown in Figure 2.14 is a typical measurement sequence. A direct current is sent to the sample heater whilst the voltage is measured, in order to calculate the power from Joule heating ($P = VI$). The heating profile has been designed such that the relaxation time method can be used to determine the specific heat. The heat pulses are spaced sufficiently far apart that the system can reach thermal equilibrium between subsequent pulses, implying the 1- or 2-τ model (discussed previously) can be employed to describe the individual heating curves with reasonable accuracy. However, as mentioned, we have designed a bespoke analysis better suited to our measurement procedure, and therefore the 2-τ model only serves as a useful first approximation. This measurement specific analysis is discussed in Appendix B. We now list some other considerations, designed to improve the measurement accuracy.

Heating Profile - The measured DC voltage at the heater is shown in Figure 2.14.

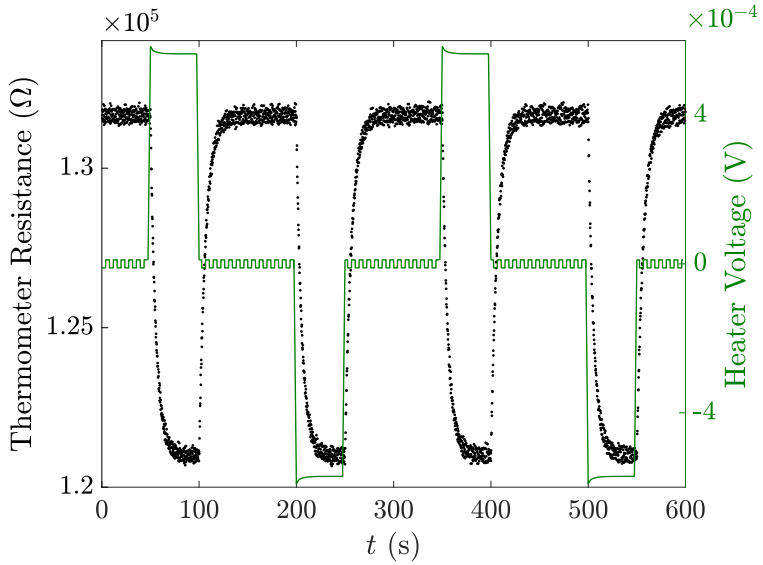

Figure 2.14 *Typical specific heat measurement sequence. Shown in black is the thermometer resistance, and in green is the heater voltage. This is from a measurement in zero field at 180 mK.*

The four heat pulses are provided by alternating positive and negative direct currents. This gives an identical heating power, but allows thermal EMFs to be corrected for in the analysis. During the 'zero' power stages, there is purposefully a small direct current, which oscillates between positive and negative 1 % of the heat pulse current. This is in order to measure the heater resistance at 'zero' power, and provides a useful sanity check if required. Finally, despite there being a constant direct current supplied during each of the heat pulses, the measured voltage shows some variation. In particular, it exhibits a short exponential decay at the beginning of each heat pulse. This is due to the temperature dependence of the heater resistance - as it heats up, the resistance falls and therefore so does the power. This is one source of inaccuracy in the 2-τ model analysis, which assumes a constant heater power. Our own analysis - described in Appendix B - corrects for this.

Time Constant - Regardless of method, the accuracy of the analysis can suffer if the relaxation time constant τ is inappropriate. If τ is too short, the discrete measurement points can fail to accurately capture the temperature variation. Similarly, if τ is too long then the measurement can take excessive time, or else the stage will not reach thermal equilibrium between heat pulses. Ideally, we would have that $1 < \tau < 10$ s. The relaxation time constant will necessarily vary as a function of sample mass and material specific heat, but it can also be

adjusted by varying the strength of the thermal link between the sample platform and the thermal reservoir. As such, and as is visible in Figure 2.12 (b), we initially spot weld three gold wires to the sample platform. The strength of the thermal link will then depend on how many of these are clamped to the thermal reservoir. Obviously however, the choice of how many to clamp will require some knowledge of the sample mass and specific heat, as well as the thermal resistance of the gold wires (see next).

Thermal Link - Regardless of model, the accuracy of the specific heat measurement relies on an accurate determination of $R\,(=\Delta T/P_C)$ - the thermal resistance between the sample platform and the thermal reservoir. In our investigations, this thermal link is provided by a gold wire, and should - at these low temperatures - have a thermal conductivity which is linear in temperature (Section 1.3). A plot of $1/R$ - or the thermal conductance - as a function of temperature therefore provides a useful sanity check. Figure 2.15 shows an example of this being an effective probe. In the first data set, there is a discontinuity as the conductance shifts between two linear trends, implying an error in the measurement. This was found to be an electrical short between two solder joints. At ~ 550 mK, the current exceeds the critical current of the $Pb_{60}Sn_{40}$ solder and the short is no longer present. For the second curve, this was corrected for, and the conductance is now completely linear. Note, the slightly different gradient is simply due to the thermal link having been remade.

Heater Power - The relaxation time method is only strictly valid in the limit $\Delta T \to 0$ (Equation 2.19). Therefore, although increasing the heater power should increase the precision of the measurement, it is important that ΔT remains small. Similar to the thermal transport measurements, ΔT may be set by the direct current supplied to the heater, and specifically from

$$I = \sqrt{\frac{\Delta T}{R\rho_H}}, \tag{2.30}$$

where R is the thermal resistance between the sample platform and thermal reservoir, ρ_H is the electrical resistance of the heater and we have calculated the heating power using $P = I^2\rho_H$. Therefore, if we assume that the thermal conductance is linear in temperature (or $1/R = KT$), and that the optimum

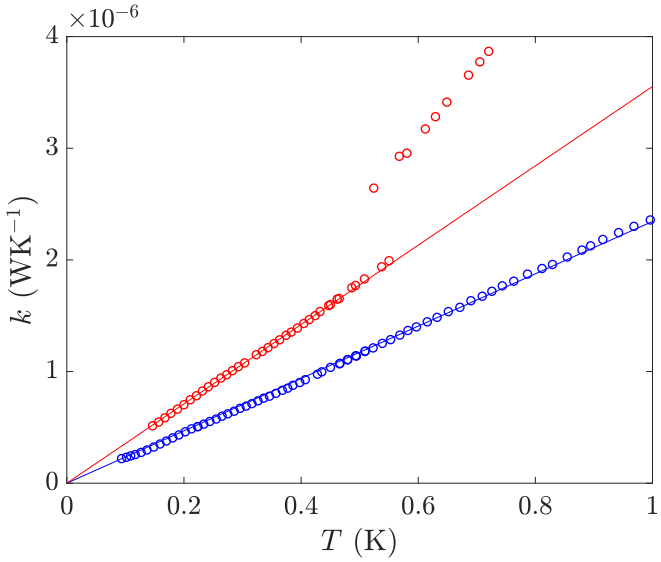

Figure 2.15 *Thermal conductance of the gold wire heat link between the sample stage and thermal reservoir. Ideally, the conductance should pass through the origin and - at these temperatures - be linear with temperature.*

$\Delta T = 0.03T$, the appropriate heater current is given by

$$I = \sqrt{\frac{0.03K}{\rho_H}}T. \tag{2.31}$$

In our measurements, we estimate ρ_H as the heater resistance at the previous data point (from $\rho_H = V/I$). The constant K is instead estimated from those previous data sets in which have used an identical thermal link. For example, the blue curve in Figure 2.15 gives $K = 2.34 \times 10^{-6}$ WK^{-2}.

Addenda - In every investigation, the addenda contribution must be subtracted from the specific heat. However, as previously mentioned, we will often try to use the same sample stage for multiple investigations, such that the addenda remains approximately constant. Shown in Figure 2.16 is an example of the addenda heat capacity for our setup. Importantly, it does not show any significant features as a function of temperature - this is reflective of the various components [67, 69, 70]. Further, above $\sim$ 200 mK, the magnitude is less than 2 % of the heat capacity of any of the samples measured in these investigations, largely due to their heavy fermion nature. The steep rise observed at the lowest temperatures is a fairly prevalent feature in specific heat measurements, and can often be attributed to a Schottky anomaly (as discussed in Appendix C). In this instance, it is suspected

that the rise is due to the nuclear quadrupolar moment of the gold atoms (in the sample platform).

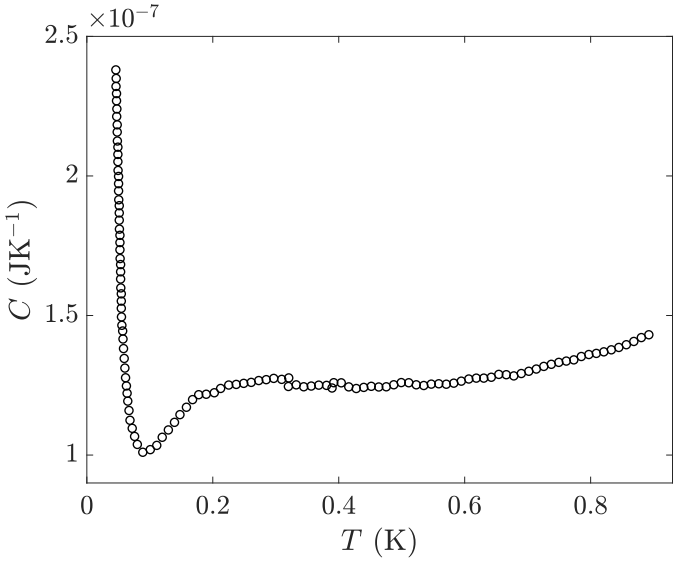

Figure 2.16 *Typical measured heat capacity of the addenda. For reference, the lowest measured heat capacity throughout these investigations was approximately double the largest value shown here.*

Alternative Methods

The relaxation time method was chosen for these investigations as it was deemed the most accurate method to give absolute values, under the conditions necessary for our measurements. However, this approach fails to capture features which vary more rapidly than the applied change in temperature ΔT, and is therefore inappropriate for studying - for example - sharp phase transitions. To study these, we may instead employ the sweep method [64]. In this technique, the sample is heated to a significantly higher temperature than the sample stage ($T \gg T_0$), then the heater power is switched off. The heat flow equation (Equation 2.22) thus reduces to

$$C\frac{dT_c}{dt} = -\int_{T_0}^{T} \frac{dT'}{R(T')}, \tag{2.32}$$

where R is the thermal resistance of the thermal link between the sample platform and the thermal reservoir, and $T_c(t)$ is the cooling profile. This method is less accurate than the relaxation time method, and the two are often used in tandem. This approach is particularly suited to our low temperature measurements, as we expect the gold wire thermal link to have a thermal conductance which is linear

in temperature, implying $R(T)$ is easy to determine. The sweep method has been used in Section 5.3 in order to ensure that the superconducting transition observed in our UTe_2 samples is not a double transition.

The sweep method may be also be modified in order to remove any dependence on the thermal resistance R. In the dual slope method [71], the measurement procedure is identical, but the specific heat is determined from a comparison of the heating and cooling profiles:

$$C(T) = \frac{P_h(T)}{\frac{\partial T_h}{\partial t} - \frac{\partial T_c}{\partial t}}, \tag{2.33}$$

where P_h is the power supplied whilst heating. This method has the benefit of acquiring data rapidly - and continuously - over a large temperature range. However, in our measurements, we have already accurately calculated the thermal resistance R by the relaxation time method, and therefore we prefer to use the sweep method (which relies on the accuracy of only one temperature profile).

Finally, we briefly mention the steady-state AC heating method [72]. For this, the experimental setup is similar to the relaxation time method, but an alternating current of frequency ω is passed through the sample heater. Neglecting any contact resistances, the temperature of the sample stage will respond at a frequency of 2ω, and have a peak amplitude of

$$T = \frac{P_H}{4\omega C}, \tag{2.34}$$

where P_H is the peak power supplied, and C is the combined specific heat of the sample and the addenda. This analysis may then be extended to account for more realistic conditions. The steady-state AC method can rival the accuracy of the relaxation time method, but has the advantage of providing data as a continuous function of temperature. Further, this method can be adapted to measure the specific heat of samples under pressure, for which thermal isolation of the sample is not so straightforward [73]. However, AC calorimetry cannot give absolute values of the specific heat, and must therefore be used alongside other measurement techniques (if absolute values are required).

Chapter 3

$SrCu_2(BO_3)_2$

The majority of quantum spin antiferromagnets emerge upon cooling from a paramagnetic state, however this long-range order may be suppressed by quantum fluctuations at the lowest temperatures, or in a system of reduced dimensionality. In these cases, there often emerges a competition between long-range order and short-range correlations, leading to what is termed a spin liquid, or glass, state. $SrCu_2(BO_3)_2$ comprises magnetic dimers lying in a two-dimensional frustrated geometry, and therefore essentially isolated from one another. As a result, the material possesses only the second known example of a two-dimensional spin-singlet ground state - the first being CaV_4O_9 [74] - and by extension, is the perfect candidate to host a quantum spin liquid phase.

The magnetic structure of $SrCu_2(BO_3)_2$ has been shown to be topologically equivalent to the Shastry-Sutherland model [75] - a two-dimensional square lattice of spins with an exactly solvable ground state [76]. The material is therefore particularly amenable to theoretical analysis, and has a history of unique experimental findings (such as the spin-gapped ground state [77], or magnetisation plateaus [78]) being consistently and adequately explained by theory. This has culminated in the recent theoretical assertion that the magnetic excitations in $SrCu_2(BO_3)_2$ should form topologically non-trivial bands, and further, that the material should exhibit a thermal Hall effect. This forms the basis of our experimental interest.

3.1 Previous Work

Research into $SrCu_2(BO_3)_2$ has given rise to a remarkable concordance between experiment and theory, and it therefore seems sensible to discuss both in tandem. The heat capacity and thermal conductivity data are extremely informative, but will instead be discussed alongside our own experimental results, in Section 3.3.

Material Characterisation

$SrCu_2(BO_3)_2$ crystallises in a tetragonal structure with the space group $I-42m$ (No.121), a single layer of which shown in Figure 3.1 (a). There is a localised $S = \frac{1}{2}$ moment on each of the Cu^{2+} ions, which form nearest neighbour spin dimers via superexchange (J) through the O^{2-} ion. The bridging angle Cu-O-Cu is 102.42° at room temperature, suggesting that J should be antiferromagnetic (as determined by the Goodenough-Kanamori rules [79]). This intradimer interaction J competes with an interdimer superexchange interaction J' through the molecular orbital of $(BO_3)^{3-}$. Finally, there is only a negligible magnetic interaction between layers, as the mediating Sr^{2+} ion has a closed shell [80].

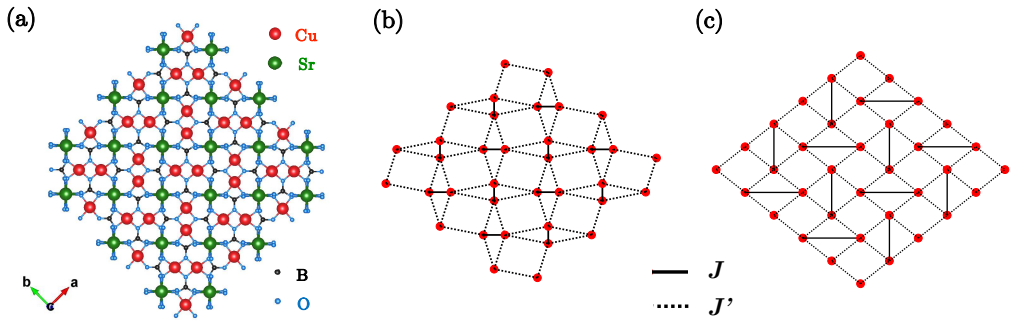

Figure 3.1 *Evolution of (a) the atomic structure of each two-dimensional layer in $SrCu_2(BO_3)_2$ (where the Sr and $CuBO_3$ planes are displaced), through (b) the magnetic structure of the same layer, where the $S = \frac{1}{2}$ moments on the Cu^{2+} sites have been isolated, to (c) the theoretical Shastry-Sutherland lattice. Figure amended from [81].*

The magnetic structure of $SrCu_2(BO_3)_2$ is shown in Figure 3.1 (b), and is topologically equivalent to the square lattice in Figure 3.1 (c) - known as the Shastry-Sutherland lattice [76]. Both can therefore be described by the same

Hamiltonian,

$$\mathcal{H} = J \sum_{nn} \mathbf{S}_i \cdot \mathbf{S}_j + J' \sum_{nnn} \mathbf{S}_i \cdot \mathbf{S}_j, \tag{3.1}$$

or in words, a two-dimensional Heisenberg model with different strength coupling between nearest and next-nearest neighbours. Shastry and Sutherland showed that, regardless of coupling strengths, the above Hamiltonian will have the corresponding eigenstate

$$|\psi\rangle = \prod_{nn} |s\rangle_{nn} = \prod_{nn} \frac{1}{\sqrt{2}} (|\uparrow\downarrow\rangle_{nn} - |\downarrow\uparrow\rangle_{nn}), \tag{3.2}$$

or a direct product of singlet states on J bonds.

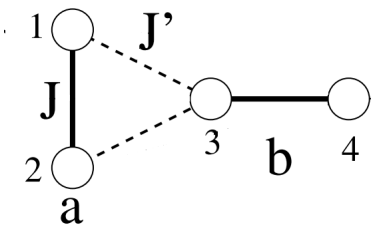

Figure 3.2 *The magnetic unit cell of $SrCu_2(BO_3)_2$, with sites labelled to aid calculations. Taken from [75].*

In order to demonstrate this is true, it is useful to rewrite $\mathcal{H}$ as a sum over the individual triangles, each of which has the Hamiltonian

$$\begin{aligned} \mathcal{H}_t &= \mathcal{H}_J + \mathcal{H}_{J'} \\ &= \frac{J}{2}(\mathbf{S}_1 \cdot \mathbf{S}_2) + J'(\mathbf{S}_1 \cdot \mathbf{S}_3 + \mathbf{S}_2 \cdot \mathbf{S}_3), \end{aligned} \tag{3.3}$$

where the spin operators are labelled with reference to Figure 3.2. A straightforward calculation then gives $\mathcal{H}_{J'} |s\rangle_a |s\rangle_b = 0$, and since $|\psi\rangle$ is clearly an eigenstate for $J' = 0$, $|\psi\rangle$ must always be an eigenstate. Further, for $0 < J' \leq J/2$, the ground state energy for an individual triangle is equal to the eigenvalue of $|\psi\rangle$ $(-\frac{3}{8}J)$, implying that, in this region of parameter space, the dimer singlet state $|\psi\rangle$ is also the ground state. In actuality, a series expansion calculation gives that $|\psi\rangle$ should remain the ground state for J' up to $\sim 0.68J$ [82].

Outside of this parameter range the ground state has not been solved exactly, however the case in which $J = 0$ is clearly equivalent to the two-dimensional square lattice Heisenberg model, which is strongly believed to exhibit long-range antiferromagnetic order [83]. This implies that at some critical J'/J there will

be a phase transition between short-range correlations and long-range order. Determining the relative coupling strengths in $SrCu_2(BO_3)_2$ is therefore crucial to understanding its physical properties.

The Spin-Singlet Ground State

The above discussion implies that a determination of the magnetic ground state in $SrCu_2(BO_3)_2$ will shed some light on the relative coupling strengths. To this end, magnetic susceptibility data is shown in Figure 3.3. Immediately obvious is that the two sets of data taken in perpendicular fields are almost identical (with the small difference being attributable to an anisotropic g-factor [84]). This provides some justification for using the Heisenberg model in defining the Hamiltonian (Equation 3.1). However, in this context, the most significant feature is the vanishing susceptibility at the lowest temperatures. This is indicative of a non-magnetic ground state, and an energy gap in the spin excitation spectrum.

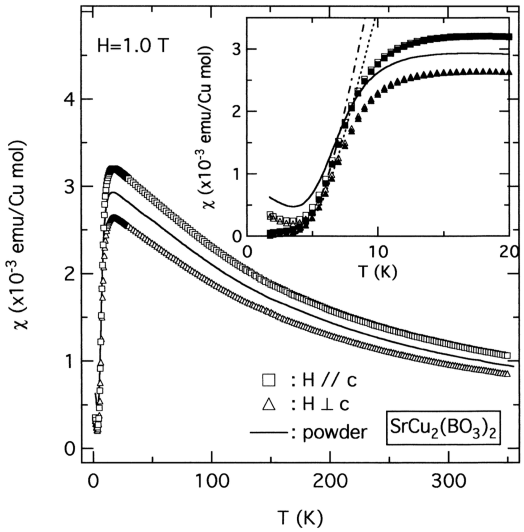

Figure 3.3 *Magnetic susceptibility of $SrCu_2(BO_3)_2$. Inset is an enlarged plot of the low-temperature region, with the dashed and dot-dash lines giving the fitted curves of $\chi_\perp$ and $\chi_{//}$ respectively, as described in the main text. Taken from [78].*

In order to estimate this energy gap, the data can be fit using an $S = \frac{1}{2}$ isolated antiferromagnetic dimer model. More specifically, the appropriate energy levels (as shown in Figure 3.4) can be inserted into the Van Vleck equation for magnetic

susceptibility [85] in order to give

$$\chi = \frac{2Ng^2\mu_B^2\beta}{3 + e^{\Delta_s\beta}}, \tag{3.4}$$

where N is the Avogadro number, μ_B is the Bohr magneton and $\beta = 1/k_BT$, with k_B the Boltzmann constant. A fit in the low temperature region then gives $\Delta_s = 34 \pm 1$ K, which is in excellent agreement with those values obtained via inelastic neutron scattering [86], ESR [84] and heat capacity [87] measurements (the latter of which will be discussed in Section 3.3.1).

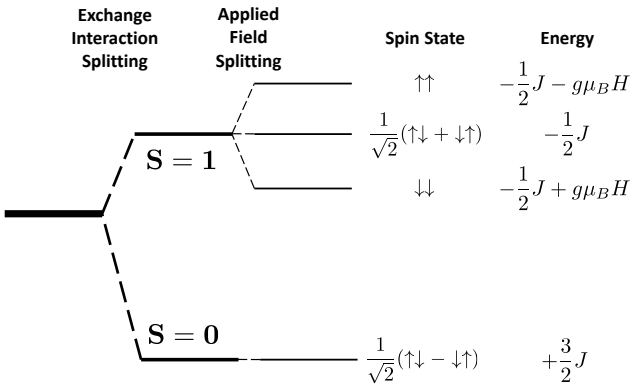

Figure 3.4 *Energy levels for a pair of antiferromagnetically coupled $S = \frac{1}{2}$ moments. The zero-field energy gap is therefore $-2J$.*

Although the model correctly estimates the energy gap, the fit deviates substantially from the experimental data at higher temperatures (as shown in the inset of Figure 3.3). This suggests that the dimers are not entirely isolated, or in other words, that J' is not negligible compared to J. Therefore, in order to get a quantitative estimate of J'/J, [88] has used the transfer matrix method to calculate, and fit, the magnetic susceptibility for various relative coupling strengths. This method allows the partition function of a finite system (20 dimers in this case) to be written exactly as the trace of a product of matrices. The susceptibility can thus be calculated as

$$\chi = -\left(\frac{\partial^2 f}{\partial h^2}\right)_T, \tag{3.5}$$

where f, the free energy, is a function of the partition function, and h is the applied field. Using this method, a relative coupling strength of $J'/J = 0.635$ gave the best fit. This value agrees with the value obtained from a similar analysis of the heat capacity data (also in [88]).

The conclusion, therefore, is that $SrCu_2(BO_3)_2$ does indeed possess a spin-singlet ground state. However, when compared to the theoretically derived critical J'/J (~ 0.68), the experimentally determined ratio of 0.635 implies that $SrCu_2(BO_3)_2$ is teetering on the brink of a phase transition to long-range order. In fact, using hydrostatic pressure, which acts to reduce J faster than J', recent studies have been successful in pushing the material over the edge of this precipice. At a pressure of 1.85 GPa (and a ratio $J'/J = 0.66$), ESR data shows evidence of a transition to an intermediate plaquette phase [89], wherein four adjacent parallel dimers interact to form an effective singlet. Further, above 5 GPa, neutron studies have shown evidence for a transition to an antiferromagnetically ordered state [90]. However, this is accompanied by a structural phase transition, and is probably not, therefore, long-range order in a two-dimensional system - something which is prohibited by the Mermin-Wagner theorem [91].

Dispersionless Magnetic Excitations

The preceding discussion concluded that the ground state of $SrCu_2(BO_3)_2$ must be one of only short-range correlations, or more specifically, a system of uncorrelated dimers, each of which is bound in a singlet. The promotion of an individual dimer from singlet to triplet pairing therefore represents the lowest energy magnetic excitation. Arguably the best experimental tool for investigating such excitations is neutron scattering.

The first inelastic neutron scattering studies on $SrCu_2(BO_3)_2$ showed evidence for three distinct magnetic excitations [86] - the anticipated triplet excitation at 3 meV ($\sim$ 34 K), as well as two at higher energies. These higher energy features have been interpreted as bound triplet excitations, and are relevant to the discussion of the thermal conductivity data in Section 3.3.2. Importantly however, the single triplet excitations were found to be extremely localised. This is at odds with the aforementioned strong interdimer interactions, but can be reconciled by considering the geometry of the system. Specifically, the orthogonality of adjacent dimers gives rise to a magnetic frustration, which strongly suppresses the propagation of single triplet excitations. This localisation has also been demonstrated theoretically - hopping between neighbouring dimers is only permitted at the sixth order of a perturbative expansion of J'/J [92].

One consequence of the localised excitations in $SrCu_2(BO_3)_2$ is the emergence of plateaus in the high-field magnetisation data, as shown in Figure 3.5. These

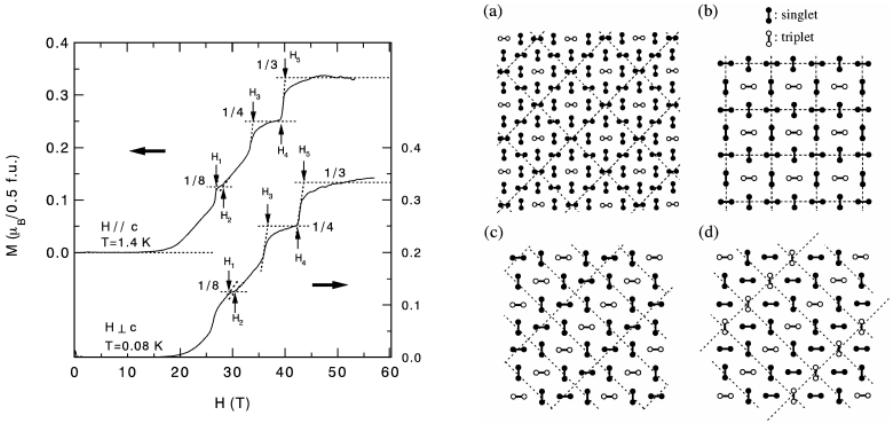

Figure 3.5 *Left hand panel shows magnetisation data at two different temperatures, taken in perpendicular fields. Right hand panel shows potential magnetic superstructures at (a) 1/8, (b) and (c) 1/4, and (d) 1/3 plateaus. Taken from [93].*

plateaus occur at fractions of the Cu^{2+} saturation moment and are independent of field direction, implying that they do not originate from magnetic anisotropy [81]. This behaviour can be explained rather effectively through the use of a hard-core boson model [94], which considers the triplet excitations as particles in a sea of singlets. Within this model, there arises a competition between the kinetic energy of the excitations and the repulsive interaction between them. At certain densities of triplet excitations (or applied fields), it is energetically favourable for the excitations to crystallise into a magnetic superstructure. The resulting energy gap is stable over a range of fields, which gives rise to magnetisation plateaus.

Up to this point, the experimental data has been adequately explained using just the Shastry-Sutherland model. However, more recent (and more precise) ESR [95] and inelastic neutron [96] studies have shown that the single triplet excitations acquire a small dispersion. This will be crucial in deriving a thermal Hall effect, and importantly, suggests there are more complex interactions to be considered. Nonetheless, it is rather satisfying that a simple model - initially constructed solely to manufacture an exact ground state - has the capacity to shed so much light on such an intricate material.

3.2 Anticipated Thermal Hall Effect

With reference to the derivation outlined in Section 1.1, it is clear that $SrCu_2(BO_3)_2$ is beginning to accrue those ingredients necessary for a thermal Hall effect carried by magnons. Specifically, the material has a two-dimensional magnetic structure which plays host to dispersive magnetic excitations. All that remains is to demonstrate that these excitations form topologically non-trivial bands. The key to this, and indeed the small dispersion, is the Dzyaloshinskii-Moriya interaction.

The Dzyaloshinskii-Moriya Interaction in $SrCu_2(BO_3)_2$

The Dzyaloshinskii-Moriya (DM) interaction is a higher order correction to the superexchange interaction between two neighbouring spins, and derives from spin-orbit coupling [97]. Most generally, it can be expressed as

$$\mathcal{H}_{DM} = \mathbf{D}_{ij} \cdot (\mathbf{S}_i \times \mathbf{S}_j), \tag{3.6}$$

and therefore favours a canting of (anti)parallel spins. With reference to Figure 3.6 (a), the orientation of $\mathbf{D}_{ij}$ is given by $\mathbf{r}_i \times \mathbf{r}_j$, which implies that the DM interaction must vanish for a centrosymmetric bond centre. As such, in $SrCu_2(BO_3)_2$, the slight corrugation of the layers below a structural transition at 395 K is essential, allowing for a non-zero DM interaction on all bonds in the magnetic structure [98]. These interactions act to relieve the magnetic frustration, and give rise to a small dispersion of the single triplet excitations, first observed via inelastic neutron scattering [96].

More formally, the DM interactions may be included as additional terms in the Hamiltonian, which now reads

$$\mathcal{H} = \sum_{nn} \left[J\mathbf{S}_i \cdot \mathbf{S}_j + \mathbf{D}_{ij} \cdot (\mathbf{S}_i \times \mathbf{S}_j) \right] + \sum_{nnn} \left[J'\mathbf{S}_i \cdot \mathbf{S}_j + \mathbf{D}'_{ij} \cdot (\mathbf{S}_i \times \mathbf{S}_j) \right] - g_z h^z \sum_i S_i^z, \tag{3.7}$$

where the final term has been included to account for an applied field h^z perpendicular to the two-dimensional plane, and g_z is the g-factor. The allowed components of the $\mathbf{D}_{ij}$ vectors may then be determined from the symmetries of

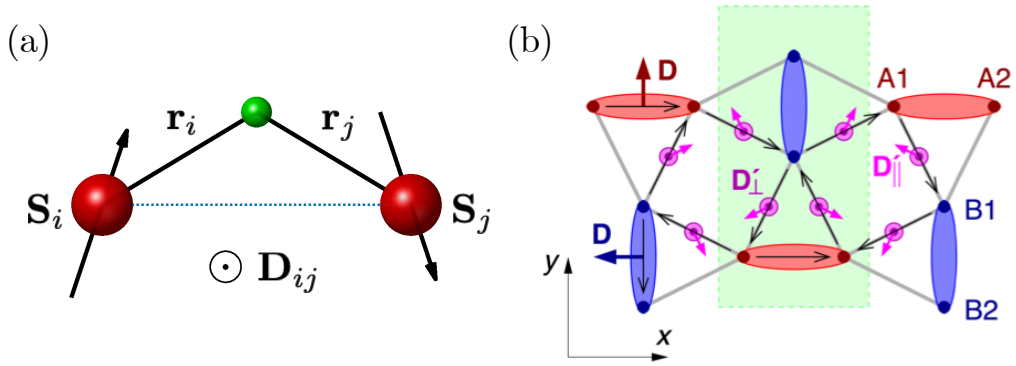

Figure 3.6 *(a) Schematic of the DM interaction for two neighbouring spins interacting via superexchange through a non-magnetic ion (shown in green). (b) Magnetic structure of a single layer of $SrCu_2(BO_3)_2$, showing the direction of all of the DM interactions. The interdimer coupling is split into an in-plane ($\mathbf{D}'_{\parallel}$, pink arrows) and an out-of-plane ($\mathbf{D}'_{\perp}$, pink dots) component. The black arrows on bonds represent the order of spins, $i \to j$, in calculating the DM vector. The magnetic unit cell is indicated by the green region. Taken from [99].*

the crystal [100]. With reference to the labelling and axes in Figure 3.6 (b), the intradimer vectors are $\mathbf{D}_A = (0, D, 0)$ and $\mathbf{D}_B = (-D, 0, 0)$. The interdimer vectors are slightly more complicated, and can point in any arbitrary direction. However, once one has been defined, the remainder are fixed. Importantly, when moving round a triangle of nearest neighbour bonds, one of the in-plane components will swap sign and therefore cancel - for example, the x-component in the central triangle of Figure 3.6 (b). As such, this component can be ignored. The key interdimer DM interaction is then the out-of-plane component, which points in the same direction for each bond, and thus encodes a sense of rotation. This is what drives the anticipated thermal Hall effect in $SrCu_2(BO_3)_2$.

Triplon Dispersion

Having better defined the Hamiltonian, the logical next step is to calculate the energies of the system. At this point, it will be useful to switch to the bond-operator formalism, which is a second quantised notation wherein the operators $s^\dagger$ and $t^\dagger_{x,y,z}$ create dimer singlet and triplet states out of the vacuum, respectively [101, 102]. Specifically, we have that

$$|s\rangle = s^\dagger |0\rangle = \frac{1}{\sqrt{2}}(|\uparrow\downarrow\rangle - |\downarrow\uparrow\rangle), \tag{3.8}$$

$$|t_x\rangle = t_x^\dagger |0\rangle = \frac{i}{\sqrt{2}}(|\uparrow\uparrow\rangle - |\downarrow\downarrow\rangle), \tag{3.9}$$

$$|t_y\rangle = t_y^\dagger |0\rangle = \frac{1}{\sqrt{2}}(|\uparrow\uparrow\rangle + |\downarrow\downarrow\rangle) \tag{3.10}$$

and

$$|t_z\rangle = t_z^\dagger |0\rangle = -\frac{i}{\sqrt{2}}(|\uparrow\downarrow\rangle + |\downarrow\uparrow\rangle). \tag{3.11}$$

However, before recasting the Hamiltonian within this formalism, we note some important considerations. For one, unlike for the Shastry-Sutherland lattice, the ground state will not be a direct product of singlets. The intradimer DM interaction will cant the spins, and thus admix some triplet contribution, with the degree of admixture being given by the strength of D. Second, also as a result of the DM interactions, the two orthogonal dimers will be inequivalent. Fortunately however, both of these details may be accounted for by an appropriate transformation of the operators [99], which we therefore relabel $s'^\dagger$ and $t'^\dagger_{x,y,z}$. The Hamiltonian then becomes

$$\mathcal{H} = \sum_{\mathbf{r}} \left[J \sum_{\mu=x,y,z} t'^\dagger_{\mu,\mathbf{r}} t'_{\mu,\mathbf{r}} + ih^z (t'^\dagger_{x,\mathbf{r}} t'_{y,\mathbf{r}} - t'^\dagger_{y,\mathbf{r}} t'_{x,\mathbf{r}}) \right] + \sum_{\mathbf{r}\in\Lambda} \sum_{\boldsymbol{\delta}} \sum_{\mu,\nu=x,y,z} t'^\dagger_{\mu,\mathbf{r}+\boldsymbol{\delta}} M_{\mu\nu}(\boldsymbol{\delta}) t'_{\nu,\mathbf{r}}, \tag{3.12}$$

where Λ denotes the lattice of dimers, $\boldsymbol{\delta}$ are the four nearest neighbour unit vectors, and the hopping matrix, M, is a function of the DM vectors. Rather than write the explicit form of M, we simply note that the effect of the DM interactions is to allow the hopping of single triplet excitations between adjacent dimers. In light of the fact that these excitations are now dispersive bosons, we rename them triplons.

In order to calculate the triplon band energies, we Fourier transform the Hamiltonian to give

$$\mathcal{H}_{\mathbf{k}} = \sum_{\mathbf{k}} \sum_{\mu=x,y,z} \tilde{t}'^\dagger_{\mu,\mathbf{k}} M_{\mu\nu}(\mathbf{k}) \tilde{t}'_{\nu,\mathbf{k}}, \tag{3.13}$$

where, explicitly this time,

$$M(\mathbf{k}) = \begin{pmatrix} J & -ih^z g_z + 2iD'_\perp \gamma_3 & \tilde{D}_\parallel \gamma_2 \\ -ih^z g_z - 2iD'_\perp \gamma_3 & J & -\tilde{D}_\parallel \gamma_1 \\ \tilde{D}_\parallel \gamma_2 & -\tilde{D}_\parallel \gamma_1 & J \end{pmatrix}. \tag{3.14}$$

In this expression, $\gamma_1 = \sin k_x$, $\gamma_2 = \sin k_y$, $\gamma_3 = \frac{1}{2}(\cos k_x + \cos k_y)$ and $\tilde{D}_\parallel = \tilde{D}_{\parallel,s} - \frac{DJ'}{2J}$, where $\tilde{D}_{\parallel,s}$ refers to the in-plane component which does not cancel when moving around a triangle of nearest neighbour bonds (Figure 3.6 (b)). Finally, this hopping matrix may be re-expressed

$$M(\mathbf{k}) = J\mathbf{I} + \mathbf{d}(\mathbf{k}) \cdot \mathbf{L}. \tag{3.15}$$

which is exactly analogous to the Hamiltonian for the simple two-band model considered in Section 1.1 (Equation 1.18), but with the spin-1/2 Pauli matrices replaced by their spin-1 counterparts, $\mathbf{L}$.

From this, a number of results straightforwardly follow. For example, the band energies can be read off as $\{J + |\mathbf{d}(\mathbf{k})|, J, J - |\mathbf{d}(\mathbf{k})|\}$, where

$$\mathbf{d}(\mathbf{k}) = \left[\tilde{D}_\parallel \gamma_1, \tilde{D}_\parallel \gamma_2, h^z g_z - 2D'_\perp \gamma_3\right]. \tag{3.16}$$

At zero field, the three bands therefore touch at the corners of the structural Brillouin zone. As such, the magnetic excitation spectrum in $SrCu_2(BO_3)_2$ forms Dirac cones, and represents a spin-1 generalisation of systems such as graphene [7]. As shown in Figure 3.7, the calculated triplon band dispersion reproduces inelastic neutron data fairly well, although requires the inclusion of a second neighbour dimer-dimer interaction K, which locally shifts the triplon energies by $2K \cos k_x \cos k_y$ [99]. With this additional term, the agreement between experiment and theory gives some confidence that this simple three-band model is appropriate.

Thermal Hall Effect of Triplons

Recall the expression derived in Section 1.1 for the thermal Hall conductivity of a two-dimensional system of magnons -

$$\kappa^{xy} = -\frac{k_B^2 T}{\hbar V} \sum_{n,\mathbf{k}} c_2(\rho^B(\varepsilon_{n\mathbf{k}})) \mathcal{F}_{n,z}(\mathbf{k}), \tag{3.17}$$

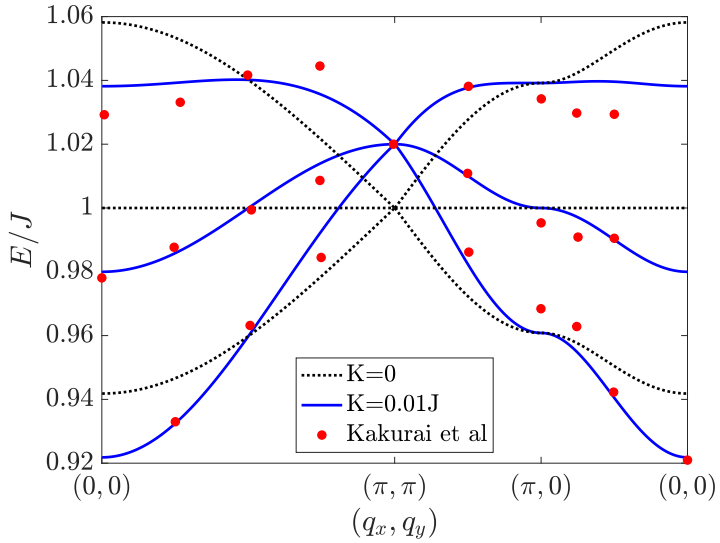

Figure 3.7 *Single triplon dispersion in $SrCu_2(BO_3)_2$, showing the band energies calculated using the hopping matrix in Equation 3.15. K is a second neighbour dimer-dimer interaction, and is included by shifting $J \to J - 2K \cos k_x \cos k_y$ [99]. Also included is the inelastic neutron scattering data from [103], normalised to the degenerate point at (π, π).*

where $\mathcal{F}_{n,z}$ is the z-component of the Berry curvature for the nth magnon band, and ρ^B is the Bose-Einstein distribution function. From the above, the triplons in $SrCu_2(BO_3)_2$ form three, non-degenerate, dispersive bands. All that remains in deriving a thermal Hall effect, therefore, is to demonstrate that these bands have regions of non-zero Berry curvature.

Without calculation, it is clear from the hopping matrix (Equation 3.14) that the interdimer DM interactions lead to complex hopping amplitudes. The triplons therefore acquire a phase when hopping between dimers, or equivalently, they feel the effect of a **k**-space vector potential - this is the Berry connection. As a result, when moving around closed loops, the triplons acquire a Berry phase. This simple argument implies the triplon bands should have a Berry curvature. However, in order to give a quantitative estimate for the thermal Hall effect, this must be made more formal.

From the above expression, a calculation of the thermal Hall conductivity should require knowledge of the Bloch wavefunctions of the system, in order to determine the Berry curvature of each band (Equation 1.16). However, the problem can be drastically simplified by analogy with the two-band model of Section 1.1. In that

model, the Chern number of each band is given by the number of times $\hat{\mathbf{d}}(\mathbf{k})$ wraps around the unit sphere as a function of $\mathbf{k}$ [6]. In this system, $\mathbf{d}(\mathbf{k}) = 0$ is similarly the point at which the bands become degenerate, and as such, it is a Berry monopole. We can therefore use a similar technique to determine the topological invariant of each band. Specifically, consider the surface defined by $\mathbf{d}(\mathbf{k})$; we find that the number of times this surface encloses the origin is equal to the Chern number of the band. This is shown in Figure 3.8. From this, and also Equation 3.16, we see that an applied magnetic field acts to shift the surface along z, and thus may be used to tune topological transitions.

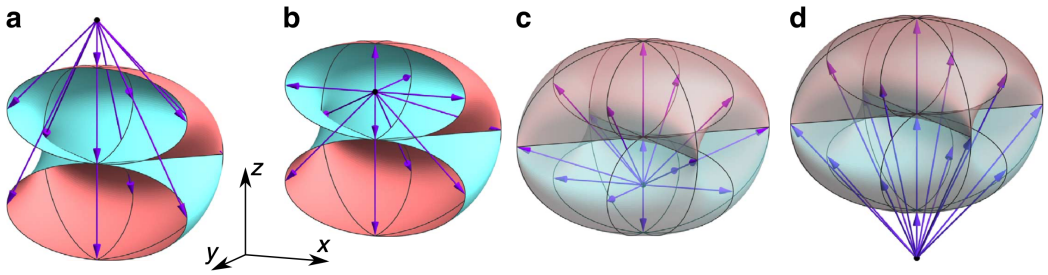

Figure 3.8 *Surfaces obtained from mapping each point in the Brillouin zone to the vector* $\mathbf{d}(\mathbf{k})$*, showing the topological transitions as a function of field. For each surface, the applied field and Chern number of the upper band - $[H, C]$ - are (a) $[3H_c/2, 0]$, (b) $[H_c/2, 2]$, (c) $[-H_c/2, -2]$ and (d) $[-3H_c/2, 0]$, where H_c is the field at which the topological transition occurs. Taken from [99].*

Using the above method, and after some simplification [99], the expression for the thermal Hall conductivity may be written

$$\kappa^{xy} \simeq \left(\frac{\varepsilon_0\beta}{2\sinh\frac{\varepsilon_0\beta}{2}}\right)^2 \int_{BZ} d^2\mathbf{k} \frac{2}{|\mathbf{d}|^2}\mathbf{d}\cdot\left(\frac{\partial\mathbf{d}}{\partial k_x}\times\frac{\partial\mathbf{d}}{\partial k_y}\right), \tag{3.18}$$

where ε_0 is the energy of the middle band. Note that, although this expression comes from summing over all bands, the three bands have been approximated as having same energy ε_0, as the band dispersions and splittings are significantly smaller than the gap between the bands and the ground state. The thermal Hall conductivity may therefore be calculated, and the contribution from individual layers summed, to give a quantitative estimate of thermal Hall effect in $SrCu_2(BO_3)_2$. This is shown in Figure 3.9 as a function of field, and at a constant temperature. Note that, unlike the analogous integer quantum Hall effect, the conductivity is not quantised. As discussed previously, a thermal Hall effect of magnons depends on the magnitude of the Berry curvature in thermally occupied

parts of the band, rather than the Chern number of occupied bands

Finally, motivated by improved inelastic neutron scattering data, a more recent study [104] has refined the description of the magnetic excitation spectrum in $SrCu_2(BO_3)_2$ further still. Specifically, by including additional anisotropic intradimer interactions in the Hamiltonian, they found remarkable agreement between experiment and theory, even correctly accounting for a relatively dispersive triplon bound state at higher energies. This improved model leads to additional topological transitions as a function of field. However, as shown in Figure 3.9, this only gives small corrections to the thermal Hall effect.

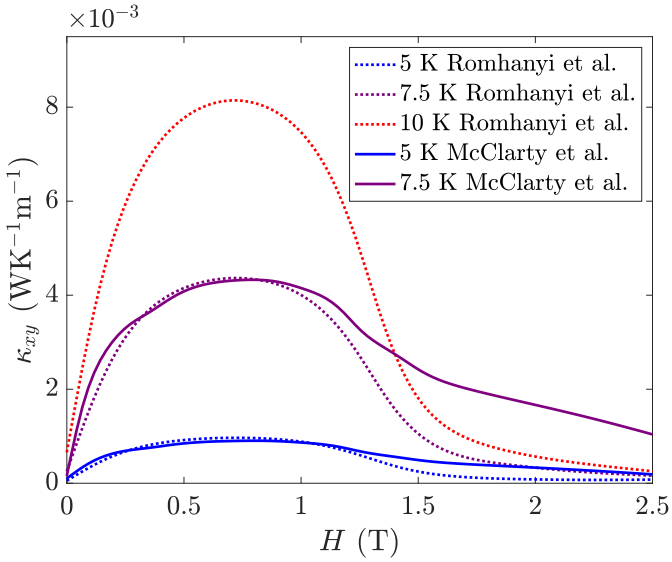

Figure 3.9 *Calculated thermal Hall effect in $SrCu_2(BO_3)_2$, plotted as a function of field. Data taken from [104] (McClarty et al.) and [99] (Romhanyi et al.).*

3.3 Experimental Results and Interpretation

In the following, we present our own specific heat and thermal transport measurements on the material $SrCu_2(BO_3)_2$. The former is used to estimate the energy scale of the lowest order magnetic excitation, whilst the latter reveals a coupling between these excitations and the lattice vibrations. Finally, measurements of the transverse thermal conductivity look to establish whether the anticipated topologically non-trivial triplons manifest as a detectable thermal Hall effect.

We are grateful to Dharmalingam Prabhakaran of the University of Oxford for providing single crystals of $SrCu_2(BO_3)_2$. These were grown with 99%-enriched ^{11}B by the optical floating zone technique at 0.25 mmh^{-1} under 3 bar oxygen pressure. All the data presented here was taken using the same sample - a 2.7 x 1.9 x 0.3 mm, 5.02 mg single crystal, fully indexed with the $I-42m$ structure by Laue X-ray diffraction.

3.3.1 Specific Heat

The specific heat was measured using a Quantum Design Physical Property Measurement System (PPMS). As shown in Figure 3.10, the sample is adhered to an alumina chip using Apiezon N grease, alongside a RuO_2 heater and Cernox thermometer, both permanently fixed to the chip. The chip is then weakly thermally coupled to the cryostat by 8 Au-Pd wires, which also provide the electrical connections to the heater and thermometer, as well as the structural support for the sample stage. The measurements are performed using the relaxation time method, and the data analysed using the 2-τ model, both of which are described in Section 2.3. The measurement procedure is also detailed in [66].

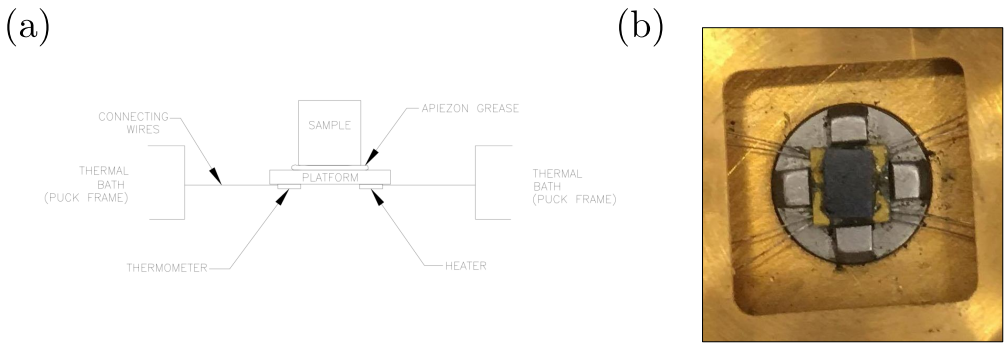

Figure 3.10 *(a) Experimental setup used to measure the specific heat. Taken from [66]. (b) Image of the sample mounted on the sample stage.*

Zero-Field Specific Heat

Shown in Figure 3.11 is the zero-field specific heat data for $SrCu_2(BO_3)_2$. Immediately obvious is the peak occurring around 7.5 K, which we attribute to a Schottky anomaly. In order to justify this, consider the simplest approximation

in which $SrCu_2(BO_3)_2$ may be treated as a system of isolated dimers, with each dimer having a finite energy gap between the spin-singlet ground state and the lowest excited triplet state (as illustrated in Figure 3.4). As discussed in Appendix C, this is exactly the situation - a limited number of discrete energy levels - that can result in a Schottky anomaly appearing in the specific heat.

We now fit the data in the low-temperature region ($T < 7$ K), where - in this lowest order approximation - the only contributions will come from the Schottky anomaly and lattice vibrations. The heat capacity per mole of dimers (or Schottky centres) has been derived in Appendix C, and is given by [35]

$$C_{sch} = \frac{R}{T^2}\left[\frac{1}{Z}\sum_i \varepsilon_i^2 e^{-\varepsilon_i/T} - \left(\frac{1}{Z}\sum_i \varepsilon_i e^{-\varepsilon_i/T}\right)^2\right]. \tag{3.19}$$

where Z is the partition function for each dimer, R the gas constant and ε_i are the discrete energy levels, measured in Kelvin. Taking the spin-singlet ground state to have $\varepsilon_i = 0$, and the zero-field excitation gap to be Δ, the above expression reduces to

$$C_{sch} = 3R\left(\frac{\Delta}{T}\right)^2 \frac{e^{\frac{\Delta}{T}}}{(1+3e^{\frac{\Delta}{T}})^2}. \tag{3.20}$$

As discussed in Section 1.3, at temperatures well below the Debye temperature, the lattice vibrations will contribute a T^3 dependence to the specific heat. The Debye temperature of $SrCu_2(BO_3)_2$ has been calculated to be $\sim$ 450 K from sound velocity measurements [105], and it is therefore appropriate to fit the low-temperature specific heat using

$$C = 3R\left(\frac{\Delta}{T}\right)^2 \frac{e^{\frac{\Delta}{T}}}{(1+3e^{\frac{\Delta}{T}})^2} + \beta T^3. \tag{3.21}$$

This fit is shown by the solid line in Figure 3.13, and gives $\Delta = 34.4 \pm 1$ K. This value is consistent with that determined by a variety of other experimental techniques [84, 86, 106]. The lowest order approximation of isolated dimers is thus valid at the lowest temperatures.

At temperatures above the Schottky peak, the fit deviates substantially from the experimental data, implying that the isolated dimer model is insufficient in describing the full energy spectrum of $SrCu_2(BO_3)_2$. In fact - as will be discussed in more detail alongside the thermal conductivity data - the phonon contribution is overestimated by the above expression. The lattice vibrations are scattered by localised triplet excitations, and the signal is therefore suppressed at higher

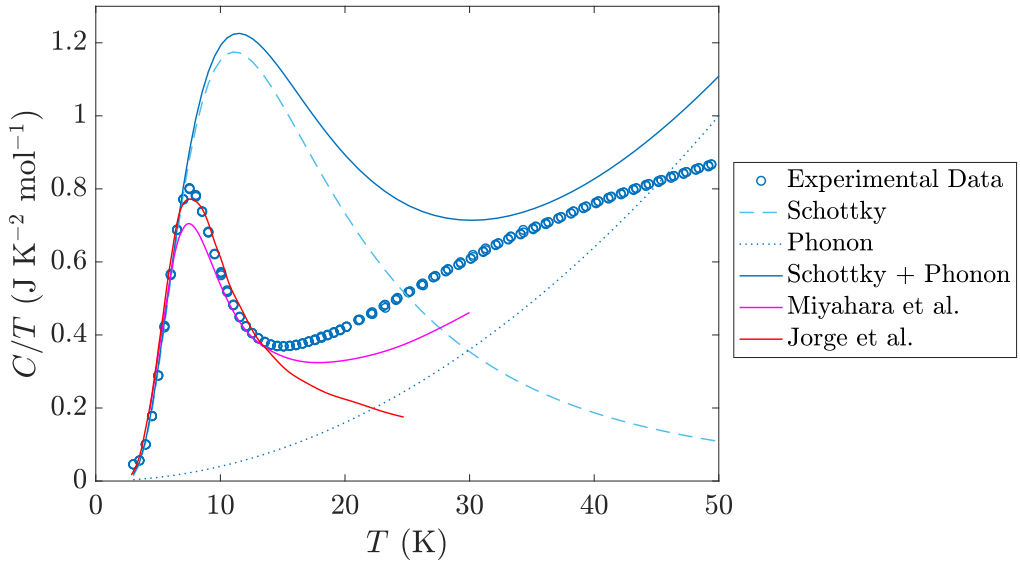

Figure 3.11 *Zero-field specific heat of $SrCu_2(BO_3)_2$, plotted as a function of temperature. Also included is the low temperature fit to Equation 3.21, as well as the isolated Schottky and phonon contributions, all of which have been extended over the full temperature range of measurement. The fits from Miyahara et al. and Jorge et al. are from [88] and [107] respectively, as discussed in the text.*

temperatures. However, this cannot explain the drastic reduction of the specific heat above the Schottky peak, which even falls below the estimated Schottky contribution (given by the dashed line in Figure 3.11). Instead, the observed discrepancy results from the assumption of isolated dimers, which was already shown to be inappropriate in the previous section.

Unfortunately, interdimer interactions introduce significant complications, such that the specific heat can only be calculated - and fit - via numerical methods. Previous studies have been somewhat successful in this approach. For example, the 'transfer matrix method for finite clusters' has been employed to calculate the free energy, and therefore specific heat, for a system of 20 dimers with a finite interdimer exchange interaction J' [88]. As shown in Figure 3.11, this reproduces the drastic suppression above the Schottky peak, but fails to match the peak height - something which is ascribed to there being so few dimers considered. In a separate study, the specific heat has been calculated via a finite-temperature 'Lanczos diagonalization' of the full Hamiltonian (Equation 3.7), which additionally includes DM interactions [107]. This fitting is also included

in Figure 3.11 and matches the low temperature data faily well, despite similarly considering only 20 dimers. This would suggest that the deviation observed by [88] is due to the absence of DM interactions, rather than the small number of dimers. Neither study made any attempt to account for the higher temperature data, however - as will be discussed - this is complicated by a coupling between lattice vibrations and the magnetic excitations.

Field Measurements

Shown in Figure 3.12 is the specific heat data for $SrCu_2(BO_3)_2$, taken in three different applied fields. The field has been aligned parallel to the c-axis in each case. As a function of field, the Schottky peak moves to lower temperatures and reduces in size. This is straightforwardly interpreted as a Zeeman splitting of the triplet energy level, which removes the degeneracy and reduces the size of the spin gap. This is also illustrated in the energy level diagram in Figure 3.4. All three data sets fall onto approximately the same curve at higher temperatures, implying that the higher temperature contributions to the specific heat are independent of field.

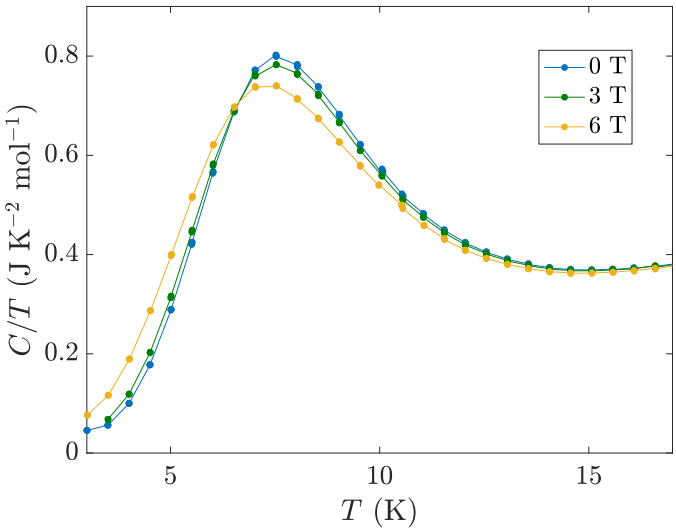

Figure 3.12 *Zero-field specific heat of $SrCu_2(BO_3)_2$, plotted as a function of temperature. The lines simply connect experimental data points, in order to emphasise the changing features of the Schottky peak with field.*

As with the zero-field data, we can estimate the energy splittings by fitting the low temperature portion of the in-field data to a Schottky anomaly. This contribution

is again given by Equation 3.19, but this time with three non-degenerate excited states at $\{\Delta - \delta, \Delta, \Delta + \delta\}$, where $\delta = g\mu_B H/k_B$ is the Zeeman splitting, and we have assumed an isotropic g-factor of 2. Shown in Figure 3.13 are fits to the low temperature data, from which we calculate $\Delta = 34.2 \pm 1$ K, averaged over the three fits. Again, this is consistent with previous studies [84, 86, 106]. Also included is the calculated spin gap to the lowest excited state, $(\Delta - \delta)$, which falls linearly with increasing field, as anticipated.

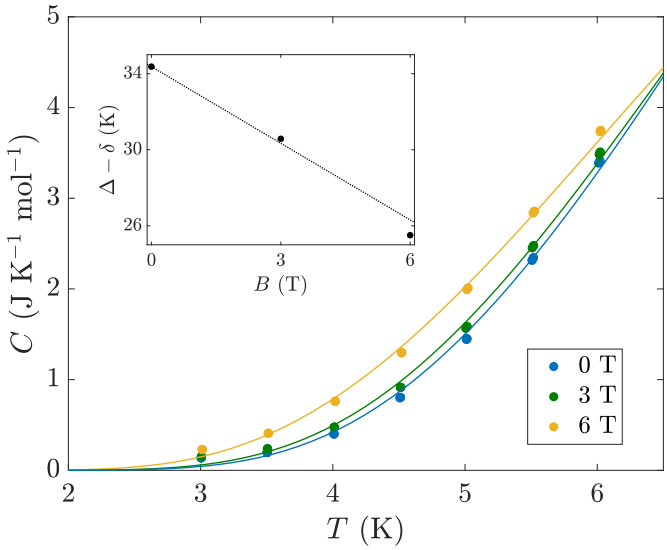

Figure 3.13 *Fits of the low temperature ($T < 7$ K) specific heat data to Equation 3.21, in order to determine the spin excitation gap Δ. Inset shows the calculated spin gap to the lowest excited state, with the dotted line giving the values expected from Zeeman splitting.*

3.3.2 Thermal Conductivity

This investigation was intended to measure the thermal Hall effect in $SrCu_2(BO_3)_2$, however, as discussed in Section 2.2, this necessitates a measurement of the thermal conductivity. We therefore briefly discuss the thermal conductivity data here. The measurement procedure is also outlined in Section 2.2. However, that section is largely focused on our investigations at mK temperatures, and therefore Figure 3.14 shows the experimental setup specific to this investigation. Thanks go to Jean-Philippe Reid, formerly of the University of St.Andrews, for the design - and majority of the construction - of this experimental setup. Measurements were taken using a liquid ^{4}He cryostat designed by Cryogenic Limited, and located at the University of St.Andrews. The sample probe was housed inside an

evacuated stainless steel canister, which was cooled by submerging in the liquid ^{4}He reservoir. Throughout all measurements, the thermal current was applied parallel to the a-axis, with the field along c. The heater power was set such that $\Delta T_x \sim 0.05T$ across all temperatures (the method for achieving this is described in Section 2.2).

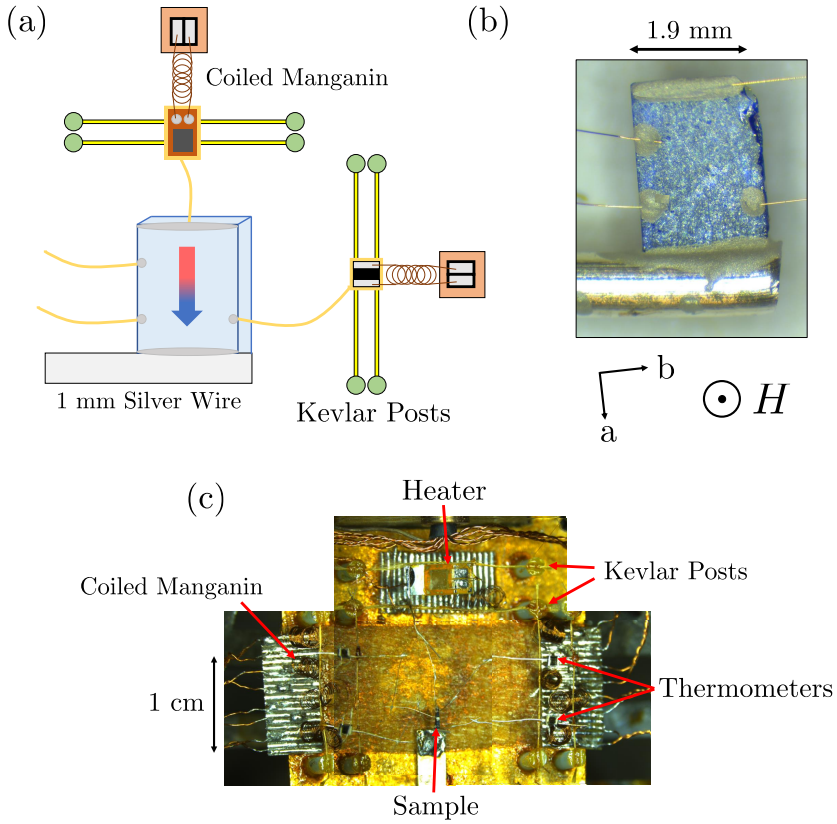

Figure 3.14 *(a) Schematic of the experimental setup used to measure the thermal transport coefficients of $SrCu_2(BO_3)_2$, the components labelled are those which differ from the setup described in Section 1.3. (b) Microscope image of the sample, with the axes and direction of the applied magnetic field labelled. (c) Mosaic of microscope images of the extended setup. This is actually an old iteration, in which we used four thermometers rather than three.*

Zero-Field Thermal Conductivity

The zero-field thermal conductivity data for $SrCu_2(BO_3)_2$ is shown in Figure 3.15. At first glance, this appears similar to the specific heat, with a low-temperature peak followed by a drastic suppression of the signal. However, it is the minima which occurs at a similar temperature to the Schottky anomaly in specific heat,

rather than the maxima. Unlike the specific heat, the thermal conductivity is entirely driven by dispersive excitations. As the magnetic excitations in $SrCu_2(BO_3)_2$ are strongly localised (Figure 3.7), the thermal current must instead be carried by lattice vibrations. The observed features are therefore due to the coupling between the phonon current and the localised magnetic excitations.

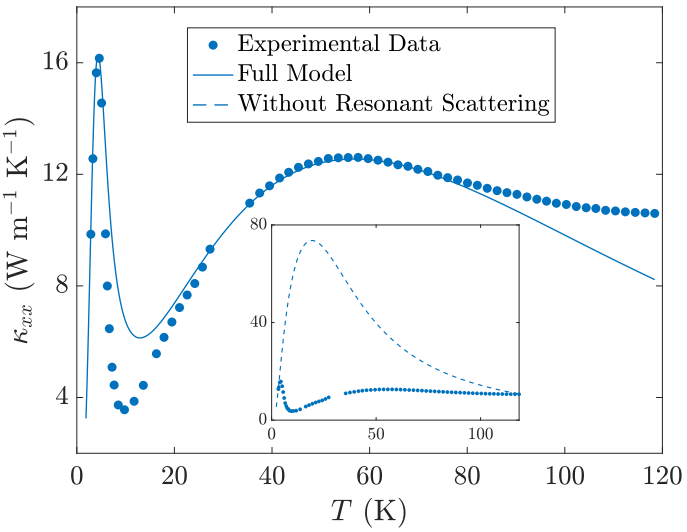

Figure 3.15 *Zero-field thermal conductivity data for $SrCu_2(BO_3)_2$, plotted as a function of temperature. The thermal current has been applied along the a-axis. The solid line shows a fit to the Debye model described in the text. The inset shows that same fit with the resonant scattering term removed.*

The thermal conductivity due to lattice vibrations can be interpreted using the Debye model [39], described briefly in Section 1.3. This gives

$$\kappa_{ph} = \frac{k_B}{2\pi^2 v}\left(\frac{k_B}{\hbar}\right)^3 T^3 \int_0^{\Theta_D/T} \frac{x^4 e^x \tau}{(e^x-1)^2} dx, \tag{3.22}$$

where v is the sound velocity, Θ_D is the Debye temperature (both estimated by [105]), τ^{-1} is the total scattering rate and $x = \hbar\omega/k_B T$ (with ω the phonon frequency). The analysis is somewhat simplified by Matthiessen's rule, which says that the total scattering rate may be written as a sum of the individual scattering rates, arising due to the various different processes. In a typical non-magnetic

insulator, the total scattering rate may therefore be written

$$\tau^{-1} = \tau^{-1}_{boundary} + \tau^{-1}_{point\ defect} + \tau^{-1}_{3-phonon} + \tau^{-1}_{umklapp} \tag{3.23}$$

$$= \frac{v}{L_c} + A_{pd}\omega^4 + A_{3ph}\omega^2 T^3 + A_{um}\omega^2 T e^{-\frac{\Theta_D}{3T}}, \tag{3.24}$$

where we have only included the dominant forms of scattering. In this expression, the characteristic sample length $L_c = 1.12\sqrt{wt}$, with w and t the width and thickness [108], and A_x are parameters to be determined. A fit only including the above scattering terms is shown in the inset of Figure 3.16. As expected, the curve follows the characteristic behaviour of a non-magnetic insulator (Figure 1.9), and as a result, deviates wildly from the measured data.

In order to account for the strong suppression of the thermal conductivity at intermediate temperatures, [109] considers the inclusion of a resonant scattering term, resulting from scattering from the magnetic subsystem. In a resonant scattering process, a phonon is absorbed by a dimer - which is then excited into the triplet state - and subsequently re-emitted in a random direction as the dimer relaxes. Importantly, the translationally invariant ground state of $SrCu_2(BO_3)_2$ is incapable of scattering a phonon, since, by definition, the scattered phonon must change momentum. The dimer involved in the absorption process must therefore be adjacent to a second, thermally excited dimer. This necessity gives the thermal conductivity its strong temperature dependence - the magnetic subsystem can only act as an effective scatterer of phonons once there is sufficient thermal energy, with the relevant energy scale determined by the spin gap Δ.

This resonant scattering term takes the form

$$\tau^{-1}_{resonant} = A_{res}\frac{F(T)}{(\omega^2 - \Delta^2)^2}, \tag{3.25}$$

where Δ is the energy splitting between the two lowest energy levels and $F(T)$ contains information on the two-level system - essentially the probability of there being an adjacent thermally excited triplet. A fit to the Debye model including this additional resonant term is shown by the solid line in Figure 3.16. Clearly it matches the data far better, but still fails to reproduce the size of the suppression at intermediate temperatures. Potentially this is a result of the model only considering scattering from localised magnetic excitations. As discussed (and required for a thermal Hall effect), the triplet excitations do acquire a small dispersion. This dispersion is too small for the triplons

to contribute appreciably to the thermal conduction, but may introduce an additional scattering mechanism for the phonons, further inhibiting the thermal current at intermediate temperatures.

Finally, we note that the model also deviates at the highest temperatures. However, from comparison to previous studies [109], this would appear to be a failure of our experimental procedure rather than the model. Most likely, this is due to heat leakage via thermal radiation, leading to an overestimation of the power supplied to the sample, and therefore an overestimation of the thermal conductivity. The power lost from thermal radiation may be estimated from

$$\Delta P = \frac{\sigma A \varepsilon_1 \varepsilon_2 (T_1^4 - T_2^4)}{\varepsilon_1 + \varepsilon_2 - \varepsilon_1 \varepsilon_2}, \tag{3.26}$$

where $\sigma = 5.67 \times 10^{-8}$ WK^{-2}m^{-4}, A is the area of the radiative surface, and ε_i and T_i are the emissivity and temperature of the two surfaces under consideration [44]. Unfortunately, our experimental setup does not include a radiation shield between the sample stage and the inner vacuum chamber wall, which will be at liquid ^{4}He temperature. Inserting appropriate values into the above expression, we find that - at higher temperatures - the radiative losses are indeed significant (as compared to the heater power). We note however, from the same expression, the radiative losses will be negligible at the temperatures of our thermal Hall investigation ($\Delta P < 10^{-6} P_H$ for $T < 10$ K, where P_H is the power supplied to the sample).

Field Measurements

The in-field thermal conductivity data comes as a necessary by-product of the thermal Hall investigations, and therefore only extends to ~ 15 K. This is shown alongside the zero-field data in Figure 3.16. Similar to the specific heat data, the field has the effect of reducing the magnitude of the peak, and shifting it to lower temperatures.

This behaviour is again a consequence of the Zeeman splitting of the triplet energy level, which reduces the energy splitting Δ between the two lowest energy levels (Figure 3.4). The density of magnetic excitations - and therefore scattering centres - will increase as a function of applied field, and hence the thermal conductivity will decrease. As such, the in-field data can be fit using an identical function to the zero-field data, but with a modified Δ, as determined from

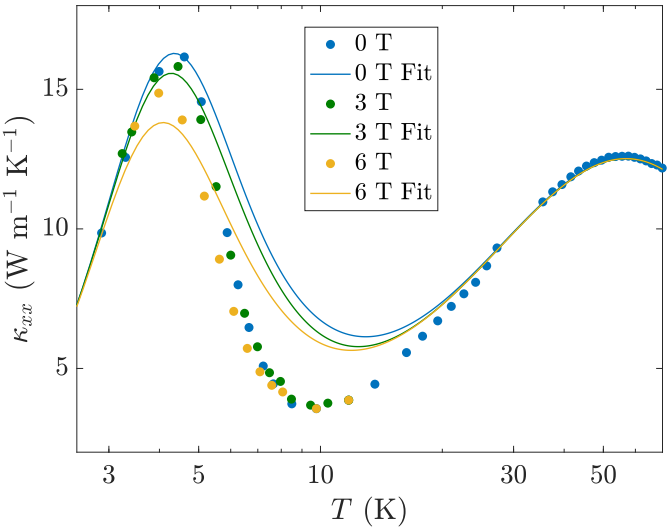

Figure 3.16 *Thermal conductivity data for $SrCu_2(BO_3)_2$, taken at three different applied fields as a function of temperature. The thermal gradient was applied along the a-axis and the field along the c-axis. Dots represent experimental data and lines are fits to this data, as described in the text.*

the specific heat data. As shown in Figure 3.16, this reproduces the observed changes in the low temperature peak, but slightly overestimates the reduction in magnitude.

3.3.3 Thermal Hall Effect

The transverse thermal conductivity of $SrCu_2(BO_3)_2$ was measured using the experimental setup shown in Figure 3.14. In order to ensure that this setup was capable of the required sensitivity, the same configuration was used to investigate the material $Lu_2V_2O_7$. This is an insulating ferromagnet that has previously been demonstrated to exhibit a thermal Hall effect, similar in magnitude to that which is predicted for $SrCu_2(BO_3)_2$ [16]. These measurements are discussed in the following section, and were successful in detecting a thermal Hall effect, giving us some confidence that the same setup should be appropriate for the investigation of $SrCu_2(BO_3)_2$.

Shown in Figure 3.17 is the transverse thermal conductivity data for $SrCu_2(BO_3)_2$. The data was collected by performing temperature sweeps at a constant field, so as to improve the accuracy of calibration (as discussed in Section 2.2). However,

in Figure 3.17, the data is plotted as a function of field - essentially a cut through the various temperature sweeps - in order to draw direct comparison to the theoretically predicted behaviour [99, 104]. Unfortunately, at all measured fields and temperatures there is no appreciable thermal Hall signal within our experimental resolution, and therefore no thermal Hall effect of the predicted magnitude.

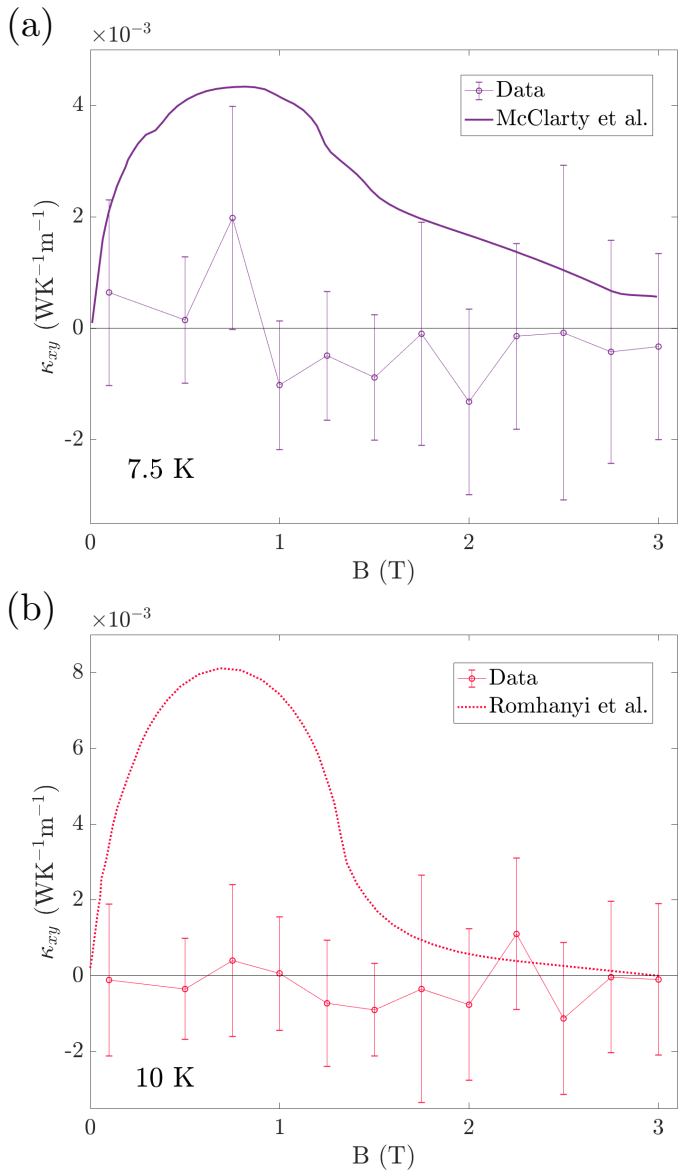

Figure 3.17 *Transverse thermal conductivity of $SrCu_2(BO_3)_2$, plotted as a function of field at (a) 7.5 K and (b) 10 K. The errorbars account for standard statistical error, as well as errors arising from the temperature calibration. Also included are the theoretical predictions from McClarty et al. [104] and Romhanyi et al. [99] for comparison.*

As acknowledged in both those studies which predict a thermal Hall effect, there is only a narrow temperature window in which it should be experimentally feasible to detect a signal. At too low a temperature, the thermal occupation of the triplon bands (and therefore triplon density) is insufficient to produce a perceptible thermal current. The calculated filling fraction has been shown to drop off exponentially with decreasing temperature, and is already as low as $\sim$ 0.2 % at $\sim$ 5 K [99]. Likewise, inelastic neutron studies have shown that the intensity of single triplet excitations effectively disappears above 13 K [86], implying that triplons cannot act as thermal carriers at higher temperatures. This provides some justification for the temperature range under investigation, but the question still remains why there should be no measurable signal.

The accuracy with which the model from [104] is able reproduce the experimentally determined triplon band structure suggests that there is nothing considerable which has been overlooked. Further, the same method of calculating a thermal Hall signal has been applied successfully in previous studies of magnonic systems [16, 110], and should therefore be applicable here. Instead, in $SrCu_2(BO_3)_2$, it is possible that triplon-triplon interactions play a more significant role than anticipated. As discussed in Section 1.1 - and acknowledged in [99] - the theoretical derivation of dissipationless edge states assumes that triplon-triplon interactions are negligible. If this were not the case, those states which drive the thermal Hall effect would be disrupted, and the resultant signal would be reduced. As discussed in the following section, this same phenomenon is observed in $Lu_2V_2O_7$, where the anticpated thermal Hall effect - calculated from the same theory - overestimates the magnitude of the signal at higher temperatures. This is similarly attributed to magnon-magnon interactions. In $SrCu_2(BO_3)_2$, these interactions will necessarily depend on the thermal occupation of the triplon bands; consequently, future studies might seek to improve the experimental resolution at lower temperatures. However, this is particularly challenging due to the maximum in the thermal conductivity at $\sim$ 5 K.

3.4 $Lu_2V_2O_7$

In 2010, an experimental study demonstrated the first ever thermal Hall effect carried by magnons, in the material $Lu_2V_2O_7$ [16]. Our own thermal Hall investigation was therefore not to search for novel phenomena, but instead to confirm that our experimental setup was adequate to detect the same effect

in $SrCu_2(BO_3)_2$. The two materials share a number of similarities - both are insulators with localised spin-1/2 moments, and importantly, according to theoretical work into $SrCu_2(BO_3)_2$ [99, 104], both should exhibit a thermal Hall effect carried by magnons, at a similar temperature and field, and of a similar magnitude. $Lu_2V_2O_7$ therefore represents the ideal testing ground for our experimental apparatus.

Single crystals of $Lu_2V_2O_7$ were grown by the optical floating zone technique, and provided by Robin Perry, of University College London. The measured sample was 2.1 x 1 x 0.3 mm in size, with a mass of 4.22 mg, and fully indexed with the correct crystal structure - shown in Figure 3.18 - by Laue X-ray diffraction.

Material Characterisation and Thermal Hall Effect

In $Lu_2V_2O_7$, the Lu and V atoms form identical sublattices, displaced by half a unit cell. These sublattices are commonly referred to as pyrochlore lattices, and comprise corner sharing tetrahedra, as shown in Figure 3.18. The material is a ferromagnetic Mott insulator, with the V^{4+} sites having one $3d$ electron, and therefore a localised $S = 1/2$ magnetic moment. Below approximately 70 K, these moments order ferromagnetically. In this phase, the simplest magnetic excitation is therefore to flip a single spin. As demonstrated by [16], in $Lu_2V_2O_7$, the dispersion of these excitations can lead to a experimentally detectable thermal Hall effect.

A detailed calculation of the thermal Hall effect in $Lu_2V_2O_7$ is given in [17], here we simply note a few important steps. The derivation follows a similar path to that outlined in Section 1.1 for a two-dimensional system of magnons. By extension, it also closely resembles the derivation of a thermal Hall effect in $SrCu_2(BO_3)_2$ (Section 3.3.3). In both materials, by demonstrating that Dzyaloshinskii-Moriya (DM) interactions on bonds lead to the magnon bands having a non-zero Berry curvature, we can show that these excitations should acquire anomalous velocity terms, perpendicular to the applied thermal gradient.

Consider a single tetrahedron, with a localised $S = 1/2$ moment at each vertex. Immediately we can see that the centre of each bond is not a point of inversion, and neighbouring spins will therefore have non-zero DM interactions. As such,

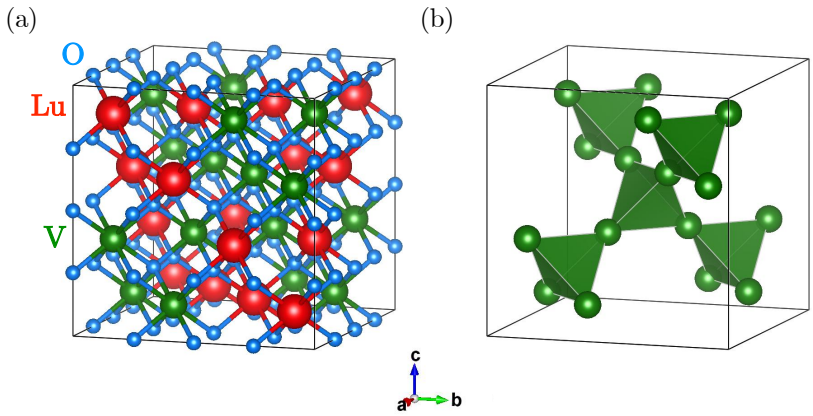

Figure 3.18 *(a) The crystal structure of $Lu_2V_2O_7$, which is cubic with space group $Fd\bar{3}m$ (No.227) and lattice parameter 9.94 Å [111]. (b) The same schematic with just the V sublattice, to emphasise the pyrochlore structure.*

the spin Hamiltonian reads

$$\mathcal{H} = \sum_{<ij>} \left[-J\mathbf{S}_i \cdot \mathbf{S}_j + \mathbf{D}_{ij} \cdot (\mathbf{S}_i \times \mathbf{S}_j) \right] - g\mu_B \mathbf{H} \cdot \sum_i \mathbf{S}_i, \tag{3.27}$$

where the terms account for, respectively, ferromagnetic and DM interactions between neighbouring spins, and the interaction of each spin with an applied magnetic field **H**. The direction of the **D**-vector on each bond can be determined from the symmetries of the crystal [112], and is perpendicular to the bond and parallel to the face of the surrounding cube, as shown in Figure 3.19 (a).

Deep inside the ferromagnetically ordered phase - wherein the magnon density is low - we can disregard interactions between magnons. A single magnon can therefore be modelled as a Bloch state [17], as

$$|\mathbf{k}\rangle = \frac{1}{\sqrt{N}} \sum_i e^{i\mathbf{k}\cdot\mathbf{r}_i} |i\rangle \,, \tag{3.28}$$

where $|i\rangle$ is the magnon state, implying that the spin at $\mathbf{r}_i$ is $S-1$, and all the other spins are completely aligned with the applied field. From Equation 3.27, the matrix element corresponding to the transfer of magnons is then

$$\langle i| \left[-J\mathbf{S}_i \cdot \mathbf{S}_j + \mathbf{D}_{ij} \cdot (\mathbf{S}_i \times \mathbf{S}_j) \right] |j\rangle = -\frac{1}{2}(J + i\mathbf{D}_{ij} \cdot \hat{\mathbf{n}}), \tag{3.29}$$

where $\hat{\mathbf{n}}$ is the unit vector along the field direction. Hence, the magnons acquire a phase when hopping between sites, with the phase factor determined by the orientation between the applied field and the DM interaction. This amounts to a $\mathbf{k}$-space vector potential, or a Berry connection. Further, by drawing an analogy between this and the familiar magnetic vector potential, the phase factor acquired by a magnon traversing a closed loop can be re-interpreted as a fictitious magnetic flux through that loop. As illustrated in Figure 3.19 (b), the $Lu_2V_2O_7$ lattice is comprised of inequivalent loops, around which there is not a complete cancellation of the phase factor. The magnon bands thus acquire a non-zero Berry curvature, which ultimately drives a thermal Hall effect.

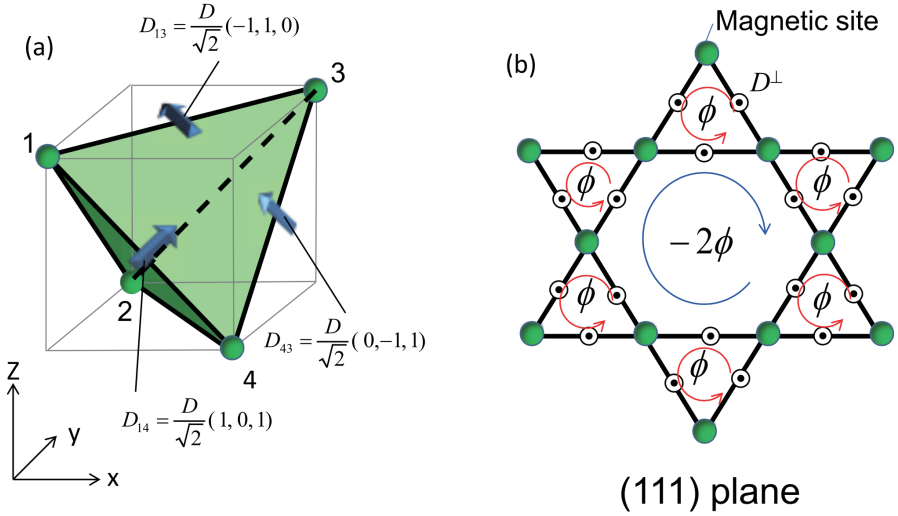

Figure 3.19 *(a) Direction of the DM vectors in a single tetrahedron of V atoms in $Lu_2V_2O_7$. (b) The (111) plane, wherein the V atoms form a kagome lattice, and the out of plane DM vectors all point in the same direction. As discussed in the text, this may be interpretted as a fictitious flux through inequivalent closed loops. Taken from [17].*

Without repeating the derivation of Section 1.1 (or [14]), the resulting thermal Hall conductivity is given by

$$\kappa_{\alpha\beta} = \frac{8k_B^2 T}{\hbar a} \sum_n \int_{BZ} \frac{d^3k}{(2\pi)^3} c_2(\rho^B(\mathbf{k})) \mathrm{Im} \left\langle \frac{\partial \psi_n(\mathbf{k})}{\partial k_\alpha} \middle| \frac{\partial \psi_n(\mathbf{k})}{\partial k_\beta} \right\rangle, \tag{3.30}$$

where $a(= 9.94$ Å$)$ is the lattice constant, $|\psi_n(\mathbf{k})\rangle$ are obtained by diagonalising

the spin-wave Hamiltonian at each $\mathbf{k}$, and

$$c_2(\rho^B) = (1+\rho^B)\left[\log\left(\frac{1+\rho^B}{\rho^B}\right)\right]^2 - (\log\rho^B)^2 - 2\mathrm{Li}_2(-\rho^B). \tag{3.31}$$

Finally, at low temperatures, only the lowest band will be occupied, and the thermal Hall conductivity may be approximated by

$$\kappa_{\alpha\beta} \simeq \Phi_{\alpha\beta}\frac{4k_B^2T}{3\pi^2\hbar a}\left(\frac{k_BT}{2JS}\right)^{\frac{5}{2}}\int_0^\infty c_2\left(\frac{1}{e^{t+\frac{g\mu_BH}{k_BT}}-1}\right)t^{\frac{3}{2}}dt. \tag{3.32}$$

In this expression, $\Phi_{\alpha\beta} = \varepsilon_{\alpha\beta\gamma}n_\gamma D/8\sqrt{2}J$, where n_γ is the field direction, D is the magnitude of the DM vector, and $\varepsilon_{\alpha\beta\gamma}$ is the totally antisymmetric tensor. This implies that the thermal Hall signal is independent of the current direction, so long as it is perpendicular to the applied field. This is yet another reason that $Lu_2V_2O_7$ was the ideal proving ground for our experimental apparatus.

Experimental Results

As this was designed to validate the thermal Hall investigation of $SrCu_2(BO_3)_2$, the experimental procedure was identical, albeit with the CX-1050 thermometers replaced by CX-1070 - to account for the slightly higher temperature range. This procedure has been described in detail in Section 2.2.

Our experimental data is shown in Figure 3.20, alongside the data from [16], and the calculated values from Equation 3.32. Clearly, we were able to resolve a thermal Hall effect in $Lu_2V_2O_7$, with the maximum signal occurring at approximately 50 K. The drop in magnitude either side of this peak may be explained straightforwardly. At low temperatures, the magnon bands are not sufficiently thermally occupied, implying there are too few thermal carriers to give a detectable transverse conductivity. At higher temperatures, the signal vanishes primarily due to the paramagnetic transition at approximately 70 K. The magnons exist as excitations on top of the ferromagnetic state, and therefore are not defined in the paramagnetic state.

Also shown in Figure 3.20 is the thermal Hall effect calculated from Equation 3.32. In that expression, the only free parameters are D and J. The original experimental paper estimated J from specific heat data, and then set $D/J = 0.32$ to match the data at 20 K [16]. This significantly overestimates the magnitude

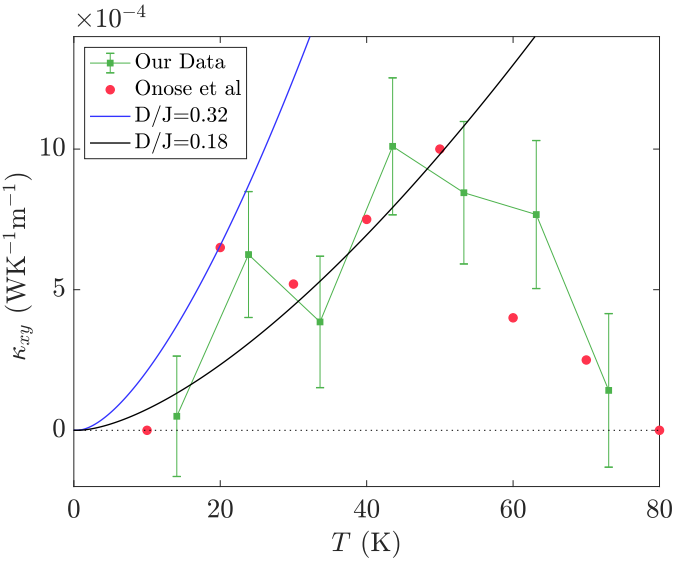

Figure 3.20 *Thermal Hall effect in $Lu_2V_2O_7$, showing our own experimental data compared to the data from [16] and calculated values from Equation 3.32, using the magnetic interaction strengths reported in [16] (blue curve) and [111] (black curve). All data were taken at 1 T. The errorbars on our own data account for standard statistical error, as well as errors arising from the temperature calibration.*

of the signal at higher temperatures, something which the authors ascribe to magnon-magnon interactions, which have been neglected in the derivation of Equation 3.32. As previously mentioned, this same effect might also explain the results for $SrCu_2(BO_3)_2$. However, a recent inelastic neutron scattering investigation gave $D/J = 0.18$ [111]. The calculated thermal Hall signal using this ratio is also included in Figure 3.20, and more closely matches the experimental data. Note that Equation 3.32 does not attempt to account for the magnetic transition at ~ 70 K, which explains the difference between the experimental and calculated values approaching this temperature.

3.5 Summary

We have measured the specific heat of $SrCu_2(BO_3)_2$ in order to determine the lowest energy spin-gap. The calculated value of $\Delta = 34.2 \pm 1$ K - taken from Schottky fits to the low temperature portion of the data - agrees with that estimated by a variety of other experimental techniques [84, 86, 106]. The in-field specific heat data reveal a reduction in the spin-gap, approximately linear in

field, and therefore attributable to a Zeeman splitting of the first excited triplet energy level. At higher temperatures, as anticipated, the isolated dimer model becomes wildly inappropriate. Previous studies have been somewhat successful in estimating the specific heat for a system with inter-dimer interactions included, although exclusively via numerical methods [88, 107].

As a by-product of our thermal Hall investigation, we have measured the longitudinal thermal conductivity. Due to the highly localised nature of the magnetic excitations, this may be adequately described by the Debye model of lattice vibrations, albeit with the inclusion of an additional resonant contribution to the total scattering rate [109]. This is a result of scattering from magnetic excitations, and necessary in order to reproduce the strong suppression of the thermal conductivity observed at intermediate temperatures, as well as the suppression of the low temperature peak with increasing field. The fitting deviates slightly at intermediate temperatures, possibly due to a scattering from dispersive magnetic excitations, unaccounted for by the model.

Finally, we have attempted to verify the theoretical prediction of a thermal Hall effect of triplons in $SrCu_2(BO_3)_2$ [99, 104]. Unfortunately, within the experimental resolution, no such signal has been observed. In order to verify that this null result was not a failing of our experimental technique, we have successfully measured a thermal Hall effect - of a similar magnitude - in the material $Lu_2V_2O_7$, using an identical experimental setup. The lack of a signal in $SrCu_2(BO_3)_2$ is potentially a result of triplon-triplon interactions playing more of an inhibitory role than anticipated. This is certainly the case for $Lu_2V_2O_7$, wherein magnon-magnon interactions suppress the observed thermal Hall signal far below that which is theoretically predicted to occur.

Future studies of the thermal Hall effect in $SrCu_2(BO_3)_2$ might look to improve the experimental resolution at lower temperatures, where the triplon density is sufficiently low that the edge current might remain approximately dissipationless. However, this is made challenging by the maximum in the thermal conductivity at ~ 5 K - recall that the experimental resolution is given by the thermal Hall angle, rather than the magnitude of the thermal Hall signal.

Chapter 4

UPt_3

UPt_3 was one of the earliest discovered heavy fermion superconductors, and the first to unambiguously be shown to possess multiple superconducting phases. This can only be explained by an unconventional pairing state. However, despite decades of research, the pairing symmetry is still somewhat up for debate, with various experimental techniques giving credence to conflicting representations of the superconducting order parameter. Regardless, UPt_3 remains one of the best understood unconventional superconductors to date, and - as will be discussed - one of the most promising candidates to host a topological form of superconductivity.

One method of distinguishing between some of the leading theories would be to determine whether the low temperature, low field B-phase is chiral - meaning that the superconducting condensate has a non-zero angular momentum. This is where our research interests lie. A recent theoretical prediction has suggested that, if the B-phase were to be chiral, it should exhibit an anomalous thermal Hall effect. Observation of such an effect would also be the first definitive proof of bulk chiral superconductivity.

4.1 Previous Work

The fervent interest in UPt_3 has spurned a huge volume of prior research, the majority of which has been collated into a number of review papers [113–115]. We therefore only briefly cover those features relevant to our own investigations.

Normal State Properties

UPt_3 crystallises in a $MgCd_3$-type hexagonal structure, with space group $P6_3/mmc$, as shown in Figure 4.1 (a). Directly above the superconducting transition, the specific heat is approximately linear, with a Sommerfeld coefficient of ~ 440 mJK^{-2}mol^{-1} [116], implying strong electron correlations. This feature marks UPt_3 as a heavy fermion compound (discussed in Section 5.1), however the resistivity shows no hints of a Kondo coherence peak, instead decreasing monotonically with temperature, before following a Fermi liquid-like $\rho_0 + AT^2$ behaviour above the superconducting transition (regardless of current direction). At the lowest temperatures - with the normal state enforced by the application of a magnetic field - the Wiedemann-Franz law is obeyed [117]. The heavy quasiparticles therefore also act as thermal carriers.

At 1 K, inelastic neutron studies reveal there to be a fluctuating magnetic moment localised at each uranium site, with strength $2\mu_B$. This co-exists with the Fermi liquid state, which also contributes longer wavelength magnetic fluctuations. Below 5 K, a small component ($0.01\mu_B$/U) of the moments order antiferromagnetically, with adjacent moments antiparallel in the hexagonal planes, and parallel between planes [118]. However, evidence for the transition to magnetic order has not been observed in specific heat, nor in nuclear spin resonance, leading some to suggest it is not truly static order [119].

The Superconducting Phases

The superconducting phase diagram of UPt_3 is shown in Figure 4.1 (b). At zero field, the material exhibits two superconducting transitions as a function of temperature, first observed in heat capacity studies [116]. The large jump ($\Delta C/\gamma_N T_c$) at both transitions indicates that it is the heavy fermion quasiparticles which condense to form the superconducting state. With increasing field, the two transitions first merge at a tetracritical point, and then re-emerge either side of a third superconducting phase, first resolved by ultrasonic attenuation measurements [121]. Due to the multiple superconducting phases, UPt_3 must host an unconventional form of superconductivity.

As discussed in Section 1.2, there is no fully accepted microscopic theory to explain any form of unconventional superconductivity. The pairing mechanism in UPt_3 is therefore yet to be determined. In a number of unconventional

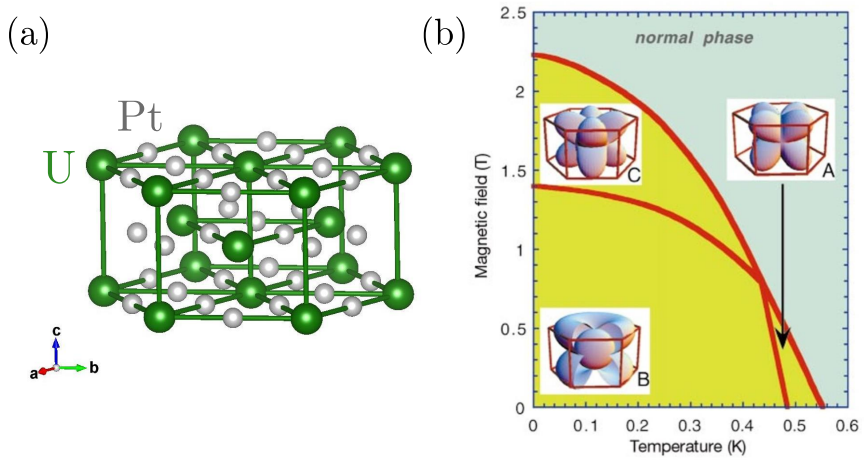

Figure 4.1 *(a) Crystal structure of UPt_3. $a = 5.764$ Å and $\tilde{c} = 4.899$ Å, where $\tilde{c}$ is the distance between neighbouring planes rather than the length of the unit cell [113]. (b) Superconducting phase diagram of UPt_3, showing the three separate phases. Also included are example superconducting gap functions corresponding to the E_{2u} irreducible representation. Phase diagram taken from [120].*

superconductors, there are indications that spin fluctuations might have a role to play, and possibly mediate the effective attractive interaction [122, 123]. Similarly, in UPt_3, the superconductivity and magnetic order appear to be strongly linked. For instance, the application of pressure acts to merge the zero-field transitions, and simultaneously suppress the antiferromagnetic order [124].

Without a microscopic theory, the superconductivity in UPt_3 must be interpreted through phenomenological models. The most successful of these models - Ginzburg-Landau theory - has been discussed in Section 1.2. Very briefly, within this framework, the superconducting free energy is expressed as an expansion of a complex order parameter, which falls to zero at the transition temperature. The form of this free energy functional puts constraints on the superconducting order parameter, and by extension the Cooper pair wavefunction. Therefore, despite this being a purely phenomenological approach, it provides information that is integral to the microscopic theory. Let us now follow the procedure outlined in Section 1.2 in order to determine the superconducting order parameter for UPt_3.

The Cooper pair wavefunction must conform to the crystalline symmetry. UPt_3 has a D_{6h} point group symmetry, and therefore the pair wavefunction can be associated with any one of the 12 corresponding irreducible representations. However, we may immediately discard the majority of these representations by

noting that

(i) The close proximity of the two zero-field transitions argues in favour of a multi-component representation - rather than two separate representations being accidentally almost degenerate.

(ii) The B-phase appears to be chiral (as will be discussed).

Only the E_{1g} and E_{2u} representations satisfy both of these requirements; these correspond to a singlet d-wave and a triplet f-wave pairing respectively. Rather than give the full character table (which can be found in [113]), we instead only give details of these two representations, in Figure 4.2.

Both the the E_{1g} and E_{2u} representations will have a two-component order parameter, implying the zero-field free energy functional will read

$$F = \int dV \left[\alpha(T-T_c)\boldsymbol{\eta}\cdot\boldsymbol{\eta}^* + \beta_1(\boldsymbol{\eta}\cdot\boldsymbol{\eta}^*)^2 + \beta_2|\boldsymbol{\eta}\cdot\boldsymbol{\eta}|^2 - b|\mathbf{M}_S\cdot\boldsymbol{\eta}|^2 + c\mathbf{M}_S^2\boldsymbol{\eta}\cdot\boldsymbol{\eta}^* \right], \quad (4.1)$$

where $\boldsymbol{\eta} = (\eta_x, \eta_y)$ is the superconducting order parameter, and $\mathbf{M}_S$ is the magnetisation [113, 115]. The magnetisation should be treated as a second order parameter, however, given that the magnetic transition temperature is an order of magnitude larger than the superconducting transition temperature, this may instead be treated as an effective field $\mathbf{M}_S = M_S\hat{x}$. The free energy functional may then be expressed

$$F = \int dV \left[\alpha(T-T_c^+)|\eta_x|^2 + \alpha(T-T_y)|\eta_y|^2 + \beta_1(\boldsymbol{\eta}\cdot\boldsymbol{\eta}^*)^2 + \beta_2|\boldsymbol{\eta}\cdot\boldsymbol{\eta}|^2 \right], \quad (4.2)$$

where $T_c^+ = T_c - cM_S^2/\alpha + bM_S^2/\alpha$ and $T_y = T_c - cM_S^2/\alpha$. Immediately then, we see that a two-component order parameter can naturally account for the split zero-field transition. At the higher temperature transition (occurring at T_c^+), only one component of the order parameter becomes non-zero, whereas below the second transition (occurring at $T_c^- \neq T_y$), both components are non-zero. The A-phase therefore has an associated order parameter $(1, 0)$, and the B-phase has $(1, i)$, to account for the relative phase between the two components. This justifies the assumption of a two-component order parameter, but makes no distinction between the different two-component representations.

With the application of field, gradient terms must be included in the free energy

functional. These take the form

$$K_1(D_i\eta_j)(D_i\eta_j)^* + K_2(D_i\eta_i)(D_j\eta_j)^* + K_3(D_i\eta_j)(D_j\eta_i)^* + K_4(D_z\eta_j)(D_z\eta_j)^*, \quad (4.3)$$

where repeated indices are summed over x and y, and the derivative is defined as

$$D_i = -i\partial_i + \frac{2\pi}{\phi_0}A_i, \quad (4.4)$$

where A_i is the magnetic vector potential. Under the E_{1g} representation, the split transition in field is - again - naturally explained by the two components of the order parameter becoming non-zero at different applied fields. However, in the E_{2u} representation, the transitions should occur at an identical field. Instead, the split transition is accounted for by a coupling between the magnetism and the supercurrent [115]. Both representations are therefore able to adequately explain the temperature-field phase diagram, which again provides no distinction between them. In both cases, the $(1, 0)$ A-phase is stabilised by a coupling to the magnetisation, the $(0, 1)$ C-phase by a coupling to the magnetic field, and the $(1, i)$ B-phase is a combination between the two.

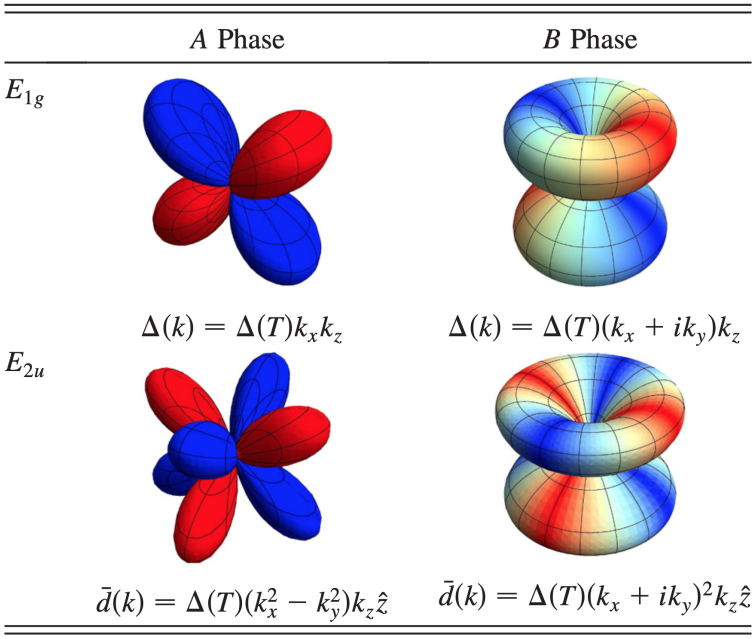

Figure 4.2 *The two leading candidate representations for the UPt_3 superconducting gap function. Shown are the simplest representative functions for the two zero-field phases. The colour scheme corresponds to the phase difference across the gap, with red/blue sections having a phase difference of $\pi/2$. Taken from [125].*

Distinguishing Between Candidate Representations

We now review some of the experimental evidence that marks the E_{1g} and E_{2u} representations as leading candidates, and further, that which might distinguish between them.

As discussed in Section 1.3, the thermodynamic properties of an unconventional superconductor will be strongly influenced by the nodal features of the superconducting gap. Schematics of the simplest gap functions corresponding to the E_{1g} and E_{2u} representations are included in Figure 4.2, both of which possess point and line nodes. In UPt_3, for a current parallel to both the b- and c-axes, the low temperature thermal conductivity rises too rapidly to be explained by conventional models of superconductivity [126] (see Figure 1.10 (b)). This implies that there are nodes along both directions, and therefore lends support to either of the E_{1g} or E_{2u} representations. Similarly, measurements of the nuclear spin relaxation rate reveal a temperature dependence typical of an unconventional superconductor with nodal features in the superconducting gap [127].

In distinguishing between the two representations, thermal conductivity measurements - as a directional probe - prove particularly useful [126]. The gap functions in the low temperature B-phase have a subtly different angular dependence - $\sin\theta\cos\theta$ compared to $\sin^2\theta\cos\theta$ for the E_{1g} and E_{2u} representations respectively, corresponding to a linear/quadratic dispersion away from the point nodes. The ratio of the low temperature transverse conductivities, κ_c/κ_b, will exhibit a markedly different behaviour in each case. Measurements on UPt_3 point towards a quadratically dispersive point node, and therefore the E_{2u} representation. However, the theory also predicts a residual linear term in the thermal conductivity, which is not observed for either current direction.

An alternative route to distinguishing between the two representations is a measurement of the Knight shift through the superconducting transition. This is essentially a measure of the local magnetic field at a (chosen) nuclear site, and should therefore drop to zero for an s-wave superconductor. In UPt_3, the Knight shift remains approximately constant through the transition, although decreases very slightly [128]. Although this argues against the E_{1g} singlet representation, it is not a strong argument in favour of E_{2u}. Further, similar measurements into Sr_2RuO_4 - another unconventional superconductor - have recently been called into question [129]. The applied magnetic pulse was found to instantaneously raise the material above the transition temperature, and therefore the constant

Knight shift was simply due to the material being in the normal state.

More recently, there have been a number of studies which appear to argue decisively in favour of the E_{2u} representation, these include:

- [130] - using an array of Josephson junctions attached to a curved surface, this study was able to demonstrate that, in the A-phase, the supercurrent vanishes along specific momentum directions, corresponding to the points at which the E_{2u} gap function vanishes (Figure 4.2).
- [120] - a small-angle neutron scattering investigation, which showed a re-alignment of the flux line lattice at the A-B transition, also consistent with those gap functions corresponding to the E_{2u} representation.
- [125] - using Josephson interferometry, this study performed phase sensitive measurements of the B-phase superconducting gap, and found phase shifts matching the gap function corresponding to the E_{2u} representation (also Figure 4.2).

Hence, aside from a few exceptions [131, 132], the experimental evidence points overwhelmingly towards the E_{2u} representation, or an f-wave triplet pairing. In this representation, the B-phase pair wavefunction is defined by

$$\mathbf{d}(\mathbf{k}) \sim (k_x + ik_y)^2 k_z \hat{z}, \tag{4.5}$$

which may be re-expressed in terms of spherical harmonics, as

$$\mathbf{d}(\mathbf{k}) \sim Y_2^{+2} Y_1^0 \hat{z} \propto Y_3^{+2} \hat{z}. \tag{4.6}$$

Under the E_{2u} representation, the B-phase thus comprises Cooper pairs with a non-zero angular momentum. Polar Kerr effect measurements have identified the B-phase as breaking time-reversal symmetry [133], which lends support to it being a chiral phase. However, definitive proof that the chirality is a bulk property requires a bulk experimental probe. The theoretically predicted anomalous thermal Hall effect might therefore be the key to an unambiguous confirmation of the first chiral superconducting phase.

4.2 Prediction of an Anomalous Thermal Hall Effect

An anomalous thermal Hall effect has been theoretically predicted to occur in UPt_3 via two different mechanisms. [28] has shown that chiral *edge* states, emanating from the polar point nodes in the superconducting gap, should carry a topological transverse thermal current. [24] instead argues that the skew scattering of Bogoliubov quasiparticles from finite-size impurities in the *bulk* should lead to a thermal Hall signal, significantly larger in magnitude than the purely topological effect. Importantly however, both phenomena are dependent on the superconducting condensate having a non-zero chirality. Hence, whilst the detection of an anomalous thermal Hall effect might not distinguish between the two, it would be the first experimental evidence for bulk chiral superconductivity. The two predictions will now, separately, be briefly introduced.

4.2.1 UPt_3 as a Topological Superconductor

In Section 1.2, it was demonstrated that the point nodes in the gap function of the ^{3}He A-phase were equivalently Weyl points, and as such, the surface Brillouin zone should host a topological edge state, referred to as a Fermi arc. Following an identical procedure, we will now show that the B-phase of UPt_3 should possess similar features, and thus exhibit an anomalous thermal Hall effect [28].

As before, the starting point is the Bogliubov de-Gennes Hamiltonian, given by

$$\mathcal{H} \sim \sum_{\mathbf{k}} \psi_{\mathbf{k}}^{\dagger} \mathcal{H}(\mathbf{k}) \psi_{\mathbf{k}}, \tag{4.7}$$

with $\psi_{\mathbf{k}}^{\dagger} = \begin{pmatrix} c_{\mathbf{k}\uparrow}^{\dagger} & c_{-\mathbf{k}\downarrow} & c_{\mathbf{k}\downarrow}^{\dagger} & c_{-\mathbf{k}\uparrow} \end{pmatrix}$. Note that, unlike with the ^{3}He example, we have not assumed that the system is spin-polarised. Despite this, the reduced Hamiltonian can similarly be expressed in terms of the Pauli matrices τ_i, as

$$\mathcal{H}(\mathbf{k}) = \mathbf{N}(\mathbf{k}) \cdot \boldsymbol{\tau} \otimes \mathbf{I}, \tag{4.8}$$

where $\mathbf{I}$ is the 2×2 identity matrix. For the UPt_3 B-phase - the $\mathbf{d}$-vector for

which is given in Equation 4.5 - we have that

$$\mathbf{N}(\mathbf{k}) = \left(\frac{\Delta_0}{k_F^3} k_z(k_x^2 - k_y^2), \frac{2\Delta_0}{k_F^3} k_x k_y k_z, \xi_{\mathbf{k}}\right), \tag{4.9}$$

where the non-interacting dispersion is approximated by $\xi_{\mathbf{k}} = \frac{\mathbf{k}^2}{2m}$.

The above expression for $\mathcal{H}(\mathbf{k})$ appears similar to the Hamiltonian for a two-band model, utilised in Section 1.1 to demonstrate topological phenomena. As in that example, the Berry curvature may be expressed as a function of the unit vector $\hat{\mathbf{n}}(\mathbf{k}) = \mathbf{N}(\mathbf{k})/|\mathbf{N}(\mathbf{k})|$, and specifically

$$\mathcal{F}_{\mathbf{k},a} = \frac{1}{4}\epsilon_{abc}\ \hat{\mathbf{n}}(\mathbf{k}) \cdot \left[\frac{\partial \hat{\mathbf{n}}(\mathbf{k})}{\partial k_b} \times \frac{\partial \hat{\mathbf{n}}(\mathbf{k})}{\partial k_c}\right], \tag{4.10}$$

where ϵ_{abc} is the totally antisymmetric tensor. As discussed in Section 1.1 (Figure 1.3), the Berry curvature integrated over a closed surface must be quantised in units of 2π - corresponding to the topological invariant, or Chern number C, for that surface. Without explicit calculation, we find that for a surface enclosing either point node in the UPt_3 B-phase superconducting gap, the Chern number will be ± 2. Each point node therefore acts as a strength 2 monopole/antimonopole of Berry curvature. Compare this result to the analogous case of the ^{3}He A-phase (discussed at the end of Section 1.2), for which the point nodes have an associated Chern number of ± 1. The topological invariant of nodal points is therefore defined by the angular momentum (L_z) of the Cooper pair wavefunction.

As with ^{3}He, the point nodes in the superconducting gap function of UPt_3 can equivalently be considered double Weyl points [28]. Following an identical procedure to that outlined in Section 1.2, we can argue that this implies there will be edge states [33]. As in that discussion, if we construct a surface perpendicular to k_z, which lies between the two point nodes, that surface will represent a two-dimensional system with two well separated, topologically non-trivial bands. By extension, any such surface defined in this way may be considered a two-dimensional strong topological superconductor - the superconducting analogue of an integer quantum Hall effect system - and therefore host chiral edge modes. It can be shown that [28], for a $(1, 0, 0)$ surface, these zero-energy states should satisfy

$$\sqrt{2}k_y = \pm\sqrt{k_F^2 - k_z^2}. \tag{4.11}$$

Hence, as illustrated in Figure 4.3, there are two degenerate Fermi arcs on the

surface Brillouin zone. More generally, we find that the number of Fermi arcs will be equal to the angular momentum L_z of the superconducting condensate.

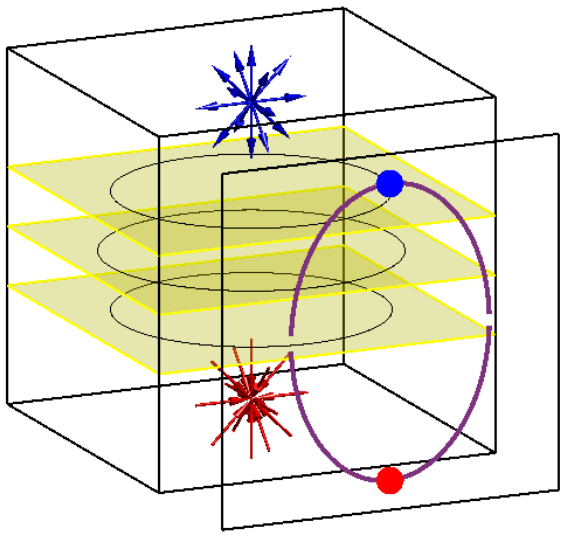

Figure 4.3 *Schematic to show the two Weyl points in the gap function of the UPt_3 B-phase. As in Figure 1.7, the two Weyl points act as a source and sink of Berry curvature. The empty cube is the bulk Brillouin zone, and each yellow surface individually represents a two-dimensional strong topological superconductor. The black circle on each yellow surface is the intersection of the Fermi surface. The empty square represents the surface Brillouin zone, with the projection of the two Weyl points shown by the red and blue dots, and the Fermi arcs given by the purple lines between them. Note, the Fermi arcs have a discontinuity at $k_z = 0$, where they are intersected by the equatorial line node.*

Finally, these chiral edge states should manifest as an anomalous thermal Hall effect. Without explicit derivation (which may be found here - [134, 135]), the thermal Hall conductivity may be expressed as a function of the Berry curvature, as

$$\kappa_{ab} = -\frac{k_B^2 T}{\hbar}\epsilon_{abc}\int \frac{d^3k}{(2\pi)^3}\mathcal{F}_{\mathbf{k},c}\int_{E_\mathbf{k}}^{\infty} dE\frac{\partial f(E)}{\partial E}E^2, \tag{4.12}$$

which, in the low temperature limit, reduces to

$$\kappa_{xy} = \frac{k_B^2 T\Delta k}{3\hbar}L_z. \tag{4.13}$$

The anomalous thermal Hall effect is therefore a function of

- $\Delta k = 2k_F$ - the separation of the point nodes. From the schematic in

Figure 4.3, the length of the Fermi arc - and therefore the number of states available to carry the transverse thermal current - will scale with the separation between the two Weyl points. It makes sense that the thermal Hall signal should have a similar scaling.

- T - although the magnitude must fall to zero at the A-B phase transition, upon the restoration of time reversal symmetry. The maximum signal should thus occur at $\sim T_c^B/2$, where T_c^B is the zero-field B-phase transition temperature.

- L_z - the angular momentum of the superconducting condensate. In principle, a sufficiently accurate measurement could therefore distinguish between the E_1 and E_2 representations.

Typical values of all the above parameters give a maximum $\kappa_{xy} \sim 10^{-3}\,\mathrm{WK^{-1}m^{-1}}$, although this value might increase once the multiple Fermi surface sheets are taken into account. This corresponds to a thermal Hall angle of $\sim 5 \times 10^{-4}$, which is at the limit of experimental detection. Unfortunately, any infinitesimally weak disorder will act to destroy the topological properties. However, rather than render this entire discussion meaningless, [28] suggests that this should give rise to a diffusive phase. In this phase, if the impurity potential varies sufficiently smoothly, the backscattering effects may be small enough that the edge states - and by extension the anomalous thermal Hall effect - survive. In any case, within this model, impurity effects can only act to reduce the thermal Hall signal, and therefore probably push it beyond the realm of experimentally detectable signals.

4.2.2 Impurity Driven Anomalous Thermal Hall Effect

In contrast to the above, [24] predicts an anomalous thermal Hall effect *driven* by impurities. The effect still relies on the B-phase of UPt_3 being chiral - and also a weak topological superconductor - however, the transverse thermal current is carried by the bulk quasiparticles, rather than the edge states. As such, for reasonable impurity densities, the impurity driven anomalous thermal Hall effect is anticipated to be significantly larger in magnitude than the purely topological effect. Once again, in order to understand this effect, we first consider a simpler, analogous effect which occurs in the A-phase of ^{3}He.

As a result of the force balance between repulsive interactions and surface tension,

a single electron injected into superfluid ^{3}He will create a bubble with radius approximately 20 times larger than the Fermi wavelength of the ^{3}He quasiparticles [23]. The electron bubble may therefore be treated as a finite-size impurity. Further, if the surrounding superfluid is in the topologically non-trivial A-phase, the electron bubble defines a topological boundary, which - from bulk-boundary correspondence - must host topologically protected edge states. These states are identical to the edge states that traverse the ^{3}He sample boundary, but in this case, it is the topologically non-trivial region that surrounds the 'normal' region. The electron bubble will therefore be cloaked in chiral fermions, and acquire an angular momentum of the opposite sign to that of the condensate. This is illustrated in Figure 4.4 (a).

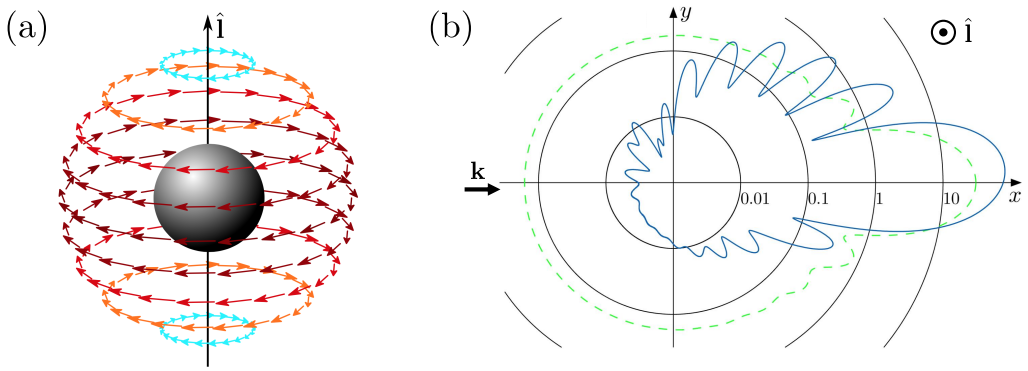

Figure 4.4 *(a) Schematic to show the chiral modes circulating an electron bubble in ^{3}He. $\hat{\mathbf{l}}$ is the chiral axis defining the ^{3}He Cooper pair angular momentum, and the colour bar gives the current density, increasing from blue to red. (b) Differential cross section for the scattering of quasiparticles from an electron impurity in ^{3}He, plotted as a function of the in-plane scattering angle. $\mathbf{k}$ is the quasiparticle momentum and, again, $\hat{\mathbf{l}}$ is the chiral axis. The dashed green line shows the differential cross section for quasiparticle-ion scattering in the normal state. Both schematics are taken from [23].*

When a current of electrons is injected into the A-phase of ^{3}He, it exhibits a measurable anomalous Hall effect [136]. In the original experimental paper, the transverse force on the electrons was likened to the Magnus force experienced by a classical sphere, rotating inside a fluid. Subsequent theoretical work has somewhat vindicated this schematic. Due to the chiral fermions, the superfluid quasiparticles scatter anisotropically from the electron bubble (Figure 4.4 (b)). This results in a finite force perpendicular to the direction of motion, and ultimately drives the anomalous Hall effect. The size of the topological boundary defines the spectrum of chiral edge states, and by extension, the differential cross

section for the scattering of quasiparticles. As the electron bubble has a fixed size, [23] was able to calculate the magnitude of the anomalous Hall effect in ^{3}He, and found a remarkable agreement with the experimental data.

An analogous effect occurs within the superconducting B-phase of UPt_3 [24]. In this case however, the impurities are not electron bubbles, but rather the defects of the crystalline lattice. As with ^{3}He, these finite-size impurities are cloaked by chiral edge states, and therefore anisotropically scatter the superconducting quasiparticles. Unlike with ^{3}He however, the impurities are fixed - instead it is the itinerant quasiparticles which carry the transverse (thermal) current, and thus give rise to an anomalous thermal Hall effect.

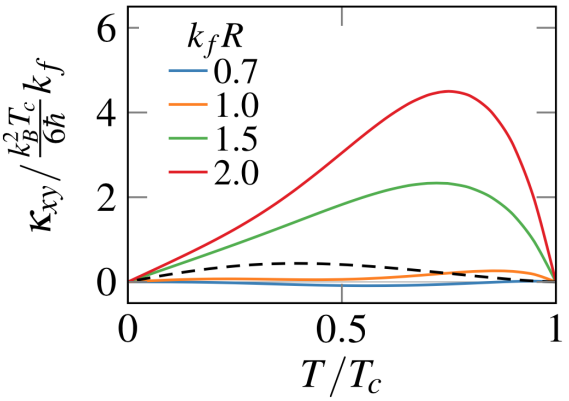

Figure 4.5 *Impurity driven thermal Hall effect for a superconductor with E_{2u} chiral pairing, plotted as a function of temperature and impurity size k_fR, where k_f is the Fermi wave vector and R the hard-disk radius of the impurities. The impurity density has been set to the optimum value. The dotted line shows the maximum signal expected from the topological edge states, discussed in the previous section [28]. For UPt_3, the red curve peaks at $\sim 6 \times 10^{-3}$ $WK^{-1}m^{-1}$. Taken from [24].*

The situation in UPt_3 is further complicated by the fact that the impurities are not of a fixed size. As previously mentioned, the spectrum of chiral fermions will vary as a function of the impurity size, and therefore so will the magnitude of the transverse current. For example, point size impurities cannot give rise to an anomalous thermal Hall effect. The anomalous thermal Hall signal will also vary as a function of the impurity density - if this is too small, there are too few scattering centres, whereas if it is too large, the bulk superconductivity will be suppressed. The anomalous thermal Hall effect in UPt_3 therefore varies as a function of a range of parameters. Figure 4.5 shows this variation as a function

of impurity size, with the impurity density set to the optimum value. For the optimum impurity size, the impurity driven bulk effect is significantly larger than the topological edge effect over all temperatures. Although, as mentioned, the observation of either effect would be groundbreaking.

4.3 Experimental Results and Interpretation

In the following, we present our own electrical and thermal transport measurements on UPt_3. These will be discussed in parallel, first concentrating on the longitudinal transport properties, and then the transverse. This is primarily to draw comparison between the two. Longitudinal transport in UPt_3 has been investigated previously, and will therefore only briefly be covered in order to characterise the samples and highlight relevant details. The transverse transport properties are instead - for the most part - novel findings.

Two samples were measured during this investigation - we refer to these as S1 and S2. Both are single crystals which have been cut from the same larger crystal. This original crystal was grown by the Czochralski method and oriented by Laue X-ray diffraction. Thanks go to Andrew Huxley for providing this. Both samples are plate-like, with the largest flat face perpendicular to the c-axis. After being spark cut, samples S1 and S2 were reduced to a thickness of 55 µm and 88 µm respectively, using the polishing jig shown in Figure 2.7. For all the measurements that follow, the field was applied perpendicular to the flat face (along the c-axis), and the current parallel (along a). This is also shown in Figure 4.6.

The thermal Hall effect was measured using the procedure outlined in Section 2.2, and the experimental setup shown in Figures 2.3 and 2.5. This setup comprises three ruthenium oxide bare chip thermometers and a strain gauge heater, all of which have been thermally isolated from everything but the sample. The sample is adhered to an OFHC copper block - which acts as a thermal reservoir - using silver epoxy, and then clamped between this and the sample stage. For each measurement, a known power is provided by Joule heating of the strain gauge, the sample is allowed to reach thermal equilibrium, at which point the temperature at each thermometer is recorded. This gives the longitudinal and transverse thermal gradients across the sample, from which the thermal conductivities may be calculated. Throughout all measurements, the heater power was set such that $\Delta T_x \sim 0.05T$. This process is described in detail in Section 2.2.

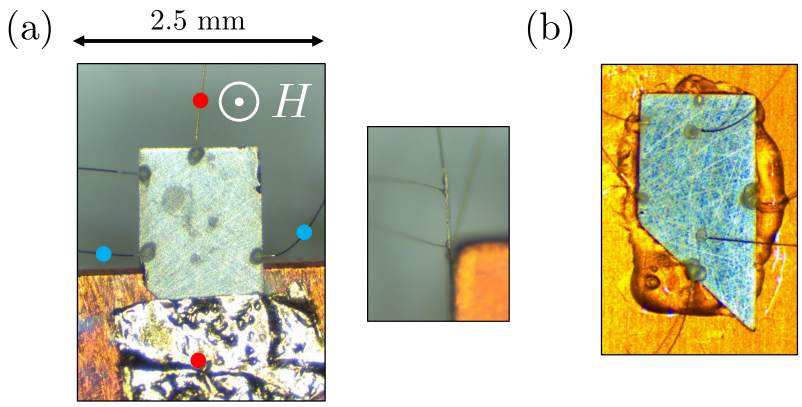

Figure 4.6 *Microscope images of sample S1, which has been prepared for measurement. (a) Thermal Hall setup, reproduced from Figure 2.3. The sample is oriented with the c-axis parallel to the applied field. In the left image, the red/blue dots show where the current/voltage contacts are made for the simultaneous electrical resistivity measurement (discussed in the text). The right image is a side-on image of the same sample (for comparison, the attached wires are 25 μm). (b) The same sample, subsequently prepared for a standalone electrical resistivity measurement, with two additional contacts added such that the longitudinal and transverse transport may be simultaneously measured by the 4-probe method.*

The electrical resistivity has been measured by two separate methods:

(i) In tandem with the thermal Hall measurement, with the contacts made along the thermal contacts, as shown in Figure 4.6 (a). Data acquired by this method is exclusively plotted as open circles.

(ii) In a standalone experiment, and measured via the 4-probe technique with contacts made directly to the sample, as shown in Figure 4.6 (b).

The second is obviously the more accurate method. The first was initially employed to determine the point at which the sample became superconducting during a thermal Hall measurement. However, it has produced some useful supplementary data. Note, for the first technique, the longitudinal and transverse resistivities have been calculated by - respectively - symmetrising and antisymmetrising the same data.

4.3.1 Longitudinal Transport

The electrical resistivity is shown in Figure 4.7, plotted as a function of temperature. Above the superconducting transition, the resistivity follows a Fermi liquid $\rho_0 + AT^2$ behaviour. This may be extrapolated to zero temperature in order to give the residual resistivity. In zero field, ρ_0 =0.49 µΩ cm for sample S1, and ρ_0 =0.6 µΩ cm for sample S2 (not shown) - this implies our samples are comparatively pure [113]. As shown in the inset of Figure 4.7, the application of field acts to increase ρ_0 linearly (whereas A remains approximately constant), as observed previously [137]. Finally, the zero-field superconducting transition occurs at $\sim$ 0.55 K in both samples; again, this marks them as being relatively pure.

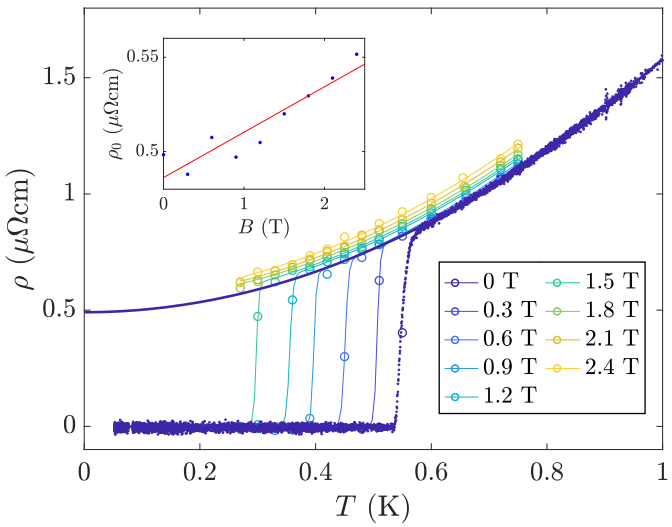

Figure 4.7 *Electrical resistivity data for sample S1, plotted as a function of temperature for a range of fields. The open points are data taken alongside the thermal Hall measurement, whereas the dots were taken in a separate resistivity measurement. The lines show fits to* $\rho_0 + AT^2$*, multiplied by a step function, where the in-field transition width has been set equal to the zero-field transition width. The thicker dark blue line is the zero-field normal state contribution extended over the full temperature range. The inset is a plot of the residual resistivity* ρ_0 *as a function of field, with the red line showing the linear fit through the points.*

In Figure 4.8, the electrical resistivity has been plotted as a function of field. At all temperatures, the data approximately follows a $B^{1.4}$ dependence. This has been observed previously [138], and taken as evidence for UPt_3 being a compensated

metal (having an equal number of electrons and holes). The inset of Figure 4.8 shows a Kohler plot, wherein all the data falls onto the same curve regardless of temperature. This follows from Boltzmann transport theory, in which an applied field will only act to alter the scattering rate, and thus $B/\rho(0)$ encapsulates all the possible scattering processes [15]. This would suggest that the charge carriers in UPt_3 remain in a Fermi liquid state - and are therefore adequately described by Boltzmann transport theory - up to high fields. Note, the slight deviation of the lowest temperature data is partly due to the difficulty in defining $\rho(0)$, as the material is superconducting below ~ 2 T.

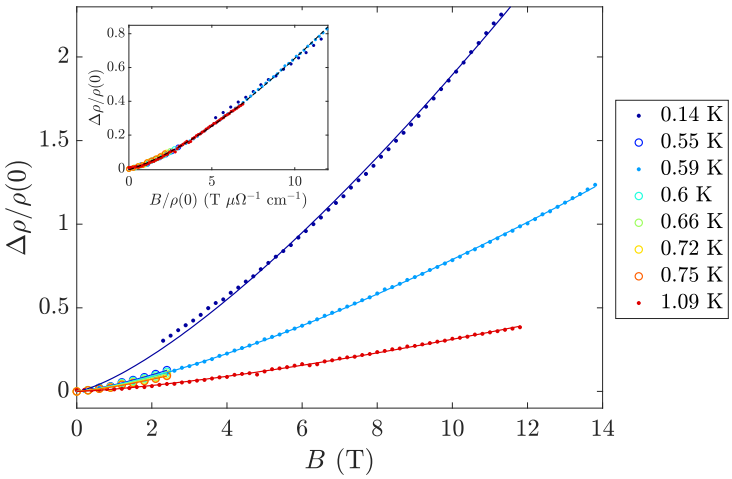

Figure 4.8 *Electrical resistivity data for sample S1, plotted as a function of field for a range of temperatures. In these plots, $\Delta\rho = \rho(B) - \rho(0)$, where $\rho(0)$ is the resistivity at zero field. The curves show fits to $aB^{1.4}$. The inset shows a Kohler plot. In both plots, the open points represent data taken alongside the thermal Hall measurements, whereas the dots are from a separate resistivity measurement.*

Shown in Figure 4.9 is the thermal conductivity, plotted as a function of temperature. At these temperatures, the lattice contribution will be negligible, and we therefore expect the thermal and electrical conductivities to be comparable. Indeed, at the lowest temperatures, the thermal conductivity appears to be tending towards the value calculated from the Wiedemann-Franz law (Section 1.3),

$$\frac{\kappa}{T} \simeq \frac{L}{\rho_0} \simeq 4.5 \text{ WK}^{-2}\text{m}^{-1}, \tag{4.14}$$

calculated for the 2.4 T data. In this, the electrical conductivity has been approximated as $1/\rho_0$.

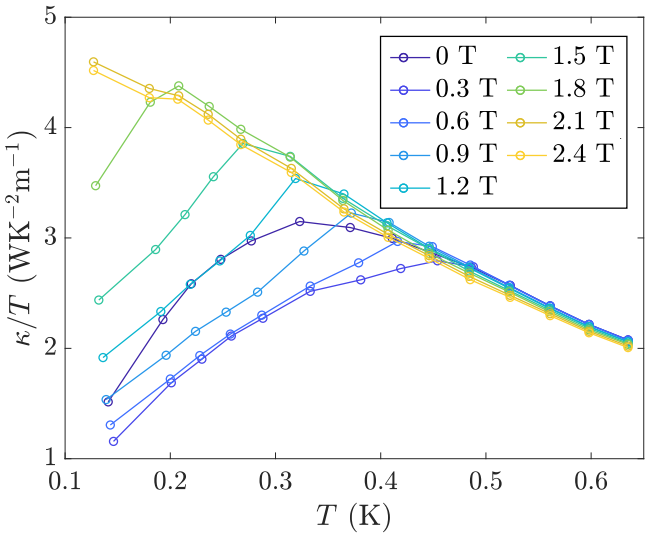

Figure 4.9 *Thermal conductivity of sample S1, plotted as a function of temperature for a range of fields. The lines simply join adjacent points, and are intended as guides for the eye.*

Upon the application of field, the normal state thermal conductivity is reduced in magnitude slightly. This is consistent with the positive magnetoresistance (Figure 4.8). More noticeably however, with increasing field the change of gradient at the superconducting transition becomes more sharply defined. In zero field, the gradual change of gradient is due to the thermal carriers (electrons) instead forming the superconducting condensate, and therefore no longer capable of transporting heat. The change of gradient becomes sharper as the field is increased due to the additional effect of scattering from vortices, which penetrate the material in the mixed state. Both of these effects are discussed in Section 1.3.

Previous studies have been successful in mapping out parts of the superconducting phase diagram using the thermal conductivity. The phase transitions become evident upon differentiating the thermal conductivity with respect to temperature [126] or field [139]. However, our data points are too coarse for this analysis to be accurate. Instead, shown in Figure 4.10 is the thermal conductivity plotted as a function of both temperature and field, with the phase boundaries extrapolated from the resistivity data. Clearly, the thermal conductivity gives some indications as to where these should occur, particularly for the C-N transition at low temperatures.

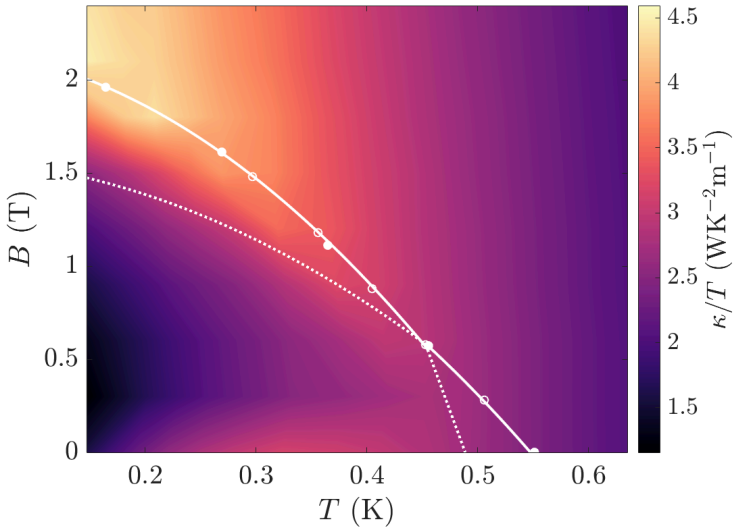

Figure 4.10 *Thermal conductivity of sample S1, plotted as a function of both temperature and field, with the colour bar giving the magnitude. The white lines show estimates for the superconducting phase boundaries, with the open/filled dots taken from sample S1/S2 resistivity data (labelling the point at which resistivity has fallen to half its normal state value).*

4.3.2 Transverse Transport

In the ordinary Hall effect, the Hall resistivity will vary as $\rho_{xy} = R_H B$, where R_H is the Hall coefficient. For a single band, $R_H = \frac{1}{nq}$, where n is the charge carrier density and q the charge. Measurements of the Hall coefficient can therefore be used to determine the type of charge carriers, as well as measure the Fermi surface volume [140]. However, in materials with multiple bands at the Fermi energy, the picture is not so clear cut. Additionally, there can be 'anomalous' contributions to the Hall effect, arising due to skew scattering (typically $\rho_{xy} \propto \rho_{xx}$), side-jump scattering ($\propto \rho_{xx}^2$) and intrinsic Berry phase effects ($\propto \rho_{xx}^2$) [141].

Shown in Figure 4.11 is the Hall resistivity for UPt_3, plotted as a function of field. The data has been collected by the four-probe technique, with the contact geometry shown in Figure 4.6 (b). The data presented has been antisymmetrised in field. Immediately obvious is that the Hall resistivity appears to increase in magnitude as the temperature is decreased. This is markedly different from the behaviour predicted for a generic heavy fermion compound [142], for which the Hall coefficient is expected to fall to a constant value as $T \to 0$. This prediction is a consequence of the coherent state, which - as discussed in Section 5.1 - develops

in the majority of heavy fermion compounds at the lowest temperatures. In this state, both normal and skew scattering from ions on the lattice become coherent and therefore vanish. This implies that - at the lowest temperatures - the Hall effect should entirely be driven by the applied field, and thus fall to the constant, ordinary Hall effect value (plus a small contribution from defects or impurities).

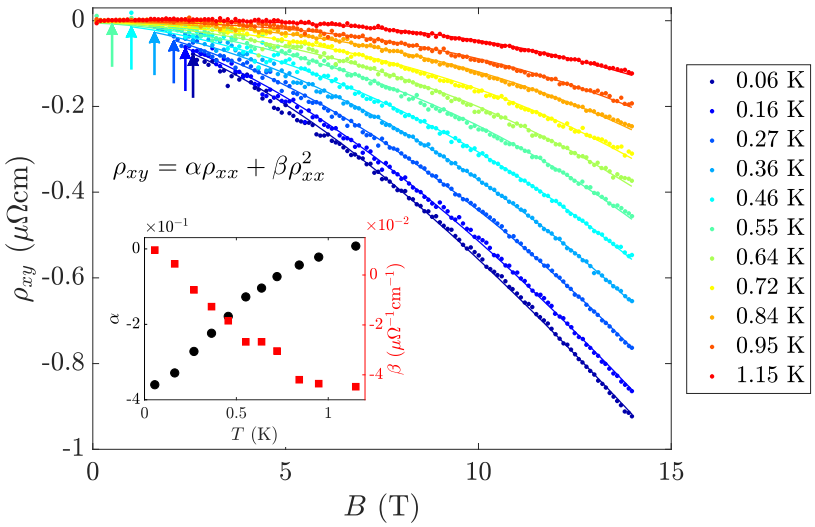

Figure 4.11 *Electrical Hall resistivity of sample S2, plotted as a function of field. Arrows show the positions of the superconducting transitions, and the lines are fits to* $\rho_{xy} = \alpha\rho_{xx} + \beta\rho_{xx}^2$. *The inset shows the coefficients of those fits, plotted as a function of temperature.*

At these temperatures - as indicated by the Fermi liquid behaviour in resistivity - the coherent state is well established in UPt_3, it is therefore strange that our measurements deviate so strongly from the anticipated behaviour. Further, the Hall resistivity has been investigated previously (for field/current perpendicular/parallel to the c-axis - the opposite configuration to our measurements) and shown to match the predicted behaviour almost perfectly [143]. In that study, the low temperature Hall resistivity was observed to follow

$$\rho_{xy}(B) = R_{sk}(T)B - R_H B^2. \tag{4.15}$$

where the first term is due to skew scattering - with R_{sk} linearly proportional to temperature - and the second is the ordinary Hall effect (with R_H a constant). Note, in this case the ordinary Hall effect has a quadratic (rather than linear) dependence on field due to UPt_3 being a compensated metal, implying that the electron/hole band linear contributions cancel [140].

Clearly, the difference in behaviour is attributable to the different measurement geometry, but it is difficult to account for such a stark contrast. In that previous study [143], the skew scattering is claimed to be from un-ordered magnetic moments. At low temperatures, these are deviations from the full antiferromagnetic order. The degree of skew scattering is therefore expected to be proportional to $[m_Q^2(0) - m_Q^2(T)]$, where m_Q is the antiferommagnetic sublattice magnetisation. This quantity has been measured by neutron scattering, and observed to vary linearly with temperature [118], which accounts for the linear dependence of R_{sk}. Such a contribution therefore cannot account for the increase in Hall resistivity we observe as the temperature is lowered. Similarly, the side-jump mechanism cannot explain our observations, as it is related to the presence of impurities (or phonons), and would not give the observed temperature dependence [141]. Finally, the ordinary Hall effect is expected to tend to a constant value as $T \to 0$ (as observed in [143]), which, again, cannot account for the increase in Hall resistivity.

One potential explanation for our observations is an intrinsic Berry phase effect. This effect was briefly discussed in Section 1.1, and refers to the anomalous, Berry curvature dependent velocity acquired by a charge carrier in the presence of an electric field (Equation 1.22), due to interband coherence [141]. This phenomenon has been used to account for the large anomalous Hall effects observed in a number of noncollinear antiferromagnets [144, 145] - a property which UPt_3 may share [119]. Such an effect would explain the increase in Hall resistivity as the temperature is lowered - as the antiferromagnetic order becomes more firmly entrenched - as well as the large discrepancy between the two different measurement geometries - as they are each probing different regions of the Fermi surface. This contribution to the Hall effect can be 'straightforwardly' calculated from first-principles electronic structure techniques [141]. As the band structure of UPt_3 is now well established [146], a calculation of this Berry phase contribution - and therefore a check of this hypothesis - is certainly feasible.

However, the Hall resistivity resulting from an intrinsic Berry phase effect should vary as ρ_{xx}^2 [141], whereas in our data, it is instead the ρ_{xx} coefficient which rises as the temperature is lowered (shown in the inset of Figure 4.11). As previously mentioned, only skew scattering can give such a contribution [141]. In the original theory of skew scattering in itinerant ferromagnets [147], the scattering introduces a momentum perpendicular to the magnetisation. Within the coherent Kondo regime, skew scattering is not so well understood [148], but we might similarly

expect some directional dependence. If the magnetic fluctuations which give rise to the skew scattering are only along a single direction, this would account for the marked differences observed between opposite measurement geometries [143]. There are suggestions that UPt_3 should transition to long range magnetic order at the lowest temperatures, as implied by a peak in the specific heat, centred at 20 mK [149], and also by neutron scattering [150]. The increase in Hall resistivity as the temperature is lowered might therefore arise due to skew scattering from fluctuations associated with this magnetic order.

We now consider the transverse thermal conductivity, shown in Figure 4.12 plotted as a function of field. Also included in Figure 4.12 is the measurement sequence. This sequence is particularly relevant for the following section, in which the effect of chirality will be investigated. For now, we simply note that although the data has been acquired by a slightly different method to the usual constant-field temperature sweeps, the data processing is identical to that which is described in Section 2.2. For example, the thermometers are still calibrated by constant-field temperature curves, and the antisymmetrisation is still taken between identical measurements at positive and negative fields.

The thermal Hall data exhibits two different regimes, characterised by a positive and negative signal respectively. In order to understand the negative signal, the transverse electrical conductivity, calculated from

$$\sigma_{xy} = \frac{\rho_{xy}}{\rho_{xx}^2 + \rho_{xy}^2}, \tag{4.16}$$

is shown in the inset of Figure 4.12 (a). Clearly this displays an almost identical behaviour to the negative signal in the thermal Hall conductivity. This would imply that the normal state thermal Hall signal is entirely electronic, and therefore attributed to the same cause. Note that, unlike with the electrical Hall effect, the negative signal does not fall to zero immediately upon entering the superconducting state. In this respect, it is similar to the thermal conductivity (Figure 4.9), for which the density of thermal carriers falls off only gradually due to there being nodal regions in the superconducting gap function.

The positive signal instead occurs exclusively within the superconducting state - this is shown more clearly in Figure 4.13. This thermal Hall effect is therefore most likely carried by the superconducting quasiparticles, although the signal is sufficiently weak that phonons may also have a role to play. However, we save the discussion of potential interpretations until after we have investigated whether

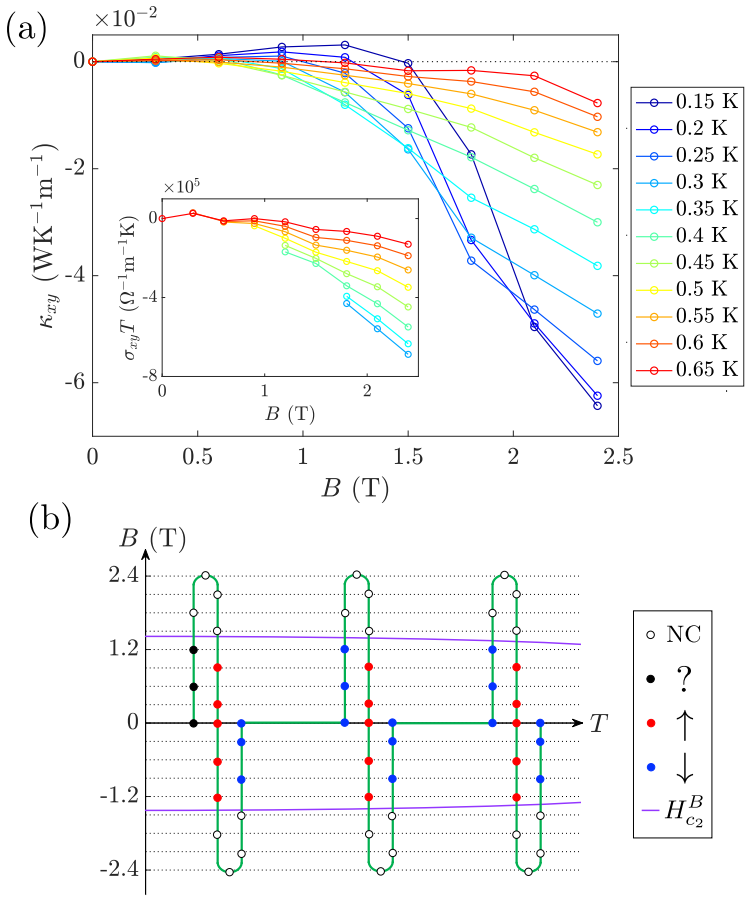

Figure 4.12 *(a) Thermal Hall conductivity of sample S1, plotted as a function of field for a range of temperatures. The inset shows the transverse electrical conductivity (multiplied by temperature) plotted in the same way, with the superconducting portions not included. (b) Measurement sequence in acquiring the thermal Hall data. The green line shows the path taken in field/temperature, whilst the dots are the points at which a measurement is taken. Each individual field ramp sequence takes place at a constant temperature, the variation in T over a single loop is only for clarity. Black, red and blue dots imply the superconducting condensate is in an unknown, positive and negative chiral state respectively. White implies there is no chirality, either due to the material being in the superconducting C-phase or the normal state. The purple line shows the B-C phase transition.*

the signal might be linked to the chiral nature of the superconducting B-phase, in the following section.

We briefly mention one less glamorous explanation - that we are picking up a Hall signal from the thermal reservoir. Recall our experimental setup, shown in

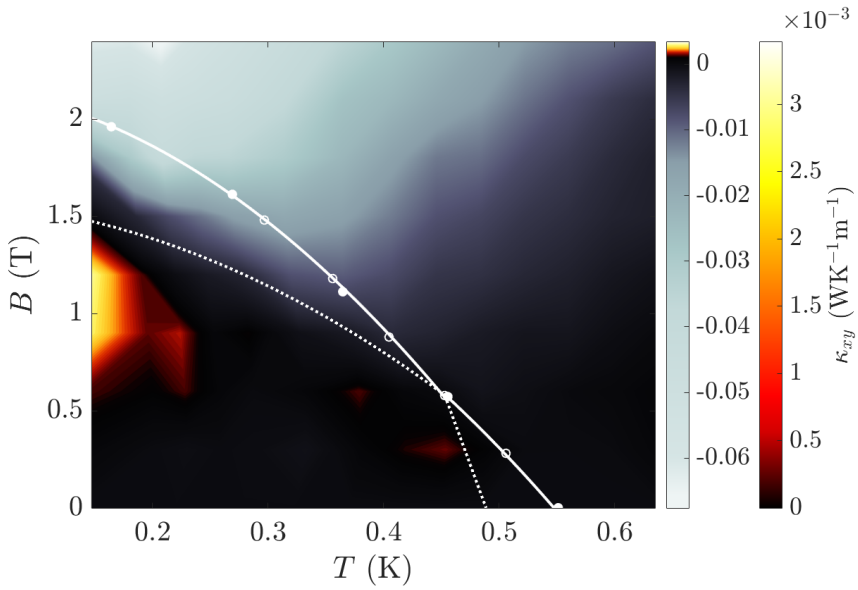

Figure 4.13 *Thermal Hall conductivity plotted as a function of both field and temperature, with the colour bar chosen to exaggerate the positive signal. The white lines show estimates for the superconducting phase boundaries, with the open/filled dots taken from sample S1/S2 resistivity data (labelling the point at which resistivity has fallen to half its normal state value).*

Figure 4.6, wherein the sample is adhered to a copper block using silver paint, and clamped between this and a gold sheet. All the components of the thermal reservoir are metallic, and all have been demonstrated to have a finite Hall coefficient at the lowest temperatures [140]. However, the resulting transverse thermal gradient in the sample stage can be estimated from the Wiedemann-Franz law, and - due to the large thickness and high thermal conductivity of the copper block - is negligible in comparison to the measured thermal gradient in the sample. Importantly also, the Hall coefficient is negative for all three materials which make up the thermal reservoir. This would correspond to a thermal Hall effect of the opposite sign to that which we observe inside the superconducting state. The sample stage might contribute negligibly to the negative, normal state signal. However, from a comparison to electrical Hall effect measurements, this thermal Hall effect is also certainly intrinsic to UPt_3.

4.3.3 The Effect of Chirality

The initial purpose of these measurements was to investigate whether the B-phase of UPt_3 might play host to an anomalous thermal Hall effect. This was predicted to occur at zero field, and be driven by the intrinsic chirality of the superconducting condensate. However, one crucial aspect of our measurements is antisymmetrisation (taking the difference between identical measurements at positive and negative field). In order to apply this technique to zero-field data, we must distinguish between states of different chirality. Our method for doing this is illustrated in Figure 4.12 (b): we assume that the superconducting condensate will have a positive chirality - which we label ↑ - if the field was positive upon entering the B-phase (and vice versa). This field-induced chirality has been demonstrated previously by Kerr effect measurements (although we note this is only a surface probe) [133]. In this way, we can antisymmetrise the zero-field data by taking the difference between opposite-chirality runs.

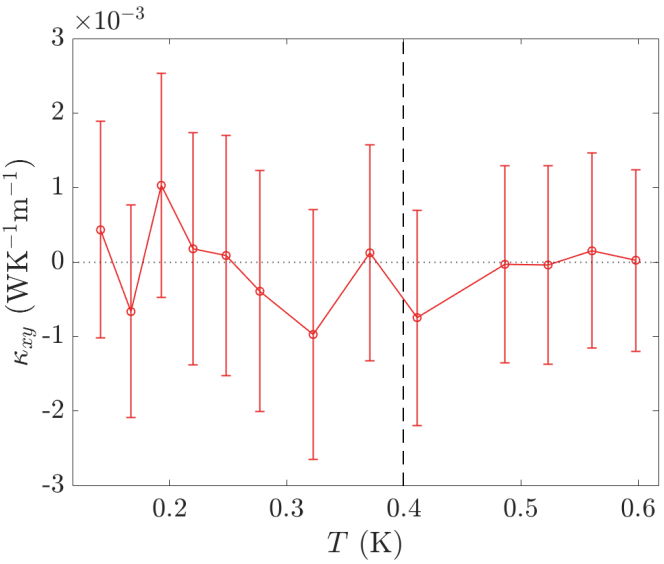

Figure 4.14 *Zero-field thermal Hall effect for sample S1, with the data acquired as described in the text. The vertical dashed line is the temperature at which the maximum signal predicted by [24] should occur. Error bars include statistical error, as well as error from thermometer calibration and sample dimensions. In this data set, the largest measured transverse temperature gradient is* $< 80\ \mu K$.

Shown in Figure 4.14 is the thermal Hall data collected by antisymmetrising the zero-field data by this method. Unfortunately, there appears no chiral signal. As discussed in Section 4.1, the purely topological signal is estimated to be at most

$\sim 10^{-3}$ $WK^{-1}m^{-1}$ [28]. The residual resistivity of our samples would imply they are exceptionally pure, however they will inevitably contain impurities, and even a low impurity density will most likely render this topological signal imperceptibly small. The impurity driven effect instead relies on finely tuned sample-dependent parameters - such as the impurity size or density (Figure 4.5) - in order to give a detectable signal [24]. These results (and those which follow) would suggest our samples do not satisfy these requirements. Obviously these samples have been cut from the same crystal, and we therefore do not expect much difference between them - it would be interesting to investigate a range of samples of variable quality.

A recent study has observed differences in the vortex lattice configuration - measured by small angle neutron scattering - depending on the chirality of the superconducting state [151]. These measurements were taken at ± 1.1 T, for fields parallel to c, and with the chirality induced by the field history. This motivated us to investigate whether the positive signal observed in the transverse thermal conductivity - occurring under almost identical conditions - might be linked to chirality, rather than simply being driven by the applied field.

With the application of field, note there are now six different ways to antisymmetrise the data, deriving from the four possible combinations of field/chirality - $[+\uparrow]$, $[+\downarrow]$, $[-\uparrow]$ and $[-\downarrow]$. As such, we have chosen to focus on just a single field (± 1 T). These measurements were also performed on sample S2, which allowed a number of useful sanity checks. The method of realising the four different combinations of field and chirality is shown in Figure 4.15 (b): the sample is cooled to base temperature in the training field, and then at base temperature, the applied field is set. For these measurements, we have reverted to collecting data using temperature ramps at a constant field, as described in Section 2.2.

The results of these measurements are shown in Figure 4.15 (a). Note that, from the original thermal Hall effect measurements in Figure 4.12 (a), we have already observed that the positive signal is present irrespective of chirality. For example, measurements taken at 0.9 T and 1.2 T both show evidence for a positive signal, despite the chirality being reversed ($[+\uparrow, -\downarrow]$ compared to $[+\downarrow, -\uparrow]$). From these measurements, we have additionally demonstrated that the chirality appears to have no bearing on the magnitude of the positive signal, nor on the reduction in magnitude of the negative signal upon entering the superconducting state.

The absence of a chiral contribution to the thermal Hall effect may be attributed to the same factors as for the absence of a zero-field signal. However, it may

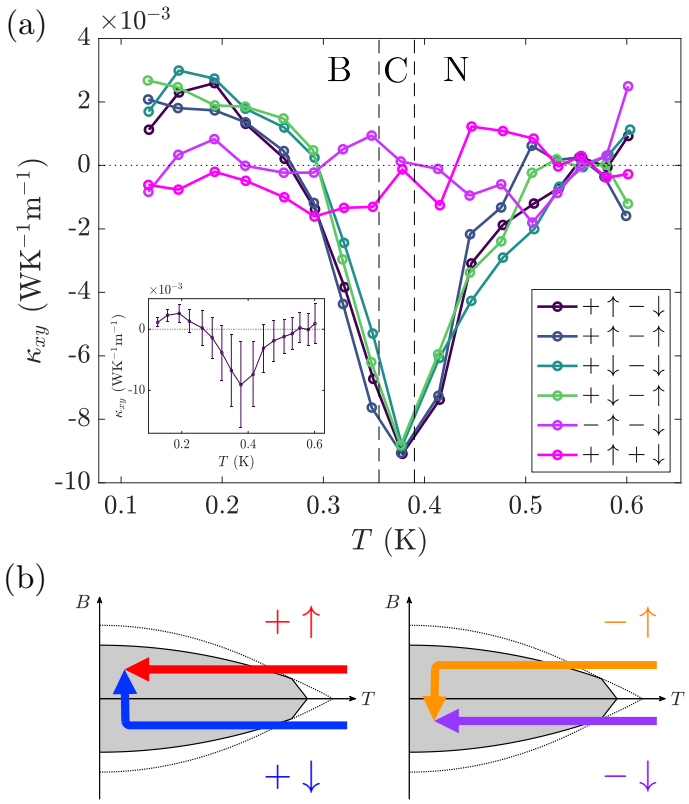

Figure 4.15 *(a) Thermal Hall conductivity of sample S2, plotted as a function of temperature. All data was taken at 1 T. The legend gives the two data sets being antisymmetrised, where +/− gives the field and ↑ / ↓ the chirality. For example, [+ ↑ − ↑] implies a positive field, positive chirality run being antisymmetrised with a negative field, positive chirality run. The vertical dashed lines show the approximate position of the phase transitions, with the B-phase, C-phase and normal state labeled. The inset shows an example of some typical error bars, which come from statistical error, as well as error from thermometer calibration. The error from sample dimensions has not been included, but this would only act to shift all the data by a constant value. (b) Path taken in field/temperature in order to realise the four different combinations of chirality and field, plotted over the superconducting phase diagram for UPt_3, with the B-phase indicated by the shaded region.*

instead be that our assumptions of the chiral state are incorrect. As shown in Figure 4.15 (b), in order to give the $[+,\downarrow]$ state, the sample is cooled in negative field, and the field is then ramped to positive at base temperature ($\sim$ 30 mK). Previous studies have observed periodic heat spikes upon ramping the field too rapidly [152] - attributed to magnetic flux piercing the sample [153]. If these heat spikes were to raise the sample above the B-phase transition temperature, the

field-trained chirality would be lost, and our assumption of the chirality would therefore be incorrect.

For these measurements, the ramp rate was set at 0.074 T/min - above the threshold at which heat spikes were observed in that previous study. The sample temperature was monitored whilst the field was ramped and we see no evidence for the characteristic periodic heat spikes. However, with this sample mass and geometry, we expect the time constant (estimated from $\tau = C/K$, where C is the heat capacity and K the thermal conductance) to be significantly shorter than the time constant of the thermometry measurements, implying that we may be averaging over the heat spikes. Instead, we observe a significant decrease of the thermometer resistance during field ramping. At constant field, this would correspond to a large increase in temperature. In this case however, it is difficult to determine whether there is actually significant heating - resulting from a cascade of heat spikes - or this is simply the influence of the changing field on the thermometer resistance. In any case, it would be useful to repeat these measurements with a slower ramp rate.

Finally, let us consider some potential causes for the positive thermal Hall signal observed within the superconducting B-phase. Figure 4.13 is particularly informative - showing the thermal Hall effect overlaid with the superconducting phase transitions. From this, we see that the signal only occurs at the lowest temperatures, and peaks within the B-phase, before falling to zero at the B-C phase transition. Unfortunately we are hampered by the large negative normal state signal, which makes it difficult to determine whether the positive signal is a feature of the superconductivity more generally, or specifically of the superconducting B-phase. Importantly however, in either case, the signal occurs within the mixed state. Further, we can assume the thermal Hall effect is carried by the superconducting quasiparticles. In UPt_3, the superconducting gap has nodal regions, which implies there will be zero-energy excitations which can act as thermal carriers. Additionally, these nodal regions will be broadened in the mixed state, as the quasiparticle spectrum is Doppler shifted due to currents around the normal state vortices (as discussed in Section 1.3). At these temperatures, we also expect the phonon contribution to be negligible.

Previous studies have observed a thermal Hall effect in the superconducting mixed state, in a number of the high-temperature superconductors [154, 155], and also $CeCoIn_5$ [156]. In the former case, this has often been attributed to a skew scattering of the superconducting quasiparticles from normal state vortices, which

penetrate the material in the mixed state. This asymmetric scattering has been theoretically demonstrated for a single vortex impurity [157], although it is less clear whether this would imply a transverse quasiparticle current in the presence of a regular vortex lattice. Instead - as with the anomalous electrical Hall effect due to skew scattering [141] - it seems more likely that a thermal Hall effect would be driven by disorder, rather than a perfect vortex lattice.

In UPt_3, a re-alignment of the flux line lattice has been observed at the A-B phase transition via small-angle neutron scattering [120]. This occurs as the superconducting gap has a different symmetry in each of the two phases (Figure 4.2), and - although not observed experimentally - the same phenomenon is expected to occur at the B-C phase transition. Upon approach to this transition, we expect the vortex lattice to become increasingly disordered. This disorder might lead to a skew scattering of quasiparticles, and therefore drive the thermal Hall effect we observe.

Finally, we note that the thermal Hall effect has been employed previously to probe the gap structure in multi-band superconductors [155]. In this case, the positive sign of the thermal Hall effect in UPt_3 would imply that the minimal gap of the superconducting phase resides in a hole band.

4.4 Summary

We have measured the transport properties of UPt_3 in order to test predictions of a chirality-driven, anomalous thermal Hall effect in the superconducting B-phase. Unfortunately, there appears no zero-field chiral signal within our experimental resolution. This may be due to our samples not having the appropriate impurity density - or impurity size - required to give a measurable thermal Hall effect.

Instead, regardless of chirality, we observe a positive thermal Hall effect in the superconducting B-phase. This is expected to be carried by the superconducting quasiparticles, and potentially driven by skew scattering from the vortex lattice. It is unclear whether this is a feature of the B-phase or the superconductivity more generally. However, it seems likely that skew scattering would only occur if there were disorder in the flux line lattice. We expect this disorder to manifest on approach to the B-C phase transition, at which the vortex lattice must re-align in accordance with the changing gap function. Additionally, within our experimental

resolution, we see no evidence for a chiral dependence of this thermal Hall signal. However, further work is necessary to clarify the effects of field ramping on the sample temperature.

We also observe a large, negative, normal state Hall effect, both in the electrical and thermal conductivity. This contrasts strongly with previous measurements on UPt_3, taken using a different measurement geometry. This may be linked to an intrinsic Berry phase effect, or alternatively to skew scattering from magnetic fluctuations. However, based on the field dependence of the Hall resistivity, it seems more likely that it is the latter.

Chapter 5

Specific Heat Measurements on Heavy Fermion Systems

UTe_2 and UAu_2 - and indeed UPt_3 from the previous section - belong to a class of materials termed heavy fermion compounds, labelled as such due to the large effective mass of their charge carriers. However, this eponymous feature is only symptomatic of the underlying physics which has led to these compounds being so scrutinised. In heavy fermion materials, the competition between magnetic order and Kondo physics gives rise to a zero-temperature, quantum critical phase transition. This is a universal phenomenon, and these materials thus offer a unique experimental opportunity to investigate the physics of quantum criticality. Further, the quantum critical point is often masked by a region of unconventional superconductivity, and as such, the heavy fermion materials appear closely related to the high temperature cuprate superconductors. Therefore, before detailing our own measurements, we briefly characterise heavy fermion materials, so as to fully appreciate the scope of our investigations.

5.1 Heavy Fermion Materials

Heavy fermion materials were first identified as such by the huge linear term in their specific heat. In some, this is measured to be more than 1000 times larger than the value for copper. As discussed in Section 1.3, this linear - otherwise known as Sommerfeld - coefficient is proportional to the effective mass

of the charge carriers in a material. It is now well established that the heavy quasiparticle masses are a result of the strongly localised moments hybridising with the conduction band. Hence, heavy fermion materials exclusively contain actinide (or lanthanide) ions, with partially filled f-orbitals forming a lattice of localised magnetic moments. At the heart of this hybridisation, and therefore the physics of heavy fermion materials, is the Kondo effect.

The Kondo Effect

The Kondo effect concerns a single magnetic impurity inside a metal, and specifically, the hybridisation of its associated magnetic moment with the conduction electrons [158]. The simplest Hamiltonian to describe this situation is

$$\mathcal{H} = \sum_{k\sigma} \varepsilon_k c^\dagger_{k\sigma} c_{k\sigma} + J\mathbf{S}\cdot\boldsymbol{\sigma}, \tag{5.1}$$

where $c^\dagger_{k\sigma}$ creates a conduction electron with energy ε_k, momentum k and spin σ - the first term therefore gives the total energy of the conduction electrons. The second term accounts for the interaction between a localised magnetic moment $\mathbf{S}$ and the conduction electrons, where $\boldsymbol{\sigma}$ is the spin density of the electron fluid at the localised moment. Finally, and essentially, J is an antiferromagnetic ($J < 0$) interaction. This is a form of superexchange, and reflects the fact that spin-exchange processes between the conduction electrons and the localised moment require that the two spins be anti-parallel.

Using the above Hamiltonian, and treating the second term as a perturbation, Kondo was able to calculate the magnetic scattering rate, given by

$$\frac{1}{\tau} \propto \left[J\rho + 2(J\rho)^2 \ln\frac{D}{T} \right], \tag{5.2}$$

where ρ is the density of states of the conduction sea and D is the half-width of the electron band [20]. This result was put forward to explain the resistivity minimum observed in metals with dilute magnetic impurities - a longstanding problem of the time. However, at a temperature

$$T_K \sim De^{-\frac{1}{2J\rho}}, \tag{5.3}$$

at which the two terms become comparable, this perturbative treatment is no longer valid. This is reflected in the unphysical divergence of the scattering rate

at low temperatures, given by the logarithmic term in Equation 5.2.

Beyond perturbation theory this problem is not straightforward, and requires the renormalisation group concept, or the appreciation that the behaviour of a spin inside a metal is dependent on the energy scale at which it is probed. Instead, phenomenologically, we can say that the logarithmic term comes from the degeneracy of the up/down spin configurations of the local moment. This leads to spin fluctuations on a timescale τ_{sf}, which are enabled by a spin-exchange process with the conduction electrons,

$$e^-_\downarrow + S_\uparrow \longleftrightarrow e^-_\uparrow + S_\downarrow. \tag{5.4}$$

At a temperature comparable to the scattering rate (or $k_B T_K \sim \frac{\hbar}{\tau_{sf}}$), there is a resonant effect and the scattering cross section is enhanced, leading to a corresponding increase in the resistivity. However, at low temperatures, the coupling is sufficiently strong that the conduction electrons become bound to the local moment, forming a singlet state. This bound state instead behaves as a non-magnetic impurity, and hence the resistivity saturates at the lowest temperatures, as is observed in experiment (and demonstrated in Figure 5.1 for the dilute Kondo system $Ce_{0.5}La_{0.5}Cu_6$ [159]). In all this, the only relevant energy scale is the Kondo temperature (T_K), marking the crossover between the high temperature, localised moment, weak scattering regime, and the low-temperature, screened moment, Kondo singlet state.

The Doniach Phase Diagram

The discussion so far has focused on dilute magnetic impurities within a metal. We now consider the case where the localised moments are densely packed, and instead form a 'Kondo lattice' [160]. As the name suggests, Kondo physics is still relevant, however due to their close proximity, the interactions between localised moments can no longer be ignored. This drastically alters the behaviour of the system. The Kondo lattice is physically realised in heavy fermion compounds, wherein localised moments - resulting from partially filled $4f$ (or $5f$) orbitals - are locked into a periodic arrangement by the crystalline lattice.

As with the single impurity Kondo effect, the Kondo lattice has a characteristic temperature, T_K, below which the localised moments will be effectively screened by the conduction electrons. However, the scattering centres are no longer

randomly distributed and the scattering will instead develop a coherence. In the same way that a perfect crystal will have no resistance, the Kondo lattice exhibits a precipitous drop in the resistivity below T_K. This is often a feature of the heavy fermion compounds, as shown in Figure 5.1 (a) for UAu_2 and UTe_2. Additionally, as a result of the aforementioned spin-exchange processes, the conduction band will have some localised f-electron character. This hybridisation explains the enhanced mass of the charge carriers; a feature which is also observed in the heavy fermion materials.

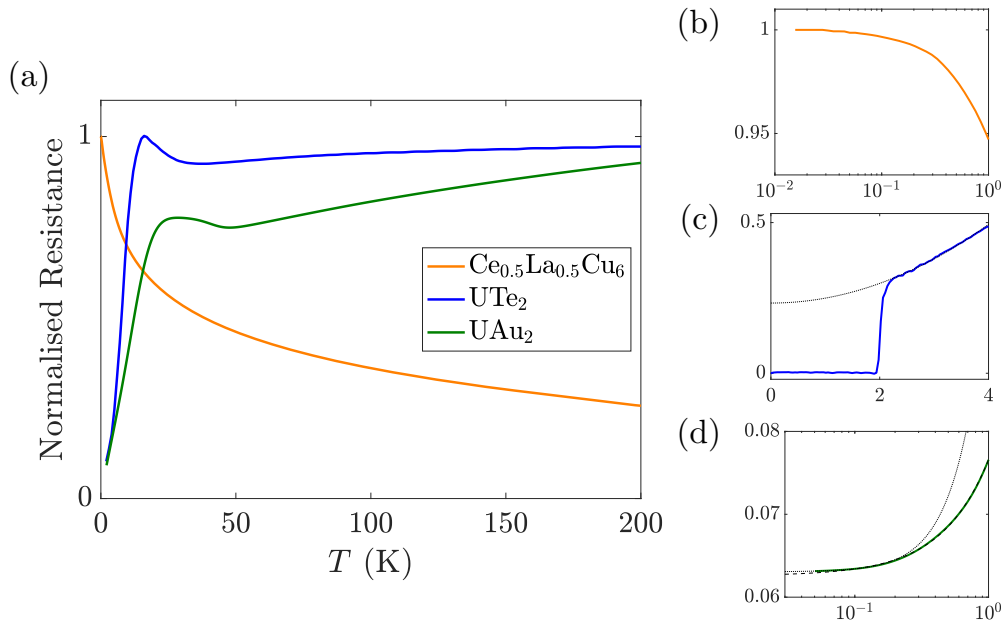

Figure 5.1 *(a) Electrical resistance of three different heavy fermion compounds, plotted as a function of temperature, with each normalised to their largest respective measured value. Also included is the low temperature resistance for (b) $Ce_{0.5}La_{0.5}Cu_6$, showing the saturation typical of a dilute Kondo system (taken from [159]), (c) UTe_2, showing the T^2 (dotted line) Fermi liquid behaviour above the superconducting transition, and (d) UAu_2, showing the transition between a quantum critical $T^{1.2}$ dependence (dashed line) and a Fermi liquid T^2 dependence (dotted line) at ~ 0.2 K. Note, UAu_2 is additionally antiferromagnetically ordered below ~ 43 K, as will be discussed in the UAu_2 section.*

However, the key difference between the single impurity model and the Kondo lattice is that we must now consider interactions *between* localised moments. This comes in the form of an indirect exchange - the so-called RKKY interaction - which describes how a localised moment will polarise the sea of conduction electrons, and thus couple to a neighbouring moment. More specifically, the

RKKY Hamiltonian for two neighbouring spins is given by

$$\mathcal{H}_{RKKY} \sim -J^2\rho\frac{\cos 2k_F r}{k_F r}\mathbf{S}_1 \cdot \mathbf{S}_2, \tag{5.5}$$

where ρ is again the conduction sea density of states, k_F is the Fermi wave-vector and r is the distance between the two localised moments $\mathbf{S}_1$ and $\mathbf{S}_2$ [158]. Hence, the conduction electron spin density decays in an oscillatory fashion, as a function of distance from the magnetic moment. The strength, and nature, of the interaction is therefore determined by the separation of the localised moments.

From the above, the energy scale of the RKKY interaction will be approximately

$$T_{RKKY} \sim J^2\rho, \tag{5.6}$$

whilst the Kondo temperature remains identical to Equation 5.3. We thus have two competing energy scales, both of which depend on the magnitude of $J\rho$. This competition is illustrated in Figure 5.2, in what has become known as the Doniach phase diagram. At small $J\rho$, neighbouring moments are not screened and therefore couple magnetically; instead, at large $J\rho$, Kondo physics will dominate. Importantly, at zero temperature, the transition between magnetic order and the the Kondo ground state is a continuous phase transition, and thus corresponds to a quantum critical point (QCP). Quantum criticality is a universal phenomenon, and hence the Kondo lattice may provide a route to understanding a variety of other systems.

This quantum critical behaviour is the primary reason for the keen interest in heavy fermion compounds. In the majority of metals containing localised moments, antiferromagnetic order sets in at low temperatures without any hint of Kondo physics. In heavy fermion materials however, the situation is not so clear-cut, and the two energy scales are often comparable. As such, by varying some parameter - such as field, pressure or chemical doping - it is often possible to transition between the two regimes, and thus gain access to the QCP (or more accurately the finite temperature, quantum critical region above the QCP). Heavy fermion compounds thus present an experimental opportunity to study quantum criticality [161]. Further, in a number of heavy fermion materials, the QCP is cloaked by a dome of superconductivity. The phase diagram therefore shares significant similarities with that of the cuprate superconductors, and may provide an alternative route to understanding high temperature superconductivity.

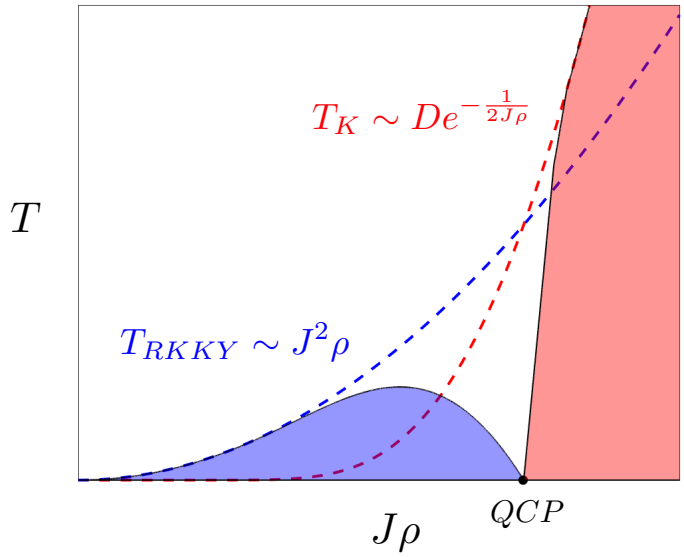

Figure 5.2 *The Doniach phase diagram, showing the competition between magnetic order (T_{RKKY}) and Kondo physics (T_K) in a metal containing localised magnetic moments, plotted as a function of the magnitude of $J\rho$. In the blue region, magnetic order will set in, whereas in the red region Kondo physics will dominate. Experimentally, $J\rho$ is typically varied by the application of field or pressure, or by chemical doping.*

Experimental Consequences of the Kondo Lattice

We now discuss some physical consequences of the above discussion. One particularly relevant phenomenon in all that follows is that of the Fermi liquid state [20]. This was originally put forward in order to explain why the essential features of liquid ^{3}He were adequately accounted for by a system of non-interacting fermions, in spite of the undeniably strong interactions. Fermi liquid theory posits that the elementary excitations in a strongly interacting system are not identical to free particles, but instead composite quasiparticles. Unlike the particles from which they are constructed, these quasiparticles interact only weakly with one another, thus justifying the non-interacting model. Importantly however, the quasiparticles behave identically to the particles which comprise them, but with renormalised dynamical properties, such as effective mass or magnetic moment.

For our purposes, the Fermi liquid state can be used to describe the regime in which Kondo physics dominates, on account of the strong electron-electron

interactions present. Further, the quantum critical region above the QCP is often associated with a breakdown of the Fermi liquid state, and thus characterised by so-called 'non-Fermi liquid behaviour'. In the following, we describe experimental hallmarks of the two regimes. Note however, quantum criticality is not exclusive to Kondo systems, and even within these systems, there are a range of features associated with non-Fermi liquid behaviour [162]. We therefore only focus on those signatures of quantum criticality most relevant to our own investigations.

Resistivity - Well below T_K, the resistivity of heavy fermion compounds often varies as

$$\rho = \rho_0 + AT^2. \tag{5.7}$$

This is typical of a Fermi liquid, with the constant ρ_0 acting as a measure of impurity content, and A being proportional to the square of the quasiparticle effective mass. Often, in the region above a quantum critical point, deviations from Fermi liquid behaviour are observed. Specifically, in a number of heavy fermion materials [163, 164], the resistivity is observed to instead vary as

$$\rho \sim T^{1+\eta}, \tag{5.8}$$

or quasilinearly, with $0 < \eta < 0.2$. This behaviour is sometimes ascribed to a breakdown of the Kondo effect [158]. Indeed, measurements of the Hall coefficient in the heavy fermion compound $YbRh_2Si_2$ appear to support this, showing evidence for an abrupt change of the Fermi volume upon passing through the quantum critical region [165].

Specific Heat - Similar to the electronic specific heat - discussed in Section 1.3 - the Fermi liquid specific heat will vary as

$$C = \gamma T = \frac{\pi^2 k_B^2}{3} D^*(\varepsilon_F) T, \tag{5.9}$$

where γ is the Sommerfeld coefficient, and $D^*(\varepsilon_F) = D(\varepsilon_F)\frac{m^*}{m}$ is the renormalised density of states at the Fermi energy. The Sommerfeld coefficient therefore provides some measure of the quasiparticle effective mass. This implies that the ratio A/γ^2 - or the Kadowaki-Woods ratio - should be approximately constant, regardless of the quasiparticle mass enhancement. This is observed experimentally [166]. In the quantum critical region, we similarly expect deviations from Fermi liquid behaviour. In those same materials previously mentioned to exhibit a quasilinear resistivity [163, 164], the specific heat is

observed to vary logarithmically, or as

$$C \sim \ln\left(\frac{T^*}{T}\right), \tag{5.10}$$

where T^* is some constant. This might also be linked to a breakdown of the Kondo effect. However, in other heavy fermion compounds, a similar logarithmic dependence of the specific heat is instead attributed to the interaction between the heavy quasiparticles and quantum spin fluctuations [167], or alternatively, the two-channel Kondo effect [168]. This latter effect will be discussed in the context of our investigations into UAu_2.

Magnetic Susceptibility - In a Kondo lattice system, the magnetic moments are unscreened above T_K, and the magnetic susceptibility (χ) will exhibit a Curie-Weiss $(T + \theta)^{-1}$ dependence. At low temperatures, the susceptibility will instead tend towards a constant value, which is the typical behaviour of a paramagnet. From Fermi liquid theory, this constant value will be proportional to the renormalised density of states $D^*(\varepsilon_F)$. This implies that the Wilson ratio,

$$W = \frac{\chi_P}{\gamma}, \tag{5.11}$$

where χ_P is the Pauli susceptibility and γ is the Sommerfeld coefficient, should be approximately constant for heavy fermion materials. This is indeed observed experimentally [169].

Superconductivity - As previously mentioned, in heavy fermion compounds the QCP is often masked by a region of superconductivity. At the QCP - where the magnetic ordering temperature has been suppressed to zero - the magnetic fluctuations are expected to be large. Additionally, in the heavy fermion superconductors, the size of the superconducting jump in specific heat will scale with the Sommerfeld coefficient (as shown in Figure 5.12 for UTe_2), implying that it is the heavy fermion quasiparticles which condense to form the superconducting state. It therefore seems likely that superconductivity is borne out of an effective attractive interaction between magnetic fluctuations and the heavy quasiparticles. Indeed, although there is no fully accepted microscopic theory, there is growing experimental evidence to suggest that this is the case [122, 123].

5.2 UAu_2

UAu_2 was first synthesised and characterised more than two decades ago [170, 171]. However, since those initial studies, the material has been consistently passed over in favour of other heavy fermion compounds. The vast majority of work on UAu_2 therefore comes from within our own group, and is the subject of a thesis by a former PhD student, Julian Schmehr [172]. In that work, UAu_2 was found to possess some remarkable properties; most notably, the material exhibits non-Fermi liquid behaviour, deep within an incommensurately modulated, antiferromagnet state. In this respect, UAu_2 is uniquely different from those typical heavy fermion compounds discussed in the previous section, wherein non-Fermi liquid behaviour is often attributed to a close proximity to a magnetic quantum critical point. In the following, we have employed specific heat measurements in order to shed some light on the origins of the non-Fermi liquid behaviour in UAu_2.

5.2.1 Previous Work

As mentioned, the majority of prior work on UAu_2 is contained within [172]; we only review the salient details here. The material crystallises in the AlB_2-type structure, with space group $P6/mmm$ (No.191, D_{6h}, shown in Figure 5.3 (a)) [171]. The magnetic moments are localised at the uranium sites and therefore feel a frustration. The material orders antiferromagnetically below 43.5 K. Within this state, neutron studies [172] and a resonant magnetic X-ray scattering investigation (Appendix A.2) observe magnetic Bragg reflections at $(1/3, 1/3, \delta)$, with $\delta \sim 1/8$ at the Néel temperature, rising to $\sim 1/7$ at the lowest temperatures. As confirmed in Appendix A.2, this implies the moments are incommensurately modulated in magnitude parallel to the c-axis, with adjacent moments $\pi/3$ out of phase - the magnitudes therefore sum to zero over any in-plane triangle. The magnetic structure of this so-called δ-phase is illustrated in Figure 5.3 (b).

As shown in Figure 5.1, the resistivity (for current applied parallel to the c-axis) shows a discontinuity at the antiferromagnetic transition. Below T_N, there occurs a broad maximum followed by a precipitous drop towards lower temperatures, typical of a Kondo system. However, at the lowest (< 4 K) temperatures, the resistivity does not exhibit the expected Fermi liquid behaviour. Similarly,

the magnetic susceptibility follows a logarithmic dependence [173], rather than tending to a constant value, as Fermi liquid theory would predict. These are the first hints of quantum criticality, something which will be explored further alongside the specific heat data.

Finally, resistivity, magnetisation and neutron scattering data all show evidence for a transition to a ferrimagnetic state at high fields [173]. Within this state, the moments are arranged in an $\{\uparrow, \uparrow, \downarrow\}$ configuration on each in-plane triangle. The field-temperature phase diagram for UAu_2 is shown in Figure 5.3 (c), with the ferrimagnetic state labelled as the F-state.

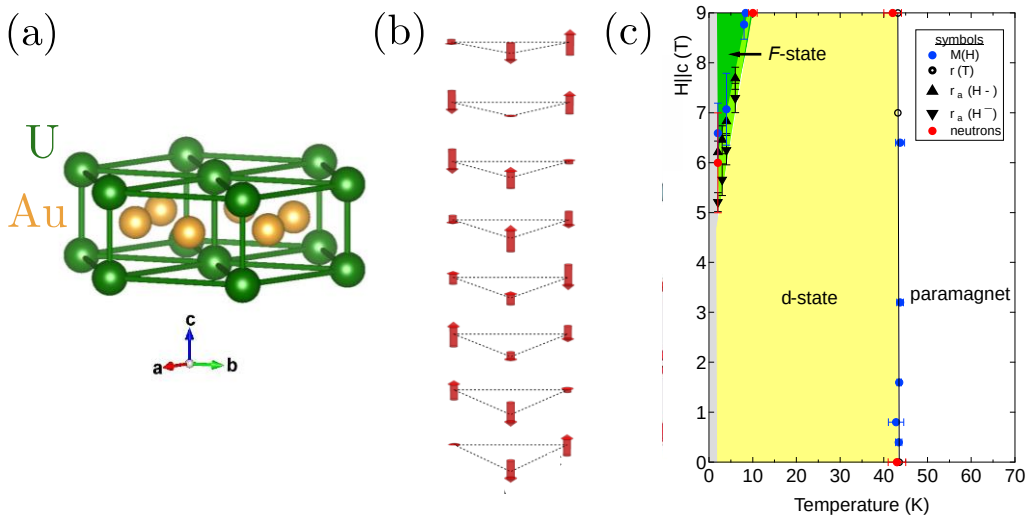

Figure 5.3 *(a) Crystal structure of UAu_2. $a = 4.756$ Å and $c = 3.110$ Å [171]. (b) Magnetic structure of the δ-phase. (c) Field-temperature phase diagram, with the points measured by magnetisation (blue), resistivity (black) and inelastic neutron scattering (red). Taken from [173].*

5.2.2 Results and Discussion

In the following, we present our own specific heat measurements on UAu_2. All measurements were performed on high quality single crystals, grown by the Czochralski method. Thanks go to Chris O'Neill for providing these crystals. Three different samples have been measured in these investigations, which we refer to as samples U1, U2 and U3. We use the residual resistivity ratio (RRR) - for currents parallel to the a-axis - as a a determinant of sample quality. Following [173], a high quality crystal is defined as having RRR$>$ 50.

The high temperature (> 4 K), zero-field specific heat measurements were performed on sample U1. This was an unoriented single crystal, of mass 6.66 mg and RRR ~ 100. These measurements were taken using a Quantum Design Physical Property Measurement System (PPMS). The data was collected by the relaxation time method, and analysed using the 2-τ model, as described in Section 2.3. The experimental setup and method have been detailed in Section 3.3.1, and also [66].

The low temperature specific heat data were instead collected using the bespoke setup described in Section 2.3, and shown in Figure 2.12. The data has been collected by the relaxation time method - also described in detail in Section 2.3 - and analysed by the technique outlined in Appendix B. Throughout all the low temperature measurements, the heater power was set such that $\Delta T \sim 0.005T$. The addenda contribution was subtracted in all cases, with this being at most 5 % of the total contribution, and < 1 % for the majority of the data - as a result of the heavy fermion nature of UAu_2. A typical addenda measurement is shown in Figure 2.16.

The zero-field measurements were performed on both samples samples U2 and U3. For in-field measurements, the field is applied parallel to the sample platform. Samples U2 and U3 were therefore chosen as they each have a large flat face parallel to the axis along which we wished to apply the magnetic field. A flat face is also necessary for a good thermal contact between the sample and sample platform. Sample U2 - of mass 24.06 mg and RRR ~ 100 - was used for the field-along-a measurements, and sample U3 - of mass 28.45 mg and RRR ~ 80 - for fields parallel to c.

Finally, we note that the sample stage thermometer has a magnetoresistance, and is therefore uncalibrated in field. As discussed in Section 2.1, regardless of field, the sample stage temperature is stabilised according to this thermometer. However, for field measurements, the absolute temperature of the sample stage is instead determined by a second thermometer, which is thermally coupled to the stage, but placed in a position of negligible field.

Zero-Field Specific Heat

The high temperature, zero-field specific heat data for UAu_2 is shown in Figure 5.4. The red curve shows the phonon contribution, given by

$$C_{ph} = 9NR\left(\frac{T}{\Theta_D}\right)^3 \int_0^{x_D} \frac{x^4 e^x dx}{(e^x - 1)^2}, \tag{5.12}$$

or the Debye model (discussed in Section 1.3), with $N(= 3)$ the number of atoms in a unit cell, and $\Theta_D = 210$ K (determined from specific heat data extended to a higher temperature than measured here [172]). The residual contribution (given by the green data points) exhibits a broad peak around 40 K, as well as a sharper transition at 43.5 K, clearly due to the antiferromagnetic transition at this temperature. The broader peak may instead be attributed to the crystal field splitting of the uranium $5f$ orbitals, giving a Schottky-type contribution. From the resonant X-ray analysis in Appendix A.2, the uranium atoms in UAu_2 will have a valence of ~ 2.7, or a mix between U^{3+} ($5f^3$, $J = 9/2$) and U^{4+} ($5f^2$, $J = 4$). In a hexagonal environment, this implies a splitting into - respectively - 5 Kramers doublets, or 3 non-Kramers doublets and 3 singlets [174]. The exact Schottky contribution which results from this splitting is therefore complex (derived from Equation C.2). However, an approximate fit to a two-level model - shown in Figure 5.4 - gives the energy scale to be the same order of magnitude as that of the antiferromagnetic transition.

We now turn to the low temperature, zero-field specific heat. This is shown in Figure 5.5, and fit using

$$\frac{C}{T} = A_{nfl} \ln\left(\frac{T}{T^*}\right) + \frac{A_{sch}}{T^3}, \tag{5.13}$$

where the first term is typical of a quantum critical system, and the second approximates a Schottky anomaly. Note, this Schottky contribution only occurs at the lowest temperatures, and is completely separate to the feature used to describe the higher temperature data. The specific heat therefore agrees with the resistivity data (Figure 5.1 (d)), in that UAu_2 exhibits non-Fermi liquid behaviour. However, the resistivity shows a crossover to a T^2-dependence below ~ 200 mK (typical of a Fermi liquid). In order to check for a similar crossover in the specific heat, the Schottky contribution can be subtracted from the data. As shown in Figure 5.5, the residual contribution approximately follows a logarithmic dependence to the lowest temperatures, and therefore shows no evidence for

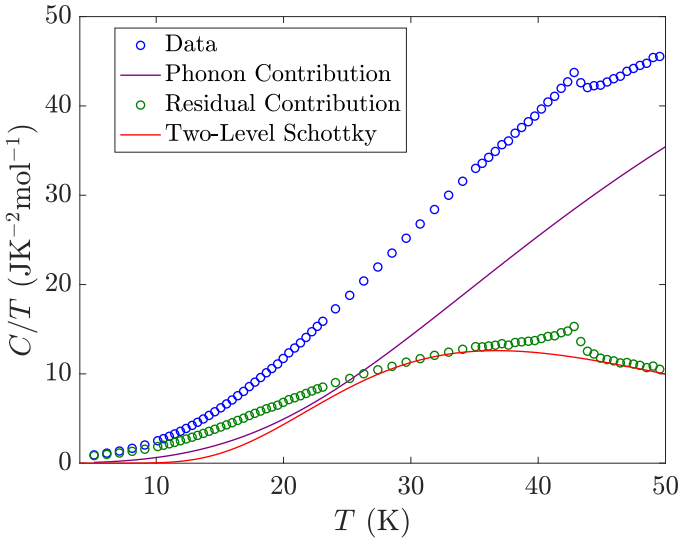

Figure 5.4 *High temperature specific heat of sample U1. The purple line shows a fit to the Debye model, and therefore gives the phonon contribution, which has been subtracted from the data to give a residual contribution (green). The red curve shows a fit to a two-level Schottky model.*

this crossover feature. Obviously the specific heat captures a broader range of excitations than the resistivity, but it seems strange that there would be no hint of a similar crossover.

Regardless, the essential feature is that UAu_2 exhibits non-Fermi liquid behaviour within the antiferromagnetic state. Clearly therefore, this is not due to a proximity to a magnetic quantum critical point, and this 'quantum critical' behaviour is thus distinctly different to that observed in typical heavy fermion systems (discussed in the previous section). Instead, the non-Fermi liquid behaviour must be linked to some other degree of freedom. This idea will be explored alongside the in-field data, which gives further indications as to the origin.

The low temperature Schottky anomaly may be explained as resulting from the interaction between nuclear quadrupole moments and electric field gradients (as discussed in Appendix C). Specifically, the gold nuclear energy levels are split into two doublets, separated by $\sim$ 9 mK - as estimated from band structure calculations [173, 175]. Additionally, there will be a small contribution from the ^{235}U quadrupolar moment (discussed in detail in Section 5.3, for UTe_2). Finally, we note there is a small feature around $\sim$ 450 mK, which rises above

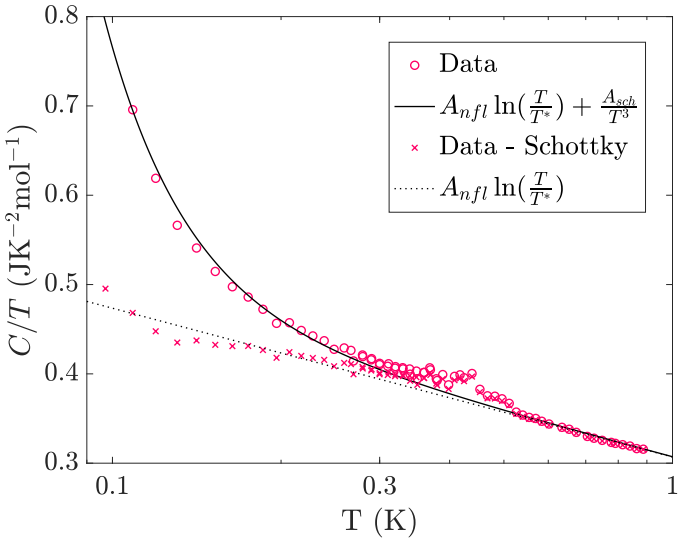

Figure 5.5 *Low temperature specific heat of sample U2. The solid line shows a fit to a quantum critical logarithmic behaviour, plus a low temperature Schottky anomaly (Equation 5.13), whilst the dotted line has this contribution subtracted. The open points show experimental data, whereas the crosses show the data with the calculated Schottky contribution subtracted. Data in the range* $300-600$ *mK was ignored when performing the fits, so as to avoid the feature at* ~ 450 *mK.*

the logarithmic fit. This is only present in the zero-field specific heat data, and the cause is presently unknown. However, the feature shows a slight sample dependence - implying it may scale with the impurity content - and also vanishes with the application of a small field (Figure 5.7). A potential explanation might therefore be the presence of defect moments.

In-Field Specific Heat

The low temperature specific heat data for fields parallel to the a- and c-axis are shown in Figures 5.6 and 5.7 respectively. Clearly there are marked differences upon changing the direction of the applied field. For fields along a, regardless of the strength of the applied field, the data may be adequately fit using Equation 5.13, implying that the non-Fermi liquid behaviour survives to fields up to at least 14 T. The effect of a field is only to shift the magnitude downwards slightly, and also reduce the gradient. For fields along c, there is a similar behaviour at low fields. However, at high fields there appears evidence for the aforementioned transition into the ferrimagnetic state, accompanied by a

switching to Fermi liquid behaviour.

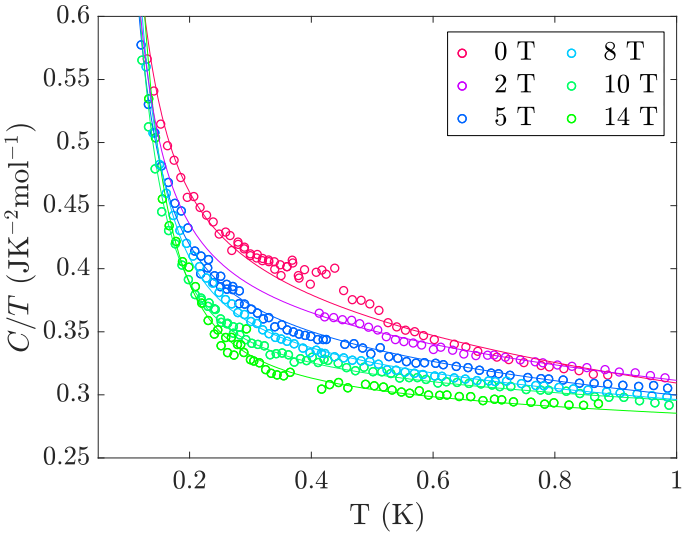

Figure 5.6 *In-field specific heat of sample U2 for fields parallel to the a-axis. The solid lines show fits to a quantum critical behaviour (Equation 5.13).*

Let us first briefly discuss the ferrimagnetic state. Recall, this comprises an $\{\uparrow,\uparrow,\downarrow\}$ configuration on each in-plane triangle, with the moments aligned parallel to the c-axis. It makes sense therefore that the sample should only transition for fields along c. Additionally, as shown in Figure 5.7, the magnitude of the specific heat drops by more than half at the transition. Again this is to be expected, as the moments are significantly more constrained in the ferrimagnetic state, as compared to the incommensurately modulated antiferromagnetic state. Within the ferrimagnetic state, the specific heat follows a Fermi liquid behaviour,

$$\frac{C}{T} = \gamma_N + \frac{A_{sch}}{T^3}, \tag{5.14}$$

where γ_N is the Sommerfeld coefficient. For the 8 T data, $\gamma_N = 136$ mJK^{-2}mol^{-1}; this large value of γ_N is symptomatic of strong electron-electron interactions - typical of heavy fermion materials. Finally, contrasting the 8 and 9 T data reveals that the magnetic state is dependent on the field history. In acquiring the 8 T data, the sample was cooled in field, and thus begins - and remains - in the ferrimagnetic state. Instead, for the 9 T run, the sample was cooled to base temperature in zero field, and then the field was ramped. In this case, the sample remains in the antiferromagnetic state as the field is ramped, before undergoing a ferrimagnetic transition at higher temperatures, as thermal motion disrupts the

antiferromagnetic order.

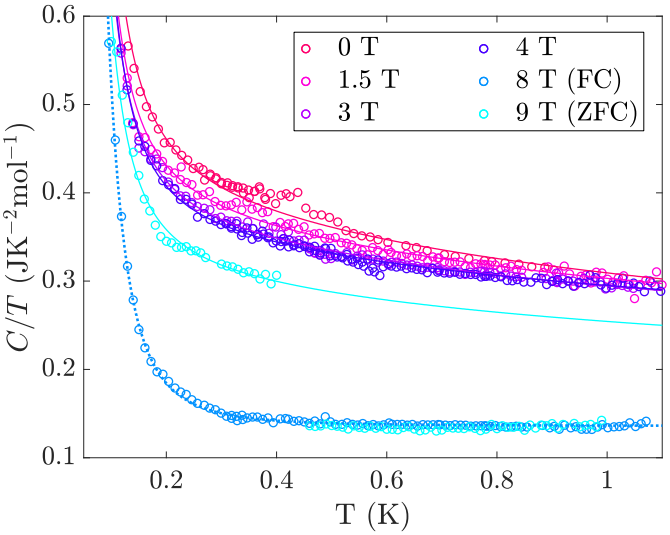

Figure 5.7 *In-field specific heat for sample U3, for fields parallel to the c-axis. The solid lines show fits to a quantum critical behaviour (Equation 5.13), whereas the dotted line shows a fit to a Fermi liquid behaviour (Equation 5.14). All data was taken by field cooling the sample, except for the 9 T run, which was zero-field cooled.*

We now return to consider the origins of the non-Fermi liquid behaviour. From the magnetic field data, we see that:

(i) It is robust to an applied field.

(ii) It is only present within the antiferromagnetic state.

Additionally, the thermal expansion - measured by X-ray diffraction - is proportional to the specific heat at these temperatures [173]. This implies that the Gruneisen parameter, defined by

$$\Gamma \propto \frac{\alpha}{C} \tag{5.15}$$

where α is the volume expansion, will remain constant. This parameter should diverge at a quantum critical point, regardless of origin [176]. This rules out - for example - quantum criticality arising from quadrupolar order, or a valence transition, as the explanation for the non-Fermi liquid behaviour in UAu_2.

An alternative scenario which might produce the observed temperature dependencies is the two-channel Kondo effect [177, 178]. This is simply an extension

of the Kondo effect, wherein the local moment can now equally be screened via two degenerate channels. The result is a ground state where the moment is only partially screened, and a breakdown of Fermi liquid behaviour. Recall from our previous discussion, the single-channel Kondo effect requires a degeneracy at the local moment. Typically this is provided by the degeneracy of the up/down spin configurations of the local moment, and the conduction electrons thus hybridise by inducing fluctuations between these two configurations. In UAu_2, it is instead the crystal field splitting of the U^{4+} nuclear energy levels which provides this degeneracy, and specifically the non-Kramers ground state doublet. The two-channel Kondo effect then arises as the spin up/down conduction electrons interact identically with this doublet. For clarity, this interaction is schematised in Figure 5.8 (a).

In order to understand the logarithmic behaviour of the specific heat, consider the schematic illustrated in Figure 5.8 (b). If the local quadrupolar moment is simultaneously screened by two degenerate channels, the new composite object cannot be 'neutral'. Instead, we will simply have an identical situation, but on a larger length scale [179]. This composite quadrupolar moment can similarly simultaneously interact with the two conduction electron channels, and the process will repeat. Hence, unlike with the single-channel Kondo effect, the degeneracy of the 'impurity' is never lifted. Importantly, this ever-increasing length scale corresponds to an ever-decreasing energy scale ($T_K k_B = \frac{\hbar v_F}{l}$, where v_F is the Fermi velocity). This implies a residual entropy $\frac{R}{2}\log(2)$, inherent to each two-channel Kondo site, and a logarithmically divergent specific heat as $T \to 0$.

Note however, a magnetic field should act to break the degeneracy of the two-channel interaction, at which point the residual entropy will be released on a temperature scale T_s (related to the energy splitting). From Figure 5.7, this is not observed in UAu_2. The crucial feature of UAu_2 is the incommensurate antiferromagnetic order. The energy splitting will be proportional to the *local* field at the uranium site, or the applied field summed with the internal field. Due to the incommensurate order, regardless of field, there will be an almost identical distribution of energy splittings, and thus temperature scales, over all the uranium sites. For this model, the specific heat of an individual site is given

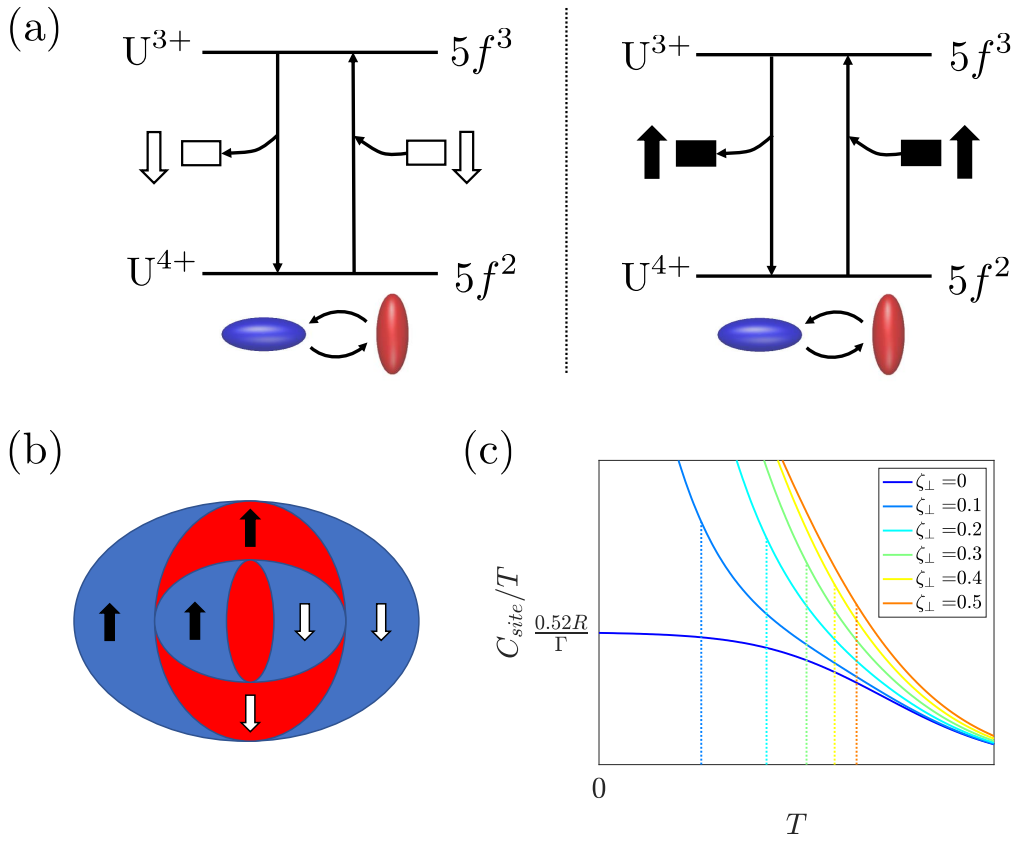

Figure 5.8 *(a) Schematic to show the energy levels of the two-channel Kondo effect in UAu_2. The U^{4+} and U^{3+} are non-Kramers and Kramers ground state doublets respectively, implying the U^{4+} has two degenerate quadrupolar configurations, as schematised by the red and blue spheroids. The black/white areas represent the up/down conduction electron bands. These bands contain both quadrupolar configurations, and can therefore independently hybridise with the U^{4+} level, via the regular Kondo effect. The two-channel Kondo effect then arises due to the two bands (up/down spin) interacting identically and simultaneously with the U^{4+} level. (b) Schematic to illustrate the ever-increasing length scale which results from the simultaneous interaction of the degenerate bands. Each new composite object adds two new conduction electrons, but retains a quadrupolar moment. (c) Plot to show how the specific heat of a single two-channel Kondo site (Equation 5.16) evolves as a function of the energy splitting of the up/down conduction bands, $\zeta_\perp$. The vertical lines show the temperature scale over which the residual entropy $\frac{R}{2}\log(2)$ is released once the bands are no longer degenerate. The temperature is plotted on a logarithmic scale.*

by

$$\frac{C_{site}}{T} = \frac{R\Gamma}{2\pi T^2}\left[1 - \frac{\Gamma}{2\pi T}\psi^{(1)}\left(\frac{1}{2} + \frac{\Gamma}{2\pi T}\right)\right] + \frac{R\Gamma\zeta_\perp^2}{2\pi T^2}\left[1 - \frac{\Gamma\zeta_\perp^2}{2\pi T}\psi^{(1)}\left(\frac{1}{2} + \frac{\Gamma\zeta_\perp^2}{2\pi T}\right)\right], \quad (5.16)$$

where $\psi^{(1)}$ is the first derivative of the Digamma function, Γ is the energy cut-off and $\zeta_\perp$ is the energy splitting of the ideally degenerate levels [173]. The behaviour of this function - and the energy scale over which the residual entropy is released - is illustrated in Figure 5.8 (c) as a function of $\zeta_\perp$. The specific heat for the entire material may then be calculated by integrating over all the uranium sites, each of which will have a different local field and therefore energy scale. This indeed gives the observed logarithmic dependence [173]. Finally, this interpretation also explains why the non-Fermi liquid behaviour is not observed within the ferrimagnetic state - without the incommensurate order, there are no sites appropriately tuned to host the two-channel Kondo effect.

As is clear from Figures 5.6 and 5.7, although the non-Fermi liquid behaviour survives in field, the data is not identical. Figure 5.9 shows how the coefficients A_{nfl} and A_{sch} vary as a function of field. The former decreases in magnitude as the applied field increases, and appears to be tending towards zero. This is readily explained within the above framework, as there becomes a lower density of appropriately tuned sites - and therefore a smaller contribution to the specific heat - as the field is increased. The Schottky coefficient instead increases as a function of field, approximately linearly. This is also straightforwardly explained, as the field further splits the gold quadrupolar energy levels [175], which necessarily leads to a larger Schottky contribution.

Finally, we briefly mention that - under this interpretation - the two-channel Kondo effect should result in a change of the valence state of the uranium atoms, as the U^{4+} and U^{3+} configurations are mixed. This was investigated via resonant X-ray scattering, as detailed in Appendix A.2, but not observed. Future investigations are planned to repeat this experiment to a greater degree of accuracy.

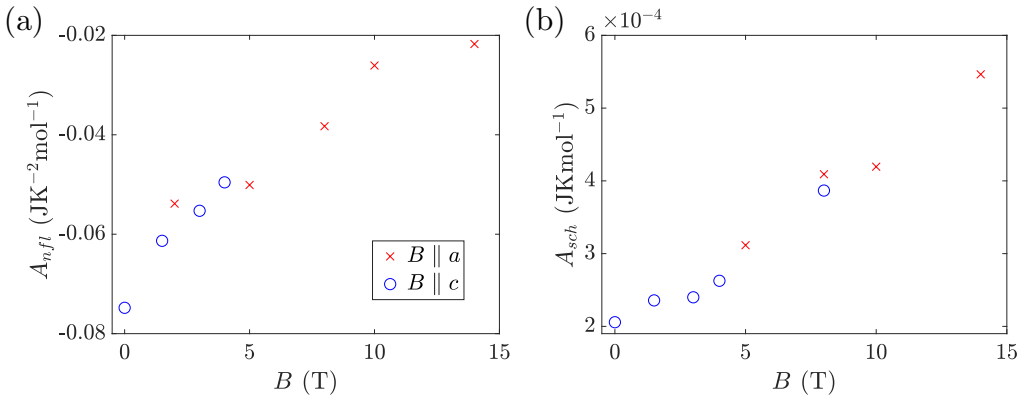

Figure 5.9 *Coefficients from those fits shown in Figures 5.6 (red crosses) and 5.7 (blue circles), plotted as a function of field. (a) A_{nfl} coefficient from quantum critical δ-phase fit (Equation 5.13). (b) A_{sch}, strength of the Schottky anomaly, common to all data.*

5.2.3 Summary

We have investigated the non-Fermi liquid behaviour of UAu_2 by measurements of the low temperature specific heat. This has revealed that (i) non-Fermi liquid behaviour exists within the antiferromagnetically ordered phase, (ii) this behaviour survives in field, but (iii) is destroyed upon transition to the ferrimagnetic state. From all this, the most likely explanation for the logarithmic dependence of the specific heat appears to be the two-channel Kondo effect. In UAu_2, the required degeneracy of the two-channel interaction is satisfied only at some sites, as a result of the addition of the applied field and incommensurate magnetism. This ties the non-Fermi liquid behaviour to the antiferromagnetic state, and thus adequately accounts for all of the observed behaviour. However, there are still some issues to resolve, such as why the low temperature crossover to Fermi liquid behaviour observed in resistivity, is not observed in other measurements, or why the two-channel Kondo state is not accompanied by a change in the valence of the uranium ions.

5.3 UTe_2

UTe_2 is a recent addition to the family of heavy fermion superconductors, and arguably the most spectacular example of unconventional superconductivity to date. The material is paramagnetic, but closely related to the ferromagnetic

superconductors (UGe_2 [180], URhGe [181] and UCoGe [182]), in which ferromagnetic spin fluctuations are widely believed to mediate the superconductivity. Similar to these materials, UTe_2 also exhibits field re-entrant superconductivity, albeit at a significantly larger field [183]. Further, the material likely plays host to equal spin Cooper pairs [184, 185]. This has led some to suggest the material might realise a topological form of superconductivity, and indeed, one STM study has reported evidence for chiral modes existing inside the superconducting gap [29].

However, this whirlwind of activity has been accompanied by some controversy surrounding the low temperature behaviour of the superconducting state. To this point, the majority of specific heat studies observe a residual Sommerfeld coefficient [27, 29, 186], γ^*, which has been interpreted by many as evidence for non-unitary pairing [184]. The magnitude of this residual contribution is typically measured to be approximately half of the normal state value, γ_N, leading some to further suggest that only one of the two spin directions is paired in the superconducting state [185]. More recent investigations additionally report an upturn of C/T at the lowest temperatures, with the situation being further confused by different studies observing a different form of upturn [187, 188].

Clearly therefore, this low temperature feature must be understood in order to determine whether a residual Sommerfeld coefficient is present, and by extension, whether it is worth entertaining the idea that only one spin direction is paired. However, given the disparate behaviour observed by different groups, it is perhaps more important to establish the extent to which sample quality, or composition, impacts the physics.

5.3.1 Previous Work

UTe_2 crystallises in an orthorhombic, centrosymmetric structure, with space group *Immm* (No.71, D_{2h}) [189, 190]. As shown in Figure 5.10 (a), the Uranium atoms form chains parallel to the a-axis, spaced 3.78 Å apart. The structural anisotropy is reflected in the low temperature magnetic susceptibility (shown in Figure 5.10 (b) [191]), which is over 3 times larger for fields along the a-axis - as compared to the susceptibility for fields along the perpendicular axes. The resistivity data displays a peak at some intermediate temperature - dependent on current direction - with a T^2 dependence below ~ 4 K [185] (Figure 5.1). Both of these features are indicators of Kondo physics (as discussed in Section 5.1).

Finally, there is no evidence for any zero-field magnetic transitions. Thus, the normal-state picture of UTe_2 is that of a heavy fermion paramagnet, which exhibits Fermi liquid behaviour at the lowest temperatures and has a magnetic easy a-axis.

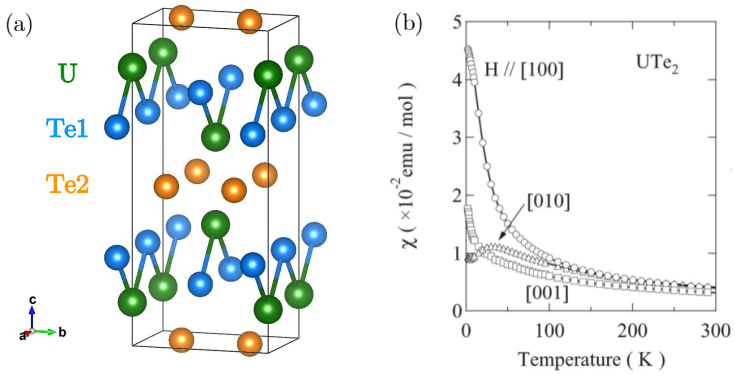

Figure 5.10 *(a) Crystal structure of UTe_2, with the cuboid indicating the unit cell and lattice parameters $a = 4.161$ Å, $b = 6.122$ Å and $c = 13.955$ Å. (b) Magnetic susceptibility for the three principle axes, plotted as a function of temperature. Taken from [191].*

The above characterisation would mark UTe_2 as a fairly typical heavy fermion material. However, subsequent research to lower temperatures identified a superconducting transition at $\sim$ 1.6 K [184]. Thus followed a number of remarkable results, with perhaps the most spectacular being field re-entrant superconductivity to fields above 65 T [183]. This is far larger than the Pauli limit ($H_P = 1.84T_c$ [192]), which strongly argues against the superconductivity in UTe_2 being conventional BCS type. Further support for unconventional superconductivity comes from NMR data - which show that the value of the ^{125}Te Knight shift remains constant below T_c [184] - and the measured heat capacity - which exhibits a power law behaviour within the superconducting state [184], in contrast to the exponential temperature-dependence expected of a BCS superconductor (Section 1.3). The heat capacity data also exhibits a residual component as $T \to 0$ K. This feature is highly unconventional, but also somewhat controversial, and will be discussed alongside our own results in the following section.

Unconventional superconductivity further suggests that there should be an unconventional pairing mechanism. For UTe_2 - as shown in the superconducting phase diagram in Figure 5.11 - re-entrant superconductivity only occurs when

there is some component of the field perpendicular to the magnetic easy axis (a metamagnetic transition switches this to the b-axis at high fields). This would suggest that the re-entrant phases are linked to strong spin fluctuations transverse to the easy axis of the magnetic moment. The idea of magnetic fluctuations having a role to play is further supported by μSR data [122], which show evidence for magnetic fluctuations within the superconducting state. Finally, UTe_2 displays many similarities to - and is widely regarded as the paramagnetic end member of - the family of uranium-based ferromagnetic superconductors [187], UGe_2 [180], URhGe [181] and UCoGe [182]. In these materials, ferromagnetic spin fluctuations are believed to mediate superconductivity [123]. As such, the same can probably be said for UTe_2.

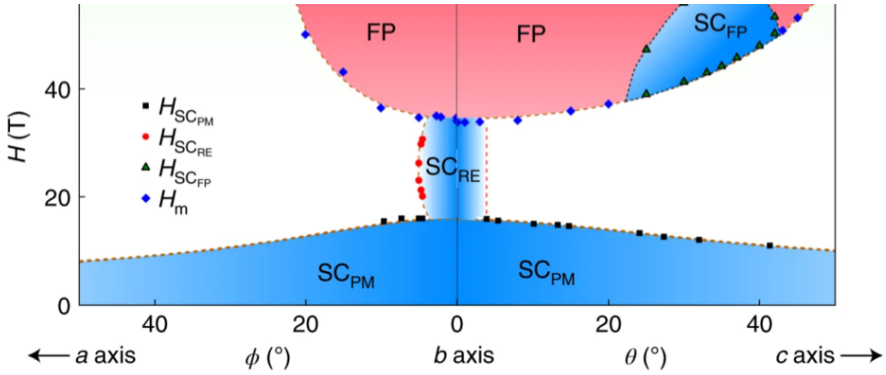

Figure 5.11 *Superconducting phase diagram for UTe_2, plotted as a function of field strength and field angle, with temperature kept constant at 0.35 K. The labels PM, RE, m and FP stand for paramagnetic, re-entrant, metamagnetic and field-polarised, respectively. Taken from [193].*

The question then turns to the exact form of the superconducting gap. As described in Section 1.2 - wherein UTe_2 is treated as an example - the point group D_{2h} corresponds to just 8 irreducible representations for the superconducting order parameter (given in Table 1.2), all of which are single component. Various experimental techniques suggest the superconducting gap function should contain point nodes [29, 187, 188] - this leaves just three possible spin-triplet representations. However, recent polar Kerr effect measurements [194] would imply that the superconducting phase breaks time-reversal symmetry, and therefore requires two co-existent irreducible representations. Further, studies have revealed a second superconducting phase under pressure [27, 193], suggesting that two separate, single component - and accidentally degenerate - phases are split by the application of pressure. Additional support for this theory comes

from the observation of a split transition at ambient pressure in some samples [194]. However, the situation is muddied by various groups - including ourselves - being unable to detect this split transition, despite investigating a multitude of samples [188]. This appears to hint at the theme of this work - the extreme sensitivity of experimental observations to the sample under investigation.

5.3.2 Results and Discussion

Sample Synthesis and Characterisation

In order to investigate the composition dependence of the superconducting properties of UTe_2, it was necessary to grow high quality single crystals of different stoichiometries. Samples were grown via the chemical vapour transport (CVT) method, with the uranium having been electrochemically etched to remove surface oxide, and iodine as the transport reagent. Growths containing three different starting ratios of uranium to tellurium were attempted, as detailed in Table 5.1. Growths A and B were intended to replicate those previous studies which had produced, respectively, superconducting [184] and non-superconducting [191] samples of UTe_2. Growth C used an intermediate ratio for comparison. Finally, all samples were identified as having the correct crystal structure by Laue X-ray diffraction. Thanks go to Callum Stevens for the growth and characterisation of all samples in this investigation.

Growth/Study	CVT Te/U atomic ratio	Range of EDX Te/U atomic ratio	T_c (K)
[184]	1.5	-	1.6
A	1.71	1.46 - 1.50	1.74
C	1.85	1.72 - 1.87	2.00
[191]	2	-	No SC reported
B	2.14	1.79 - 2.06	< 50 mK if present

Table 5.1 *Growth conditions and average superconducting transition temperature for samples from growths A, B and C, as well as from [191] and [184] (discussed in the text). Also included for our samples is the range of Te/U atomic ratio measured by EDX. Note, the rows have been ordered by starting ratio of Te/U for the CVT.*

In order to characterise each of the growths, multiple samples from each were investigated using energy dispersive X-ray analysis (EDX). This technique involves focusing a beam of X-rays (10 kV, I=500 pA in this case) onto the

sample and then measuring the characteristic emission, from which it is possible to identify the composition and homogeneity variations. The measurements were carried out on a Zeiss Crossbeam 550 FIB/SEM from Quorum Technologies, and the results have been recorded in Table 5.1. Also included in Table 5.1 is the superconducting transition temperature as measured by zero-field resistivity. Regardless of sample, the behaviour of the resistivity is broadly similar, with a maximum at some intermediate temperature, falling with a T^2, Fermi liquid-like, dependence at the lowest temperatures; this is typical of a Kondo lattice system. This behaviour is shown in Figure 5.1, and appears similar to that observed in previous studies [184].

Clearly from Table 5.1, the superconducting transition temperature is strongly influenced by the growth details. This trend is further highlighted by including the data from two previous studies:

- [191] - a study that started with a stoichiometric Te/U ratio of 2. This is typical of earlier studies [189, 190], none of which report superconductivity.
- [184] - the first study to report superconductivity. Almost all subsequent studies which report on the superconducting properties of UTe_2 follow the growth method outlined in this study, and therefore start with a Te/U ratio of 1.5.

At first glance, it would appear the superconducting transition temperature rises with Te content, before being dramatically suppressed at higher composition ratios. This idea will be explored in the following sections.

Specific Heat

As mentioned previously, studies fail to agree on the low temperature specific heat behaviour of UTe_2 [184, 185, 187]. Therefore, motivated by the expectation that this disparate behaviour may have some composition dependence, the specific heat was measured for three samples from growth C (see Table 5.1), and compared to previous studies. These samples have been labelled C5 - an unoriented single crystal - and C6 and C7 - spark-cut, oriented single crystals. All data were taken using the dilution refrigerator experimental apparatus and procedure described in Section 2.3, and analysed using the procedure outlined in Appendix B. The addenda contribution has been subtracted in all cases, and was less than 25%

of the total magnitude at the lowest temperatures, falling to less than 2% above 1 K.

Shown in Figure 5.12 is the zero-field specific heat data for samples C5, C6 and C7. The data shows small differences at the lowest temperature, but otherwise, all samples exhibit similar behaviour and have a superconducting transition temperature of ~ 1.77 K. This is the largest bulk T_c reported in uranium telluride to date. Note however, this is slightly lower than the transition temperature measured by resistivity ($T_c = 2.00$ K, for sample C5). Given the aforementioned dependence of the superconducting transition temperature on composition, this may be explained if a part of the sample - such as a particular surface - has a slightly different stoichiometry compared to the bulk. Based on our EDX data, this would be consistent with a higher Te content of surfaces grown in contact with the inner quartz tube wall. This suggests that bulk samples with T_c as high as 2 K may be possible with increased Te content, before reaching the value at which superconductivity is suppressed.

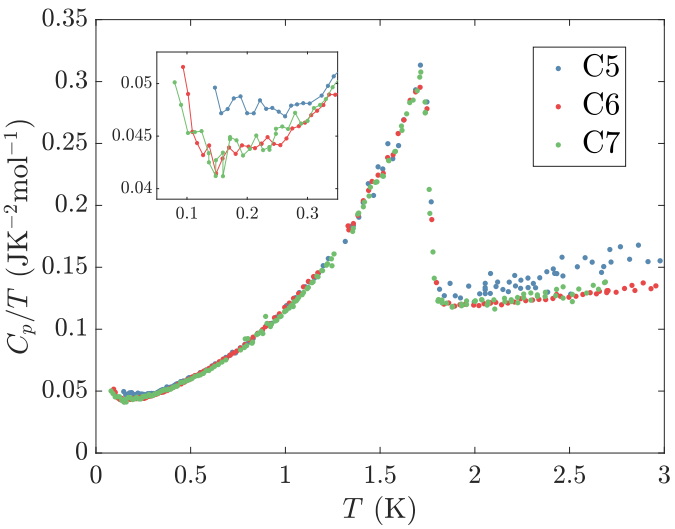

Figure 5.12 *Zero-field specific heat, plotted as a function of temperature for samples C5, C6 and C7. The inset shows the low temperature behaviour.*

In order to make a quantifiable comparison between the different samples (and

with previous studies), the function

$$\frac{C}{T} = \beta T^2 + \left[\frac{1}{2} + \frac{1}{2}\tanh\left(\frac{T-T_c}{\delta}\right)\right]\gamma_N - \left[\frac{1}{2}\tanh\left(\frac{T-T_c}{\delta}\right) - \frac{1}{2}\right](\alpha T^{\lambda} + \gamma^*) + \frac{A_{sch}}{T^3} \quad (5.17)$$

was used to describe the data. This function is purely phenomenological, but useful in extracting the parameters T_c, ΔT_c (the 10-90% transition width, $\Delta T_c = 2.2\delta$) and γ_N (the normal state Sommerfeld coefficient). The expression also provides an estimate of the phonon contribution (βT^2), which is subtracted to give the electronic heat capacity. In addition, terms have been included to account for the previously reported unconventional superconductivity (αT^{λ}), residual Sommerfeld coefficient (γ^*) and Schottky anomaly (A_{sch}), all of which will be discussed below. Shown in Figure 5.13 is the fit for sample C6, with the curves used to estimate the normal state (γ_N) and residual (γ^*) Sommerfeld coefficients included for reference. Also included is the size of the jump at the superconducting transition.

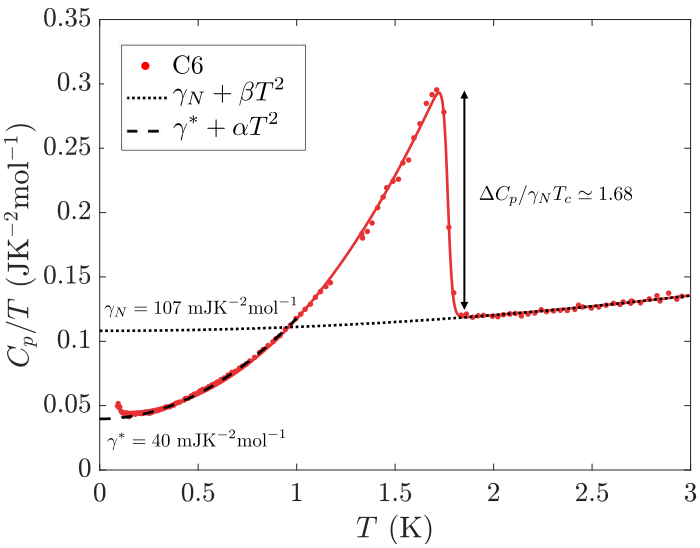

Figure 5.13 *Sample C6 specific heat data and fit to Equation 5.17 (solid line). Also shown is the low temperature (< 1 K) fit to Equation 5.20 minus the Schottky contribution (dashed line) - giving the residual term γ^* - and the normal state contribution extrapolated to zero temperature - giving the Sommerfeld coefficient γ_N.*

Figure 5.14 (a) shows similar fits to the zero-field specific heat data from previous studies [185–188], in order to draw comparison to our samples. The parameters

extracted from these fits are collated in Table 5.2. The data from [27, 29, 184] were also analysed in a similar way, but have been omitted from the figure for clarity. From Figure 5.14 (a) (and Table 5.2), three things are immediately obvious: our growth C samples (i) have the largest T_c, (ii) show the largest jump at the superconducting transition, and (iii) have the smallest Sommerfeld coefficient of any study. Whilst these factors are often linked to sample quality and homogeneity, it is clear that these significant discrepancies are down to differences in stoichiometry. This is most evident from the behaviour within the superconducting state, where the data from our samples lie on a separate curve to all the others, which they share regardless of transition temperature. Note however, in calculating the specific heat, the average stoichiometry from the EDX measurements was taken ($UTe_{1.77}$). Therefore, in order to demonstrate that the observed difference in superconducting behaviour is not an artefact of this normalisation, the data has also been compared after normalising to the normal state Sommerfeld coefficient. This is shown in the inset of Figure 5.14 (a).

Let us now consider the low temperature behaviour, which, as shown in Figure 5.14 (b), varies between different investigations. Previous specific heat studies can be divided into two categories:

(A) Those which do not measure low enough in temperature to see an upturn [27, 29, 184, 186]. The majority fit the lowest temperature data using

$$\frac{C}{T} = \alpha T^2 + \gamma^*, \tag{5.18}$$

which leads to the inevitable conclusion of a residual contribution γ^*.

(B) Those which do go low enough in temperature to see an upturn [185, 187, 188]. In one study [187], this behaviour is described by a 'divergent quantum-critical contribution'

$$\frac{C}{T} = \alpha T^2 + A_{div} T^{-m}, \tag{5.19}$$

where $m \sim 0.33$, such that a residual term γ^* is unnecessary.

Our data falls into the second category, in that there is an upturn, however this upturn is found to be modelled better using

$$\frac{C}{T} = \alpha T^2 + \gamma^* + \frac{A_{sch}}{T^3}. \tag{5.20}$$

Importantly, we find that in order to fit the data from samples C5, C6 and C7

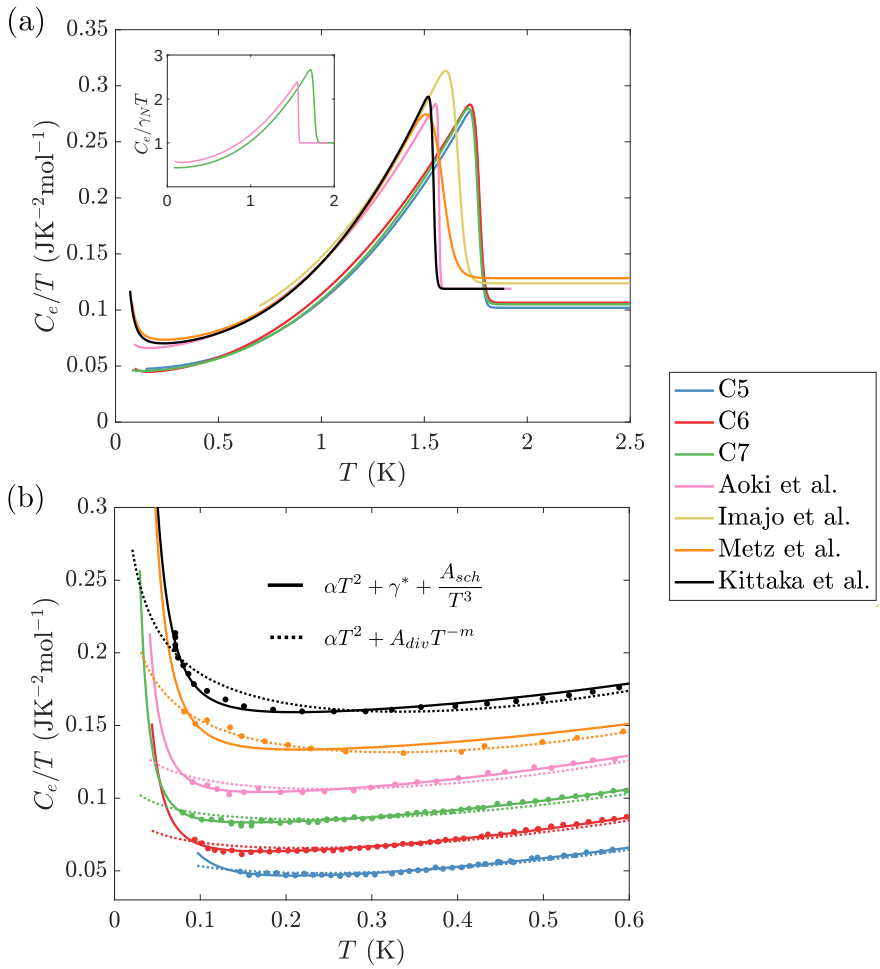

Figure 5.14 *(a) Fits of the data from samples C5, C6 and C7, as well as the zero-field specific heat from previous studies ([185], [186], [187] and [188] in the order listed in the legend), to Equation 5.17, with the phonon contribution subtracted. The extracted parameters are listed for comparison in Table 5.2. The inset shows a comparison of sample C7 to that from [185], both normalised to their respective normal state Sommerfeld coefficient. (b) Low temperature fits to a Schottky model (solid lines) and a quantum critical model (dotted lines), described in the text. The data sets have been offset for clarity.*

adequately, we also require a residual term γ^*. It is worth noting that, as discussed in Section 1.3, the goodness of the T^2 fit in all cases is taken to be evidence for point nodes in the superconducting gap.

In order to draw comparison to previous studies, shown in Figure 5.14 (b) are all those data sets (including ours) which extend low enough in temperature to see an upturn. Also shown are fits to Equation 5.19 (with $0 < m < 1$) and

Equation 5.20, only including the low temperature ($T < 1$ K) data. Clearly, one set of data [187] is described better by the quantum critical scenario of Equation 5.19. This quantum critical divergence perhaps implies that the material is being tuned about a ferromagnetic quantum critical point (as is present in the uranium based ferromagnetic superconductors [195]). However, as is clear from Table 5.2, the value of T_c observed in [187] is not near an extremum. This argues against interpreting the low temperature specific heat data of this one study as evidence for quantum critical fluctuations. Further, no such behaviour was observed in samples with almost the same T_c, and sharper transitions [185, 188]. The comparatively broad superconducting transition possibly suggests a range of stoichiometry.

	C5	C6	C7	[184]	[185]	[185]	[29]	[27]	[186]	[187]	[188]
T_c (K)	1.77	1.77	1.76	1.64	1.57	1.46	1.53	1.45	1.66	1.58	1.54
ΔT_c (K)	0.05	0.05	0.05	0.05	0.02	0.05	0.07	0.04	0.06	0.12	0.03
γ_N (mJK^{-2}mol^{-1})	102	107	105	112	119	122	132	122	124	128	119
$\Delta C/\gamma_N T_c$	1.86	1.68	1.81	1.41	1.39	1.11	1.26	1.15	1.63	1.16	1.58
A_{sch} (μJKmol^{-1})	-	71 ± 23	47 ± 21	-	78 ± 29	-	-	-	-	*	191 ± 18
γ^* (mJK^{-2}mol^{-1})	42	40	40	55	60	70	59	68	52	68	63
γ^*/γ_N	0.41	0.37	0.38	0.46	0.51	0.57	0.45	0.55	0.42	0.53	0.53

Table 5.2 *Parameters from fits to Equations 5.17 and 5.20 (see Figures 5.14 (a) and 5.14 (b)). The Schottky coefficient (A_{sch}) is only listed for those data sets which extend below 100 mK. The error corresponds to the A_{sch} at which χ^2 has reached twice its minimum value. * indicates the fit was not appropriate, as shown in Figure 5.14 (b).*

For the remainder of studies - [185, 186, 188] and our growth C samples - the low temperature specific heat data is described reasonably well by Equation 5.20, and the observed upturn might therefore be attributed to a Schottky anomaly (Appendix C). The simplest model to give such a contribution is that of two non-degenerate energy levels, for which, as given in Equation 5.20,

$$A_{sch} = nR\Delta^2 \frac{e^{-\Delta/T}}{(1+e^{-\Delta/T})^2}, \tag{5.21}$$

where R is the gas constant, n the density of Schottky centres per mole of $UTe_{1.77}$ and Δ the energy splitting. Figure 5.15 shows combinations of the two parameters in Equation 5.21 consistent with fitting the low temperature specific heat data. From Figure 5.15, it is clear that

(i) There is significant variation between samples which exhibit similar behaviour close to T_c ([185] and [188]), suggesting that the Schottky anomaly is uncorrelated with stoichiometry.

(ii) Only a small concentration of Schottky centres is required to give a reasonable energy splitting

One potential explanation is therefore that the Schottky contribution is associated with defects that are not directly correlated with stoichiometry, although it seems coincidental that a defect should give rise to such an appropriate energy splitting.

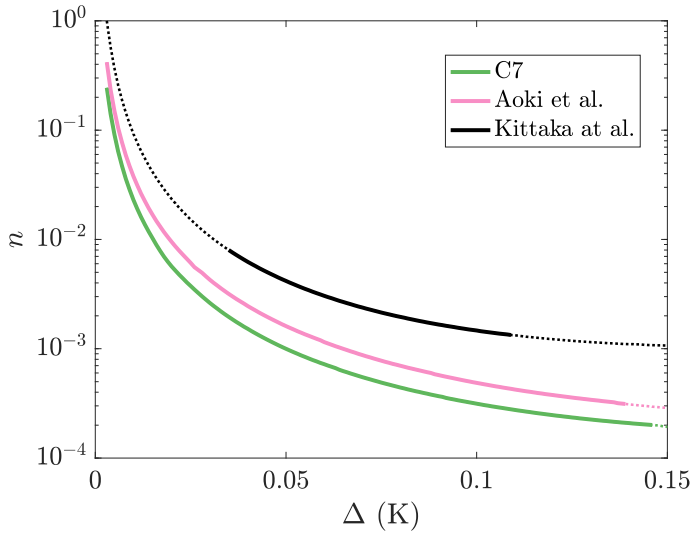

Figure 5.15 *The relation between the two free parameters in the expression for the Schottky anomaly (Equation 5.21), consistent with the low temperature specific heat data of Figure 5.14 (b). Dotted lines correspond to χ^2 10% larger than its minimum value; note the expression in Equation 5.21 gives a peak at $T \sim 0.42\Delta$ K. The other studies are [185] and [188], in the order listed in the legend.*

A second, arguably more probable, explanation for the Schottky anomaly is the interaction of a nuclear quadrupole moment with a crystalline electric field gradient [196]. For such a contribution,

$$A_{sch} = \frac{R}{40}\frac{(I+1)(2I+3)}{2I(2I-1)}\left[\frac{e^2qQ}{k_B}\right]^2, \tag{5.22}$$

where e^2qQ is the quadrupolar coupling constant, and I is the spin of the atomic nucleus (this expression is derived in Appendix C). In this compound, ^{235}U is the only sufficiently abundant isotope to possess a quadrupole moment. The total energy splitting for a spin-$\frac{7}{2}$ nucleus is given by

$$\Delta E = |E_{Q\ \pm 7/2} - E_{Q\ \pm 1/2}| = \frac{3e^2qQ}{7}. \tag{5.23}$$

Therefore, by estimating the quadrupolar coupling constant from the specific heat data, the energy splitting could be calculated. For our samples, assuming an abundance of 0.2 % (for depleted uranium), the measured Schottky coefficients correspond to an energy splitting of approximately 50 mK. This value is in the same range as that observed in other materials, such as UO_2 [197], and importantly, matches the observed upturn reasonably well. Further, the significantly larger A_{sch} in the specific heat data of [188] might then be explained by the variation in the abundance of ^{235}U. If this study were to have used natural uranium (with a ^{235}U abundance of 0.7 %), the Schottky term would be expected to be 3-4 times larger, as is observed.

For all data sets, the residual contribution γ^* has been extracted by subtracting the Schottky contribution and then extrapolating to zero temperature - this is exemplified in Figure 5.13 for sample C6. Importantly, all the data sets (except [187]) require the inclusion of this residual term in order to be fit adequately. The residual term has been included in Table 5.2, alongside the ratio γ^*/γ_N, which is smaller for our growth C samples than any previous study. Furthermore, as shown in Figure 5.16 (a), this ratio appears to be negatively correlated with the superconducting transition temperature. Previous studies had measured this ratio to be approximately 0.5, and interpreted this as evidence for non-unitary pairing [184], with some going so far as to suggest that only one of the two spin directions is paired in the superconducting state [185]. The fact that γ^*/γ_N is significantly lower than 0.5 in our growth C samples, and further, that there appears to be a correlation between γ^*/γ_N and T_c, argues against this interpretation. Rather, our EDX data (Table 5.1) would suggest that both of these effects are linked to composition, and that going from left to right in Figure 5.16 (a) should correspond to increasing Te content, although there is no published data on the actual Te content for those crystals grown and studied by others.

This interpretation thus leads to the conclusion that all samples of UTe_2 which show superconductivity are deficient in Te, and further, that the superconducting properties vary as a function of the extent of this deficiency. Arguably, this is supported by the negative correlation between the residual Sommerfeld coefficient and T_c (Figure 5.16 (a)) - something which has been observed in other unconventional superconductors, namely UPt_3 [116] and $CeCoIn_5$ [198], and linked to the density of defects. In these materials, scattering from point-like defects acts to broaden the nodal features in the superconducting gap, resulting

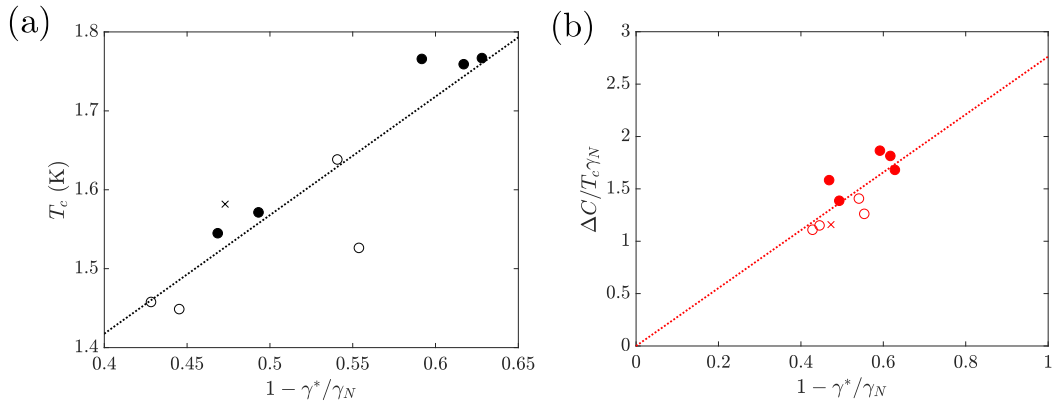

Figure 5.16 *The dependence of (a) the superconducting transition temperature and (b) the normalised heat capacity jump on $1-\gamma^*/\gamma_N$, where γ^*/γ_N is the ratio of residual and normal state Sommerfeld heat capacity coefficients. Data have been taken from Table 5.2. An open (filled) point implies the lowest temperature measured was above (below) 150 mK. Crosses represent the data from [187].*

in a residual normal-state-like density of states [38]. The same interpretation may be valid for UTe_2, however this has to be consistent with the sharp X-ray Laue diffraction patterns, absence of precipitates in the EDX studies and sharp superconducting specific heat transitions. For example, the latter of these would require the defect density to remain uniform over length scales larger than the coherence length.

What is perhaps more surprising is that which is implied by the resistivity measurements (Table 5.1) - that the superconducting transition is suppressed completely above some critical Te content. This suggests either the presence of an as yet unidentified competing phase or that Te deficiency plays some additional role in bringing about the superconductivity. A previous observation of a low temperature structural change in the stoichiometric material [190], not seen in superconducting samples [199], may be relevant to this.

One final point to make from a comparison with previous studies is the correlation between the jump in the specific heat at the superconducting transition ($\Delta C/\gamma_N T_c$) and the temperature of this transition. This is made clear in Figure 5.16 (b). The simplest way to link this jump to the ratio γ^*/γ_N is to consider that a fraction of the sample is superconducting, while a fraction remains

in the normal state. This implies

$$\frac{\Delta C}{\gamma_N T_c} = \left(1 - \frac{\gamma^*}{\gamma_N}\right) a, \tag{5.24}$$

where $a = 1.43$ for BCS superconductivity [37], with higher values possible for strong coupling. As shown in Figure 5.16 (b), the existing data is adequately described by this relation with $a = 2.76$, which would indicate strong coupling. This analysis is clearly over-simplistic, and more information on the origin of superconductivity, γ^* and the metallurgy of UTe_2 are required to make further progress.

One previous study claims to have observed a split transition at ambient pressure [194]. This is potentially related to the multiple superconducting phases observed in pressure studies [27]. In order to test for this, the data points at the transition have been analysed the 'large pulse method' [64], as described in Section 2.3. This showed no evidence for a split transition, in agreement with that reported by [188]. This again appears to be a sample dependent feature - based on our findings, the reported double transition might be attributed to the presence of two distinct composition ratios.

Finally, we briefly note that regardless of interpretation, the entropy balance between the normal and superconducting states,

$$\frac{\int_0^{T_c} \frac{C_e}{T} dT}{\int_0^{T_c} \gamma_N dT} = 1, \tag{5.25}$$

should be satisfied, where C_e is the electronic contribution to the specific heat. This calculation is visualised in Figure 5.17. The normal state contribution is assumed to be given by the Sommerfeld coefficient extrapolated to zero, whereas the superconducting contribution is given by

$$\frac{C_e}{T} = \frac{C}{T} - \beta T^2 - \frac{A_{sch}}{T^3}. \tag{5.26}$$

For the sample C6 data, we calculate the above ratio to be 1.11±0.02. If instead we subtract the residual contribution γ^* from both the normal and superconducting state contributions, the ratio increases to 1.17±0.03. This discrepancy potentially arises due to a slight increase in the normal state specific heat at lower temperatures. Indeed, this slight increase has been observed with in-field (7 T $\parallel a$) - and therefore normal state - specific heat data [188].

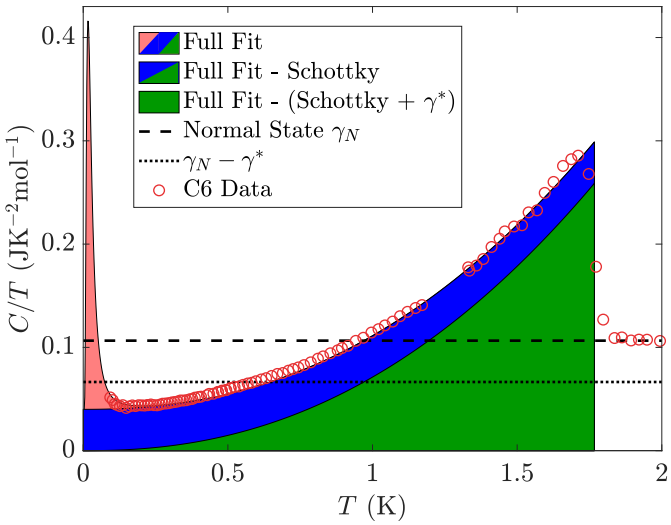

Figure 5.17 *Entropy balance calculation illustrated for the sample C6 data. The full fit is given by the superconducting portion of Equation 5.17.*

5.3.3 Summary

We have investigated how the superconducting properties of UTe_2 vary with composition. By adjusting the elemental ratios in the CVT growths, we have produced samples which exhibit markedly different properties. In growths A and B, we have, respectively, reproduced the non-superconducting and $T_c \sim 1.6$ K samples investigated previously by other groups [184, 191]. In growth C - comprising an intermediate stoichiometry - we have observed the largest superconducting transition temperature of any uranium telluride compound to date.

Motivated by this, we have measured the specific heat of three samples from growth C, all of which show broadly similar behaviour. These samples have the largest superconducting jump, and smallest residual Sommerfeld coefficient, of any reported thus far. A quantitative comparison against previous studies further reveals that the superconducting transition temperature - and the specific heat jump - are negatively correlated with the residual Sommerfeld coefficient. This argues strongly against this feature being intrinsic, and specifically, against only one of the two spin directions being paired in the superconducting state. Finally, we have demonstrated that the observed low temperature Schottky anomaly may be adequately explained as resulting from the ^{235}U quadrupolar moment.

Chapter 6

Conclusions

This work has primarily involved the development of experimental apparatus to measure the low-temperature thermal Hall effect - which has recently emerged as a powerful probe of charge-neutral, topologically non-trivial systems. The signatures of topology are often faint, and these measurements therefore call for extreme sensitivity. Additionally, the two materials under investigation have each required a different setup, optimised to be effective over different temperature ranges. As a result, we now have the capability to measure the thermal Hall angle to a precision of better than 10^{-3} rad, over three decades in temperature.

This work has also involved measurements of the specific heat of various materials. The heat capacity is the most fundamental thermodynamic property, and low temperature measurements are particularly important in revealing the properties of unconventional superconductors, or Kondo systems inside the coherent regime. In this work, we have made significant improvements to a bespoke heat capacity stage - capable of measurements down to mK temperatures - in order to characterise both types of material.

Summary of Main Findings

$SrCu_2(BO_3)_2$ - Theoretical work had suggested the triplet excitations (triplons) in $SrCu_2(BO_3)_2$ should form topologically non-trivial bands, and therefore manifest as an experimentally detectable thermal Hall effect. However, within our experimental resolution, no such signal was observed. This is potentially a

result of the inhibitory effect of triplon-triplon interactions - the theory relies on these interactions being negligible, such that the triplon number is conserved and the edge states remain dissipationless. Our results would suggest that - in the temperature range under investigation - this is not a valid approximation. Additionally - as a proof of concept - we were able to detect a thermal Hall signal in $Lu_2V_2O_7$ using an identical experimental setup. This is a material which has previously been demonstrated to exhibit a thermal Hall effect of a similar magnitude to that which was predicted to occur for $SrCu_2(BO_3)_2$.

UPt_3 - There is growing evidence to suggest that the superconducting B-phase of UPt_3 should be chiral. Various theories therefore predict that this phase should host a thermal Hall effect. Whilst we observe no evidence for a chirality-driven signal within our experimental resolution, there does appear to be a positive thermal Hall effect in the superconducting state. This is expected to be carried by the superconducting quasiparticles, and potentially driven by skew scattering from the vortex lattice. However, it is unclear whether this is a feature of the B-phase or the superconductivity more generally. There is additionally a large, negative, normal state Hall effect, observed in both the electrical and thermal conductivity. This may be linked to an intrinsic Berry phase effect, or alternatively to skew scattering from magnetic fluctuations. However, based on the field dependence of the Hall resistivity, it seems more likely that it is the latter.

UAu_2 - Specific heat measurements have been used to investigate the low-temperature properties of UAu_2 as a function of temperature, field and field direction. This has revealed an unprecedented form of non-Fermi liquid behaviour, occurring deep within the antiferromagnetically ordered phase, and characterised by a specific heat which varies logarithmically with temperature. This behaviour survives in field, but is destroyed upon transition to the ferrimagnetic state - induced by applying a field greater than $\sim$ 8 T along the *c*-axis. The most likely explanation for this behaviour appears to be the two-channel Kondo effect. The required degeneracy is always satisfied at some sites - regardless of field - due to the incommensurate magnetic order. Fermi liquid behaviour then returns upon transition into the ferrimagnetic state, as the incommensurate order is destroyed, and there are no longer two-channel Kondo sites.

UTe_2 - The specific heat of UTe_2 - the most recent addition to the family of heavy fermion superconductors - has been the subject of numerous recent studies, and

various groups report differing results. In particular, the residual Sommerfeld coefficient (or finite heat capacity as $T \to 0$) has been the source of some debate. In this work, we have shown that the disparate results are - in part - due to differences in composition. Through measurements of the specific heat, and comparison with those previous studies, we have shown that the superconducting transition temperature - and the specific heat jump - appear to be negatively correlated with the residual Sommerfeld coefficient. This argues strongly against this feature being intrinsic (as some have claimed) and specifically against only one of the two spin directions being paired in the superconducting state. We have also demonstrated that the low-temperature Schottky anomaly - which also varies between different studies - might result from the ^{235}U quadrupolar moment.

Future Work

Measurements of the thermal Hall effect at ^{4}He temperatures have now become routine. In order to facilitate faster data acquisition and improved accuracy, many groups are turning to capacitive thermometry, or thermocouples, to measure the transverse thermal gradient. This may be one route to improving the thermal Hall effect measurements on $SrCu_2(BO_3)_2$. However, in order to avoid the inhibitory effect of triplon-triplon interactions, the measurement must be taken to lower temperatures, at which these alternative techniques have not yet been optimised.

For the UPt_3 measurements, one straightforward improvement - previously mentioned - is simply to reduce the field ramp rate between measurements, in order to ensure that the chirality of the superconducting state is preserved, and we are indeed antisymmetrising states of opposite chirality. Further than this, and assuming that the impurity driven thermal Hall effect is present - as it is in ^{3}He - the logical next step would be to investigate the effect of impurity density, or size of impurity. The former is straightforward to vary - through growth techniques or annealing studies - and also to estimate - as the residual resistivity gives a well calibrated handle on the impurity concentration (purely from the wealth of prior data). The impurity size might also be controlled through, for example, the intercalation of different elements.

The specific heat measurements on UAu_2 appear fairly conclusive. However - as a result of the material being relatively novel - there are a variety of properties which have not yet been investigated. For example, in a number of heavy fermion compounds, pressure can be applied in order to suppress the magnetic order and

gain access to the quantum critical region. It would certainly be interesting to investigate the behaviour of the two-channel Kondo state under pressure, potentially also by specific heat measurements. Alternatively, the thermal conductivity of UAu_2 has not yet been investigated. In such an unprecedented system, we might expect there to be novel emergent excitations. Measurements of the thermal conductivity might be capable of revealing these excitations.

Finally, for UTe_2, despite the ongoing frenzied research into some of the more exotic properties, there remain deep, sample-dependent issues which must be resolved. In order to shed light on these issues, future studies will investigate growths of different stoichiometries, in order to further investigate the impact of sample composition on the material properties. Separate to this, there is evidence to suggest that the superconducting state may be chiral. Similar to UPt_3, a thermal Hall effect measurement might provide a definitive signature of this chiral superconductivity.

More generally, the fact that thermal Hall effect measurements - searching for signals often at the limits of experimental feasibility - are one of the best probes of topological non-triviality is a testament to how elusive the signatures of topology can be. There is a huge volume of theoretical work dedicated to topology in condensed matter, but only a handful of materials to have been definitively demonstrated to harbour topological excitations. This perhaps suggests that alternative techniques are necessary if we hope to convert this theoretical understanding into new material technologies. One - perhaps not so novel - route is through surface sensitive probes, such as ARPES or STM, the latter of which has, for example, recently claimed to detect chiral states on the surface of UTe_2. Alternatively, thin film deposition is becoming an increasingly effective means of sample synthesis, and - with the appropriate experimental tools - may be a fruitful means to investigate topological properties. Topological phenomena are often confined to surfaces in two-dimensions - both these alternatives avoid some of the complexities induced by bulk measurements of three-dimensional materials.

Appendix A

X-ray Beamline Investigations

This thesis has involved two separate central facility experiments, both at synchrotron light sources, and both to investigate the material UAu_2. Very briefly, a synchrotron light source functions by accelerating an electron beam to relativistic speeds and then confining that beam to travel along a circular path by the application of a magnetic field. A relativistic electron being accelerated around a circular path will continuously emit a tightly collimated cone of radiation at a tangent to the path. The synchrotron facility therefore has a number of 'beamlines' which lie along these tangents, collecting the high-brilliance x-ray off-shoots from the storage ring in order to perform experiments.

In these investigations, we have used the XMaS beamline at ESRF in order to measure the charge and magnetic order in UAu_2, and the I18 beamline at the Diamond Light Source in order to investigate how the valence state of the uranium atoms changes as a function of temperature. Thanks go to Didier Wermeille and Konstantin Ignatyev, respectively, for their aid in operating the beamline equipment. Both measurements will be discussed in turn, but first we include a brief discussion of X-ray scattering theory.

A.1 X-Ray Scattering Theory

An electromagnetic wave will predominantly interact with an atomic configuration via elastic scattering from electronic dipole moments. This form of scattering may be adequately understood from classical electrodynamics, and can explain

Laue diffraction - the technique used to characterise all of the crystals in these investigations - as well as the measurements of charge modulation in UAu_2, presented here. However, the extraordinarily high brilliance of third generation synchrotron sources has made accessible alternative forms of scattering. These instead require a quantum mechanical interpretation. For example, within a quantum mechanical framework, a bound electron is capable of transitioning between atomic energy levels, and therefore has a finite probability to absorb an incident photon. This absorption process produces a resonant form of scattering, employed here to probe the electronic configuration of the uranium ions inside UAu_2. Additionally, the high polarisability of synchrotron radiation may be exploited in order to observe magnetic scattering, which results from the interaction between an incident beam and a magnetisation density. This form of scattering has allowed us to measure the local moment configuration in UAu_2. This section will now briefly review each of these different forms of scattering, in order to better appreciate the measurement techniques and experimental results which follow.

Scattering from an Electric Dipole

An oscillating electric field ($\mathbf{E}_{in}$) incident on a charge distribution will drive that charge distribution to oscillate at the same frequency. From classical electrodynamics, this oscillation (or acceleration) will result in the emission of an electromagnetic wave, with the same wavelength as the incoming wave, but in antiphase. This classical picture is the basis for elastic scattering. Let us now describe this process - and the form of the scattered wave - more formally [200].

An oscillating charge distribution might equivalently be considered a charge distribution with current density $\mathbf{J}(\mathbf{r}')$, which - from Maxwell's equations - results in a vector potential

$$\begin{aligned}\mathbf{A}(\mathbf{r},t) &= \frac{1}{4\pi\epsilon_0 c^2}\int_V \frac{\mathbf{J}(\mathbf{r}', t-|\mathbf{r}-\mathbf{r}'|/c)}{|\mathbf{r}-\mathbf{r}'|}d\mathbf{r}' \\ &\simeq \frac{1}{4\pi\epsilon_0 c^2 r}\int_V \mathbf{J}(\mathbf{r}', t-\frac{r}{c})d\mathbf{r}',\end{aligned}$$

where ε_0 is the vacuum permittivity and c is the speed of light. The second line follows from the assumption that the spatial extent of the charge distribution is much smaller than the wavelength of the incident wave (the dipole

approximation). The above integral may then be re-expressed as

$$\int_V \mathbf{J} d\mathbf{r}' = \int_V \rho \mathbf{v} d\mathbf{r}' = \sum_i q_i \mathbf{v_i} = \frac{d}{dt'} \sum_i q_i \mathbf{r'_i}, \tag{A.1}$$

where the integral over the charge density ρ has been replaced by a sum over discrete charges q_i. The vector potential is now

$$\mathbf{A}(\mathbf{r}, t) = \frac{1}{4\pi\epsilon_0 c^2 r} \dot{\mathbf{p}}(t'), \tag{A.2}$$

where $\mathbf{p}(t') = \sum_i q_i \mathbf{r'_i}$ is the electric dipole moment. Hence, the vector potential at a position $\mathbf{r}$ and time t will vary as a function of the time derivative of the electric dipole moment of the charge distribution at a time $t' = t - \frac{r}{c}$.

This vector potential will correspond to a magnetic field $\mathbf{B} = \nabla \times \mathbf{A}$, and therefore

$$\mathbf{B}(\mathbf{r}) = \frac{1}{4\pi\epsilon_0 c^2} \frac{1}{cr} \ddot{\mathbf{p}}(t') \times \hat{\mathbf{r}}. \tag{A.3}$$

By extension, and since $\hat{\mathbf{r}}$ will point in the direction of the propagation of the electromagnetic wave, we also have that

$$E(t) = \frac{1}{4\pi\epsilon_0 c^2} \frac{1}{r} \ddot{p}(t') \cos\psi, \tag{A.4}$$

where ψ is the angle between the plane perpendicular to the electric dipole and the unit vector $\hat{\mathbf{r}}$ (as illustrated in Figure A.1).

The above expression describes the radiated, or scattered, wave. We now wish to express this as a function of the incident wave. In order to do this, consider the dipole polarisation which results from this incident wave,

$$\ddot{p}(t') = q\ddot{z} = q\frac{qE_{in}(t')}{m} = \frac{q^2}{m} E_0 e^{-i\omega(t'-r/c)}, \tag{A.5}$$

where we have inserted the most general expression for the incident wave. Substituting this into Equation A.4 thus gives

$$E(t) = -\left(\frac{q^2}{4\pi\varepsilon_0 mc^2}\right)\left(\frac{e^{ikr}}{r}\right) E_{in}(t)\cos\psi \tag{A.6}$$

with $w/c = k$, the wave vector. Hence, as anticipated, the scattered wave will have the same wavelength as the incident wave, but be in antiphase. Therefore,

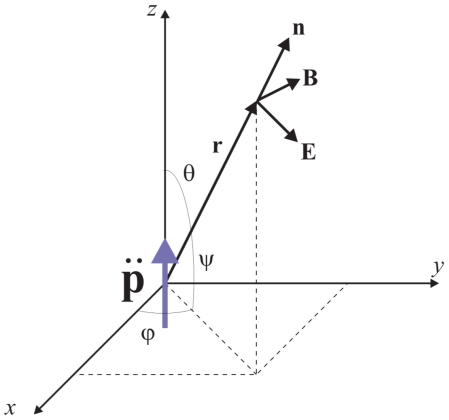

Figure A.1 *Schematic to show the direction along which the electric dipole oscillates, and the resultant electromagnetic field at* $\mathbf{r}$*, which - in the far field limit - approximates to a plane wave with* $\mathbf{E}$ *and* $\mathbf{B}$ *components perpendicular to the direction of propagation. Also shown is the angle* ψ*, defined as the angle between the direction of propagation and the plane perpendicular to the oscillation. Taken from [200].*

for scattering from a single electron, we have that

$$\frac{E(t)}{E_{in}(t)} = -r_0\left(\frac{e^{ikr}}{r}\right)|\hat{\boldsymbol{\varepsilon}}\cdot\hat{\boldsymbol{\varepsilon}}'|, \tag{A.7}$$

where $\hat{\boldsymbol{\varepsilon}}$ and $\hat{\boldsymbol{\varepsilon}}'$ are the polarisations of the incident and radiated fields respectively, and $r_0 = \frac{e^2}{4\pi\epsilon_0 mc^2}$ is the Thomson scattering factor.

In a scattering experiment, the fundamental quantity is the differential scattering cross section, defined as

$$\frac{d\sigma}{d\Omega} = \frac{N}{j_I}, \tag{A.8}$$

or the number of particles (N) scattered in a specified direction, per unit time per unit solid angle, divided by the flux incident on the scattering object (j_I). For scattering of an electromagnetic wave, this may be expressed

$$\frac{d\sigma}{d\Omega} = \frac{|\mathbf{E}_{rad}|^2 R^2}{|\mathbf{E}_{in}|^2}, \tag{A.9}$$

where R is the distance of the 'observer'. Therefore, from the above discussion, the differential scattering cross section for a single electron is given by

$$\left(\frac{d\sigma}{d\Omega}\right)_{el} = r_0^2|\hat{\boldsymbol{\varepsilon}}\cdot\hat{\boldsymbol{\varepsilon}}'|^2. \tag{A.10}$$

Electromagnetic scattering from a macroscopic object is overwhelmingly from electrons, and hence this expression will prove particularly useful in what follows.

Scattering from a Crystal

Let us now expand the above discussion - which concerns scattering from a single electric dipole - to consider scattering from a general charge distribution [200]. The most important development is that, for a finite sized charge distribution, waves may be scattered from different points and can thus interfere with one another. To see this, consider the schematic in Figure A.2 which shows two separate - but parallel and in phase - waves incident on a charge distribution, being scattered identically from different positions in order to reach an observer at X. In this scenario, the waves have traveled different distances to reach the observer, and will therefore be out of phase. A calculation of this phase difference is simply geometric, and given by

$$\Delta\phi = (\mathbf{k} - \mathbf{k}') \cdot \mathbf{r} = \mathbf{Q} \cdot \mathbf{r}, \tag{A.11}$$

where $|\mathbf{k}| = |\mathbf{k}'|$ for elastic scattering, and $\mathbf{Q}$ is the wave vector transfer, or scattering vector.

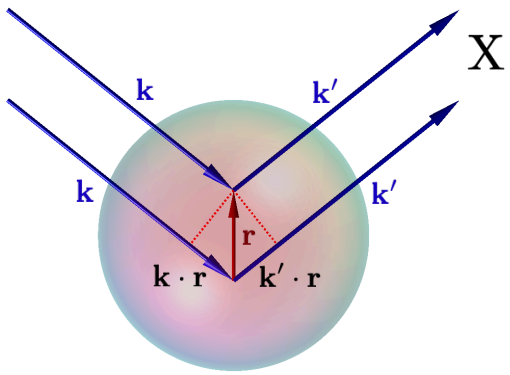

Figure A.2 *Schematic to make clear the phase difference between two waves that have been scattered from different points in a charge distribution.*

This idea may be straightforwardly extended to describe scattering from a charge distribution. However, let us first specify this charge distribution as being the electronic cloud which surrounds an atomic nucleus. This distribution will have an associated charge density $\rho(\mathbf{r})$, which may be divided into volume elements

$d\mathbf{r}$, centred at a position $\mathbf{r}$. Each of these infinitesimal volume elements might be considered a point-like scatterer, and therefore - from the above - will contribute to the scattered field with a phase factor $e^{i\mathbf{Q}\cdot\mathbf{r}}$. Summing over the entire charge distribution thus gives

$$\int \rho(\mathbf{r}) e^{i\mathbf{Q}\cdot\mathbf{r}} d\mathbf{r} = f(\mathbf{Q}), \tag{A.12}$$

where $f(\mathbf{Q})$ is known as the atomic form factor. The differential cross section for the whole atom is then

$$\frac{d\sigma}{d\Omega} = \left(\frac{d\sigma}{d\Omega}\right)_{el} |f(\mathbf{Q})|^2, \tag{A.13}$$

which is the differential cross section for one of the constituent point-like scatterers (electrons), multiplied by the atomic form factor. Hence, the atomic form factor is essentially a measure of how the spatial extent and shape of the electron distribution will modify the scattering amplitude. Further, this scattering amplitude is proportional to the Fourier transform of the charge density. This will remain true regardless of the size or complexity of the scattering object.

The above analysis may be applied iteratively in order to derive an expression for scattering from a crystal. A crystal comprises a lattice of atoms, and is completely defined by the unit cell. We therefore begin by calculating the form factor for a unit cell,

$$f^{UC}(\mathbf{Q}) = \sum_j e^{i\mathbf{Q}\cdot\mathbf{r_j}} f_j(\mathbf{Q}). \tag{A.14}$$

where $\mathbf{r}_j$ are the positions of the different atoms, each of which have an associated form factor $f_j(\mathbf{Q})$. The entire crystal will then have a form factor

$$F^{crystal}(\mathbf{Q}) = f^{UC}(\mathbf{Q}) \sum_n e^{i\mathbf{Q}\cdot\mathbf{R}_n}. \tag{A.15}$$

where, similarly, $\mathbf{R}_n$ gives the positions of each unit cell, all of which have a form factor $f^{UC}(\mathbf{Q})$.

For the above expression to be non-zero in the limit $n \to \infty$ - and therefore for a wave to be scattered coherently from the crystalline lattice - we require that $\mathbf{Q}\cdot\mathbf{R}_n = 2\pi m$, where m is an integer. By considering the dot product of the reciprocal and real space lattice vectors,

$$\mathbf{G}\cdot\mathbf{R}_n = (h\hat{\mathbf{a}}_\mathbf{1}^* + k\hat{\mathbf{a}}_\mathbf{2}^* + l\hat{\mathbf{a}}_\mathbf{3}^*)\cdot(n_1\hat{\mathbf{a}}_\mathbf{1} + n_2\hat{\mathbf{a}}_\mathbf{2} + n_3\hat{\mathbf{a}}_\mathbf{3}) \tag{A.16}$$

$$= 2\pi(hn_1 + kn_2 + ln_3) = 2\pi m, \tag{A.17}$$

we see that this condition is equivalently $\mathbf{Q} = \mathbf{G}$. Hence, for coherent scattering, we require that the wave vector transfer be equal to a reciprocal lattice vector. This is the relation which forms the basis of X-ray diffraction, and therefore allows us to understand Laue diffraction - employed to characterise the single crystals in all our investigations - as well as the measurements of the charge modulation in UAu_2 (Figure A.8).

As a final point of note, the above relies on the kinematical approximation, which assumes that the wave is scattered only once and then leaves the crystal. In general this is a fair assumption when the interaction between the incident x-ray beam and the crystal is weak.

Resonant Scattering

The discussion thus far has been entirely classical, with scattering due to the oscillations of free electrons. In deriving the atomic form factor, we constrained these electrons to exist within a region surrounding the atomic nucleus, but they remained otherwise free. Instead, quantum mechanics tells us that the electrons bound inside an atom will form discrete energy levels, with those lower energy levels being more heavily influenced by the atomic potential. In order to account for this, we modify the atomic form factor to include energy dependent terms, as

$$f(\mathbf{Q}, \hbar\omega) = f^0(\mathbf{Q}) + f'(\hbar\omega) + if''(\hbar\omega), \tag{A.18}$$

where $\hbar\omega$ is the energy of the incident photon. The supplementary terms essentially correspond to the solutions of a damped harmonic oscillator, as the electron oscillation is damped by the atomic potential. Additionally, in this revised scenario, the bound state electron has a finite probability to absorb - or emit - an incident phonon, and thus transition between levels. As such, the scattering cross section will be drastically enhanced at specific incident energies, referred to as absorption edges. This is a resonant form of scattering, and is captured by the strong energy dependence of the additional terms in the atomic form factor [201].

Shown in Figure A.3 is the typical absorption spectrum for an isolated atom. This demonstrates the sharp steps which occur at absorption edges, as well as the associated nomenclature. In an absorption process, the system will transition between two states under the influence of a weak perturbation (the incident

wave), and may therefore be described using perturbation theory. Specifically, the transition probability is given by Fermi's golden rule, or

$$W = \sum_f |\langle i|\mathcal{H}_1|f\rangle|^2(\delta(\omega + E_i - E_f) + \delta(\omega - E_i + E_f)), \tag{A.19}$$

where ω, E_i and E_f are, respectively, the energies of the incident photon, initial and final states, the sum is over all final states, and $\mathcal{H}_1$ is the perturbation. The exact details of the calculation will obviously be measurement specific, although it is clear that the transition probability will be strongly enhanced at particular incident energies. Unfortunately, the complexity of real materials often prevents an accurate determination of this transition probability, and by extension, the theoretically expected absorption cross section. However, as will be discussed, the above expression still retains some predictive power.

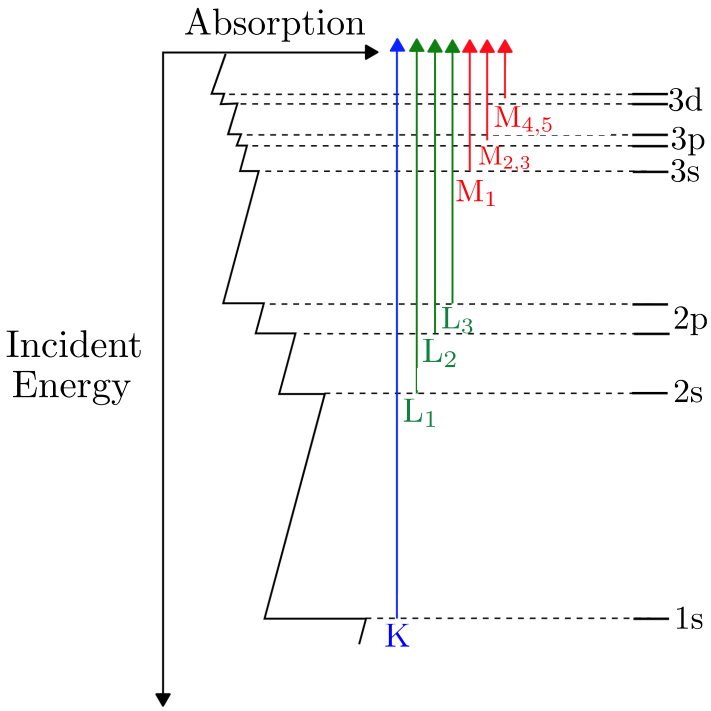

Figure A.3 *Typical absorption spectrum for an isolated atom, alongside the absorption edge nomenclature, which is split by principal quantum number and total angular momentum of the core electron.*

Features of the Absorption Spectrum

In these investigations, resonant X-ray emission spectroscopy has been used in order to probe the electronic (and atomic) configuration of UAu_2. The full results will be discussed in Appendix A.2, but we reproduce a typical energy scan through the uranium $M_{4/5}$ absorption edges in Figure A.4. Note the marked differences between this and the idealised absorption spectrum for a single isolated atom shown in Figure A.3. In general, those features occurring within ~ 10 eV of an absorption edge are referred to as X-ray absorption near edge structure (XANES), and may be analysed in order to extract details of the electronic configuration. This analysis is somewhat material specific, and will therefore be discussed in the results section. Alternatively, those features occurring at higher energies are referred to as extended X-ray absorption fine structure (EXAFS). As we will now show, EXAFS can give information on the physical environment which surrounds the scattering centre [202].

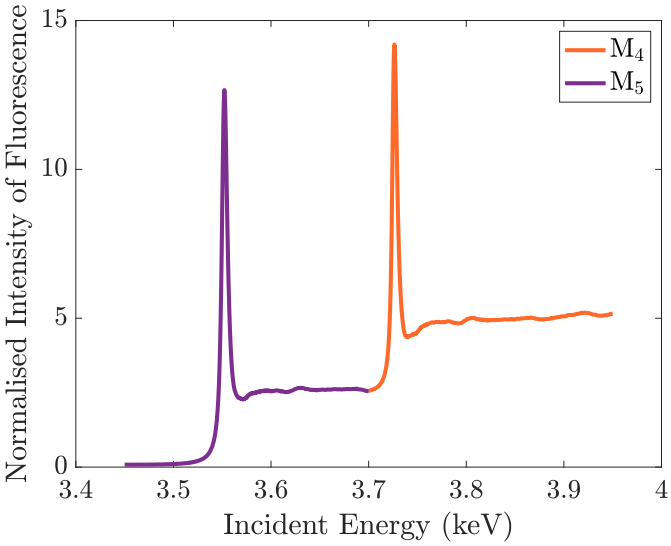

Figure A.4 *Normalised intensity of fluorescence plotted as a function of incident energy for a UAu_2 crystalline sample. The data has been normalised such that the intensity before the M_5 absorption edge is approximately zero.*

In an experiment, we often measure the absorption coefficient μ, defined by

$$I = I_0 e^{-\mu t}, \tag{A.20}$$

where I_0 is the incident x-ray intensity, t is the sample thickness, and I is

the transmitted intensity. The quantity μ is therefore directly related to the absorption cross section, and may similarly be expressed

$$\mu(E) \propto |\langle i|\mathcal{H}_1|f\rangle|^2. \tag{A.21}$$

Recall, the absorption process corresponds to the absorption of an incident photon by a core electron, which then gains sufficient energy to escape the atomic potential, and leave as a photoelectron. Let us now consider the effect of a neighbouring atom on this process - the initial state should remain the same as the core electron is tightly bound, whereas the final state photoelectron is free and will thus interact with the neighbouring atom. The final state may therefore be written $|f_0\rangle + |\Delta f\rangle$, where the second term accounts for the effect of the neighbouring atom. The absorption coefficient will now read

$$\mu(E) \propto |\langle i|\mathcal{H}_I|f_0\rangle|^2\left[1 + \langle i|\mathcal{H}_I|\Delta f\rangle\frac{|\langle f_0|\mathcal{H}_I|i\rangle^*}{|\langle i|\mathcal{H}_I|f_0\rangle|^2} + C.C\right], \tag{A.22}$$

or

$$\mu(E) = \mu_0(E)[1 + \chi(E)]. \tag{A.23}$$

This second expression has been written such that $\mu_0(E)$ corresponds to the isolated atom absorption coefficient, and $\chi(E)$ can be used to characterise the EXAFS.

In order to relate $\chi(E)$ to the physical system it is describing, we may write it more explicitly as

$$\chi(E) \propto \langle i|\mathcal{H}_I|\Delta f\rangle \propto \int \delta(r)e^{ikr}\psi_{scat}(r)dr, \tag{A.24}$$

where the initial bound state has been approximated by $\delta(r)$ and the additional contribution to the final state ($|\Delta f\rangle$) is given by the wavefunction of a photoelectron which has been scattered from the neighbouring atom, ψ_{scat}. The interaction term will be $\mathbf{p}\cdot\mathbf{A}$, where $\mathbf{p}$ is the momentum of the photoelectron and $\mathbf{A}$ is the vector potential of the incident photon field. In the above expression, this has been rewritten as e^{ikr}, where k is the wave vector of the photoelectron. The above integral is then evaluated as $\psi_{scat}(0)$, implying that the effect of a neighbouring atom will be determined by the amplitude of the scattered photoelectron at the absorbing atom (depicted schematically in Figure A.5).

Finally, without derivation, the EXAFS portion of the absorption coefficient may

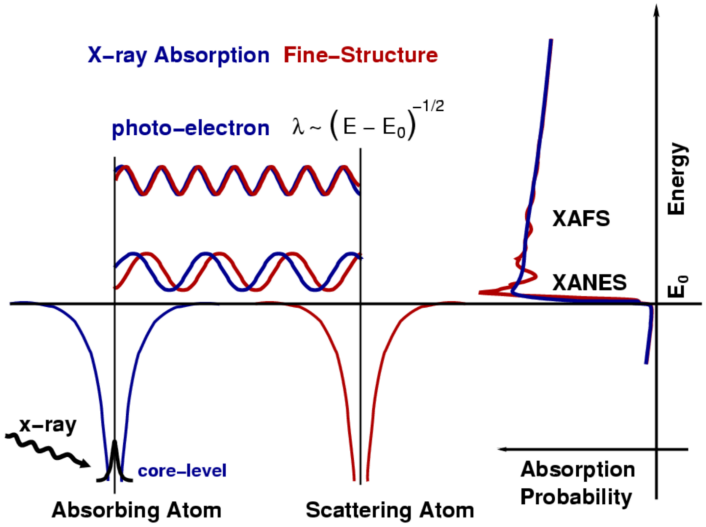

Figure A.5 *Schematic of the absorption process, relating it to the x-ray absorption fine structure. The photoelectron will be scattered back to the absorbing atom by neighbouring atoms, leading to an interference. The scattered photoelectron wavefunction at the absorbing atom will be a function of its energy, and hence the absorption probability will be a function of the incident x-ray energy, as well as the physical environment surrounding the absorbing atom. Taken from [202].*

be expressed as

$$\chi(k) = \sum_j \frac{N_j f_j(k) e^{-k^2\sigma_j^2}}{kR_j^2} \sin[2kR_j + \delta_j(k)], \tag{A.25}$$

where $f(k)$ and $\delta(k)$ are scattering properties of those atoms which neighbour the excited atom, N is the number of neighbouring atoms, R_j is the distance to the neighbouring atom j, and σ^2 is a term to account for any disorder. The oscillations of the EXAFS can therefore be analysed in order to determine the nearest neighbour configuration. This process is detailed for UAu_2 in Appendix A.2.

Magnetic Scattering

We now consider that a photon is more than simply an electric field, and similarly that an electron will have an associated spin, or magnetic moment. The two can therefore interact magnetically, and as such, X-ray scattering may be used to probe the magnetisation density of a material [201, 203]. To account for this, the atomic form factor given previously must be modified again to include the effects

of magnetic interactions, to give

$$f(\mathbf{Q},\hbar\omega) = f^0(\mathbf{Q}) + f^{mag}(\mathbf{Q}) + f'(\hbar\omega) + if''(\hbar\omega). \tag{A.26}$$

In the case of non-resonant magnetic scattering, and without derivation, the magnetic form factor is given by

$$f^{mag} = ir_0\frac{\hbar\omega}{mc^2}\left(\frac{1}{2}\mathbf{L}(\mathbf{Q})\cdot\mathbf{A} + \mathbf{S}(\mathbf{Q})\cdot\mathbf{B}\right)f_D, \tag{A.27}$$

where $\mathbf{L}(\mathbf{Q})$ and $\mathbf{S}(\mathbf{Q})$ are the Fourier transforms of the spin and orbital magnetisation densities respectively, $\mathbf{A}$ and $\mathbf{B}$ are functions of the incident and scattered photon geometries, and f_D is the Debye-Waller factor, included to account for deviations from an ideal crystalline lattice due to thermal motion.

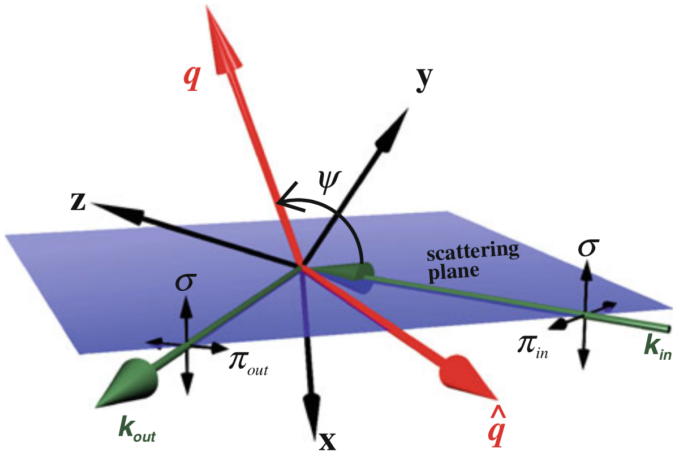

Figure A.6 *Schematic of a scattered photon. The linear polarisations reference the scattering plane, with π being parallel and σ being perpendicular. The incident and reflected polarisation vectors can then be written as linear combinations of π and σ. Taken from [201]*

An essential feature of magnetic scattering is that the incident and radiated waves are polarised perpendicular to one another. Due to the highly polarised nature of synchrotron radiation, this may be exploited in order to simplify the experimental analysis. One such analytical tool is to define polarisations with respect to the scattering plane, as shown in Figure A.6. The magnetic form factor can then be divided by the four potential scattering geometries, as

$$f^{mag} = ir_0\frac{\hbar\omega}{mc^2}\begin{pmatrix} M_{\sigma\sigma'} & M_{\pi\sigma'} \\ M_{\sigma\pi'} & M_{\pi\pi'} \end{pmatrix} f_D, \tag{A.28}$$

where each of the matrix elements is a function of the scattering angle and the angular momenta (projected onto the coordinate axis). Importantly, the different matrix elements each describe a specific form of scattering - for example, the off-diagonal terms will contain no contributions from charge scattering. Our measurements of magnetic modulation in UAu_2 configured the experimental setup in order to exploit this fact.

This technique of isolating the magnetically scattered radiation is for more than just experimental convenience. Consider the ratio of the cross sections - essentially the probability a scattering event will occur - between charge and magnetic scattering:

$$\frac{\sigma_{mag}}{\sigma_{charge}} \simeq \left(\frac{\hbar\omega}{mc^2}\right)^2 \left(\frac{N_m}{N}\right)^2 \langle M\rangle^2 \left(\frac{f_{mag}}{f}\right)^2, \tag{A.29}$$

where $N_{(m)}$ are the number of (magnetic) electrons per atom and $\langle M\rangle$ is the magnetic order parameter. Even generous estimates for all of the parameters gives a ratio of $\sim 10^{-7}$. Hence, without exploiting the $\pi/2$ shift in polarisation between the incident and magnetically scattered radiation, any magnetic signal would be washed out by the contribution from charge scattering. However, even with third generation synchrotron sources, the signal due to magnetic scattering is often imperceptibly small. Fortunately, we can again turn to resonant scattering.

Resonant Magnetic Scattering

As discussed previously, the scattering cross section will be resonantly enhanced at an absorption edge - this similarly applies to magnetic scattering. Note however, the non-resonant magnetic form factor (Equation A.27) will vanish at $\mathbf{Q} = 0$, and therefore does not contribute to absorption effects. Unlike non-resonant magnetic scattering - which originates from magnetic couplings - resonant magnetic scattering will depend on the available states for an electron to transition into, and thus can act as an indirect probe of local magnetic moments [203].

Resonant magnetic scattering will (in the majority of cases) be dominated by electric dipole transitions. For such transitions - and after simplifications arising from the dipole selection rules - the resonant contribution to the atomic form

factor may be written

$$f_{E1}^{Res} = (\hat{\epsilon}_{out} \cdot \hat{\epsilon}_{in})F^{(0)} - i(\hat{\epsilon}_{out} \times \hat{\epsilon}_{in}) \cdot \hat{\mathbf{z}}_n F^{(1)} + (\hat{\epsilon}_{out} \cdot \hat{\mathbf{z}}_n)(\hat{\epsilon}_{in} \cdot \hat{\mathbf{z}}_n)F^{(2)}, \quad \text{(A.30)}$$

where $\hat{\epsilon}$ are the polarisation vectors and $\hat{\mathbf{z}}_n$ points in the direction of the local moment at site n [204]. $F^{(i)}$ are linear combinations of F_{LM}, defined by

$$F_{LM}(\omega) = \sum_{i,f} \left[\frac{P_i P_i(f)}{[x(i,f) - i]} \right] \frac{\Gamma_x(iMf)}{\Gamma(f)}, \quad \text{(A.31)}$$

where i and f represent the initial and excited states, P_i is the probability of an ion being in a state i, and $P_i(f)$ is the probability of that ion transitioning to a state f. Γ_x/Γ is the ratio of the partial line widths of pure dipole radiative decay to that of all radiative processes. Finally, $x = (E_i - E_f - \hbar\omega)$ is a measure of the deviation from the resonance condition. Hence, as before, the scattering cross section will be enhanced at material-specific energies. However, in addition, the strength of this resonant enhancement will be influenced by the orientation of the local moments (with respect to the measurement geometry).

Equation A.30 is written such that each term describes a different form of scattering. The first term has no dependence on the magnetic moment and therefore relates to charge scattering. The second term gives a magnetic scattering amplitude at the same point in reciprocal space as the usual magnetic scattering. Finally, the third term is simply the second-harmonic of this magnetic scattering. As with non-resonant magnetic scattering, the contributions to each term in the above expression may be divided by the four potential scattering geometries. For example, the second term - being the dominant contribution to resonant magnetic scattering - may be expressed

$$-iF^{(1)} \begin{pmatrix} 0 & z_1 \cos\theta + z_3 \sin\theta \\ z_3 \sin\theta - z_1 \cos\theta & -z_2 \sin 2\theta \end{pmatrix}, \quad \text{(A.32)}$$

where θ is the Bragg angle and $\hat{\mathbf{z}}_n$ has been resolved into orthogonal components, along the axes defined in Figure A.7 [205]. Therefore, given the scattering geometry and Bragg angle - both of which we have complete control over - we are able to determine the configuration of the localised moments. This technique has been applied to UAu_2 in the following section.

A.2 Experimental Results

UAu_2 has been characterised in Section 5.2, and we therefore only briefly discuss some relevant details here. As shown in Figure 5.3, UAu_2 crystallises in a hexagonal structure, with localised moments at the uranium sites. These moments order antiferromagnetically below ~ 43.5 K. Within the magnetically ordered phase, a previous inelastic neutron study has measured magnetic peaks at wave vectors $(\frac{1}{3}, \frac{1}{3}, \delta)$, with $\delta \sim \frac{1}{7}$ at the lowest temperatures, falling to $\sim \frac{1}{8}$ at the Néel temperature [172]. Hence, the physical picture in UAu_2 is that of moments pointing parallel to the c-axis, with their magnitudes being incommensurately modulated along that same axis with periodicity δ. Adjacent moments in the $a-b$ plane are then 120° out of phase in order to give the antiferromagnetic state (this magnetic structure is also included in Figure 5.3).

A.2.1 XMaS at ESRF

XMaS is a tangential beamline off the ESRF particle accelerator, capable of delivering a 2.4 keV - 15 keV, continuously tunable, monochromatic X-ray beam to a 0.4 mm^2 surface on our sample. This investigation was largely focused on the charge and spin density wave modulation of the δ-phase. We were also able to investigate a theoretically hypothesised $(\frac{1}{3}, \frac{1}{3}, 0)$ modulation at higher temperatures, as well as perform azimuthal scans to confirm the orientation of the localised moments.

Experimental

We applied a variety of different experimental techniques in this investigation, and therefore the specifics of each will be discussed alongside the relevant experimental data. Throughout all measurements, the sample was kept under vacuum inside a beryllium cryostat dome, chosen for its low absorption coefficient. The sample was cooled using a ^{4}He ILL Joule-Thomson Cryostat, with the temperature stabilised by a Lakeshore 340 temperature controller, giving a temperature resolution of ~ 3 mK. The incident energy was selected using the (111) reflection from cryogenically cooled silicon monochromator. The beam was focused using rhodium-coated toroidal mirrors, with an incident angle of 4.5 mrad. Finally, two 300 mm long silicon mirrors were used to remove the higher energy harmonics

from the monochromator.

Charge Density Modulations in the δ-phase

To investigate charge density modulations we have employed the technique of non-resonant charge scattering. This was therefore a diffraction experiment, and the measurements were configured in the specular scattering geometry shown in Figure A.7. The beam was incident on a polished, flat face of the UAu_2 sample, with the a-axis perpendicular to the face. The **Q**-vector under investigation was thus aligned parallel to the a-axis.

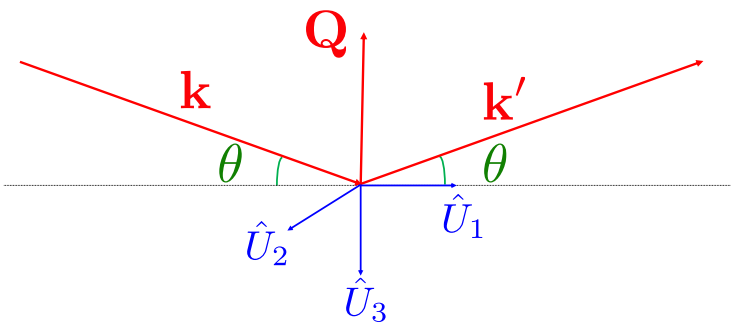

Figure A.7 *Specular scattering geometry for a diffraction measurement.* $\mathbf{k}$ *and* $\mathbf{k}'$ *are the incident and scattered wave vectors,* $\mathbf{Q} = \mathbf{k} - \mathbf{k}'$ *is the wave vector transfer and* θ *is the Bragg angle.* $\hat{U}_i$ *are the laboratory frame unit vectors, in reference to the formalism used to describe resonant magnetic scattering in the previous section, and also therefore the azimuthal scan measurements.*

In order to maximise the scattered intensity, it is desirable to set the incident energy as high as possible. However, we must simultaneously avoid any strong absorption edges, above which there will be significant photoluminescence as excited electrons return to their original state, disrupting the measurement. After consulting [206] - which gives a comprehensive list of the absorption edge energies for all materials - the beam energy was set at 11.8 keV, slightly below the gold L_3 edge.

At this constant energy, scans were performed around the anticipated reciprocal space lattice vector $(\frac{1}{3}, \frac{1}{3}, 2\delta)$. Note the periodicity was set to 2δ, rather than δ. The δ modulation is a result taken from neutron data, and is therefore a magnetic modulation. Any charge modulation will instead be due to charge shielding of the localised moments (as described in Section 5.2), and we thus expect that the

modulation periodicity should be doubled.

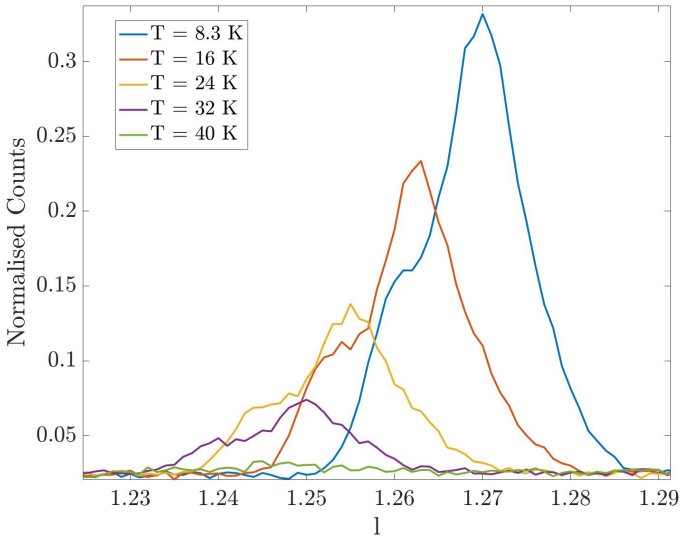

Figure A.8 *Typical scans around the* **Q***-vector* $(\frac{10}{3}, \frac{10}{3}, 1+2\delta)$*, chosen specifically for the relatively good signal to noise ratio at the lowest temperature peak. The counts are normalised to the count rate at the monitor, which is proportional to the beam intensity.*

Identical scans were performed at a range of temperatures, as shown in Figure A.8. Clearly, the anticipated charge modulation is present. At each temperature, the peak position and height can be used to determine δ and the intensity of the modulation respectively. What is immediately evident from Figure A.8 is that, as we move to higher temperatures, the peak loses intensity and moves to smaller l, where l refers to the Miller index. This is presented quantitatively in Figure A.11, alongside the magnetic modulation data. Finally, we note that all of the peaks have a shoulder feature at lower l. This has been attributed to a mosaic in the crystal, rather than an intrinsic property.

Spin Density Modulation in the δ-phase

In order to investigate the magnetic modulation we have instead employed resonant magnetic scattering, which requires tuning the incident beam energy to an absorption edge of the magnetic ion. In order to determine the absorption edge which would give the largest enhancement of the scattering amplitude, the photoluminescence of UAu_2 was measured as a function of incident energy, as shown in Figure A.9 (a). For this measurement, the detector is

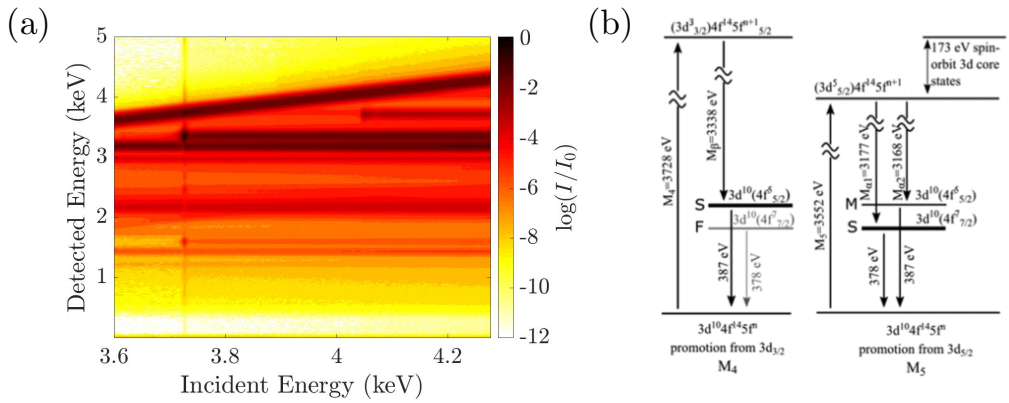

Figure A.9 *(a) Fluorescence spectrum of UAu_2, with the energy scanned around the uranium M_4 edge (as described in the text). The intensity of fluorescence is implied by the darkness of the red colour, plotted on a logarithmic scale (I_0 is the incident intensity and I the detected intensity). Note, the diagonal line of intensity is at the same energy as the incident beam, and must therefore correspond to multiple, non-resonant charge scattering. (b) Energy level diagram for the uranium $M_{4/5}$ edges, showing the relaxation process through intermediate levels. The various transitions are labelled S, M and F, corresponding to strong, medium and forbidden respectively. Taken from [207].*

placed perpendicular to the specularly reflected beam, in order to detect the isotropically emitted photoluminescence, rather than the scattered radiation. From Figure A.9 (a), the strongest feature is the fluorescence line beginning at 3.726 keV - corresponding to the uranium M_4 edge. Subsequent measurements were therefore performed at this incident energy. Note, as illustrated in Figure A.9 (b), those electrons excited at the uranium M_4 edge cascade through intermediate energy levels as they relax. This is the reason for the detected photoluminescence being at a lower energy than the incident beam. We also note a fluorescence line beginning at 4.050 keV. From a survey of the electron binding energies for all elements [206], this can only correspond to the thorium M_3 edge, implying there are thorium impurities in our sample.

Having established that the uranium M_4 edge should give the maximum achievable enhancement of the magnetically scattered signal, the beam energy was set to 3.726 keV and scans were performed around the anticipated modulation vector $(\frac{1}{3}, \frac{1}{3}, \delta)$. As discussed previously, in order to isolate the magnetically scattered radiation, the experiment was configured such that the incident and detected polarisations were perpendicular (corresponding to the $\sigma\pi'$ channel,

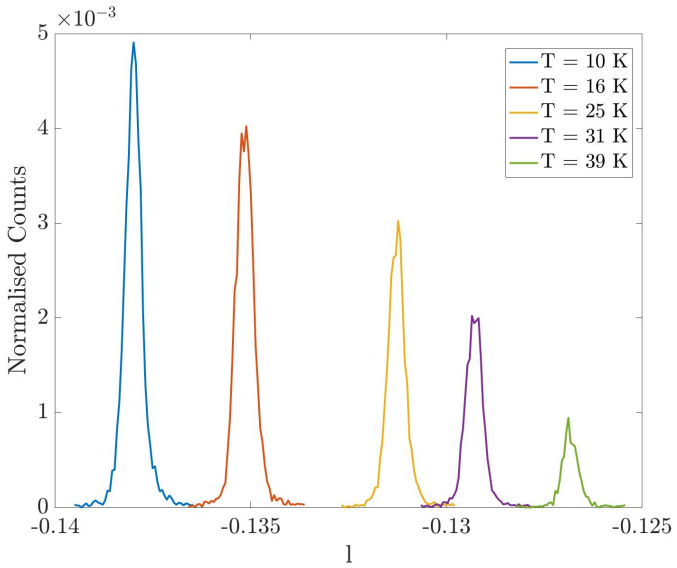

Figure A.10 *Typical scans around the* **Q***-vector* $(-\frac{1}{3}, \frac{5}{3}, -\delta)$*. Again, the counts are normalised to the count rate at the monitor.*

Figure A.6). The results are shown in Figure A.10. As with the charge density modulation, with increasing temperature both the position and intensity of the peak decrease. Again, this is presented quantitatively in Figure A.11.

From Figure A.11, it is clear that the charge and spin density modulation measurements are consistent, with the slight discrepancy due to the shoulder feature in the charge density modulation peaks. Therefore, the physical picture in UAu_2 remains that which was discussed previously - the antiferromagnetic state comprises chains of localised moments with incommensurately modulated magnitudes parallel to the c-axis, and modulation vector $(\frac{1}{3}, \frac{1}{3}, \delta)$. As a function of temperature, δ decreases slightly, whilst the strength of the magnetic order is reduced, falling to zero at the Néel temperature.

Search for Alternative Modulations

Theoretical work has suggested that there may be an energetically favourable $\{\uparrow, \downarrow, 0\}$ phase - in reference to the spins on an in-plane triangle - close to the Néel temperature. This would result in a modulation vector of $(\frac{1}{3}, \frac{1}{3}, 0)$. As such, with the incident energy still set to the uranium M_4 edge, (h, k) space was scanned around this **Q**-vector. As shown in Figure A.12, there appears no evidence for this alternative phase. An identical scan was then performed above the Néel

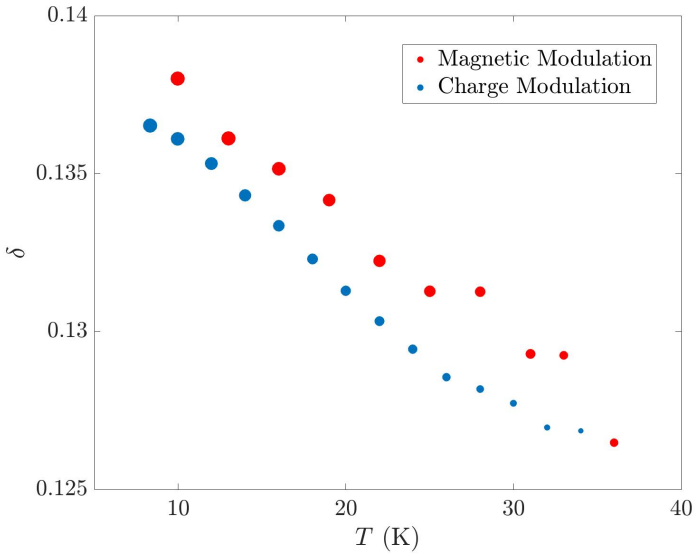

Figure A.11 *Modulation vector δ plotted as a function of temperature, taken from Figures A.10 (red) and A.8 (blue). The intensity of each peak is given by the size of the data point, normalised to the largest intensity peak in that data set.*

temperature which showed broadly similar results, implying that those features in Figure A.12 are unrelated to the magnetic order in UAu_2. The contribution from higher harmonics is expcected to be negligible - far below the intensity observed - and therefore the strong peak at $(\frac{1}{2}, \frac{1}{2}, 0)$ must be interpreted as a feature of the crystal structure, whilst the diagonal lines of increased intensity have been attributed to beryllium powdering (from the cryostat dome).

Azimuthal Scans

Finally, azimuthal scans were performed in order to determine the orientation of the magnetic moments in UAu_2. In an azimuthal scan, the sample is rotated about the **Q**-vector, which is kept constant. The scattering amplitude (and therefore the measured intensity) is then proportional to the orientation of the magnetic moment relative to the incident beam. The theory behind this has been discussed in the previous section.

The antiferromagnetic order in UAu_2 is expected to comprise sinusoidally modulated moments lying parallel to the c-axis. Let us therefore calculate the scattering amplitude we would expect from this magnetic structure, and then compare to the experimental results. For these azimuthal scans, the sample

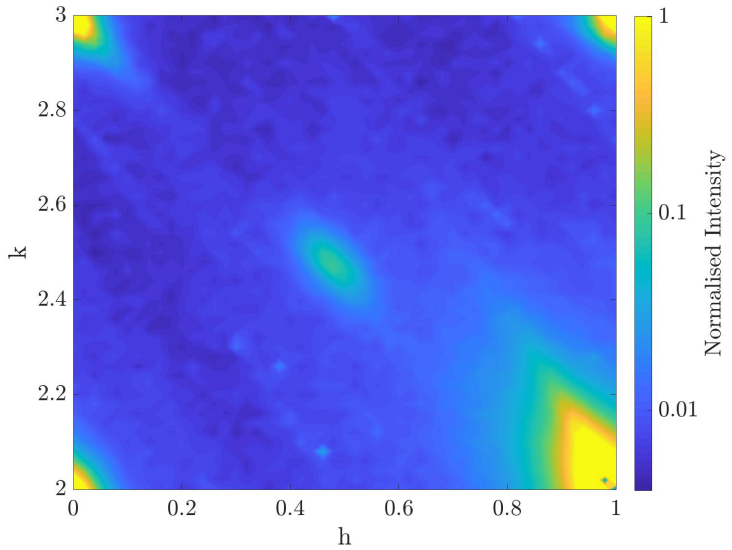

Figure A.12 *Mesh scan from (0,2,-2) to (1,3,-2) in reciprocal space, taken at 36 K with the incident energy still set to the uranium M_4 edge (3.726 keV). The detected intensity has been normalised such that the largest detected intensity is 1.*

was oriented with the c-axis parallel to the scattering face. The measurement geometry is shown Figure A.7, which also includes the three orthogonal axes we will reference in this calculation. The measurement was further configured such that the incident and detected polarisation vectors were perpendicular. We therefore need only consider the scattering channel $\sigma\pi'$, corresponding to magnetic scattering.

Let us first calculate the expected scattered intensity for c-axis parallel to the incident beam. In this case - and with reference to Figure A.7 - the moments will be parallel to $\hat{U}_1$, and the nth magnetic moment may therefore be expressed as $\mathbf{z}_n = \sin(\boldsymbol{\Delta} \cdot \mathbf{r}_n)\hat{U}_1$, where $\boldsymbol{\Delta}$ is a function of the incommensurate modulation. Note, the absolute magnitudes of the moments are irrelevant in determining their orientation, we therefore normalise to one. Recall Equation A.32, which gives the scattering amplitude due to resonant magnetic scattering, divided into the contributions of the four different scattering geometries. In this, the scattering channel $\sigma\pi'$, corresponds to the matrix element $z_3 \sin\theta - z_1 \cos\theta$, where θ is the Bragg angle. For this measurement configuration, we have that $z_1 = \sin(\boldsymbol{\Delta} \cdot \mathbf{r}_n)$ and $z_3 = 0$, and the scattering amplitude is therefore given by

$$A = \sum_n e^{i\mathbf{Q}\cdot\mathbf{r}_n}[-iF^{(1)} \sin(\boldsymbol{\Delta} \cdot \mathbf{r}_n) \cos\theta], \tag{A.33}$$

which corresponds to an observed intensity

$$I = [F^{(1)}]^2 \frac{\cos^2\theta}{4} \left[\sum_n e^{i\mathbf{Q}\cdot\mathbf{r}_n} (e^{i\boldsymbol{\Delta}\cdot\mathbf{r}_n} - e^{-i\boldsymbol{\Delta}\cdot\mathbf{r}_n}) \right]^2 \tag{A.34}$$

$$= [F^{(1)}]^2 \frac{\cos^2\theta}{4} \delta(\mathbf{Q} - \boldsymbol{\Delta}). \tag{A.35}$$

This could, in principle, be calculated explicitly with knowledge of the various experimental details, but again, is irrelevant to this calculation.

We now consider how the scattered intensity will vary as a function of the azimuthal angle. Varying the azimuthal angle - or rotating around a constant scattering vector - might equivalently be imagined as a rotation of the orthogonal reference axes $\hat{U}_i$. A rotation of the axes by an angle ϕ will act to shift the magnetic moment vector to

$$\mathbf{z}_n = \sin(\boldsymbol{\Delta}\cdot\mathbf{r}_n)\cos\phi\ \hat{U}_1 - \sin(\boldsymbol{\Delta}\cdot\mathbf{r}_n)\sin\phi\ \hat{U}_2. \tag{A.36}$$

From the above, the $\hat{U}_2$ component is irrelevant. However, from the $\hat{U}_1$ component, the observed intensity will acquire a $\cos^2\phi$ term, implying a maximum intensity when the beam is aligned with the c-axis, dropping to zero intensity when they are perpendicular.

Shown in Figure A.13 is the experimental data, taken at 10 K and 36 K. Also included are $\cos^2\phi$ fits to each data set, where ϕ is the azimuthal angle. The data approximately follows the anticipated behaviour, implying that the moments in UAu_2 do indeed lie along the c-axis. However, there are clearly deviations, which would suggest there are effects not accounted for by this model.

A.2.2 I18 at Diamond

The I18 beamline off the Diamond Light Source is capable of delivering a linearly polarised, defocused beam with an area of 250 x 400 µm. The incident energy can be continuously tuned between 2.0 and 20.7 keV. Our investigations set out to study the absorption spectrum of UAu_2, and specifically, changes in the features of the uranium M_4, M_5 and L_3 absorption edges as a function of temperature, which might indicate a change in the valence state of the uranium atoms. This is anticipated to be a consequence of the two-channel Kondo effect, employed in Section 5.2 to explain the thermodynamic properties of UAu_2. As mentioned

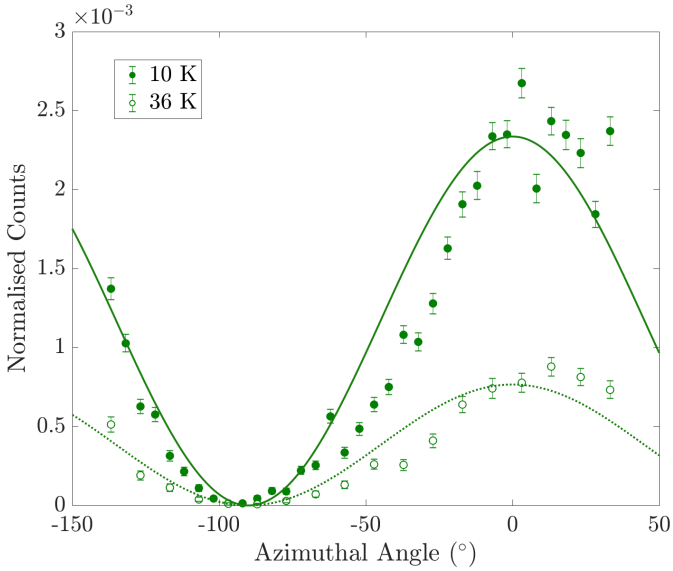

Figure A.13 *Azimuthal scans to determine the orientation of the magnetic moments in UAu_2. Scans were performed at the uranium M_4 edge (3.726 keV), and at a* **Q***-vector of $(\frac{2}{3}, \frac{2}{3}, -\delta)$, as this was the magnetic peak that gave the largest range of obtainable azimuthal angles. Also included are fits to $A\cos^2\phi$, where ϕ is the azimuthal angle.*

previously, the features about the absorption edge are typically divided into X-ray absorption near edge structure (XANES) and X-ray absorption fine structure (EXAFS), each of which give information on different properties of the material. These will therefore be discussed in turn.

Experimental Techniques

Unlike the previous investigation, the experimental technique remained broadly similar for all the measurements presented here. The procedure is identical to that described by Figure A.9 (a) - the incident energy was scanned about the relevant absorption edge, then the fluorescence at all energies was collected by a detector positioned away from the specularly reflected beam. The intensity of fluorescence is then proportional to the absorption coefficient, allowing the absorption spectrum to be mapped out. However, in a fluorescence measurement, the photoluminescent transitions are from intermediate states with smaller intrinsic linewidths (as shown in Figure A.9 (b)), and hence the predominant source of error is significantly reduced as compared to an absorption measurement.

For these measurements, the beam was incident on a polished, flat face of a UAu_2 sample, with the a-axis again being perpendicular to the face. The incident energy was selected using the (111) reflection from a double silicon crystal monochromator. For rejection of higher harmonics, two parallel silicon mirrors at an angle of 300 mrad were used. The beam was incident at 45° to the sample face, with a 4-element silicon drift detector placed perpendicular. The uranium L_3 (17.166 keV) edge occurs at a significantly larger incident energy than the M_4 (3.7276 keV) and M_5 (3.5517 keV) edges. As such, for the L_3 edge measurements, the harmonic rejection mirrors were removed, and a 1.5 mm aluminium attenuator included. The sample was attached to a copper mount using Apiezon N grease, which was screwed to a cryostat copper finger, which was in turn cooled via thermal contact with a liquid helium bath. All three absorption edges were scanned at a range of temperatures between $4 - 250$ K. The sample was kept under vacuum to avoid oxidation. Finally, the surrounding space was filled with helium gas, in order to minimise beam absorption.

XANES

The XANES analysis will largely be focused on those peaks in intensity which occur at the absorption edge. These correspond to transitions of core electrons into unfilled bound states directly below the continuum, as shown schematically in Figure A.9 (b). Unfortunately, XANES does not lend itself to simplifying assumptions, and it is therefore difficult to relate the specific features at the absorption edge to material properties. Instead, more generally, we may compare the integrated intensities at different absorption edges in order to infer details of the electronic configuration of the scattering ion. For example, via use of the magneto-optical sum rules [208], we can derive the expression

$$\frac{I_{j+}}{I_{j+} + I_{j-}} = \frac{l}{2l-1} - \frac{l-1}{2l-1}\left[\frac{\langle GS|\sum_i l_i \cdot s_i|GS\rangle}{n_h} - \Delta\right], \tag{A.37}$$

where I_x is the intensity about the absorption edge x, l corresponds to the atomic shell in question, n_h is the number of valence holes and Δ is a correction term accounting for the core-hole interaction. This expression relates the so-called branching ratio (left hand side) to the expectation value of the angular part of the valence spin-orbit operator [209]. Therefore, an experimental determination of the branching ratio may be used to determine both the valence state of a specific atomic shell, as well as the configuration of electrons within that shell.

This technique is particularly suitable for the $5f$ shells of actinide metals, due to the strong spin-orbit interaction, and the wealth of prior experimental data [210]. For the uranium $M_{4/5}$ absorption edges, the above expression becomes

$$\frac{I_{M_5}}{I_{M_5}+I_{M_4}} = \frac{3}{5} - \frac{2}{5}\left[\frac{\langle w^{110}\rangle}{n_h^{5f}} - \Delta\right], \tag{A.38}$$

for the $5f$ shell, where w^{110} is the spin-orbit coupling tensor operator [211]. Evaluation of the $M_{4/5}$ intensities, and in particular a comparison between the two, requires careful analysis [209, 212]. With reference to Figure A.14, this analysis proceeds as follows:

(a) In order to facilitate direct comparison, both sets of data are independently normalised such that the pre-edge intensity is approximately zero, and the post-edge intensity approximately one. This is done by fitting the pre- and post-edge data to a straight line (given by the dashed and dotted lines respectively in Figure A.14 (a)), and then normalising the data using

$$f_{norm}(E) = \frac{f(E) - f_{pre}(E)}{f_{post}(E) - f_{pre}(E)}. \tag{A.39}$$

(b) The two curves are then shifted such that the EXAFS overlap (as this should be identical). The origin of the energy scale is chosen to coincide with the maximum of the M_5 spectrum. This makes clear the energy shift between the two maxima, which is proportional to the spin-orbit parameter for the $5f$ states (to be discussed).

(c) Both curves are fit using a pseudo-Voigt function, which is the addition of a Lorentzian and a Gaussian, plus a step function. The step is set to the same energy for both fits, as this represents transitions to the continuum (the exact position is not too important as long as it is identical for both).

(d) The fitted curves are then integrated, and the area under the step function subtracted, in order to give the intensity of the peak. Note the M_4 fits have been multiplied by a factor of $\frac{2}{3}$, to account for there being two-thirds the number of electrons available to transition ($3d_{3/2}$ compared to $3d_{5/2}$).

XANES data for the uranium $M_{4/5}$ edges was taken at a range of temperatures ($4 - 250$ K), at various positions on the sample, and with the beamline direction orientated both parallel and perpendicular to the c-axis. Unfortunately,

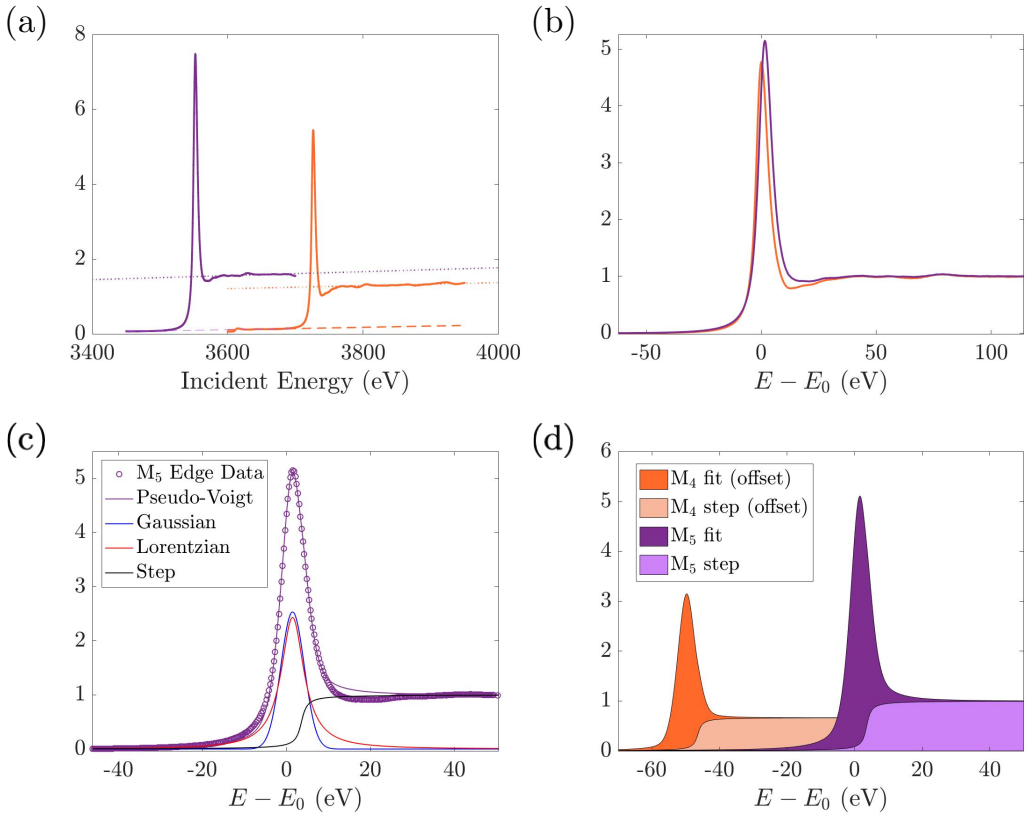

Figure A.14 *Analysis of the uranium M_4 (orange) and M_5 (purple) edge XANES. This data set was taken at 4 K, however the spectra are typical of all $M_{4/5}$ data. All vertical axes are intensity of fluorescence, in arbitrary units. See text for the details of each step.*

irrespective of experimental parameters, the data remained identical within our experimental resolution. Across all measurements, the branching ratio (left-hand side of Equation A.38) for UAu_2 was calculated to be 0.64±0.01. This implies there is no significant change in the valence state of uranium as a function of temperature. Despite this, the XANES can be used to reveal other material properties, as will now be discussed.

As shown in Figure A.14 (b), there is a small energy difference between the M_4 and M_5 peak positions, caused by the spin-orbit splitting of the $5f$ level into a $l \pm s$ $(3\pm\frac{1}{2})$ doublet. Previous studies have used this energy splitting in order to estimate the spin-orbit parameter ξ_f for the $5f$ states, via the relation $\Delta E_{SO} = \frac{7}{2}\xi_f$ [212, 213]. However, in this investigation, the calculated average energy splitting of 2 ± 0.3 eV corresponds to an unreasonably large spin-orbit parameter. This is perhaps due to this procedure only being applicable in

the case of spherically symmetric fields, which may not be the case in UAu_2. Additionally, the peak energy difference may have been skewed by re-absorption effects. Such effects can be quantified by varying the beamline angle of incidence. Unfortunately however, due to time constraints, we were unable to perform these measurements.

Finally, Equation A.38 may be used to determine the $5f$-electron configuration [210], alongside the relation

$$\langle w^{110} \rangle = n_e^{7/2} - \frac{4}{3} n_e^{5/2}. \tag{A.40}$$

From our measurements, the branching ratio (left-hand side of Equation A.38) in UAu_2 has been calculated to be 0.64 ± 0.01. If we then take $n_e^{5f} = 2.7$ (from band structure calculations) and $\Delta = 0.011$ (the calculated free ion value) [213], we have that $n^{7/2} = 1.69$ and $n^{5/2} = 1.01$. This implies there will tend to be more electrons in the lower energy $j = 7/2$ state.

EXAFS

Figure A.15 shows a typical scan of the fluorescence about the uranium L_3 edge. Clearly, the strong peak at the absorption edge is not the only deviation from the ideal step behaviour expected for an isolated atom (Figure A.3), there are also features extending much further in energy above the edge. As mentioned previously, these features are referred to as X-ray absorption fine structure (EXAFS), and result from scattering of the photoelectron. As such, the EXAFS is dependent on the physical environment surrounding the absorbing atom. For energies greater than 50 eV above the edge, single scattering events dominate, and we thus expect the EXAFS to be similar regardless of absorption edge. In the following, we therefore focus on the uranium L_3 edge, which exhibits relatively sharp features as compared to the M_4 and M_5 edges, due to the larger incident energy.

As with the XANES, careful analysis is required in order to extract useful information from the EXAFS data [202]. Specifically, as discussed in Appendix A.1 (culminating in Equation A.25), the post-edge absorption spectrum can be used to determine interatomic distances. As before, the first step is to normalise the data such that the intensities before and after the edge are approximately zero and one respectively. Following this, and with reference to Figure A.16, the analysis

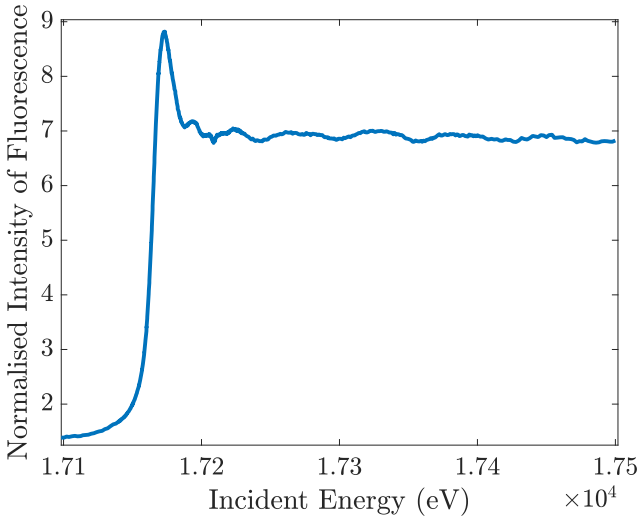

Figure A.15 *Typical fluorescence spectrum around the uranium L_3 absorption edge.*

proceeds as follows:

(a) Similar to Equation A.23, the EXAFS fine structure function can be written as

$$\chi(E) = \frac{\mu(E) - \mu_0(E)}{\Delta\mu_0(E)}, \tag{A.41}$$

where $\mu_0(E)$ is the absorption spectrum for an isolated atom, and $\Delta\mu_0(E)$ is the jump in intensity at the absorption edge. $\chi(E)$ should therefore be a function oscillating about zero.

(b) In order to draw comparisons between $\chi(E)$ and Equation A.25, the X-ray energy E can be converted to the photo-electron wave vector k via use of

$$k = \sqrt{\frac{2m_e(E - E_0)}{\hbar^2}}, \tag{A.42}$$

since, as previously discussed, any excess energy will be given to the photo-electron. E_0 is therefore chosen as the position of the steepest gradient in the original spectrum, as this should correspond to the edge energy. Finally, $\chi(k)k^2$ has been plotted instead of $\chi(k)$, in order to enhance the oscillations at larger k.

(c) $\chi(k)k^2$ can then be Fourier transformed in order to determine the frequency of oscillations, which correspond to the interatomic distances, as shown in

Equation A.25. Before Fourier transforming, the data was multiplied by a window function, so as to remove any anomalous features which might confuse the analysis.

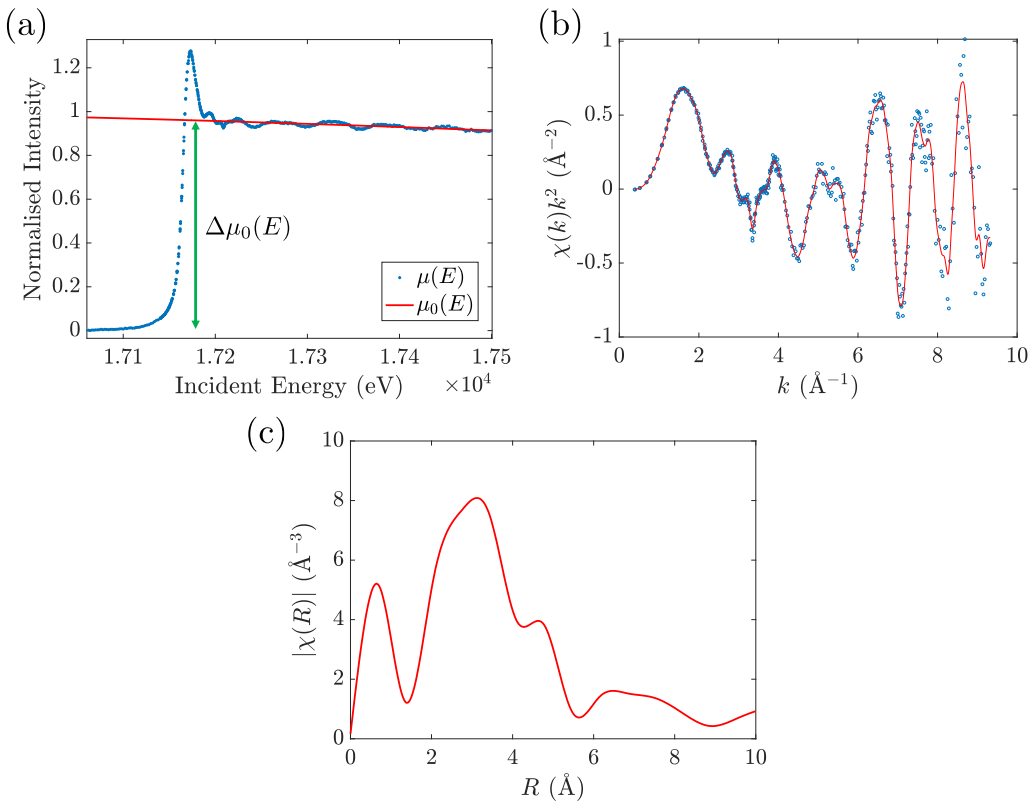

Figure A.16 *Analysis of the uranium L_3 edge EXAFS - see text for the full details of each step. (a) Typical normalised Uranium L_3 absorption spectrum ($\mu(E)$), with the expected isolated atom post-edge spectrum ($\mu_0(E)$) and step increase at the edge ($\Delta\mu_0(E)$) both shown. (b) $\chi(k)k^2$ as a function of photo-electron wave vector k. (c) Magnitude of the Fourier transform of $\chi(k)k^2$, with the peak positions corresponding to interatomic distances.*

As is clear from Figure A.16 (c), this method of determining interatomic distances is not accurate enough to measure changes as a function of temperature. The mean distance over all low temperature (< 50 K) data runs - calculated as the average position of the strongest peak in the Fourier transform - was 3 ± 0.1 Å. The higher temperature data was discarded due to inaccuracies resulting from thermal motion. The calculated value is approximately consistent with the U-U nearest neighbour distance of 3.11 Å [171], measured by X-ray diffraction. However, the small discrepancy may be corrected for with the inclusion of the scattering phase-shift δ (Equation A.25).

Finally, we note some points of interest regarding the uranium L_3 edge:

(i) [214] has plotted the L_3 edge peak position - normalised by the peak position for α-uranium - against the Sommerfeld coefficient γ (Section 1.3) for a number of uranium intermetallics. As shown in Figure A.17 (a), this exhibits a negative correlation. In uranium compounds, the Sommerfeld coefficient provides some measure of the degree of localisation of the f-electrons, as it is proportional to the effective carrier mass. With increased localisation, there are more f-electrons available to screen the $2p^{3/2}$ electrons, which therefore require more energy to excite. This results in the L_3 edge occurring at a higher energy, and ΔE_α being more negative, as observed. Note however, all the Sommerfeld coefficients included in Figure A.17 (a) have been estimated at temperatures above any magnetic transitions, in order to remove the effect of changes due to magnetic degrees of freedom. As shown in Figure A.17 (a), UAu_2 - with $\Delta E_\alpha \sim -1$ eV and $\gamma \sim 0.14$ $JK^{-2}mol^{-1}$ (taken from the ferrimagnetic state data) - similarly follows this trend.

(ii) UAu_2 oxidises readily in air; this was a potential source of error. However, previous studies [207] have shown that samples containing oxidised uranium will exhibit two distinctive peaks near to the absorption edge. As shown in Figure A.17 (b), similar features are not present in the UAu_2 data, implying the sample was not oxidised for these measurements.

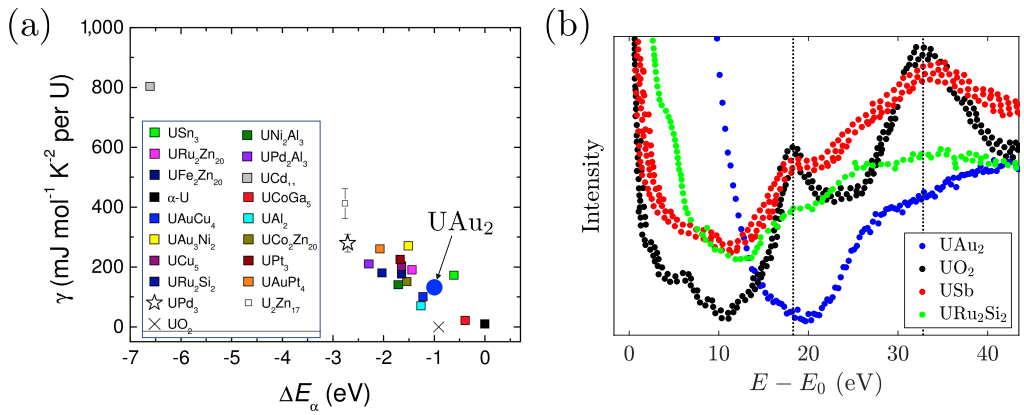

Figure A.17 *(a) L_3 absorption edge peak position (subtracted from the α-U peak position) plotted against the Sommerfeld coefficient for a number of uranium compounds, as compared to the UAu_2 values. Figure amended from [214]. (b) Comparing near-edge features for different uranium compounds. UO_2 (black) exhibits two distinct peaks, also observed in oxidised samples (as the red USb data shows). The absence of these peaks, as for URu_2Si_2 (green) and UAu_2 (blue) implies there is no oxidation. Figure amended from [207].*

Appendix B

Specific Heat Analysis

Section 2.3 describes the 2-τ model - a technique for determining the specific heat of a material via the relaxation time method. This is the technique that was employed to analyse the higher temperature specific heat data, taken using the heat capacity option on a Quantum Design PPMS. Instead, for measurements at mK temperatures, we have developed our own experimental setup. As discussed in Section 2.3, in order to maximise the sensitivity over the full range of temperatures, this setup swaps the thermometer/heater component at ~ 200 mK. As a result, the 'heater' resistance will have some temperature dependence, and it is therefore extremely difficult to apply a constant power to the sample, as required by the 2-τ model. We have therefore designed a bespoke analysis better suited to our experimental procedure. Thanks go to Andrew Huxley for the development of this analysis.

Generalised Heat Flow Equation

We begin in the same manner as the 2-τ model, by considering that the system is described by the thermal circuit in Figure 2.10. We include a finite thermal resistance r between the sample (T) and the sample platform (T_a), and also a thermal resistance R between the sample platform and the thermal reservoir (T_0). The heater power is given by $P_H(t)$. However, unlike the 2-τ model, we disregard the addenda specific heat in the knowledge that it may simply be subtracted from the final calculated value. Similar to Equations 2.25 and 2.26, the heat flow

equations will be

$$P_H(t) = \frac{T_a(t) - T_0(t)}{R} + \frac{T_a(t) - T(t)}{r}, \tag{B.1}$$

where we have allowed for some variation in the temperature of the thermal reservoir, and

$$C\frac{dT}{dt} = -\frac{T(t) - T_a(t)}{r}. \tag{B.2}$$

In what follows, we drop the explicit time dependence.

Equation B.1 may be rearranged to give

$$\frac{T}{r} = \frac{T_a}{R_\parallel} - \frac{T_0}{R} - P_H, \tag{B.3}$$

where

$$\frac{1}{R_\parallel} = \frac{1}{R} + \frac{1}{r} = \frac{R+r}{Rr} = \frac{R_S}{Rr}. \tag{B.4}$$

Equation B.3 can then be differentiated with respect to time and, after substituting in Equation B.2, we arrive at (after some rearranging)

$$R_S C\dot{T}_a + T_a = RP_H + R_S R_\parallel C\dot{P}_H + rC\dot{T}_0 + T_0, \tag{B.5}$$

where an overdot indicates a derivative taken with respect to time. In order to simplify this expression, we note that (from the discussions in Section 2.3) the sample specific heat may also be expressed $\tau = R_S C$. Equation B.5 can therefore be rewritten

$$\tau\dot{T}_a + T_a = \tau e^{-t/\tau}\left[\dot{T}_a e^{t/\tau} + \frac{T_a e^{t/\tau}}{\tau}\right] = \tau e^{-t/\tau}\frac{d}{dt}(T_a e^{t/\tau}). \tag{B.6}$$

and then integrated to give

$$T_a e^{t/\tau} - T_1 = \frac{R}{\tau}\int_0^t P_H e^{t/\tau}dt + \frac{R_S R_\parallel C}{\tau}\int_0^t \dot{P}_H e^{t/\tau}dt + \frac{rC}{\tau}\int_0^t \dot{T}_0 e^{t/\tau}dt + \frac{1}{\tau}\int_0^t T_0 e^{t/\tau}dt, \tag{B.7}$$

where $T_a(t=0) = T_1$. Note that, unlike with the analyses in Section 2.3, the above expression can account for a variable power supplied by the heater.

Correcting for Discrete Data Points

Up to this point, the derivation has been completely general - we will now begin to tailor the analysis to suit our experiment. Firstly, let us correct for the fact that an experiment will take discrete data points, rather than measuring variables continuously as a function of time. As such, the power may be divided into n discrete values, with $P_H(t) = P_n$ (a constant) between t_n and t_{n+1}. The integrals in Equation B.7 may therefore be replaced by summations, giving

$$T_a e^{t/\tau} - T_1 = \frac{R}{\tau}\left[\sum_{i=1,n} P_{i-1}(e^{t_i/\tau} - e^{t_{i-1}/\tau}) + P_n(e^{t/\tau} - e^{t_n/\tau})\right] + R_{\|}\left[\sum_{i=1,n}(P_i - P_{i-1})e^{t_i/\tau}\right] + T_0(e^{t/\tau} - 1), \quad \text{(B.8)}$$

where we have assumed that $T_0(t) = T_0(0)$, or that the thermal reservoir remains at a constant temperature (this will be corrected for in the next section). Finally, the above expression may be simplified to give

$$T_a = T_0 + \Delta T e^{-t/\tau} + RP_n - RP_0 e^{-t/\tau} - \sum_{i=1,n}(R - R_{\|})(P_i - P_{i-1})e^{-(t-t_i)/\tau}, \quad \text{(B.9)}$$

where $\Delta T = T_1 - T_0$ will vanish if the system is in thermal equilibrium at $t = 0$.

The above expression gives the temperature measured at a time t as a function of the power supplied to the sample. However, importantly, it considers that *all* the constant power steps prior to t will have an impact, but with an exponentially decreasing influence on the current temperature as we move back in time. This expression can therefore account for changes in the power applied by the heater, unlike the 2-τ model, which relies on a constant power in order to be an effective analysis.

At each measured data point, we have $T_a(t)$ and $\sum_{i=0}^{n} P_n$ extending back to the start of the measurement. From the above expression, the constants T_0, R, $R_{\|}$ and τ may be determined - at each data point - using a nonlinear least-squares method. Finally, the specific heat may be calculated from

$$C = \frac{R_S}{\tau} = \frac{R + R_{\|}}{\tau}. \quad \text{(B.10)}$$

To aid this fitting procedure, the sample stage is maintained at a constant temperature, such that the value of T_0 can be constrained by a measurement of the sample stage thermometer. Also, as discussed in Section 2.3, the thermal conductance of the gold wires (which make the thermal link between the sample platform and thermal reservoir) should - at mK temperatures - be linear in temperature. A plot of $1/R$ should therefore give a straight line, and thus acts as a useful sanity check in this procedure. This is shown in Figure 2.15.

Correcting for Variable T_0

In order to widen the scope of the above fitting procedure, we consider that the temperature of the thermal reservoir might vary as $T_0(t) = T_0(0) + \delta T_0(t)$. The final term in Equation B.8 now reads

$$\frac{rC}{\tau}\int_0^t \dot{\delta T_0} e^{t/\tau} dt + \frac{1}{\tau}\int_0^t \delta T_0 e^{t/\tau} dt + T_0(e^{t/\tau} - 1), \tag{B.11}$$

where again the explicit time dependence has been dropped. With the inclusion of this additional correction term, the fitting function (Equation B.9) becomes

$$\begin{aligned} T_a = T_0 + \Delta T e^{-t/\tau} + RP_n - RP_0 e^{-t/\tau} - \sum_{i=1,n} (R - R_\parallel)(P_i - P_{i-1}) e^{-(t-t_i)/\tau} \\ + \frac{R_\parallel}{R}(\delta T_0(t) - \delta T_0(0) e^{-t/\tau}) + \frac{e^{-t/\tau}}{\tau}\left(1 - \frac{R_\parallel}{R}\right)\left[\int_0^t \delta T_0 e^{-t/\tau} dt\right], \end{aligned} \tag{B.12}$$

and the specific heat may be determined in a similar fashion as before. In our investigations, δT_0 is measured by a third thermometer attached to the sample stage (not the sample stage thermometer).

Avoiding Errors from Temperature Calibration

The accuracy of the above expression in determining the specific heat is heavily reliant on the thermometer calibration to give T_a. This calibration procedure is described in Section 2.1. However, as we will now show, this reliance can be avoided, as the specific heat may be determined directly from the thermometer resistance.

If the thermometer is suitably chosen, the measured temperature T_a should have a one-to-one correspondence with the thermometer resistance, which we label ρ.

The constant T_0 fitting function (Equation B.9) might therefore be expressed

$$\rho = \rho_0 + \Delta\rho e^{-t/\tau} + \bar{R}P_n - \bar{R}P_0 e^{-t/\tau} - \sum_{i=1,n} (\bar{R} - \bar{R}_{\|})(P_i - P_{i-1}) e^{-(t-t_i)/\tau}. \quad \text{(B.13)}$$

In this expression, due to the change of variables, $\bar{R}$ and $\bar{R}_{\|}$ will no longer correspond to the actual thermal resistances, hence the change of notation. In fact, the two are related by

$$\bar{R} = R\frac{d\rho}{dT_a}, \quad \text{(B.14)}$$

which follows from differentiating Equations B.9 and B.13, then comparing P_0 coefficients. Using Equation B.13, the thermometer resistance heating/cooling profile can be fit in a similar manner to before, in order to determine the fitting parameters T_0, $\bar{R}$, $\bar{R}_{\|}$ and τ.

With some work, the specific heat can then be calculated from these parameters. Specifically, from Equation B.10, we have that

$$\begin{aligned} C = \frac{\tau}{R_S} = \frac{\tau}{R + r} &= \frac{\tau}{R\Big(1 + \frac{R_{\|}}{R - R_{\|}}\Big)} \\ &= \tau\left[\bar{R}\Big(1 + \frac{\bar{R}_{\|}}{\bar{R} - \bar{R}_{\|}}\Big)\frac{dT_a}{d\rho}\right]^{-1}, \end{aligned} \quad \text{(B.15)}$$

The final piece of the puzzle is therefore to determine $\frac{dT_a}{d\rho}$. From Equation B.13, we have that $\bar{R} = \frac{\Delta\rho}{P}$, which implies (from Equation B.14) that

$$\frac{\Delta\rho}{P} = R\frac{d\rho}{dT_a}. \quad \text{(B.16)}$$

Hence, if the thermal resistance R is known, the specific heat may be calculated.

At this point, we again reference our own experimental setup, and that the thermal conductance $1/R$ should be approximately linear in temperature. This implies that

$$\frac{1}{R}\frac{dT_a}{d\rho} = K_1 T\frac{dT_a}{d\rho}, \quad \text{(B.17)}$$

where K_1 is a constant, and so

$$\frac{K_1}{2}\frac{dT_a^2}{d\rho} = \frac{P}{\Delta\rho}. \quad \text{(B.18)}$$

Finally, this may be integrated over ρ to give

$$T_a(\rho) = \sqrt{[T_a(\rho_0)]^2 + \frac{2}{K_1}\int_{\rho_0}^{\rho} \frac{P}{\Delta\rho} d\rho}. \tag{B.19}$$

Hence, a fit of T_a against ρ can be used to determine the coefficient K_1, and the specific heat may be calculated as

$$C = \tau\left[\bar{R}\Big(1 + \frac{\bar{R}_{\|}}{\bar{R} - \bar{R}_{\|}}\Big)\frac{P}{\Delta\rho K_1 T}\right]^{-1}. \tag{B.20}$$

Note that, although this procedure does use a function to link the thermometer resistance to a temperature, this is only necessary for determining a single coefficient K_1. This method therefore does not rely on an accurate temperature calibration to determine the specific heat. However, as is clear from Figure 2.2, our thermometer calibrations are often sufficiently accurate that this procedure is unnecessary.

Corrections at Higher Temperatures

At higher temperatures, the phonon T^3 contribution (Section 1.3) to the thermal resistance R must be considered. Equation B.18 will therefore instead read

$$\frac{d}{d\rho}\left(\frac{K_1 T^2}{2} + \frac{K_3 T^4}{4}\right) = \frac{P}{\Delta\rho}, \tag{B.21}$$

where K_3 is a second constant. Regardless, an identical procedure may be used to calculate the specific heat, albeit with two coefficients to be determined from the temperature-resistance fit. If the above equation is integrated - and following some algebra - the resulting fitting function will be

$$T_a(\rho) = \sqrt{\left(\frac{2}{K_1}\int_{\rho_0}^{\rho}\frac{P}{\Delta\rho}d\rho + [T_a(\rho_0)]^2\right) - \frac{K_3}{2K_1}\left(\frac{2}{K_1}\int_{\rho_0}^{\rho}\frac{P}{\Delta\rho}d\rho + [T_a(\rho_0)]^2\right)^2}, \tag{B.22}$$

from which the specific heat

$$C = \tau\left[\bar{R}\Big(1 + \frac{\bar{R}_{\|}}{\bar{R} - \bar{R}_{\|}}\Big)\frac{P}{\Delta\rho(K_1 T_a + K_3 T_a^3)}\right]^{-1} \tag{B.23}$$

may be calculated.

Appendix C

The Schottky Anomaly

The Schottky anomaly corresponds to a peak in the low temperature specific heat [215]. This occurs for a system with a limited number of energy levels, for which - as each new energy level becomes available with increasing temperature - the internal energy E will increase in sharp steps. The heat capacity, given by dE/dT, will therefore exhibit sharp maxima as a function of temperature. Consider the simplest example of a two-level system, separated in energy by Δ. Only at temperatures comparable to Δ will transitions between the two levels occur in appreciable amounts. This corresponds to a rapidly changing internal energy, and a Schottky anomaly, or a peak, in the heat capacity.

As an example, consider a system of spin-S moments under the influence of a magnetic field [216]. These moments can lie in $2S + 1(= m)$ orientations with respect to this field, each with an energy ε_r, and a degeneracy g_r. From Boltzmann statistics, the probability of a single moment occupying the rth level is

$$P_r = \frac{g_r e^{-\varepsilon_r/k_B T}}{\sum_m g_m e^{-\varepsilon_m/k_B T}}. \tag{C.1}$$

For a system of N particles, the internal energy will therefore be

$$E = \frac{N \sum_m \varepsilon_m g_m e^{-\varepsilon_m/k_B T}}{\sum_m g_m e^{-\varepsilon_m/k_B T}}. \tag{C.2}$$

Assuming the levels have an equal degeneracy, this may then be differentiated with respect to temperature to give the heat capacity per mole of Schottky centres

[35],

$$C_{sch} = \frac{R}{T^2}\left[\frac{1}{Z}\sum_i \Delta_i^2 e^{-\Delta_i/T} - \left(\frac{1}{Z}\sum_i \Delta_i e^{-\Delta_i/T}\right)^2\right], \tag{C.3}$$

where Z is the partition function, R the gas constant and $\Delta_i = \varepsilon_i/k_B$, with k_B the Boltzmann constant.

For the simplest case of a two level system, and setting $\varepsilon_0 = 0$, the energy reduces to

$$E = \frac{N\varepsilon_1 g_1 e^{-\varepsilon_1/k_B T}}{g_0 + g_1 e^{-\varepsilon_1/k_B T}}, \tag{C.4}$$

from which it follows that the heat capacity is given by

$$C_{sch} = R\left(\frac{\Delta}{T}\right)^2 \frac{g_0}{g_1}\frac{e^{\Delta/T}}{(1+(g_0/g_1)e^{\Delta/T})^2}, \tag{C.5}$$

where $\Delta = \varepsilon_1/k_B$ is the energy separation, measured in Kelvin. Note that, in a range of systems, at sufficiently low temperature there will only be two energy levels to consider. Hence, this model is often physically realised.

Some general statements from the above:

- The temperature at which the Schottky peak occurs is entirely determined by the energy splitting Δ. The height of the peak is dependent on the number of energy levels. For example, for a two-level system with equal degeneracy, the maximum will occur at a temperature $\sim 0.42\Delta$, and will always peak at ~ 3.6 JK^{-1}mol^{-1} $(0.44R)$.

- Regardless of the energy splitting or number of levels, the high temperature Schottky contribution may be approximated by A_{sch}/T^2, where A_{sch} is a constant.

- The entropy is given by the integral of C/T. For a two level system, the entropy is therefore $R\ln[1 + g_1/g_0]$. For a system with n levels, each of which has the same degeneracy, the entropy will be $R\ln n$.

Some of these points are illustrated in Figure C.1.

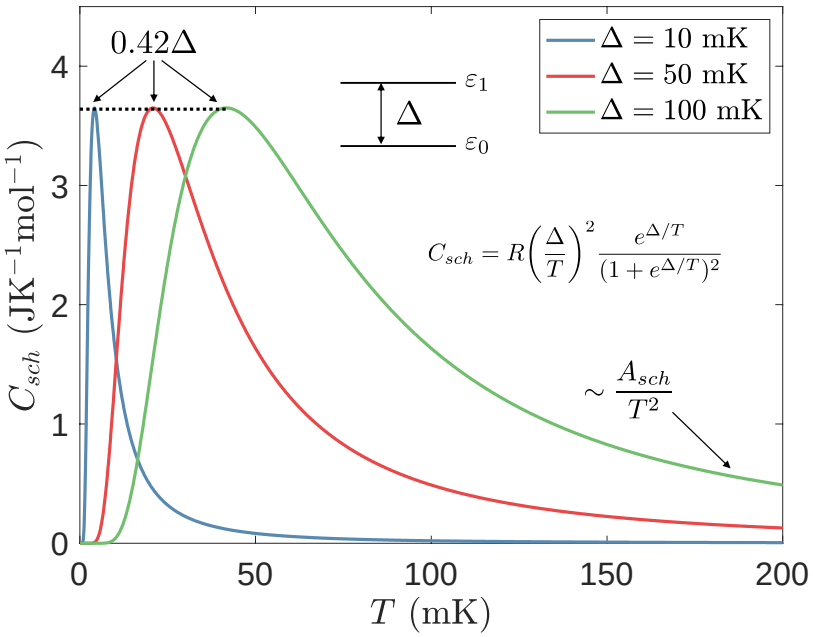

Figure C.1 *The Schottky anomaly for a two level system with equal degeneracy, for 3 different energy splittings. Shown to illustrate the consistent peak height and position (as a function of Δ), as well as the T^{-2} behaviour at higher temperatures.*

The Nuclear Quadrupole Schottky Effect

The Schottky anomaly only requires that there be isolated, discrete energy levels, separated by a similar energy to the temperature under consideration. As such, the phenomenon is not restricted to systems of magnetic moments. A range of materials - including both the heavy fermion compounds from Section 5 - exhibit a Schottky anomaly at the lowest measurable temperatures [196]. In the majority of cases, this can be attributed to the interaction of a nuclear quadrupole moment with an electric field gradient (EFG).

To understand the electric quadrupole moment, consider the electrostatic potential for a charge distribution ρ,

$$V(\mathbf{r}) = \frac{1}{4\pi\varepsilon_0}\int \frac{\rho(\mathbf{r}')}{|\mathbf{r}-\mathbf{r}'|}d^3r'. \tag{C.6}$$

For $\mathbf{r} >> \mathbf{r}'$, this may be expanded as

$$V(\mathbf{r}) = \frac{1}{4\pi\varepsilon_0 r}\int \rho(\mathbf{r}')\left[1 - \frac{\hat{\mathbf{r}}\cdot\mathbf{r}'}{r} + \frac{1}{2r^2}[3(\hat{\mathbf{r}}\cdot\mathbf{r}')^2 - r'^2] + \mathcal{O}\left(\frac{r'}{r}\right)^3\right]d^3r', \tag{C.7}$$

or as a multipole expansion [217],

$$V(\mathbf{r}) = V_{mon}(\mathbf{r}) + V_{dip}(\mathbf{r}) + V_{quad}(\mathbf{r}) + \dots . \tag{C.8}$$

In the above expression, each subsequent term essentially adds dimensionality in describing the charge distribution - the monopole potential is that due to a point charge, whereas the quadrupole term requires a three dimensional distribution. Additionally, higher order terms will interact differently with an external potential. For example, a quadrupole moment will feel the influence of an EFG (or the second spatial derivative of an external potential), whereas an electric monopole will not. This is illustrated in Figure C.2.

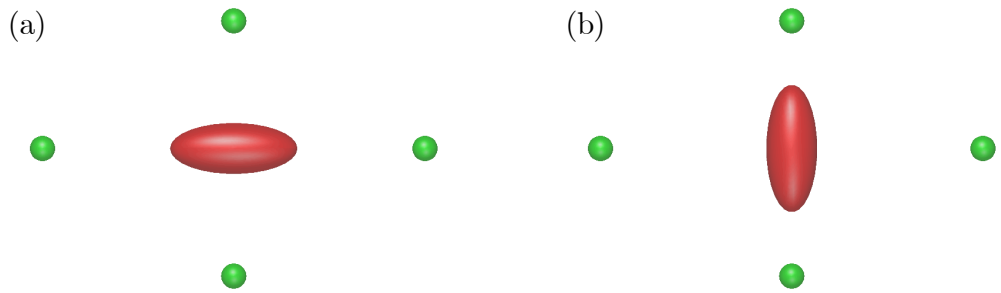

Figure C.2 *Two different configurations for a nucleus (red) with a non-zero quadrupolar moment sitting in an electric field gradient, caused by negative charges of equal magnitude (green). The configuration in (a) is less energetically favourable.*

In order to make the above more tangible, consider the pertinent example of an atomic nucleus, the energy levels of which will be determined by its interaction with an external potential. In a crystalline environment, the nucleus will sit in a position of zero electric field. If we further treat the situation where there is zero magnetic field, the lowest order interaction will be that between the nuclear electric quadrupole moment and the crystalline EFG.

Classically, and in Cartesian coordinates, this interaction energy is given by

$$E_Q = \frac{1}{6} \sum_{i,j=x,y,z} \mathcal{Q}_{ij} V_{ij}, \tag{C.9}$$

where $\mathcal{Q}_{ij}$ and V_{ij} are second rank tensors describing the quadrupolar moment and the EFG respectively [218]. From Equation C.7, the quadrupolar moment

may be written

$$\mathcal{Q}_{ij} = \int \rho(3r_i r_j - r^2\delta_{ij})d^3r. \tag{C.10}$$

However, for an atomic nucleus, and in anticipation of what follows, it will be useful to rewrite this using the quantum operator formalism [217], or as

$$\hat{\mathcal{Q}}_{ij} = \frac{eQ}{6I(2I-1)}\left[\frac{3}{2}(\hat{I}_i\hat{I}_j + \hat{I}_j\hat{I}_i) - \delta_{ij}\hat{I}^2\right], \tag{C.11}$$

where I is the total spin component of the nucleus and $\hat{I}$ are the spin operators. Q is the scalar nuclear quadrupole moment, which is a measure of the degree to which the charge distribution is ellipsoidal. To make this clearer, this may be expressed

$$Q = \sum_i \rho_i(3\cos^2\theta_i - 1)r_i^2, \tag{C.12}$$

or as a sum of elements of nuclear charge ρ_i, each specified in cylindrical coordinates. As such, a spherical charge distribution will have $Q = 0$, whereas a prolate (oblate) distribution will have $Q > 0$ ($Q < 0$). This parameter has been experimentally determined for a range of isotopes, primarily by nuclear quadrupole resonance [219]. Finally, the EFG is given by

$$V_{ij} = \left.\frac{\partial^2 V}{\partial r_i \partial r_j}\right|_{r=0}. \tag{C.13}$$

Before writing the quadrupolar Hamiltonian, we can first simplify the problem significantly by transforming to a coordinate system in which the EFG tensor is diagonalised, referred to as the principal coordinate system. Further, Laplace's equation gives that $V_{xx} + V_{yy} + V_{zz} = 0$, implying that the EFG tensor is fully defined by just two parameters. By convention, these are

$$eq = V_{zz} \tag{C.14}$$

where V_{zz} is the largest component of the EFG in the principal coordinate system, and

$$\eta = \frac{V_{xx} - V_{yy}}{V_{zz}}, \tag{C.15}$$

which is the asymmetry parameter, with $0 < \eta < 1$ necessarily satisfied in the principal coordinate system. Finally, we can write the quadrupolar Hamiltonian

$$\mathcal{H}_Q = \frac{e^2qQ}{4I(2I-1)}[3\hat{I}_z^2 - \hat{I}^2 + \eta(\hat{I}_x^2 - \hat{I}_y^2)]. \tag{C.16}$$

For an axially symmetric EFG (and therefore $\eta = 0$), this leads straightforwardly to

$$E_m = \frac{e^2qQ}{4I(2I-1)}[3m^2 - I(I+1)], \tag{C.17}$$

where $m = -I, -I+1, \ldots, I-1, I$, such that the energy levels are doubly degenerate. From the above, a nucleus with $I = 1/2$ will have just one energy level, and cannot, therefore, give a Schottky anomaly. Although this might have been established previously, from the fact that a spin-1/2 nucleus must have a spherically symmetric charge distribution, and thus no quadrupole moment. Finally, for the more general case of $\eta \neq 0$, closed form solutions are only possible for $I = 1$ or $I = 3/2$ [219].

Clearly then, the interaction between a nuclear quadrupole moment and an EFG has the necessary features to give a Schottky anomaly in the specific heat. However, from Equation C.3, the exact form of this Schottky term becomes increasingly complex with additional energy levels. Therefore, in order to draw meaningful comparison with experimental data, we instead consider only the first term of the expansion in powers of T^{-1} [196],

$$C_{sch} = \frac{R}{40}\frac{(I+1)(2I+3)}{2I(2I-1)}\left[\frac{e^2qQ}{k_BT}\right]^2, \tag{C.18}$$

which gives the heat capacity per mole of Schottky centres. As discussed, in the majority of systems, the energy splitting due to the nuclear quadrupole moment is on the order of mK, which justifies cutting the expansion after the first term. Finally, as is standard for a Schottky anomaly, the above expression has the approximate form $A_{sch}T^{-2}$ at high temperatures.

Bibliography

[1] P. Bruno, *The Berry Phase in Magnetism and the Anomalous Hall Effect*, in *Handbook of Magnetism and Advanced Magnetic Materials* (John Wiley & Sons, Ltd, 2007), pp. 540–558 (cited on page 3).

[2] M. Berry, *The Geometric Phase*, Scientific American **259** (1988) (6), pp. 46–52 (cited on page 5).

[3] D. Xiao, M.-C. Chang and Q. Niu, *Berry phase effects on electronic properties*, Rev. Mod. Phys. **82** (2010) (3), pp. 1959–2007 (cited on pages 6, 11, 11).

[4] M. Berry, *Quantal Phase Factors Accompanying Adiabatic Changes*, Proc. Royal Soc. A **392** (1984), pp. 45–57 (cited on page 6).

[5] D. Tong, *Lectures on the Quantum Hall Effect* (2016) (cited on page 6).

[6] C. L. Kane, *Topological Band Theory and the Z2 Invariant*, in *Topological Insulators* (Elsevier, 2013), vol. 6, pp. 3–34 (cited on pages 7, 85).

[7] B. A. Bernevig and T. L. Hughes, *Topological Insulators and Topological Superconductors* (Princeton University Press, 2013) (cited on pages 7, 83).

[8] K. v. Klitzing, G. Dorda and M. Pepper, *New Method for High-Accuracy Determination of the Fine-Structure Constant Based on Quantized Hall Resistance*, Phys. Rev. Lett. **45** (1980) (6), pp. 494–497 (cited on page 9).

[9] D. J. Thouless, M. Kohmoto, M. P. Nightingale and M. den Nijs, *Quantized Hall Conductance in a Two-Dimensional Periodic Potential*, Phys. Rev. Lett. **49** (1982) (6), pp. 405–408 (cited on page 10).

[10] R. Karplus and J. M. Luttinger, *Hall Effect in Ferromagnetics*, Phys. Rev. **95** (1954) (5), pp. 1154–1160 (cited on page 10).

[11] G. Sundaram and Q. Niu, *Wave-packet dynamics in slowly perturbed crystals: Gradient corrections and Berry-phase effects*, Phys. Rev. B **59** (1999) (23), pp. 14915–14925 (cited on page 10).

[12] S. Murakami, N. Nagaosa and S.-C. Zhang, *Dissipationless Quantum Spin Current at Room Temperature*, Science **301** (2003) (5638), pp. 1348 LP – 1351 (cited on page 11).

[13] R. Matsumoto and S. Murakami, *Rotational motion of magnons and the thermal Hall effect*, Phys. Rev. B **84** (2011) (18), p. 184406 (cited on page 11).

[14] S. Murakami and A. Okamoto, *Thermal Hall Effect of Magnons*, J. Phys. Soc. Jpn **86** (2016) (1), p. 11010 (cited on pages 12, 101).

[15] J. M. Ziman, *Electrons and Phonons: The Theory of Transport Phenomena in Solids* (Oxford University Press, 1960) (cited on pages 14, 47, 121).

[16] Y. Onose, T. Ideue, H. Katsura, Y. Shiomi, N. Nagaosa and Y. Tokura, *Observation of the Magnon Hall Effect*, Science **329** (2010) (5989), pp. 297–299 (cited on pages 15, 96, 98, 98, 99, 102, 102, 103, 103).

[17] T. Ideue, Y. Onose, H. Katsura, Y. Shiomi, S. Ishiwata, N. Nagaosa and Y. Tokura, *Effect of lattice geometry on magnon Hall effect in ferromagnetic insulators*, Phys. Rev. B **85** (2012) (13), p. 134411 (cited on pages 99, 100, 101).

[18] M. Hirschberger, R. Chisnell, Y. S. Lee and N. P. Ong, *Thermal Hall Effect of Spin Excitations in a Kagome Magnet*, Phys. Rev. Lett. **115** (2015) (10), p. 106603 (cited on page 15).

[19] V. P. Mineev and K. V. Samochin, *Introduction to Unconventional Superconductivity* (Gordon and Breach Science Publishers, 1998) (cited on pages 17, 18, 20).

[20] P. Coleman, *Introduction to Many-Body Physics* (Cambridge University Press, 2015) (cited on pages 18, 136, 140).

[21] M. Sigrist, *Introduction to unconventional superconductivity*, in *AIP Conference Proceedings* (American Institute of Physics, 2005), vol. 789, pp. 165–243 (cited on pages 18, 32, 32, 37).

[22] J. F. Annett, *Superconductivity, superfluids and condensates*, vol. 5 (Oxford University Press, 2004) (cited on page 20).

[23] O. Shevtsov and J. A. Sauls, *Electron bubbles and Weyl fermions in chiral superfluid ^3He-A*, Phys. Rev. B **94** (2016) (6), p. 64511 (cited on pages 20, 116, 116, 117).

[24] V. Ngampruetikorn and J. A. Sauls, *Impurity-Induced Anomalous Thermal Hall Effect in Chiral Superconductors*, Phys. Rev. Lett. **124** (2020) (15), p. 157002 (cited on pages 20, 112, 115, 117, 117, 129, 130).

[25] P. Berglund, *Picture Archive of the Low Temperature Laboratory* (cited on page 22).

[26] J. F. Annett, *Symmetry of the order parameter for high-temperature superconductivity*, Advances in Physics **39** (1990) (2), pp. 83–126 (cited on page 23).

[27] D. Braithwaite, M. Vališka, G. Knebel, G. Lapertot, J.-P. Brison, A. Pourret, M. E. Zhitomirsky, J. Flouquet, F. Honda and D. Aoki, *Multiple superconducting phases in a nearly ferromagnetic system*, Commun. Phys **2** (2019) (1), p. 147 (cited on pages 25, 155, 157, 162, 162, 164, 168).

[28] P. Goswami and A. H. Nevidomskyy, *Topological Weyl superconductor to diffusive thermal Hall metal crossover in the B phase of UPt_3*, Phys. Rev. B **92** (2015) (21), p. 214504 (cited on pages 26, 112, 112, 113, 113, 115, 117, 130).

[29] L. Jiao, S. Howard, S. Ran, Z. Wang, J. O. Rodriguez, M. Sigrist, Z. Wang, N. P. Butch and V. Madhavan, *Chiral superconductivity in heavy-fermion metal UTe_2*, Nature **579** (2020) (7800), pp. 523–527 (cited on pages 26, 155, 155, 157, 162, 162, 164).

[30] M. Takeshi, T. Yasumasa, K. Takuto, S. Masatoshi, I. Masanori and M. Kazushige, *Symmetry-Protected Topological Superfluids and Superconductors - From the Basics to ^3He*, J. Phys. Soc. Jpn **85** (2016) (2), p. 22001 (cited on page 26).

[31] J. Alicea, *New directions in the pursuit of Majorana fermions in solid state systems*, Rep. Prog. Phys **75** (2012) (7), p. 76501 (cited on page 26).

[32] M. Sato and Y. Ando, *Topological superconductors: a review*, Rep. Prog. Phys **80** (2017) (7), p. 76501 (cited on page 26).

[33] A. P. Schnyder and P. M. R. Brydon, *Topological surface states in nodal superconductors*, J. Phys. Condens. Matter **27** (2015) (24), p. 243201 (cited on pages 27, 113).

[34] X. Wan, A. M. Turner, A. Vishwanath and S. Y. Savrasov, *Topological semimetal and Fermi-arc surface states in the electronic structure of pyrochlore iridates*, Phys. Rev. B **83** (2011) (20), p. 205101 (cited on page 28).

[35] A. Tari, *The Specific Heat of Matter at Low Temperatures* (Imperial College Press, 2003) (cited on pages 30, 33, 88, 212).

[36] G. Grosso and G. P. Parravicini, *Solid State Physics* (Elsevier Science, 2000) (cited on page 31).

[37] M. Tinkham, *Introduction to Superconductivity*, 2 ed. (Dover Publications, 2004) (cited on pages 31, 168).

[38] P. J. Hirschfeld, P. Wölfle and D. Einzel, *Consequences of resonant impurity scattering in anisotropic superconductors: Thermal and spin relaxation properties*, Phys. Rev. B **37** (1988) (1), pp. 83–97 (cited on pages 32, 167).

[39] T. M. Tritt, *Thermal Conductivity: Theory, Properties, and Applications*, Physics of Solids and Liquids (Springer US, 2005) (cited on pages 33, 34, 47, 48, 58, 93).

[40] R. Gagnon, S. Pu, B. Ellman and L. Taillefer, *Anisotropy of Heat Conduction in $YBa_2Cu_3O_{6.9}$: A Probe of Chain Superconductivity*, Phys. Rev. Lett. **78** (1997) (10), pp. 1976–1979 (cited on page 36).

[41] H. Shakeripour, C. Petrovic and L. Taillefer, *Heat transport as a probe of superconducting gap structure*, New J. Phys **11** (2009) (5), p. 55065 (cited on pages 36, 37).

[42] C. Strohm, G. L. J. A. Rikken and P. Wyder, *Phenomenological Evidence for the Phonon Hall Effect*, Phys. Rev. Lett. **95** (2005) (15), p. 155901 (cited on page 38).

[43] T. Ideue, T. Kurumaji, S. Ishiwata and Y. Tokura, *Giant thermal Hall effect in multiferroics.*, Nat. Mater **16** (2017) (8), pp. 797–802 (cited on page 38).

[44] J. Ekin, *Experimental Techniques for Low-Temperature Measurements: Cryostat Design, Material Properties and Superconductor Critical-Current Testing* (Oxford University Press, 2006) (cited on pages 41, 42, 53, 56, 95).

[45] R. G. Goodrich, D. Hall, E. Palm and T. Murphy, *Magnetoresistance below 1K and temperature cycling of ruthenium oxide-bismuth ruthenate cryogenic thermometers*, Cryogenics **38** (1998) (2), pp. 221–225 (cited on page 44).

[46] S. S. Courts and P. R. Swinehart, *Stability of Cernox Resistance Temperature Sensors BT - Advances in Cryogenic Engineering* (Springer US, 2000), pp. 1841–1848 (cited on page 44).

[47] R. I. Amils, J. D. Gallego, J. L. Sebastián, S. Muñoz, A. Martín and A. Leuther, *Thermal conductivity of silver loaded conductive epoxy from cryogenic to ambient temperature and its application for precision cryogenic noise measurements*, Cryogenics **76** (2016) (C), pp. 23–28 (cited on page 51).

[48] R. A. Matula, *Electrical resistivity of copper, gold, palladium, and silver*, J. Phys. Chem. Ref. Data **8** (1979) (4), pp. 1147–1298 (cited on page 51).

[49] M. Barucci, E. Gottardi, I. Peroni and G. Ventura, *Low temperature thermal conductivity of Kapton and Upilex*, Cryogenics **40** (2000) (2), pp. 145–147 (cited on page 53).

[50] B. W. Roberts, *Survey of superconductive materials and critical evaluation of selected properties*, J. Phys. Chem. Ref. Data **5** (1976) (3), pp. 581–822 (cited on page 53).

[51] R. B. Stephens, *Low-Temperature Specific Heat and Thermal Conductivity of Noncrystalline Dielectric Solids*, Phys. Rev. B **8** (1973) (6), pp. 2896–2905 (cited on page 53).

[52] G. Ventura and V. Martelli, *Very low temperature thermal conductivity of Kevlar 49*, Cryogenics **49** (2009) (7), pp. 376–377 (cited on page 53).

[53] DuPont, *Kevlar Technical Guide* (cited on page 53).

[54] K. Sugii, M. Shimozawa, D. Watanabe, Y. Suzuki, M. Halim, M. Kimata, Y. Matsumoto, S. Nakatsuji and M. Yamashita, *Thermal Hall Effect in a Phonon-Glass $Ba_3CuSb_2O_9$*, Phys. Rev. Lett. **118** (2017) (14), p. 145902 (cited on page 56).

[55] H.-L. Kim, M. J. Coak, J. C. Baglo, K. Murphy, R. W. Hill, M. Sutherland, M. C. Hatnean, G. Balakrishnan and J.-G. Park, *Modular thermal Hall effect measurement setup for fast-turnaround screening of materials over wide temperature range using capacitive thermometry*, Rev. Sci. Instrum. **90** (2019) (10), p. 103904 (cited on page 57).

[56] C. Tinsman, G. Li, C. Su, T. Asaba, B. Lawson, F. Yu and L. Li, *Probing the thermal Hall effect using miniature capacitive strontium titanate thermometry*, Appl. Phys. Lett **108** (2016) (26), p. 261905 (cited on page 57).

[57] G. Grissonnanche, F. Laliberté, S. Dufour-Beauséjour, M. Matusiak, S. Badoux, F. F. Tafti, B. Michon, A. Riopel, O. Cyr-Choinière, J. C. Baglo, B. J. Ramshaw, R. Liang, D. A. Bonn, W. N. Hardy, S. Krämer, D. LeBoeuf, D. Graf, N. Doiron-Leyraud and L. Taillefer, *Wiedemann-Franz law in the underdoped cuprate superconductor $YBa_2Cu_3O_y$*, Phys. Rev. B **93** (2016) (6), p. 64513 (cited on page 57).

[58] D. Zhao, X. Qian, X. Gu, S. A. Jajja and R. Yang, *Measurement Techniques for Thermal Conductivity and Interfacial Thermal Conductance of Bulk and Thin Film Materials*, J. Electron. Packag. **138** (2016) (4) (cited on page 58).

[59] D. R. Flynn, *Thermal Conductivity of Loose-Fill Materials by a Radial-Heat-Flow Method* (Springer US, 1992), pp. 33–75 (cited on page 58).

[60] B. M. Zawilski, R. T. Littleton and T. M. Tritt, *Description of the parallel thermal conductance technique for the measurement of the thermal conductivity of small diameter samples*, Rev. Sci. Instrum. **72** (2001) (3), pp. 1770–1774 (cited on page 58).

[61] O. Maldonado, *Pulse method for simultaneous measurement of electric thermopower and heat conductivity at low temperatures*, Cryogenics **32** (1992) (10), pp. 908–912 (cited on page 59).

[62] D. G. Cahill, *Thermal conductivity measurement from 30 to 750 K: the 3ω method*, Rev. Sci. Instrum. **61** (1990) (2), pp. 802–808 (cited on page 59).

[63] V. Mishra, C. L. Hardin, J. E. Garay and C. Dames, *A 3 omega method to measure an arbitrary anisotropic thermal conductivity tensor*, Rev. Sci. Instrum. **86** (2015) (5), p. 54902 (cited on page 59).

[64] R. Bachmann, F. J. DiSalvo, T. H. Geballe, R. L. Greene, R. E. Howard, C. N. King, H. C. Kirsch, K. N. Lee, R. E. Schwall, H. Thomas and R. B. Zubeck, *Heat Capacity Measurements on Small Samples at Low Temperatures*, Rev. Sci. Instrum. **43** (1972) (2), pp. 205–214 (cited on pages 60, 61, 71, 168).

[65] M. Brando, *Development of a relaxation calorimeter for temperatures between 0.05 and 4 K*, Rev. Sci. Instrum. **80** (2009) (9), p. 95112 (cited on page 62, 62).

[66] Quantum Design, *Physical Property Measurement System - Heat Capacity Option User's Manual* (2004) (cited on pages 64, 87, 87, 145).

[67] O. J. Entwisle, *A Study of Magnetic Fluctuations and Ordering in Uranium Compounds by Heat Capacity and Neutron Scattering Measurements*, Ph.D. thesis, University of Edinburgh (2018) (cited on pages 64, 66, 70).

[68] N. Samkharadze, A. Kumar and G. A. Csáthy, *A New Type of Carbon Resistance Thermometer with Excellent Thermal Contact at Millikelvin Temperatures*, J. Low Temp. Phys **160** (2010) (5), pp. 246–253 (cited on page 66).

[69] Y. Volokitin, R. C. Thiel and L. J. de Jongh, *Heat capacity of thick-film resistor thermometers and pure RuO_2 at low temperatures*, Cryogenics **34** (1994) (9), pp. 771–773 (cited on page 70).

[70] A. L. Dawson and D. H. Ryan, *Heat capacity of silver paint*, Rev. Sci. Instrum. **67** (1996) (7), pp. 2648–2649 (cited on page 70).

[71] S. Riegel and G. Weber, *A dual-slope method for specific heat measurements*, J. Phys. E Sci. Instrum. **19** (1986) (10), pp. 790–791 (cited on page 72).

[72] G. M. Schmiedeshoff, N. A. Fortune, J. S. Brooks and G. R. Stewart, *Computercontrolled, small sample ac calorimetry at low temperatures and in high magnetic fields*, Rev. Sci. Instrum. **58** (1987) (9), pp. 1743–1745 (cited on page 72).

[73] H. Wilhelm, *AC-Calorimetry at High Pressure and Low Temperature* (Springer Berlin Heidelberg, 2003), pp. 889–913 (cited on page 72).

[74] T. Satoshi, N. Takashi, Y. Yukio, K. Yoshiaki, S. Masatoshi, N. Takashi, K. Masaaki and S. Kazuhiro, *Spin Gap Behavior of S=1/2 Quasi-Two-Dimensional System CaV_4O_9*, J. Phys. Soc. Jpn **64** (1995) (8), pp. 2758–2761 (cited on page 73).

[75] S. Miyahara and K. Ueda, *Theory of the orthogonal dimer Heisenberg spin model for $SrCu_2(BO_3)_2$*, J. Phys. Condens. Matter **15** (2003) (9), pp. R327–R366 (cited on pages 73, 75).

[76] B. S. Shastry and B. Sutherland, *Exact ground state of a quantum mechanical antiferromagnet*, Physica B+C **108** (1981) (1), pp. 1069–1070 (cited on pages 73, 74).

[77] H. Kageyama, K. Yoshimura, R. Stern, N. V. Mushnikov, K. Onizuka, M. Kato, K. Kosuge, C. P. Slichter, T. Goto and Y. Ueda, *Exact Dimer Ground State and Quantized Magnetization Plateaus in the Two-Dimensional Spin System $SrCu_2(BO_3)_2$*, Phys. Rev. Lett. **82** (1999) (15), pp. 3168–3171 (cited on page 73).

[78] H. Kageyama, K. Onizuka, T. Yamauchi, Y. Ueda, S. Hane, H. Mitamura, T. Goto, K. Yoshimura and K. Kosuge, *Anomalous Magnetizations in Single Crystalline $SrCu_2(BO_3)_2$*, J. Phys. Soc. Jpn **68** (1999) (6), pp. 1821–1823 (cited on pages 73, 76).

[79] J. B. Goodenough, *Theory of the Role of Covalence in the Perovskite-Type Manganites [La,M(II)]MnO_3*, Phys. Rev. **100** (1955) (2), pp. 564–573 (cited on page 74).

[80] R. W. Smith and D. A. Keszler, *Synthesis, structure, and properties of the orthoborate $SrCu_2(BO_3)_2$*, J. Solid State Chem. **93** (1991) (2), pp. 430–435 (cited on page 74).

[81] H. Kageyama, *An Experimental Realization of the Shastry-Sutherland Model*, in *Frontiers in Magnetic Materials* (Springer Berlin Heidelberg, 2005), pp. 611–651 (cited on pages 74, 79).

[82] A. Koga and N. Kawakami, *Quantum Phase Transitions in the Shastry-Sutherland Model for $SrCu_2(BO_3)_2$*, Phys. Rev. Lett. **84** (2000) (19), pp. 4461–4464 (cited on page 75).

[83] E. Manousakis, *The spin-$\frac{1}{2}$ Heisenberg antiferromagnet on a square lattice and its application to the cuprous oxides*, Rev. Mod. Phys. **63** (1991) (1), pp. 1–62 (cited on page 75).

[84] H. Nojiri, H. Kageyama, K. Onizuka, Y. Ueda and M. Motokawa, *Direct Observation of the Multiple Spin Gap Excitations in Two-Dimensional Dimer System $SrCu_2(BO_3)_2$*, J. Phys. Soc. Jpn **68** (1999), p. 2906 (cited on pages 76, 77, 88, 91, 103).

[85] R. L. Carlin, *Magnetochemistry* (Springer Berlin Heidelberg, 1986) (cited on page 77).

[86] H. Kageyama, M. Nishi, N. Aso, K. Onizuka, T. Yosihama, K. Nukui, K. Kodama, K. Kakurai and Y. Ueda, *Direct Evidence for the Localized Single-Triplet Excitations and the Dispersive Multitriplet Excitations in*

$SrCu_2(BO_3)_2$, Phys. Rev. Lett. **84** (2000) (25), pp. 5876–5879 (cited on pages 77, 78, 88, 91, 98, 103).

[87] H. Kageyama, H. Suzuki, M. Nohara, K. Onizuka, H. Takagi and Y. Ueda, *Specific heat study of $SrCu_2(BO_3)_2$*, Physica B Condens. **281-282** (2000), pp. 667–668 (cited on page 77).

[88] S. Miyahara and K. Ueda, *Thermodynamic Properties of Three-Dimensional Orthogonal Dimer Model for $SrCu_2(BO_3)_2$*, J. Phys. Soc. Jpn **69 Suppl.B** (2000), pp. 72–77 (cited on pages 77, 77, 89, 89, 90, 104).

[89] S. Takahiro, H. Yuki, H. Keigo, O. Susumu, O. Hitoshi, U. Yoshiya, K. Kazutaka and K. Yoji, *Direct Observation of the Quantum Phase Transition of $SrCu_2(BO_3)_2$ by High-Pressure and Terahertz Electron Spin Resonance*, J. Phys. Soc. Jpn **87** (2018) (3), p. 33701 (cited on page 78).

[90] S. Haravifard, A. Banerjee, J. van Wezel, D. M. Silevitch, A. M. dos Santos, J. C. Lang, E. Kermarrec, G. Srajer, B. D. Gaulin, J. J. Molaison, H. A. Dabkowska and T. F. Rosenbaum, *Emergence of long-range order in sheets of magnetic dimers*, Proc. Natl. Acad. Sci. **111** (2014) (40), pp. 14372 LP – 14377 (cited on page 78).

[91] N. D. Mermin and H. Wagner, *Absence of Ferromagnetism or Antiferromagnetism in One- or Two-Dimensional Isotropic Heisenberg Models*, Phys. Rev. Lett. **17** (1966) (22), pp. 1133–1136 (cited on page 78).

[92] C. Knetter, A. Bühler, E. Müller-Hartmann and G. S. Uhrig, *Dispersion and Symmetry of Bound States in the Shastry-Sutherland Model*, Phys. Rev. Lett. **85** (2000) (18), pp. 3958–3961 (cited on page 78).

[93] O. Kenzo, K. Hiroshi, N. Yasuo, K. Koichi, U. Yutaka and G. Tsuneaki, *1/3 Magnetization Plateau in $SrCu_2(BO_3)_2$ - Stripe Order of Excited Triplets -*, J. Phys. Soc. Jpn **69** (2000) (4), pp. 1016–1018 (cited on page 79).

[94] T. Momoi and K. Totsuka, *Magnetization plateaus as insulator-superfluid transitions in quantum spin systems*, Phys. Rev. B **61** (2000) (5), pp. 3231–3234 (cited on page 79).

[95] N. Hiroyuki, K. Hiroshi, U. Yutaka and M. Mitsuhiro, *ESR Study on the Excited State Energy Spectrum of $SrCu_2(BO_3)_2$ A Central Role of Multiple-Triplet Bound States*, J. Phys. Soc. Jpn **72** (2003) (12), pp. 3243–3253 (cited on page 79).

[96] B. D. Gaulin, S. H. Lee, S. Haravifard, J. P. Castellan, A. J. Berlinsky, H. A. Dabkowska, Y. Qiu and J. R. D. Copley, *High-Resolution Study of Spin Excitations in the Singlet Ground State of $SrCu_2(BO_3)_2$*, Phys. Rev. Lett. **93** (2004) (26), p. 267202 (cited on pages 79, 80).

[97] T. Moriya, *Anisotropic Superexchange Interaction and Weak Ferromagnetism*, Phys. Rev. **120** (1960) (1), pp. 91–98 (cited on page 80).

[98] K. Sparta, G. J. Redhammer, P. Roussel, G. Heger, G. Roth, P. Lemmens, A. Ionescu, M. Grove, G. Güntherodt, F. Hüning, H. Lueken, H. Kageyama, K. Onizuka and Y. Ueda, *Structural phase transition in the 2D spin dimer compound $SrCu_2(BO_3)_2$*, Eur. Phys. J. B **19** (2001) (4), pp. 507–516 (cited on page 80).

[99] J. Romhányi, K. Penc and R. Ganesh, *Hall effect of triplons in a dimerized quantum magnet*, Nat. Commun **6** (2015), pp. 6805 EP – (cited on pages 81, 82, 83, 84, 85, 85, 86, 97, 97, 98, 98, 99, 104).

[100] Y. F. Cheng, O. Cépas, P. W. Leung and T. Ziman, *Magnon dispersion and anisotropies in $SrCu_2(BO_3)_2$*, Phys. Rev. B **75** (2007) (14), p. 144422 (cited on page 81).

[101] S. Sachdev and R. N. Bhatt, *Bond-operator representation of quantum spins: Mean-field theory of frustrated quantum Heisenberg antiferromagnets*, Phys. Rev. B **41** (1990) (13), pp. 9323–9329 (cited on page 81).

[102] J. Romhányi, K. Totsuka and K. Penc, *Effect of Dzyaloshinskii-Moriya interactions on the phase diagram and magnetic excitations of $SrCu_2(BO_3)_2$*, Phys. Rev. B **83** (2011) (2), p. 24413 (cited on page 81).

[103] K. Kakurai, K. Nukui, N. Aso, M. Nishi, H. Kadowaki, H. Kageyama, Y. Ueda, L.-P. Regnault and O. Cépas, *Neutron Scattering Investigation on Quantum Spin System $SrCu_2(BO_3)_2$*, Prog. Theor. Phys., Suppl. **159** (2005), pp. 22–32 (cited on page 84).

[104] P. A. McClarty, F. Krüger, T. Guidi, S. F. Parker, K. Refson, A. W. Parker, D. Prabhakaran and R. Coldea, *Topological triplon modes and bound states in a Shastry-Sutherland magnet*, Nat. Phys **13** (2017), p. 736 (cited on pages 86, 86, 97, 97, 98, 99, 104).

[105] S. Zherlitsyn, S. Schmidt, B. Wolf, H. Schwenk, B. Lüthi, H. Kageyama, K. Onizuka, Y. Ueda and K. Ueda, *Sound-wave anomalies in $SrCu_2(BO_3)_2$*, Phys. Rev. B **62** (2000) (10), pp. R6097—-R6099 (cited on pages 88, 93).

[106] H. Kageyama, K. Onizuka, Y. Ueda, M. Nohara, H. Suzuki and H. Takagi, *Low-temperature specific heat study of $SrCu_2(BO_3)_2$ with an exactly solvable ground state*, J. Low Temp. Phys **90** (2000), pp. 129–132 (cited on pages 88, 91, 103).

[107] G. A. Jorge, R. Stern, M. Jaime, N. Harrison, J. Bonč, S. El Shawish, C. D. Batista, H. A. Dabkowska and B. D. Gaulin, *Crystal symmetry and high-magnetic-field specific heat of $SrCu_2(BO_3)_2$*, Phys. Rev. B **71** (2005) (9), p. 92403 (cited on pages 89, 89, 104).

[108] A. N. Vasil'ev, M. M. Markina, A. V. Inyushkin and H. Kageyama, *Thermal conductivity and specific heat of $SrCu_2(BO_3)_2$: A quasi-two-dimensional metal oxide compound with a spin gap*, J. Exp. Theor. Phys **73** (2001) (11), pp. 633–636 (cited on page 94).

[109] M. Hofmann, T. Lorenz, G. S. Uhrig, H. Kierspel, O. Zabara, A. Freimuth, H. Kageyama and Y. Ueda, *Strong Damping of Phononic Heat Current by Magnetic Excitations in $SrCu_2(BO_3)_2$*, Phys. Rev. Lett. **87** (2001) (4), p. 47202 (cited on pages 94, 95, 104).

[110] R. Matsumoto and S. Murakami, *Theoretical Prediction of a Rotating Magnon Wave Packet in Ferromagnets*, Phys. Rev. Lett. **106** (2011) (19), p. 197202 (cited on page 98).

[111] M. Mena, R. S. Perry, T. G. Perring, M. D. Le, S. Guerrero, M. Storni, D. T. Adroja, C. Rüegg and D. F. McMorrow, *Spin-Wave Spectrum of the Quantum Ferromagnet on the Pyrochlore Lattice $Lu_2V_2O_7$*, Phys. Rev. Lett. **113** (2014) (4), p. 47202 (cited on pages 100, 103, 103).

[112] M. Elhajal, B. Canals, R. Sunyer and C. Lacroix, *Ordering in the pyrochlore antiferromagnet due to Dzyaloshinsky-Moriya interactions*, Phys. Rev. B **71** (2005) (9), p. 94420 (cited on page 100).

[113] R. Joynt and L. Taillefer, *The superconducting phases of UPt_3*, Rev. Mod. Phys. **74** (2002) (1), pp. 235–294 (cited on pages 105, 107, 108, 108, 120).

[114] A. De Visser, A. Menovsky and J. J. M. Franse, *UPt_3, heavy fermions and superconductivity*, Physica B+C **147** (1987) (1), pp. 81–160 .

[115] J. A. Sauls, *The order parameter for the superconducting phases of UPt_3*, Adv. Phys **43** (1994) (1), pp. 113–141 (cited on pages 105, 108, 109).

[116] R. A. Fisher, S. Kim, B. F. Woodfield, N. E. Phillips, L. Taillefer, K. Hasselbach, J. Flouquet, A. L. Giorgi and J. L. Smith, *Specific heat of UPt_3: Evidence for unconventional superconductivity*, Phys. Rev. Lett. **62** (1989) (12), pp. 1411–1414 (cited on pages 106, 106, 166).

[117] B. Lussier, B. Ellman and L. Taillefer, *Anisotropy of Heat Conduction in the Heavy Fermion Superconductor UPt_3*, Phys. Rev. Lett. **73** (1994) (24), pp. 3294–3297 (cited on page 106).

[118] G. Aeppli, E. Bucher, C. Broholm, J. K. Kjems, J. Baumann and J. Hufnagl, *Magnetic order and fluctuations in superconducting UPt_3*, Phys. Rev. Lett. **60** (1988) (7), pp. 615–618 (cited on pages 106, 125).

[119] N. H. van Dijk, P. Rodière, B. Fåk, A. Huxley and J. Flouquet, *Weak antiferromagnetic order and superconductivity in UPt_3 studied by neutron scattering*, Physica B Condens. Matter **319** (2002) (1), pp. 220–232 (cited on pages 106, 125).

[120] A. Huxley, P. Rodière, D. M. Paul, N. van Dijk, R. Cubitt and J. Flouquet, *Realignment of the flux-line lattice by a change in the symmetry of superconductivity in UPt_3*, Nature **406** (2000) (6792), pp. 160–164 (cited on pages 107, 111, 133).

[121] S. Adenwalla, S. W. Lin, Q. Z. Ran, Z. Zhao, J. B. Ketterson, J. A. Sauls, L. Taillefer, D. G. Hinks, M. Levy and B. K. Sarma, *Phase diagram of UPt_3 from ultrasonic velocity measurements*, Phys. Rev. Lett. **65** (1990) (18), pp. 2298–2301 (cited on page 106).

[122] S. Sundar, S. Gheidi, K. Akintola, A. M. Côté, S. R. Dunsiger, S. Ran, N. P. Butch, S. R. Saha, J. Paglione and J. E. Sonier, *Coexistence of ferromagnetic fluctuations and superconductivity in the actinide superconductor UTe_2*, Phys. Rev. B **100** (2019) (14), p. 140502 (cited on pages 107, 142, 157).

[123] T. Hattori, Y. Ihara, Y. Nakai, K. Ishida, Y. Tada, S. Fujimoto, N. Kawakami, E. Osaki, K. Deguchi, N. K. Sato and I. Satoh, *Superconductivity Induced by Longitudinal Ferromagnetic Fluctuations in UCoGe*, Phys. Rev. Lett. **108** (2012) (6), p. 66403 (cited on pages 107, 142, 157).

[124] S. M. Hayden, L. Taillefer, C. Vettier and J. Flouquet, *Antiferromagnetic order in UPt_3 under pressure: Evidence for a direct coupling to superconductivity*, Phys. Rev. B **46** (1992) (13), pp. 8675–8678 (cited on page 107).

[125] J. D. Strand, D. J. Van Harlingen, J. B. Kycia and W. P. Halperin, *Evidence for Complex Superconducting Order Parameter Symmetry in the Low-Temperature Phase of UPt_3 from Josephson Interferometry*, Phys. Rev. Lett. **103** (2009) (19), p. 197002 (cited on pages 109, 111).

[126] H. Suderow, J. P. Brison, A. Huxley and J. Flouquet, *Thermal conductivity and gap structure of the superconducting phases of UPt_3*, J. Low Temp. Phys **108** (1997) (1), pp. 11–30 (cited on pages 110, 110, 122).

[127] Y. Kohori, T. Kohara, H. Shibai, Y. Oda, Y. Kitaoka and K. Asayama, *Nuclear Magnetic Relaxation in the Heavy-Fermion Superconductor UPt_3*, J. Phys. Soc. Jpn **57** (1988) (2), pp. 395–397 (cited on page 110).

[128] H. Tou, Y. Kitaoka, K. Asayama, N. Kimura, Y. Ō, E. Yamamoto and K. Maezawa, *Odd-Parity Superconductivity with Parallel Spin Pairing in UPt_3: Evidence from ^{195}Pt Knight Shift Study*, Phys. Rev. Lett. **77** (1996) (7), pp. 1374–1377 (cited on page 110).

[129] A. Pustogow, Y. Luo, A. Chronister, Y.-S. Su, D. A. Sokolov, F. Jerzembeck, A. P. Mackenzie, C. W. Hicks, N. Kikugawa, S. Raghu, E. D. Bauer and S. E. Brown, *Constraints on the superconducting order parameter in Sr_2RuO_4 from oxygen-17 nuclear magnetic resonance*, Nature **574** (2019) (7776), pp. 72–75 (cited on page 110).

[130] J. D. Strand, D. J. Bahr, D. J. Van Harlingen, J. P. Davis, W. J. Gannon and W. P. Halperin, *The Transition Between Real and Complex Superconducting Order Parameter Phases in UPt_3*, Science **328** (2010) (5984), pp. 1368–1369 (cited on page 111).

[131] P. de Réotier, A. Huxley, A. Yaouanc, J. Flouquet, P. Bonville, P. Imbert, P. Pari, P. C. M. Gubbens and A. M. Mulders, *Absence of zero field muon spin relaxation induced by superconductivity in the B phase of UPt_3*, Phys. Lett **205** (1995) (2), pp. 239–243 (cited on page 111).

[132] Y. Machida, A. Itoh, Y. So, K. Izawa, Y. Haga, E. Yamamoto, N. Kimura, Y. Onuki, Y. Tsutsumi and K. Machida, *Twofold Spontaneous Symmetry Breaking in the Heavy-Fermion Superconductor UPt_3*, Phys. Rev. Lett. **108** (2012) (15), p. 157002 (cited on page 111).

[133] E. R. Schemm, W. J. Gannon, C. M. Wishne, W. P. Halperin and A. Kapitulnik, *Observation of broken time-reversal symmetry in the heavy-fermion superconductor UPt_3*, Science **345** (2014) (6193), pp. 190–193 (cited on pages 111, 129).

[134] K. Nomura, S. Ryu, A. Furusaki and N. Nagaosa, *Cross-Correlated Responses of Topological Superconductors and Superfluids*, Phys. Rev. Lett. **108** (2012) (2), p. 26802 (cited on page 114).

[135] P. Goswami and L. Balicas, *Topological properties of possible Weyl superconducting states of URu_2Si_2* (2013) (cited on page 114).

[136] H. Ikegami, Y. Tsutsumi and K. Kono, *Chiral Symmetry Breaking in Superfluid ^{3}He-A*, Science **341** (2013) (6141), pp. 59–62 (cited on page 116).

[137] L. Taillefer, J. Flouquet and W. Joss, *High-field magnetoresistance of UPt_3*, J. Magn. Magn. Mater **76-77** (1988), pp. 218–220 (cited on page 120).

[138] N. Kimura, R. Settai, Y. nuki, H. Toshima, E. Yamamoto, K. Maezawa, H. Aoki and H. Harima, *Magnetoresistance and de Haas-van Alphen Effect in UPt_3*, J. Phys. Soc. Jpn **64** (1995) (10), pp. 3881–3889 (cited on page 120).

[139] K. Behnia, L. Taillefer, J. Flouquet, D. Jaccard, K. Maki and Z. Fisk, *Thermal conductivity of superconducting UPt_3*, J. Low Temp. Phys **84** (1991) (3), pp. 261–278 (cited on page 122).

[140] C. Hurd, *The Hall Effect in Metals and Alloys* (Springer US, 2012) (cited on pages 123, 124, 128).

[141] N. Nagaosa, J. Sinova, S. Onoda, A. H. MacDonald and N. P. Ong, *Anomalous Hall effect*, Rev. Mod. Phys. **82** (2010) (2), pp. 1539–1592 (cited on pages 123, 125, 125, 125, 125, 125, 133).

[142] A. Fert and P. M. Levy, *Theory of the Hall effect in heavy-fermion compounds*, Phys. Rev. B **36** (1987) (4), pp. 1907–1916 (cited on page 123).

[143] S. Kambe, A. Huxley, J. Flouquet, A. G. M. Jansen and P. Wyder, *Hall resistivity in the heavy Fermion normal state of up to 26 T*, J. Phys. Condens. Matter **11** (1999) (1), pp. 221–227 (cited on pages 124, 125, 125, 126).

[144] A. K. Nayak, J. E. Fischer, Y. Sun, B. Yan, J. Karel, A. C. Komarek, C. Shekhar, N. Kumar, W. Schnelle, J. Kübler, C. Felser and S. S. P. Parkin, *Large anomalous Hall effect driven by a nonvanishing Berry curvature in the noncolinear antiferromagnet Mn_3Ge*, Sci. Adv **2** (2016) (4) (cited on page 125).

[145] T. Suzuki, R. Chisnell, A. Devarakonda, Y.-T. Liu, W. Feng, D. Xiao, J. W. Lynn and J. G. Checkelsky, *Large anomalous Hall effect in a half-Heusler antiferromagnet*, Nat. Phys **12** (2016) (12), pp. 1119–1123 (cited on page 125).

[146] G. J. McMullan, P. M. C. Rourke, M. R. Norman, A. D. Huxley, N. Doiron-Leyraud, J. Flouquet, G. G. Lonzarich, A. McCollam and S. R. Julian, *The Fermi surface and f-valence electron count of UPt_3*, New J. Phys **10** (2008) (5), p. 53029 (cited on page 125).

[147] J. Smit, *The spontaneous hall effect in ferromagnetics II*, Physica **24** (1958) (1), pp. 39–51 (cited on page 125).

[148] S. Nair, S. Wirth, S. Friedemann, F. Steglich, Q. Si and A. J. Schofield, *Hall effect in heavy fermion metals*, Adv. Phys **61** (2012) (5), pp. 583–664 (cited on page 125).

[149] E. A. Schuberth, K. Kloss, J. Schupp and K. Andres, *Specific heat and magnetic susceptibility of UPt_3 and UBe_{13} at mK-temperatures*, Zeitschrift für Physik B Condensed Matter **97** (1995) (1), pp. 55–58 (cited on page 126).

[150] Y. Koike, N. Metoki, N. Kimura, E. Yamamoto, Y. Haga, Y. nuki and K. Maezawa, *Neutron scattering study of the antiferromagnetic ordering in UPt_3 at mK-temperatures*, Physica B Condens. **259-261** (1999), pp. 662–663 (cited on page 126).

[151] K. E. Avers, W. J. Gannon, S. J. Kuhn, W. P. Halperin, J. A. Sauls, L. DeBeer-Schmitt, C. D. Dewhurst, J. Gavilano, G. Nagy, U. Gasser and M. R. Eskildsen, *Broken time-reversal symmetry in the topological superconductor UPt_3*, Nat. Phys **16** (2020) (5), pp. 531–535 (cited on page 130).

[152] A. Guillaume, *Transitions de phases dans les fermions lourds sous contrainte uniaxiale*, Ph.D. thesis, Université Joseph Fourier (1999) (cited on page 131).

[153] R. G. Mints and A. L. Rakhmanov, *Critical state stability in type-II superconductors and superconducting-normal-metal composites*, Rev. Mod. Phys. **53** (1981) (3), pp. 551–592 (cited on page 131).

[154] J. G. Checkelsky, R. Thomale, L. Li, G. F. Chen, J. L. Luo, N. L. Wang and N. P. Ong, *Thermal Hall conductivity as a probe of gap structure in multiband superconductors: The case of* $Ba_{1-x}K_xFe_2As_2$, Phys. Rev. B **86** (2012) (18), p. 180502 (cited on page 132).

[155] K. Krishana, J. M. Harris and N. P. Ong, *Quasiparticle Mean Free Path in* $YBa_2Cu_3O_7$ *Measured by the Thermal Hall Conductivity*, Phys. Rev. Lett. **75** (1995) (19), pp. 3529–3532 (cited on pages 132, 133).

[156] Y. Kasahara, Y. Nakajima, K. Izawa, Y. Matsuda, K. Behnia, H. Shishido, R. Settai and Y. Onuki, *Anomalous quasiparticle transport in the superconducting state of* $CeCoIn_5$, Phys. Rev. B **72** (2005) (21), p. 214515 (cited on page 132).

[157] R. M. Cleary, *Scattering of Single-Particle Excitations by a Vortex in a Clean Type-II Superconductor*, Phys. Rev. **175** (1968) (2), pp. 587–596 (cited on page 133).

[158] P. Coleman, *Heavy Fermions: Electrons at the Edge of Magnetism* (John Wiley & Sons, Ltd, 2007) (cited on pages 136, 139, 141).

[159] A. Sumiyama, Y. Oda, H. Nagano, Y. nuki, K. Shibutani and T. Komatsubara, *Coherent Kondo State in a Dense Kondo Substance: CexLa1-xCu6*, J. Phys. Soc. Jpn **55** (1986) (4), pp. 1294–1304 (cited on pages 137, 138).

[160] P. Coleman, *Heavy Fermions and the Kondo Lattice: a 21st Century Perspective* (2015) (cited on page 137).

[161] P. Gegenwart, Q. Si and F. Steglich, *Quantum criticality in heavy-fermion metals*, Nat. Phys **4** (2008) (3), pp. 186–197 (cited on page 139).

[162] H. v. Löhneysen, A. Rosch, M. Vojta and P. Wölfle, *Fermi-liquid instabilities at magnetic quantum phase transitions*, Rev. Mod. Phys. **79** (2007) (3), pp. 1015–1075 (cited on page 141).

[163] H. v. Löhneysen, T. Pietrus, G. Portisch, H. G. Schlager, A. Schröder, M. Sieck and T. Trappmann, *Non-Fermi-liquid behavior in a heavy-fermion alloy at a magnetic instability*, Phys. Rev. Lett. **72** (1994) (20), pp. 3262–3265 (cited on page 141, 141).

[164] O. Trovarelli, C. Geibel, S. Mederle, C. Langhammer, F. M. Grosche, P. Gegenwart, M. Lang, G. Sparn and F. Steglich, $YbRh_2Si_2$*: Pronounced Non-Fermi-Liquid Effects above a Low-Lying Magnetic Phase Transition*, Phys. Rev. Lett. **85** (2000) (3), pp. 626–629 (cited on page 141, 141).

[165] S. Paschen, T. Lühmann, S. Wirth, P. Gegenwart, O. Trovarelli, C. Geibel, F. Steglich, P. Coleman and Q. Si, *Hall-effect evolution across a heavy-fermion quantum critical point*, Nature **432** (2004) (7019), pp. 881–885 (cited on page 141).

[166] A. C. Jacko, J. O. Fjærestad and B. J. Powell, *A unified explanation of the KadowakiWoods ratio in strongly correlated metals*, Nat. Phys **5** (2009) (6), pp. 422–425 (cited on page 141).

[167] A. Bianchi, R. Movshovich, I. Vekhter, P. G. Pagliuso and J. L. Sarrao, *Avoided Antiferromagnetic Order and Quantum Critical Point in $CeCoIn_5$*, Phys. Rev. Lett. **91** (2003) (25), p. 257001 (cited on page 142).

[168] H. Amitsuka, K. Kuwahara, M. Yokoyama, K. Tenya, T. Sakakibara, M. Mihalik and A. A. Menovský, *Non-Fermi-liquid behavior in $R_{1x}U_xRu_2Si_2$ (R=Th, Y and La; x0.07)*, Physica B Condens. Matter **281-282** (2000), pp. 326–331 (cited on page 142).

[169] P. A. Lee, T. M. Rice, J. W. Serene, L. J. Sham and J. W. Wilkins, *Theories of heavy-electron systems*, Comments on Condensed Matter Physics **12** (1986) (3), pp. 99–161 (cited on page 142).

[170] M. Kontani, T. Nishioka, Y. Hamaguchi, H. Matsui, H. Aruga Katori and T. Goto, *Magnetic Properties of Binary and Pseudobinary U-Au Heavy Fermion Systems*, J. Phys. Soc. Jpn **63** (1994) (9), pp. 3421–3430 (cited on page 143).

[171] R. Pöttgen, V. H. Tran, R.-D. Hoffmann, D. Kaczorowski and R. Troc, *Crystal structure and physical properties of UAuSi and UAu_2*, J. Mater. Chem. **6** (1996) (3), pp. 429–434 (cited on pages 143, 143, 144, 202).

[172] J. L. Schmehr, *Incommensurate magnetism in UAu_2*, Ph.D. thesis, University of Edinburgh (2015) (cited on pages 143, 143, 143, 146, 188).

[173] C. D. O'Neill, J. L. Schmehr, H. D. J. Keen, D. A. Sokolov, A. Hermann, D. Wermeille, Manuel, F. Kruger and A. D. Huxley, *Non-Fermi liquid behaviour below the Néel temperature in the frustrated heavy Fermion magnet UAu_2* (2020) (cited on pages 144, 144, 144, 144, 147, 150, 153, 153).

[174] U. Walter, *Treating crystal field parameters in lower than cubic symmetries*, J. Phys. Chem. Solids **45** (1984) (4), pp. 401–408 (cited on page 146).

[175] N. J. Stone, *Table of nuclear magnetic dipole and electric quadrupole moments*, At. Data Nucl. Data Tables **90** (2005) (1), pp. 75–176 (cited on pages 147, 153).

[176] L. Zhu, M. Garst, A. Rosch and Q. Si, *Universally Diverging Grüneisen Parameter and the Magnetocaloric Effect Close to Quantum Critical Points*, Phys. Rev. Lett. **91** (2003) (6), p. 66404 (cited on page 150).

[177] P. D. Sacramento and P. Schlottmann, *Low-temperature properties of a two-level system interacting with conduction electrons: An application of the overcompensated multichannel Kondo model*, Phys. Rev. B **43** (1991) (16), pp. 13294–13304 (cited on page 150).

[178] D. L. Cox and A. Zawadowski, *Exotic Kondo effects in metals: Magnetic ions in a crystalline electric field and tunnelling centres*, Adv. Phys **47** (1998) (5), pp. 599–942 (cited on page 150).

[179] D. L. Cox and M. Jarrell, *The two-channel Kondo route to non-Fermi-liquid metals*, J. Phys. Condens. Matter **8** (1996) (48), pp. 9825–9853 (cited on page 151).

[180] S. S. Saxena, P. Agarwal, K. Ahilan, F. M. Grosche, R. K. W. Haselwimmer, M. J. Steiner, E. Pugh, I. R. Walker, S. R. Julian, P. Monthoux, G. G. Lonzarich, A. Huxley, I. Sheikin, D. Braithwaite and J. Flouquet, *Superconductivity on the border of itinerant-electron ferromagnetism in UGe_2*, Nature **406** (2000) (6796), pp. 587–592 (cited on pages 155, 157).

[181] F. Lévy, I. Sheikin, B. Grenier and A. D. Huxley, *Magnetic Field-Induced Superconductivity in the Ferromagnet URhGe*, Science **309** (2005) (5739), pp. 1343 LP – 1346 (cited on pages 155, 157).

[182] N. T. Huy, A. Gasparini, D. E. de Nijs, Y. Huang, J. C. P. Klaasse, T. Gortenmulder, A. de Visser, A. Hamann, T. Görlach and H. v. Löhneysen, *Superconductivity on the Border of Weak Itinerant Ferromagnetism in UCoGe*, Phys. Rev. Lett. **99** (2007) (6), p. 67006 (cited on pages 155, 157).

[183] S. Ran, I.-L. Liu, Y. S. Eo, D. J. Campbell, P. M. Neves, W. T. Fuhrman, S. R. Saha, C. Eckberg, H. Kim, D. Graf, F. Balakirev, J. Singleton, J. Paglione and N. P. Butch, *Extreme magnetic field-boosted superconductivity*, Nat. Phys **15** (2019) (12), pp. 1250–1254 (cited on pages 155, 156).

[184] S. Ran, C. Eckberg, Q.-P. Ding, Y. Furukawa, T. Metz, S. R. Saha, I.-L. Liu, M. Zic, H. Kim, J. Paglione and N. P. Butch, *Nearly ferromagnetic spin-triplet superconductivity*, Science **365** (2019) (6454), pp. 684–687 (cited on pages 155, 155, 156, 156, 156, 158, 158, 158, 159, 159, 159, 162, 162, 164, 166, 169).

[185] A. Dai, N. Ai, H. Fuminori, L. DeXin, H. Yoshiya, S. Yusei, S. Y. J., K. Georg, B. Jean-Pascal, P. Alexandre, B. Daniel, L. Gerard, N. Qun, V. Michal, H. Hisatomo and F. Jacques, *Unconventional Superconductivity in Heavy Fermion UTe_2*, J. Phys. Soc. Jpn **88** (2019) (4), p. 43702 (cited on pages 155, 155, 155, 159, 161, 162, 163, 163, 164, 164, 164, 164, 164, 165, 166).

[186] I. Shusaku, K. Yoshimitsu, M. Atsushi, D. Chao, T. Masashi, F. Jacques, K. Koichi and A. Dai, *Thermodynamic Investigation of Metamagnetism in Pulsed High Magnetic Fields on Heavy Fermion Superconductor UTe_2*, J. Phys. Soc. Jpn **88** (2019) (8), p. 83705 (cited on pages 155, 162, 163, 164, 164).

[187] T. Metz, S. Bae, S. Ran, I.-L. Liu, Y. S. Eo, W. T. Fuhrman, D. F. Agterberg, S. M. Anlage, N. P. Butch and J. Paglione, *Point-node gap structure of the spin-triplet superconductor UTe_2*, Phys. Rev. B **100** (2019) (22), p. 220504 (cited on pages 155, 157, 157, 159, 162, 162, 163, 164, 164, 164, 166, 167).

[188] S. Kittaka, Y. Shimizu, T. Sakakibara, A. Nakamura, D. Li, Y. Homma, F. Honda, D. Aoki and K. Machida, *Orientation of point nodes and nonunitary triplet pairing tuned by the easy-axis magnetization in UTe_2*, Phys. Rev. Research **2** (2020) (3), p. 32014 (cited on pages 155, 157, 158, 161, 162, 163, 164, 164, 164, 164, 165, 166, 168, 168).

[189] W. Suski, *Magnetic properties of uranium chalcogenides with composition close to UY_2*, J. Solid State Chem **7** (1973) (4), pp. 385–399 (cited on pages 155, 159).

[190] K. Stöwe, *Contributions to the Crystal Chemistry of Uranium Tellurides: III. Temperature-Dependent Structural Investigations on Uranium Ditelluride*, J. Solid State Chem **127** (1996) (2), pp. 202–210 (cited on pages 155, 159, 167).

[191] S. Ikeda, H. Sakai, D. Aoki, Y. Homma, E. Yamamoto, A. Nakamura, Y. Shiokawa, Y. Haga and Y. nuki, *Single Crystal Growth and Magnetic Properties of UTe_2*, J. Phys. Soc. Jpn **75** (2006) (Suppl), pp. 116–118 (cited on pages 155, 156, 158, 158, 158, 159, 169).

[192] A. M. Clogston, *Upper Limit for the Critical Field in Hard Superconductors*, Phys. Rev. Lett. **9** (1962) (6), pp. 266–267 (cited on page 156).

[193] S. Ran, H. Kim, I.-L. Liu, S. R. Saha, I. Hayes, T. Metz, Y. S. Eo, J. Paglione and N. P. Butch, *Enhancement and reentrance of spin triplet superconductivity in UTe_2 under pressure*, Phys. Rev. B **101** (2020) (14), p. 140503 (cited on page 157, 157).

[194] I. M. Hayes, D. S. Wei, T. Metz, J. Zhang, Y. S. Eo, S. Ran, S. R. Saha, J. Collini, N. P. Butch, D. F. Agterberg, A. Kapitulnik and J. Paglione, *Weyl Superconductivity in UTe_2* (2020) (cited on pages 157, 158, 168).

[195] A. D. Huxley, *Ferromagnetic superconductors*, Physica C **514** (2015), pp. 368–377 (cited on page 164).

[196] N. E. Phillips, *Nuclear Quadrupole and Electronic Heat Capacities of Bismuth*, Phys. Rev. **118** (1960) (3), pp. 644–647 (cited on pages 165, 213, 216).

[197] K. Ikushima, S. Tsutsui, Y. Haga, H. Yasuoka, R. E. Walstedt, N. M. Masaki, A. Nakamura, S. Nasu and Y. Ō, *First-order phase transition in UO_2: ^{235}U and ^{17}O NMR study*, Phys. Rev. B **63** (2001) (10), p. 104404 (cited on page 166).

[198] M. A. Tanatar, J. Paglione, S. Nakatsuji, D. G. Hawthorn, E. Boaknin, R. W. Hill, F. Ronning, M. Sutherland, L. Taillefer, C. Petrovic, P. C. Canfield and Z. Fisk, *Unpaired Electrons in the Heavy-Fermion Superconductor $CeCoIn_5$*, Phys. Rev. Lett. **95** (2005) (6), p. 67002 (cited on page 166).

[199] V. Hutanu, H. Deng, S. Ran, W. T. Fuhrman, H. Thoma and N. P. Butch, *Low-temperature crystal structure of the unconventional spin-triplet superconductor UTe_2 from single-crystal neutron diffraction*, Acta Crystallogr. B **76** (2020) (1), pp. 137–143 (cited on page 167).

[200] J. Als-Nielsen and D. Mcmorrow, *Elements of Modern X-Ray Physics* (John Wiley & Sons, Ltd, 2011) (cited on pages 175, 177, 178).

[201] A. Frano, *The Technique: Resonant X-ray Scattering* (2014), pp. 19–46 (cited on pages 180, 184, 185).

[202] M. Newville, *Fundamentals of XAFS*, Rev. Mineral. Geochem. **78** (2014) (1), pp. 33–74 (cited on pages 182, 184, 200).

[203] C. Vettier, *Resonant x-ray scattering from magnetic materials*, J. Magn. Magn. Mater **129** (1994) (1), pp. 59–65 (cited on pages 184, 186).

[204] J. P. Hannon, G. T. Trammell, M. Blume and D. Gibbs, *X-Ray Resonance Exchange Scattering*, Phys. Rev. Lett. **61** (1988) (10), pp. 1245–1248 (cited on page 187).

[205] J. P. Hill and D. F. McMorrow, *Resonant Exchange Scattering: Polarization Dependence and Correlation Function*, Acta Crystallogr. A **52** (1996) (2), pp. 236–244 (cited on page 187).

[206] C. A. U. Lawrence Berkeley Lab, *X-ray data booklet Revision*, Tech. rep. (1986) (cited on pages 189, 191).

[207] K. O. Kvashnina, H. C. Walker, N. Magnani, G. H. Lander and R. Caciuffo, *Resonant x-ray spectroscopy of uranium intermetallics at the $M_{4,5}$ edges of uranium*, Phys. Rev. B **95** (2017) (24), p. 245103 (cited on pages 191, 203, 204).

[208] B. T. Thole and G. van der Laan, *Linear relation between x-ray absorption branching ratio and valence-band spin-orbit expectation value*, Phys. Rev. A **38** (1988) (4), pp. 1943–1947 (cited on page 197).

[209] A. Rogalev and F. Wilhelm, *Magnetic circular dichroism in the hard X-ray range*, Phys. Met. Metallogr. **116** (2015) (13), pp. 1285–1336 (cited on pages 197, 198).

[210] K. T. Moore and G. van der Laan, *Nature of the* $5f$ *states in actinide metals*, Rev. Mod. Phys. **81** (2009) (1), pp. 235–298 (cited on pages 198, 200).

[211] G. van der Laan and B. T. Thole, *X-ray-absorption sum rules in* jj*-coupled operators and ground-state moments of actinide ions*, Phys. Rev. B **53** (1996) (21), pp. 14458–14469 (cited on page 198).

[212] R. Bès, M. Rivenet, P.-L. Solari, K. O. Kvashnina, A. C. Scheinost and P. M. Martin, *Use of HERFDXANES at the U* L_3*- and* M_4*-Edges To Determine the Uranium Valence State on* $[Ni(H_2O)_4]_3[U(OH,H_2O)(UO_2)_8O_{12}(OH)_3]$, Inorg. Chem **55** (2016) (9), pp. 4260–4270 (cited on pages 198, 199).

[213] F. Wilhelm, J. P. Sanchez and A. Rogalev, *Magnetism of uranium compounds probed by XMCD spectroscopy*, J. Phys. D: Appl. Phys **51** (2018) (33), p. 333001 (cited on pages 199, 200).

[214] C. H. Booth, Y. Jiang, D. L. Wang, J. N. Mitchell, P. H. Tobash, E. D. Bauer, M. A. Wall, P. G. Allen, D. Sokaras, D. Nordlund, T.-C. Weng, M. A. Torrez and J. L. Sarrao, *Multiconfigurational nature of 5f orbitals in uranium and plutonium intermetallics*, Proc. Natl. Acad. Sci. **109** (2012) (26), pp. 10205–10209 (cited on pages 203, 204).

[215] F. Pobell, *Matter and Methods at Low Temperatures*, 3rd ed. (Springer, 2007) (cited on page 211).

[216] E. Gopal, *Specific Heats at Low Temperatures* (Springer, 1966) (cited on page 211).

[217] C. P. Slichter, *Principles of Magnetic Resonance*, 3rd ed. (Springer Berlin Heidelberg, 1990) (cited on pages 214, 215).

[218] D. I. Bolef and R. K. Sundfors, *Nuclear Acoustic Resonance* (Academic Press, 1993) (cited on page 214).

[219] B. H. Suits, *Nuclear Quadrupole Resonance Spectroscopy*, in *Handbook of Applied Solid State Spectroscopy* (2006), p. 70 (cited on pages 215, 216).

Publications

Luke Pritchard Cairns, J.-Ph. Reid, Robin Perry, Dharmalingam Prabhakaran and Andrew Huxley - *Thermal Hall Effect of Topological Triplons in $SrCu_2(BO_3)_2$*, JPS Conf. Proc., **30**, 011089 (2020)

Luke Pritchard Cairns, Callum R Stevens, Christopher D O'Neill and Andrew Huxley - *Composition dependence of the superconducting properties of UTe_2*, J. Phys.: Condens. Matter, **32**, 415602 (2020)